A THEORETICAL STUDY OF THE PERFORMANCE OF RESISTOJET NOZZLES

A Thesis

presented for the Degree of

DOCTOR OF PHILOSOPHY

of the

UNIVERSITY OF SOUTHAMPTON

in the

Faculty of Engineering and Applied Science

by

I. EDWARDS

September 1972

ABSTRACT

FACULTY OF ENGINEERING AND APPLIED SCIENCE

AERONAUTICS AND ASTRONAUTICS

Doctor of Philosophy

A THEORETICAL STUDY OF THE PERFORMANCE OF RESISTOJET NOZZLES

Ian Edwards

The theoretical development of four computer models of resistojet nozzle performance is reported. Five main energy loss processes are accounted for; these are (i) frozen chemical rate processes, (ii) finite rate vibrational relaxation, (iii) incomplete expansion, (iv) viscous flow and (v) radial flow.

The nozzle flow is assumed to be composed of an inviscid core and a viscous boundary layer, where the boundary layer is represented by the patching together of similar solutions of the laminar boundary layer equations. General similar boundary layer equations have been developed which include the radial dependences accounting for transverse curvature. Four simplified classes of similar equations are identified, and extensive solutions have been obtained for the Falkner-Skan equation and a modified Falkner-Skan equation which includes the effects of transverse curvature, over the range of pressure gradient parameter, β, from 0. to 10. Vibrational relaxation is modelled by using an approximate sudden freezing criterion.

Performance predictions are presented for H_2, CH_4, CO_2 and NH_3 for plenum temperatures extending from 300 to 3000^{o}K and plenum pressures from 200 to 10 kNm^{-2}. A wide variety of nozzle geometries is also considered. The results are compared with the predictions of the slender channel model of Rae and with experimental measurements.

CONTENTS

List of Figures

List of Tables

NOTATION

A	Area
A and B	Constants in the Landau-Teller equation, eq. (4.29)
A_i	Polynomial coefficients used in eq. (4.15)
B	Reynolds number based on stagnation conditions and throat radius, $B = p_T(2H_T)^{\frac{1}{2}}R^*/\mu_T$
C_D	Discharge coefficient, eq. (2.40)
C_T	Thrust coefficient, eq. (2.49)
D_{12}	Binary diffusion coefficient
F	Thrust
G	Ratio of local to geometric radius, $G = r/R$
H	Total enthalpy per unit mass, $H = h + u^2/2$
H_{tr}	Transformed form factor
ΔH_f^o	Heat of formation
I_{sp}	Specific impulse, eq. (2.48)
Kn	Knudsen number
K_p	Equilibrium constant
K_1	Factor defined by eq. (5.22)
L	Nozzle wall length
M	Mach number
$\bar{M}$	Molecular weight
N	Momentum parameter
P	Power
Pr	Prandtl number, $Pr = \mu c_p/k$
P_1 to P_5	Boundary layer integrals of similar solutions, eqs. (3.68) to (3.72)
R	Nozzle radius
R_c	Radius of curvature at nozzle throat
R_u	Universal gas constant, $R_u = 1.987$ cal mole^{-1} $^oK^{-1}$
R_1	Nozzle inlet radius
R_2	Nozzle exit radius

$\hat{R}$	Specific gas constant, $\hat{R} = R_u/\bar{M}$
Re_{D^*}	Reynolds number based on throat diameter, $Re_{D^*} = 2\rho^* u^* R^*/\mu_T$
Re_L	Reynolds number based on wall length, $Re_L = \rho^* u^* L/\mu_T$
S	Dimensionless enthalpy function, $S = H/H_T - 1$
T	Temperature
V_j	Jet velocity
X_i	Mole fraction of i^{th} species
a and b	Constants used in eq. (5.1) to define shape of nozzle divergent section
c_f	Skin friction coefficient, eq. (3.64)
c_p^o	Molar heat, $c_p^o = \sum_{i=1}^{i=n} c_{p,i}^o$
c_p	Specific heat, $c_p = c_p^o/\bar{M}$
e_v	Vibrational energy per unit mass
f	Dimensionless stream function, eq. (3.26) also, mole fraction of undissociated NH_3 not included in equilibrium calculation
g	Dimensionless total enthalpy function, $g = H/H_e$
g_o	Acceleration due to gravity, $g_o = 9.80665\ ms^{-2}$
h	Static enthalpy per unit mass
k	Thermal conductivity
ℓ	Shear parameter
$\dot{m}$	Mass flow rate
n	Correlation parameter
p	Pressure
q	Distribution of heat sources in potential flow
q_w	Rate of heat transfer at wall
r	Local radius also, recovery factor , eq. (3.79)
s	Entropy per unit mass
u	Velocity in x-direction
v	Velocity in y-direction

x	Coordinate in direction parallel to wall
y	Coordinate in direction normal to wall
y_d	Distance from wall in radial plane, $y_d = y \cos \alpha$
z	Distance along axis
z_L	Axis length
z_D	Axial distance in divergent section (see figure on page 104)
α	Local wall angle
α_e	Effective nozzle half angle at exit
α_1, α_2	Degree of dissociation
β	Pressure gradient parameter, eq. (3.40)
γ	Ratio of specific heats, $\gamma = c_p^o/(c_p^o - R_u)$
δ	Boundary layer overall thickness
δ^*	Boundary layer displacement thickness
ϵ	Nozzle area ratio, ϵ = Exit area/Throat area
η	Transformed y-coordinate, eq. (3.23) With subscript, an efficiency
η_{c^*}	c^* efficiency, eq. (2.53)
η_e	Value of η for which $u/u_e = 0.995$
η_∞	Value of η for which $\lvert 1 - u/u_e \rvert \leq 10^{-5}$
θ	Boundary layer momentum thickness
θ_1	Nozzle wall angle at start of convergent section
θ_2	Nozzle wall angle at start of divergent section
λ	Ratio of density-viscosity product, $\lambda = \rho\mu/\rho_w\mu_w$
μ	Coefficient of viscosity
ν	Kinematic viscosity
ξ	Transformed x-coordinate, eq. (3.22)
ρ	Density
σ	Hypersonic parameter, $\sigma = u_e^2/H_e$
τ	Characteristic time
τ_D	Dissociation time
$\tau_{f\ell}$	Local flow time

ϕ	Factor in vibrational rate equation, eq. (4.30) also, quantity defined by eq. (5.23)
ψ	Stream function
ω	Exponent in viscosity-temperature power law, eq. (3.42)
Θ	Transverse curvature parameter, eq. (3.46)
Φ	Rate parameter used in eq. (4.34)

Superscripts

*	denotes throat
'	denotes differential
~	denotes transformed plane (Cohen and Reshotko theory)

Subscripts

C	denotes frozen chemical rate processes
D	denotes radial flow
E	denotes incomplete expansion
F	denotes frozen vibrational rate processes
H	denotes heater
N	denotes nozzle
R	denotes recombined state
Res	denotes resistojet
T	denotes total or stagnation
V	denotes viscous flow
a	denotes adiabatic wall
d	denotes radial plane
e	denotes freestream or inviscid core
eff	denotes effective inviscid flow
el	denotes electric
eq	denotes equilibrium conditions
ex	denotes nozzle exit plane
fp	denotes freezing point

g	denotes gas at entrance to nozzle
hl	denotes heater losses
j	denotes jet
mix	denotes mixture
nl	denotes nozzle losses
pr	denotes propellant at $300^{o}K$
trans	denotes transit
tr	denotes transformed plane (Cohen and Reshotko theory)
v	denotes vibration
w	denotes wall conditons

Acknowledgements

The author would like to thank the following people:

Foremost, Dr. R.E.W. Jansson, who, as project supervisor, has provided much help and encouragement in the course of the work and in the preparation of this thesis.

Professor K.N.C. Bray, for many illuminating discussions and useful suggestions.

Mr. W.T. Lord, of the Rocket Propulsion Establishment, Westcott, for his help, interest and encouragement.

Mr. A.G. Earl, of the Royal Aircraft Establishment, Farnborough, for numerous discussions on the practical difficulties involved in resistojet research and development.

Last, but not least, to Lynne, for typing this thesis and becoming my wife.

Chapter One Introduction

1.1 General Background

The work presented in this thesis originates from an interest in the use of resistojets for various propulsion duties on spacecraft. A subject of some importance in the design of resistojet systems is the performance of the resistojet motor. It is this topic which is examined here, and in particular theoretical models are reported of the energy loss processes found in the nozzle flow.

A resistojet motor is a low-thrust rocket, consisting of a heater and a convergent-divergent nozzle. It is essentially an energy conversion device in which the heater converts electric power to thermal energy by resistance heating, the heat subsequently being transferred to the gas stream, adding to the energy inherent in the propellant. Upon expansion through the nozzle the internal energy of the propellant is converted to kinetic energy. In a conventional chemical rocket, the heat release accompanying the chemical reaction between the fuel and oxidant provides an energy source, whereas in the resistojet motor the main source of energy comes from an external electric power supply. Thus of the forms of electric propulsion - electrothermal, electrostatic and electromagnetic - the resistojet provides the simplest example of electrothermal propulsion.[1] On account of its low thrust (less than 10 N) the resistojet, like all other forms of electrothermal propulsion, is suitable only for operation in a space environment.

The most important property of rocket performance is the exhaust velocity, which in an ideal situation is limited by the enthalpy per unit mass, or specific enthalpy, of the propellant. This in turn is limited by the heater stagnation temperature and therefore by the maximum temperature which can be tolerated by the resistojet structure. Propellants with the highest specific enthalpy are the gases with low molecular weight.

The gases suitable for use in resistojets which are considered here are hydrogen, methane, ammonia and carbon dioxide. While not a complete list of the possible propellants, these gases cover a wide range of performance capabilities, from an ideal exhaust velocity of 11.2 kms^{-1} for H_2 at a stagnation temperature of 3000°K (an upper temperature limit), down to 0.67 kms^{-1} for CO_2 at 300°K. In reality these theoretical values are never achieved, since the conversion of thermal energy to kinetic energy in the resistojet motor is not an ideal process. Thus Page et al [2] measured a jet velocity of 8.22 kms^{-1}, with a hydrogen resistojet at a temperature of 2400°K, compared to an ideal jet velocity of 9.36 kms^{-1}, in other words an energy conversion efficiency of 0.77. In this study it is intended, by taking into account the various energy loss processes occurring in the nozzle flow, to make more realistic predictions of resistojet nozzle performance.

The rest of this chapter is divided into four parts. In the next section the development of the resistojet motor and of the resistojet system are discussed, and useful applications to space missions are considered. The physics of the gas flow through the heater and nozzle is examined in section 1.3, and particular emphasis is given to the losses incurred in the nozzle flow. This is followed in section 1.4 by a review of the literature on theoretical performance of resistojets. In the final section the aims of this research are described, the features included in the model of nozzle performance are defined and the contents of this thesis are outlined.

1.2 Resistojet Engineering and Applications

The first published reference to the concept of a resistojet motor was due to Jack[3] in 1961, and it was a relatively straightforward task to demonstrate the concept's feasibility in the laboratory. Howard[4] reported in 1962 on the performance of a hydrogen resistojet, where, for

an input power of 30 kW, a thrust of 6.04 N was measured, giving a specific impulse of 846 seconds. Additional complication is encountered when considering a resistojet for use in space, since the motor is then part of an independent system. The hardware of this system consists basically of four parts; propellant tankage, power source, control equipment, i.e. electronics, valves and feed lines, and the motor itself. Two consumable quantities, the propellant flow and electric power provide the primary inputs to the resistojet motor. A schematic of the resistojet system is shown below.

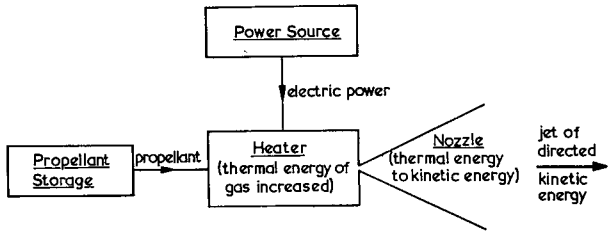

Resistojet System

In designing a system to operate in space, constraints are imposed which are not present in the laboratory. These constraints, affecting not only the resistojet system but the whole spacecraft, arise from:

(1) the limited mass which can be raised to a given orbit, and

(2) the limited amount of electric power available.

A major factor in the system design must be the mission for which it is required and a brief discussion of resistojet applications is in order.

Uses of resistojets fall into two broad categories, auxiliary propulsion and prime propulsion. Most spacecraft require some form of auxiliary propulsion for such functions as manoeuvring, station keeping and attitude control. Nearly all low-thrust (less than 10 N) systems used to date have been based on cold flow gas jets, e.g. the cold nitrogen jets on the Mariner space vehicles[5]. However by using a small amount of power, i.e. converting

a cold jet into a resistojet, weight savings and improved performance result. In this case the design involves trading-off the decreased propellant mass requirements against the increased mass of the power supply. Low-thrust resistojets, of the order of 50 mN, with power consumptions of the order of 10 - 200 W have been used, or are proposed for, the various satellite control duties.[6,7]

Lord,[8] and studies for the Manned Orbital Research Laboratory[9], have shown that the payload in final orbit can be increased significantly by injecting a satellite or spacecraft into a low parking orbit using a conventional chemical booster, and using large resistojets (thrust of order 1 N) to increase the orbital altitude by means of a spiral transfer trajectory, rather than by boosting the payload to altitude directly. The penalty is an increased transfer time. In a subsequent study Lord and Parkinson[10] have widened the scope of their work by demonstrating the advantages of combining resistojets with ion motors to produce mixed thruster systems of versatile performance. Recent calculations[11], using a two-stage transfer for large communications satellites, indicate that not only is a good trade-off between payload and transfer time possible, but also that the system offers substantial economic savings.

The importance of a mission analysis to the design of a resistojet system is that it specifies (i) the total impulse requirement and (ii) the power and mass allocations. In general the power and mass allocations are not independent of one another, and it is convenient to think of the electric power supply in terms of an equivalent mass. Solar arrays provide the usual power source for long duration space missions, so that the mass per unit power of the array is an important quantity. One approach to the design of resistojet systems is to minimise the system mass[12]. This involves an optimisation of several conflicting factors. The factors involved are:-

(1) Mass per unit power of the solar array.

(2) Mass of system hardware, i.e. propellant tankage, control

equipment, resistojet motor and thermal shielding.

(3) Mass of propellant, which depends on the propellant properties and on the performance of the resistojet motor.

It is the final factor which is investigated in this thesis.

The type of mission has obvious implications for the choice of propellant. Thus for missions of restricted lifetime, such as the orbital transfer of large space vehicles, hydrogen, with its large specific enthalpy and consequent high exhaust velocity, is the best choice of propellant.[8-10] For missions, such as satellite attitude control, in which resistojets would be operated in a pulsed mode over a period of several years, then the use of hydrogen, which has to be stored cryogenically and therefore has a restricted storage lifetime, is not feasible. For such duties other gases, such as ammonia and hydrazine, stored indefinitely as saturated liquids in a simple, thin-walled, pressure tank, are attractive propellants.[13] In manned space operations, the biowaste products of the environmental control/life support system such as carbon dioxide, methane and water can be used as resistojet propellants.[9,14] It follows that propellant supply and storage problems are then minimised, although intrinsically they are not such good propellants.

To sum up, however good the other components of the system, it is the performance of the resistojet motor which ultimately determines the usefulness of the system, so that prediction of the motor performance is very important. As already indicated the conversion of thermal energy to kinetic energy suffers from various losses, and in the next section the processes causing a reduction from the ideal performance are examined.

1.3 Gasdynamics of the Resistojet Motor

In order to simplify matters, attention is restricted in the present work to steady state operation, i.e. the resistojet motor receives a continuous supply of electric power and propellant. The models which are subsequently developed are therefore only strictly applicable to continuous operation, but it will be shown that as far as the nozzle performance is concerned these models can also be applied to pulsed operation.

1.3.1 Ideal Situation

In the ideal situation all the electric power transferred to the heater is used in increasing the thermal energy content of the propellant, in other words increasing the total enthalpy. Further, during expansion through the nozzle the propellant internal energy is converted into kinetic energy directed along the nozzle axis. Thus the energy put into the resistojet motor, by the propellant and that added as electrical energy, is converted entirely to jet energy at the nozzle exit.

There are several implications in this definition which are useful when considering the real situation. The assumption that all the electric power is converted into the internal energy of the propellant implies that no heat transfer losses occur through radiation or conduction from the resistojet body. It further implies that the gas flow through the heater and nozzle is non heat-conducting and inviscid. From a macroscopic viewpoint the gas is regarded simply as a thermal energy sink in the heater and as a kinetic energy source in the nozzle. At the microscopic level this definition demands that the internal energy processes react to changes in the equilibrium conditions with an infinitely fast rate. Since all the internal energy is assumed to be converted to kinetic energy, it is further implied that at exit from the nozzle the gas temperature is zero, so that all molecular and atomic excitation has ceased.

The ideal situation in terms of energy flow, i.e. power, is presented schematically below.

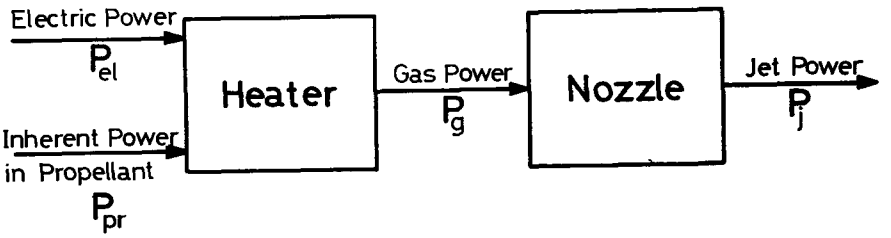

Ideal Resistojet Flow

A power balance for this ideal case gives

(a) Heater $$P_{el} + P_{pr} = P_g \tag{1.1}$$

(b) Nozzle $$P_g = P_j \tag{1.2}$$

(c) Overall $$P_{el} + P_{pr} = P_j \tag{1.3}$$

An overall resistojet efficiency is then

$$\eta_{Res} = \frac{P_j}{P_{el} + P_{pr}} \tag{1.4}$$

and in this case $\eta_{Res} = 1$

1.3.2 Real Situation

Some hint has already been given of the non-idealities occurring in the real flow. Thus, there are losses due to radiation from the heater directly to space, and due to conduction to the spacecraft body and nozzle, where it is subsequently lost by radiation. These heat transfer losses mean that not all of the electric energy is transferred to the propellant. Within the propellant flow there are various non-ideal gas-dynamic processes, not all necessarily causing a reduction in performance but complicating the picture. The gasdynamic problem is conveniently considered in two parts, (a) heater flow and (b) nozzle flow.

(a) Heater flow

There are a variety of heater designs (see, for instance Ref. 1, pages 104 - 105) and of the most recent configurations the most promising appear to be the concentric tubes scheme of Page et al[2] and the vortex heater of Murch and Krieve[15]. Two factors which may influence the performance of a resistojet heater are thermodynamic nonequilibrium and viscous flow. Considerations of these two phenomena are restricted to tubular heaters where it is easier to assess semi-quantitatively what is happening.

Thermodynamic nonequilibrium and rate processes

The establishment of thermodynamic equilibrium between the various internal energy modes - translation, rotation and vibration - and chemical equilibrium do not occur instantaneously but require finite times. Since the time taken for the gas to flow through the heater may be short, some of the processes occurring in the flow may not have time to equilibrate. Suppose that the time required to approach equilibrium can be represented by a time τ , which is a "relaxation" time for the energy mode or a chemical time for the chemical reaction, then an initial prediction of the occurrence of nonequilibrium can be made by comparing the various characteristic times, τ , with the transit time through the heater, τ_{trans}.[16] The ratio τ/τ_{trans} has two limiting cases; if $\tau/\tau_{trans} \to 0$ the process is very fast in comparison to the transit time, and equilibrium conditions exist at exit. At the other extreme, with the transit time very fast in comparison with the characteristic time, i.e. $\tau/\tau_{trans} \to \infty$, the process effectively does not take place. Nonequilibrium can occur in an excitation environment, as in the heater flow, or in a de-excitation environment, as in the nozzle flow. The characteristic time describing a process in these situations is different, with the de-excitation time being considerably shorter than the excitation time (see Ref. 16, p. 151). However for the order of magnitude arguments used in this chapter it is

assumed that the "relaxation" time is identical in both situations.

The transit time for the heater of Page[17] is calculated to be of the order of 100 msec; as this is a large device, typical transit times can be taken to be in the range 10 to 100 msec. Relaxation and chemical times are functions of temperature and pressure, and in general they are inversely proportional to pressure and increase exponentially with decreasing temperature. Translational and rotational energy modes relax very quickly, with times typically of 10^{-9} sec. for most gases[18], so these modes may be considered to be in equilibrium. Vibrational relaxation is somewhat slower. Rate data gathered from the literature is presented in Appendix B, and it can be seen from Fig. B1 that, for the polyatomics CO_2, CH_4 and NH_3, the vibrational relaxation time, τ_v, is less than 10^{-5} sec. at a pressure of 1 atm. for temperatures above 300 ^{o}K. The vibrational mode of H_2 is not significantly excited until temperatures greater than 1000^{o}K, where $p\tau_v < 10^{-4}$ sec. For the above gases vibration can be taken to be in equilibrium through the heater. However N_2, which is a product of the dissociation of NH_3, relaxes very slowly and even at 2000^{o}K, $p\tau_v \leq 10^{-3}$ atm.sec. A decision regarding vibrational nonequilibrium in nitrogen is delayed until after an examination of the chemical times.

The equilibrium constants of formation taken from the JANAF tables[19] indicate that under equilibrium conditions NH_3 would begin to dissociate into N_2 and H_2 at temperatures above 300^{o}K, but in practice kinetic considerations suggest that significant decomposition does not occur until a much higher temperature. Reaction rate data for NH_3 is sparse. Sawyer[20] notes that temperatures in excess of 1500^{o}K were required to produce measurable ammonia decomposition from the homogeneous reaction. Calculations based on the rate data of Michel and Wagner[21] for NH_3 in Ar diluent, indicate a dissociation time, $\tau_D(NH_3) = O(10^{-2})$sec. at 2000^{o}K. The decomposition rate is increased by heterogeneous catalysis on the

metallic heater surfaces and shorter dissociation times are suggested by the data of Logan and Kemball[22]. Approximate calculations give $\tau_D(NH_3) = O(10^{-2})$ sec. at 1500°K and $\tau_D(NH_3) = O(10^{-5})$ sec. at 2000°K. Miles[23] in a study of the catalytic dissociation of NH_3 by various surfaces for temperatures up to 800°K, found substantial decomposition at comparable mass flows to those of present interest, but with space velocities (mass flow rate/area) about two orders lower. Finally Perroud[24] has investigated NH_3 decomposition in tungsten tubes over the temperature range from 1000 to 3000°K. The findings of Refs. 20 to 24 indicate that NH_3 dissociates in two phases, as a gas phase reaction and as a wall catalysed reaction. A "threshold" temperature for significant homogeneous dissociation to commence exists at about 1500 to 1600°K. Heterogeneous reaction occurs at lower temperatures with "threshold" temperatures reported to vary from 1200°K[24] down to 400°K[23]. The concept of a threshold temperature is misleading, since the heterogeneous catalysis requires collision of the propellant molecules with the heater wall, while the homogeneous reaction is slow at typical resistojet temperatures (less than 2000°K). Under these conditions the chemical rate can be diffusion limited and even though the temperature is high enough to cause dissociation, the bulk of the gas may be convected through the heater before more than a fraction of the total number of molecules has a chance to react on the wall. It is difficult to infer much from the references about resistojet operations since the experimental geometries and residence times are so different from those of resistojet heaters. However, it is to be expected that at low temperatures (300°K) NH_3 will remain undissociated, and by 2000°K, say, a considerable amount of decomposition will occur. Experimental work is under way in this laboratory to measure ammonia dissociation in typical resistojet heater configurations[25].

Now re-examining the vibrational relaxation of N_2, it is apparent that N_2 will be present in an ammonia resistojet heater as part of a

mixture of N_2, H_2 and NH_3. It is well known that mixtures in which there is a fast relaxing component, such as NH_3, relax at a rate comparable to that of the fastest component (see section 4.4). Thus it is reasonable to assume that for the gases considered here vibrational energy is in equilibrium at exit from the heater.

Of the other propellants, CH_4 and H_2 can also dissociate under resistojet heater conditions. It is observed in resistojet experiments employing CH_4 [26,15] that deposition of solid carbon occurs at high temperatures. Halbach[26] using a large concentric tube heater determined an upper operating temperature of 1000°K, whereas Murch and Krieve[15] using a small vortex heater note that no measurable carbon deposition occurs below 1900°K. The difference between these observations is almost certainly caused by the different heater transit times. Equilibrium calculations for H_2 indicate that only a small amount of dissociation occurs at temperatures below 2000°K. This fact allied to $\tau_D(H_2) = O(1)$ sec, based on calculations of the rate data from Refs. 27 and 28, suggests that the presence of atomic hydrogen is unlikely at temperatures below 2000°K, and even at higher temperatures it will be present only in very small quantities.

The effect of nonequilibrium in the chemical rate processes is a reduction in the power put in to the nozzle, P_g. In the case of CH_4 a reduction in P_g is preferred to the deposition of solid carbon.

Viscosity and heat conduction

Further nonequilibrium processes which must be considered in a real gas are viscosity and heat conduction. In resistojet heaters with the stagnation pressure typically of order of 1 atm, the flow is a continuum, so the condition of no slip at the heater surface applies. Thus the gas layer adjacent to the heater wall has zero velocity and its temperature is identical to that of the wall. Gradients in velocity and temperature are set up in a direction normal to the flow since momentum and energy

are being transported through the heater by the propellant molecules. These gradients give rise to the phenomena of viscosity and heat conduction.

The effects of viscosity and heat conduction extend throughout the heater flow, and for the low speeds and small dimensions typical of resistojet heaters the flow should be laminar. From the aspect of converting electrical energy to thermal energy this is not advantageous since the heat transfer is less efficient than in a turbulent flow. Viscous flow causes a loss in momentum due to skin friction which is reflected in a drop in the total pressure. The overall effect of viscosity and heat conduction is dissipative in that it causes a reduction in the gas power, P_g. Unlike the thermodynamic rate processes, no general conclusions can be made regarding the magnitude of the viscous losses without a thorough analysis based on particular geometries.

Although the rate processes and the phenomena of viscosity and heat conduction have been considered separately, in fact they occur simultaneously and interact. In particular the chemical rate processes will couple with the viscous flow. Thus the heterogeneous decomposition of ammonia, occurring at the heater surface, does so in a region of reduced velocity and therefore increased residence time. It follows that at a given position there will be a gradient in the gas composition, as well as in the velocity and temperature. This gives rise to an additional nonequilibrium process, mass diffusion, which has already been briefly mentioned.

(b) Nozzle Flow

In the expansion process the non-idealities are again examined individually, while it is recognised that they are not independent. The non-idealities are considered to be :

(1) Chemical rate processes

(2) Vibrational rate processes

(3) Incomplete expansion, i.e. a finite area ratio nozzle

(4) Viscous flow

(5) Condensation of the efflux gas

(6) Radial flow at exit from the nozzle.

Chemical rate processes

As discussed earlier, ammonia, hydrogen and methane are gases whose chemical composition can change during passage through the heater. Dissociation of methane is not desirable and in practice resistojets would not be operated in a regime where this occurs. Therefore the following remarks regarding chemical rate processes in the nozzle are confined to ammonia and hydrogen.

Resistojet performance can be considerably influenced by variation of the chemical composition in the nozzle; as the propellant expands it experiences large drops in temperature and pressure, which, if equilibrium is to be maintained, must be accompanied by a decrease in the degree of dissociation. The recombination process is an exothermic reaction so that it acts as an apparent heat source and this sensible energy should be converted by the nozzle into useful kinetic energy. Unfortunately, the chemistry may not have time to come to equilibrium so that the contribution from chemical energy to the jet energy will lag behind its equilibrium value. Recombination times (of the same magnitude as the dissociation times) are large in comparison with the nozzle transit time, which is typically 10^{-5} to 10^{-6} seconds. Thus it is to be expected that in most of the nozzle flow, certainly in the supersonic section, recombination will not occur and the chemical composition will remain constant. The effect on performance of freezing the chemical rate processes is to cause a reduction in the jet power, P_j.

Vibrational rate processes

A further significant factor is the rate of vibrational deactivation.

As the propellant expands the temperature and pressure decrease, increasing the vibrational relaxation time, τ_{v}, so that this time can become comparable to, or larger than, the nozzle transit time, τ_{trans}. Thus, it is also possible for vibrational energy to lag behind its equilibrium value and ultimately to become constant. For diatomic gases, such as H_2 and N_2, with only a small amount of energy invested in vibration at resistojet operating temperatures, the possible loss in jet energy due to vibrational freezing is small. However, vibrational energy constitutes a considerable proportion of the total internal energy of the polyatomic molecules, NH_3, CH_4 and CO_2, so that the potential losses are much higher.

Examination of the rate data in Fig. B1 indicates the vibrational relaxation times of H_2 and N_2 are comparable to, or longer than, the nozzle transit time. Therefore it is likely that the vibrational rate processes of these propellants will freeze during expansion through the nozzle. In the case of the polyatomics, $\tau_v \leq \tau_{trans}$, so that vibrational energy may remain in equilibrium longer. The establishment of a reasonable freezing criterion is then very important.

Incomplete expansion

To expand the propellant fully, so that the jet temperature at the nozzle exit reaches absolute zero, would require an infinitely long nozzle. A more realistic nozzle with a finite area ratio (i.e. ratio of exit area to throat area) leads to the flow being underexpanded; in which case energy remains in the active internal modes of the propellant and is not converted to jet energy. Hence, there is a further reduction in the effective jet power.

Viscous flow

In conventional rocket motors the chamber pressure is of the order of 100 atm. and Reynolds numbers, characterising the nozzle flow, of 10^6 are typical. As a consequence, the dissipative effects of viscosity and

heat conduction are confined to a thin boundary layer on the nozzle surface. This affects performance in several ways. First, the free-stream properties such as density and velocity are altered from those values obtained when the flow is inviscid throughout the nozzle.

The viscous layer effectively displaces the inviscid core, so that in the nozzle divergent section (see Fig. 1) the core density is higher and the velocity is lower than in the ideal case. Thus there is a reduction in the exhaust velocity. At the nozzle throat, viscosity causes a decrease in the effective throat area and therefore in the mass flow rate. Secondly, the boundary layer, being a region of reduced velocity and mass flow, has a momentum defecit which is manifest as a reduction in thrust. At these Reynolds numbers the losses in performance are only small.

As Reynolds numbers decrease so the viscous flow occupies an increasing proportion of the nozzle flow field, and in resistojet nozzles, which operate at relatively small Reynolds numbers, the viscous effects can be pronounced. Examination of the literature on resistojets reveals that they have been operated over a range of Reynolds numbers (based on throat diameter, Re_{D^*}) from about 500 to 5000. In this regime the viscous flow is laminar. At Re_{D^*} of order 10^4 the effects of viscosity and heat conduction are still confined to a boundary layer, but as Reynolds numbers decrease (for instance, through a reduction in stagnation pressure) the boundary layer thickens rapidly and by $Re_{D^*} = O(10^2)$ the viscous effects can extend across the whole of the nozzle cross-section. In electron beam measurements on low density nitrogen nozzle flows at a nozzle area ratio of 66:1, Rothe[29] found that the whole of the nozzle flow at exit was viscous at Re_{D^*} less than 250. However at higher Reynolds numbers, $Re_{D^*} = O(650)$, his measurements indicate the existence of an effectively inviscid core throughout the nozzle. The viscous loss and the occurrence of fully viscous flow are

dependent not only on Re_{D*}, but also on the nozzle area ratio, ε . Thus, at Re_{D*} = 200 and, say, ε = 4 a resistojet nozzle flow field consists essentially of an inviscid core and a viscous boundary layer, whereas with a large area ratio, say ε = 200, apart from a inviscid core in the vicinity of the throat, virtually the whole of the supersonic portion of the nozzle is viscous.

It is well known that the thermal condition of the nozzle wall has a considerable influence on the viscous flow. Thus in the design of wind-tunnels for hypersonic, low density flow the nozzle walls are often cooled to reduce the boundary layer thickness (e.g. see Ref. 30). In resistojets the nozzle wall temperature is high, tending to the heater stagnation conditions[2], and it follows that viscous losses are severe.

A further boundary condition which must be examined in connection with the viscous phenomena arises from non-continuum flow considerations. The condition of no slip at the nozzle wall becomes questionable in low thrust engines[31] and a more appropriate boundary condition is one in which the layer of gas immediately adjacent to the nozzle surface has a finite tangential velocity. According to Schaaf and Chambré[32], for Reynolds numbers greater than unity the slip flow regime can be defined by the limits

$$0.01 < \frac{M}{\sqrt{Re}} < 0.1$$

where M and Re are the flow Mach number and Reynolds number respectively. In the divergent section of a resistojet nozzle the Mach number will increase from unity at the throat to a value of four or five, say, at the nozzle exit. The corresponding Reynolds number based on the nozzle diameter is inversely proportional to the local radius, so that it decreases as Mach number increases. Thus even at the nozzle throat for the range of Re_{D*} from 10^2 to 10^4 slip flow is the correct boundary

condition, and with increasing distance along the axis the effect becomes more pronounced.

There are two principal effects associated with slip flow, one is the previously mentioned slip velocity and the other a temperature jump between the gas and nozzle wall. Unlike the other gasdynamic processes considered here, the effect on performance is not in itself detrimental. The fact that there is a finite velocity at the nozzle wall means that the viscous flow produces a smaller velocity defect than in the continuum flow case, which in turn reduces the skin friction. Further, there is a decrease in the heat transfer between the gas and nozzle surface since there is an effective thermal contact resistance associated with the temperature jump[32]. In connection with rarefied nozzle flows it is also worth mentioning the work of Milligan[33], who has examined nozzle characteristics over a range of Reynolds numbers from 10^{-2} to 10^{2}.

It is appropriate at this point, to note that some difficulty is experienced in measuring experimentally that performance of a resistojet which is truly representative of its space operation. This results from the low stagnation pressures with which resistojets are operated. It follows that at exit from the nozzle the pressure is very low and is comparable to the ambient pressure which is maintained in the space simulation facility. Yoshida et al[7] in experiments on hydrogen and ammonia resistojets observed that the ambient pressure of the vacuum chamber has a significant effect on performance. At a cell pressure of 300 microns a specific impulse of 539 seconds was measured with hydrogen. As cell pressure was decreased, keeping all other factors constant, large improvements in performance were observed; by 10 microns the specific impulse had increased to 620 seconds and continued to do so until ambient pressures below one micron were achieved, where the specific impulse leveled off at 669 seconds. This change in performance was not caused by windage effects and was attributed mainly to the viscous interaction

of the vacuum chamber pressure with the low Reynolds number flow in the nozzle. Obviously this is of some importance in relating theoretical and experimental resistojet performance.

Condensation of the efflux gas

Under certain conditions condensation of the propellant can occur during the expansion process. When an ideal gas expands isentropically through a nozzle, the temperature and pressure decrease such that $p/T^{\gamma/(\gamma-1)}$ = constant. This isentrope will cross the saturated vapour pressure $p_{sat} = f(T)$, on a p-T plane, and the gas will tend to condense in liquid or solid droplets. Examination of entropy-enthalpy charts for NH_3 and CO_2 [34] reveals that in an isentropic expansion from stagnation conditions of 300°K and 1 atm., ammonia achieves the saturation vapour pressure of 0.23 atm. at a temperature of 210°K; the equivalent figures for CO_2 are 0.1 atm. at 170°K. The actual onset of condensation is dependent on the particular gas and the nozzle conditions. Wegener [35] notes that high temperature gradients lead to high supercooling, or supersaturation. Thus in the expansion of water vapour he observed supercooling up to 100°K in a nozzle with a temperature gradient of $100^{\circ}K\ cm^{-1}$. In resistojet nozzles temperature gradients several times this are typical so that supersaturation is likely to be high, and in turn the appearance of condensate in the efflux will be delayed. It is not immediately apparent what the effect on nozzle performance is, since condensation although returning energy to the flow through the latent heat is also likely to cause a shock which reduces the Mach number. More specific evidence could not be found in the literature.

Radial flow

The final non-ideality arises from the fact that the exhaust velocity possesses a component in the radial direction which does not contribute to thrust, so causing a reduction in jet power. In the inviscid situation, or the effectively inviscid, i.e. high Reynolds number flow with a thin

boundary layer, the radial flow loss is dependent only on the geometry of the nozzle divergent section. To minimise this loss nozzles are usually bell-shaped so that at the nozzle exit the wall angle tends to zero. This produces a flow which is directed entirely along the nozzle axis. In resistojet nozzles, boundary layers are thick and the largest components of radial velocity occur in a region of reduced momentum flux. Thus the radial flow loss is reduced and with it the need for contoured nozzles. In fact most nozzles used in resistojet motors have been of a conical divergent section.

The six processes which have been considered to occur in the resistojet nozzle are not independent of one another, and some couplings caused by the presence of viscosity are considered below. It has just been indicated that there is a coupling between the radial flow and viscous flow so that, for a given geometry, as the boundary layer thickens the radial flow loss decreases, and vice versa.

In an inviscid nozzle flow it has been assessed that little or no chemistry will occur, but with the presence of viscosity a region of reduced velocity and therefore increased residence time is found adjacent to the nozzle wall. To illustrate the possible effect on resistojet performance let us assume that the flow consists of an inviscid core and a laminar boundary layer. In the inviscid core, recombination processes will be essentially frozen, but in the boundary layer because of the increased residence time it would appear that recombination is more likely. The resistojet nozzle wall is hot, so that in the boundary layer the temperature will be increased in comparison to the freestream values, and the effect will be to reduce the recombination rate, therefore offsetting the increased residence time. Further factors influencing atomic recombination in the boundary layer are velocity slip and temperature jump at the nozzle surface. These will have conflicting trends on the chemical rate. Finally, and probably most important, are the catalytic properties

of the nozzle material. It is difficult to predict with so many contributing factors what the real situation will be, but it is likely that the amounts of atomic recombination will be less than in the more conventional cold wall case (for instance, see Ref. 36).

Vibrational processes will be affected by viscosity in a similar manner to chemistry. Since vibrational rates are considerably faster than chemical rates it is to be expected that, for the case where vibrational energy is frozen in an assumed inviscid core, some vibrational relaxation will occur in the boundary layer. Obviously when vibrational energy is in equilibrium in the core it will also be in equilibrium in the boundary layer. The effects on performance of recombination or vibrational relaxation is beneficial since energy is returned to the active degrees of freedom.

It was convenient to consider the gasdynamics of the heater and the nozzle separately. However the performance of a resistojet motor is dependent, not only on the individual performances of the heater and nozzle, but also on how they behave as a unit. This is most apparent in the losses resulting from viscous flow and frozen chemistry. Thus the viscous loss in the nozzle flow is dependent on the throat diameter Reynolds number, which is determined by the plenum pressure and by the pressure drop caused by the viscous flow in the heater. Further, the flow emanating from the heater is fully viscous, so that in the convergent section of the nozzle where one would intuitively expect viscous effects to be small, conceptual division of the flow into an inviscid core and a boundary layer is incorrect. Another example of the interaction between the heater and nozzle is to be found in the losses due to frozen chemical rate processes. The possibility that dissociation of NH_3, say, does not occur in the heater, although causing a reduction in the ideal gas power, P_g, is not necessarily a loss in overall efficiency, since recombination

losses will not be incurred. Thus the ratio of the jet power to the power input to the resistojet may actually be larger when dissociation does not occur.[37] There are other points, obvious in retrospect, which could be mentioned at this stage, but they are best dealt with in the discussion of results in Chapter Six.

In a similar manner to the ideal case a power balance for the real case gives:

(a) Heater $$P_{el} + P_{pr} = P_g + P_{hl} \tag{1.5}$$

(b) Nozzle $$P_g = P_j + P_{nl} \tag{1.6}$$

(c) Overall $$P_{el} + P_{pr} = P_j + P_{hl} + P_{nl} \tag{1.7}$$

A heater efficiency can be defined as

$$\eta_H = \frac{P_g}{P_{el} + P_{pr}} \tag{1.8}$$

and a nozzle efficiency as

$$\eta_N = \frac{P_j}{P_g} \tag{1.9}$$

so that the overall efficiency (eq. 1.4) is

$$\eta_{Res} = \eta_H \eta_N \tag{1.10}$$

In equations (1.5) and (1.6) the power losses due to gasdynamic non-idealities in the heater, P_{hl}, and in the nozzle, P_{nl}, are introduced.

The most significant point to emerge from this examination of the resistojet motor is that the physics of the flow through the heater and nozzle is extremely complex. It is apparent that to make any advance in the modelling of resistojet performance some simplification is necessary. However before considering this further, the literature on the theoretical performance of resistojets is reviewed.

1.4 Literature on the Theoretical Performance of Resistojets

As the resistojet concept is comparatively new the literature dealing specifically with the theoretical performance of resistojet motors is meagre. The approach adopted in all the references given here is to consider the performance of the heater and nozzle separately.

Two references should be mentioned in connection with heater performance. The first by Page and Short[17] describes a heat transfer analysis, based on the electrical analogy with heat transfer, which was carried out in the design of a large concentric-tube heater. Further, calculations using the conventional Hagen-Poiseuille formula, predicted values for the stagnation pressure drop through the heater which were several times smaller than those measured experimentally. In a later work, Gaubatz, James and Page[38] have computed the compositions of various biowaste propellants using both equilibrium and nonequilibrium chemistry programs for the heater flow. An empirical correlation of nozzle efficiency then enabled the prediction of the overall motor performance.

The approach adopted in other works has been to specify the plenum conditions produced by the heater, i.e. the stagnation pressure and temperature, and propellant composition, and to evaluate the nozzle performance taking into account some of the processes which were discussed in section 1.3. The first theoretical analysis of nozzle performance, reported in Ref. 39, was used in the design of a high temperature hydrogen resistojet. This model was based on an inviscid expansion in the nozzle modified by the growth of a viscous boundary layer, where the main assumptions were a one-dimensional, frozen flow with an adiabatic nozzle wall. An empirical displacement thickness - Reynolds number relation was used to characterise the boundary layer growth. Calculations at the design plenum conditions of 2600°K and 2.0 atm. were carried out for a range of conical nozzles, but no comparison between experimental and predicted

performance is given.

Jefferies and Cumbers[40] describe a computer program, capable of calculating the laminar boundary layer in an axisymmetric nozzle, which has been applied to the design of nozzles for electrothermal thrusters. The most notable feature of this work is that vibrational energy was assumed to be in equilibrium in the inviscid core. Although calculations for a specific gas are not reported it is to be expected that such a formulation would be useful in determining the performance of the polyatomic propellants.

In an experimental and analytical investigation of low-thrust nozzle performance Murch et al[41] have examined the dependence of thruster performance on nozzle geometry. Using the assumptions of quasi one-dimensional flow with vibrational energy frozen at the heater stagnation conditions, the losses accounted for were due to incomplete expansion, viscous flow and radial flow. It was realised that the inviscid core-boundary layer interaction was important, and iteration between solutions of the two regimes was carried out until the change in the effective area ratio at the nozzle exit had converged to an acceptable value. The boundary layer calculation was based on the approximate method for laminar boundary layers of Cohen and Reshotko[42], where the nozzle wall was assumed to be adiabatic. The propellants examined were hydrogen and nitrogen. Comparisons between the experimental measurements and theoretical predictions are not good, with calculated nozzle efficiencies from 5 to 20% higher than experiment. Murch remarks that for the Reynolds number range in which they were interested, i.e. a Reynolds number based on throat diameter from 600 to 3000, the boundary layer thickness at the nozzle throat was only a few percent of the throat radius. By assuming that the boundary layer thickness at the throat was zero, computations were made only for the supersonic section of the nozzle. However, in this range of Reynolds numbers the discharge coefficient, a measure of the boundary layer

thickness at the throat, is noticeably less than unity, so that this assumption is in error. This accounts partly for the large discrepancy between experiment and theory, but a more likely cause can be attributed to the vacuum chamber pressure effects on viscous flow, a phenomenon not widely recognised at that time.

Of some importance to the present study is the work carried out by Rae[43] on viscous low-density nozzle flows. The starting point in Rae's analysis was the Navier-Stokes equations. These were simplified by using the slender channel assumptions of Williams[44], which are that the ratio of radial to axial velocity components, and the ratio of axial to radial gradients are each of the order of the slenderness ratio of the nozzle, i.e. of order (R/L). The result was the slender channel equations; equations which are formally identical with the boundary layer equations, including the radial dependences that account for transverse curvature, but which are valid throughout the channel. At the nozzle wall, slip boundary conditions are allowed. After non-dimensionalising the variables, Rae represented the governing set of non-linear partial differential equations by an implicit finite difference scheme, which was then programmed to solve the direct problem of low-density flow from given reservoir conditions through a nozzle of given shape. Computations have been executed for a gas with $\gamma = 1.4$, $Pr = 0.75$ and $\omega = 0.9$, for several conical nozzles at Reynolds numbers, Re_{D*}, below 660.†

There are a number of interesting points in Rae's results, of which three are mentioned at this juncture:

1. For a nozzle of area ratio 37:1 there was effectively an inviscid core throughout the nozzle for $Re_{D*} = 650$, but by $Re_{D*} \simeq 200$ the flow was completely viscous. These findings were later confirmed experimentally by Rothe[29].

† Rae characterises nozzle flow by a Reynolds number, B, based on the stagnation enthalpy. This can be related to the throat diameter Reynolds number, Re_{D*}, and for $\gamma = 1.4$, $Re_{D*} = 0.5197B$.

2. Rae remarks that, where the flow was essentially divided into an inviscid core and a boundary layer, the conditions on the nozzle axis could be calculated within a few percent of the values predicted with the slender channel approach, by using the isentropic one-dimensional flow of an effective area ratio found by subtracting the displacement thickness from the geometric radius.

3. Heat transfer from the wall to the gas was examined by making the wall temperature identical to the stagnation temperature. It was observed that the velocity and temperature profiles were practically the same as those obtained with an adiabatic wall.

The final reference is by Kallis, Goodman and Halbach[45], who have used Rae's program, assuming an adiabatic wall, to study the viscous effects on biowaste resistojet performance. Comparison with experimental measurements of the performance of H_2, CH_4, CO_2 and H_2O over a range of Reynolds numbers, Re_{D^*}, from 800 to 4500 is good.

1.5 Present Approach

1.5.1 Aims of This Work

So far in this Introduction the resistojet system has been examined, the processes occurring in the motor identified and the literature on theoretical performance of resistojets reviewed. At this stage it is pertinent to ask, what are the aims of the present research?

In the U.K. work on resistojets is concentrated mainly in two places. At the Rocket Propulsion Establishment, Westcott, hydrogen resistojets with a design thrust of 0.65N are being investigated for use as the primary propulsion of communications satellites. At the Royal Aircraft Establishment, Farnborough, ammonia resistojets of

approximately 50 mN thrust are being developed for use in satellite attitude control. To complement the experimental and theoretical research being carried out in these two areas and to provide performance predictions for other propellants, such as CH_4 and CO_2, it was decided to develop computer models of resistojet nozzle performance which could be applied relatively quickly over a wide range of operating conditions. Before this can be done, it is necessary to quantify the processes causing a reduction in the ideal nozzle performance. Thus, modelling of the energy loss processes occurring in the nozzle is the prime concern of the present work. With a better understanding of the gasdynamic situation in the nozzle it is then possible to make realistic performance predictions.

1.5.2 Model Situation

In order to examine resistojet nozzle performance over a wide range of conditions some compromise has to be made regarding the number of processes included in the model and the degree of sophistication with which they are accounted. An immediate simplification comes from neglecting to model the heater performance. While not physically realistic it is a necessary step, since the heater losses are greatly dependent on the particular configuration. It is therefore not appropriate in what is essentially a design study to devote a considerable amount of effort to modelling the heater performance. Some loss of accuracy must result from this fundamental approximation but it is incurred with the substantial advantage that the performance model can be applied to a wide range of resistojet designs. Since the heater flow is not represented, the thermodynamic quantities - stagnation temperature, stagnation pressure and propellant composition - must be specified as input variables to the nozzle calculation. Provided that these quantities are known, or can be estimated, comparison between theory and experiment is possible.

The basic principle used in defining the model nozzle flow, is that where circumstances dictate, for instance through a lack of kinetic data,

the approximations made to the real situation are such that the energy loss is overestimated, therefore resulting in a lower bound on nozzle performance. Two of the non-idealities considered to occur in the nozzle flow, i.e. incomplete expansion and radial flow, can be accounted for in a straightforward manner, as will be shown in Chapter 2. The others require further consideration to obtain reasonable approximation.

1. Chemical rate processes

Losses arising from frozen composition are important in resistojets employing NH_3. They are also possible in hydrogen resistojets operating at temperatures of the order of 2500°K. In view of the previous discussion it is thought that only a small amount of recombination is possible in resistojet nozzles. A reasonable approximation which is consistent with an overestimate of the frozen composition loss is to assume that the chemical rate processes are frozen throughout the nozzle. This also produces some simplification of the viscous flow problem.

2. Vibrational rate processes

An upper bound on energy losses caused by vibrational nonequilibrium can be found by assuming that the vibrational rate processes are also frozen at entrance to the nozzle. Since vibrational energy relaxes very quickly, losses obtained with this approximation may be considerably overestimated. A lower bound results from assuming that vibration remains in equilibrium with translation throughout the nozzle. A third, more realistic, alternative is to adopt a model in which the rate processes remain in equilibrium up to a calculated freezing point and are frozen downstream of this position. All three approximations are examined.

3. Viscous flow

It was seen in the literature review, section 1.4, that the effects of viscosity and heat conduction on the performance of resistojet nozzles can be taken into account by considering that dissipation either,

(i) extends over the entire nozzle flow field, so that the governing equations are the complete Navier-Stokes equations,

or (ii) is confined to a region at the nozzle wall which is governed by the boundary layer equations.

The first approach, or the slender channel version used by Rae[43], is most suitable for application to resistojet nozzles at Reynolds numbers, Re_{D^*}, below about 500. At higher Reynolds numbers Rae's approach although producing useful resistojet performance predictions, as shown in Ref. 45, is extremely time consuming in comparison with more conventional methods. The boundary layer equations used in the second approach are a simplification of the Navier-Stokes equations, obtained by assuming that the boundary layer thickness is very small in comparison to a typical dimension of the body, such as the nozzle wall length. It follows that boundary layer theory is an asymptotic theory where the assumptions used are satisfied with an increasing degree of accuracy as Reynolds number increases. In the present work the assumption is made that the dissipative effects of viscosity and heat conduction are confined to a boundary layer which is not necessarily thin. It is assumed that the nozzle flow is composed of two parts - an inviscid core, and a boundary layer which is governed by the boundary layer equations.

Further assumptions are necessary regarding the boundary conditions. An adiabatic nozzle wall, shown to be a good approximation to the thermal boundary condition in resistojet nozzles [41, 43, 45], is adopted in this work. As regards to the slip condition, the earlier considerations and the results of Refs. 43 and 45 confirm that velocity slip and heat transfer do occur at the nozzle wall. The approximation used here is that the flow is a continuum, so that the no slip condition is applicable. This approximation will result in some overestimate of the viscous loss, but with the benefit of a decrease in computer time.

A point worth noting, is that in the usual thin boundary layer theory the pressure along the wall can be regarded as being "impressed" by the external flow so that it becomes a given function. However in the case of lower Reynolds numbers and consequent thick boundary layers, interaction occurs between the boundary layer and the inviscid core, so that the pressure distribution along the nozzle wall is not known a priori.

4. Condensation of the efflux gas

Condensation is a phenomenon which could occur in the expansion of such gases as NH_3, CO_2 and CH_4, when a resistojet is operated under cold or nearly cold heater conditions. Since resistojet design operating temperatures are typically $1000^{o}K$ or larger, condensation is possible only under extreme off-design conditions which are rarely encountered, e.g. during initial attitude acquisition[12], and it is therefore not modelled in this work.

The model situation is summarised schematically :-

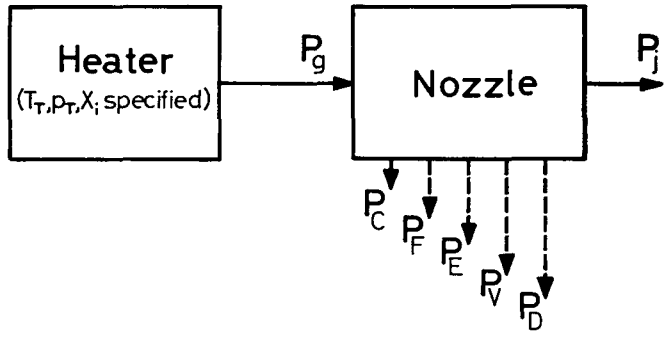

Model Resistojet Flow

where P_C, P_F, P_E, P_V and P_D represent the possible losses in jet power, P_j, due to frozen chemical rate processes, frozen vibrational rate processes, incomplete expansion, viscous flow and radial flow, respectively.

Thus from equation (1.6)

$$P_j = P_g - P_{nl}$$

where
$$P_{nl} = P_C + P_F + P_E + P_V + P_D \qquad (1.11)$$

By calculating the individual losses it is then possible to obtain the jet power and other performance variables, such as thrust and specific impulse.

At the beginning of section 1.3 it was stated that the models which are developed in this study are strictly applicable only to steady state operation. It is worth considering for a moment a resistojet operating in the transient mode, in which small impulses are used for, say, satellite attitude control. The pulse lengths (typically 10 to 100 ms) are several orders of magnitude larger than the nozzle transit time (of order 10 μs) so that the nozzle is operating under quasi steady-state conditions. The transit time through the heater (typically 1 ms) is more comparable to the pulse length, so that the plenum conditions are a function of time. But, again provided that these conditions can be estimated, some useful estimates of transient performance can be made from the predictions of a steady-state model (for instance, see Ref. 12).

The contents of the remainder of this thesis are arranged as follows. In the next chapter a framework for accounting for the five separate losses is presented. The nozzle performance is analysed by starting from the ideal situation and successively adding the various non-idealities to produce a realistic performance model. Parameters characterising the overall nozzle performance are also defined. In Chapter Three the laminar boundary layer problem is examined. The approach used in this work is based on similar solutions of the laminar boundary layer equations. The general similar equations are derived, the implications of similarity are studied and solutions are presented

for four classes of simplified similar equations. Modelling of vibrational relaxation is considered in Chapter Four. Potential flow relations are developed corresponding to the cases where the vibrational rate processes are (i) frozen, (ii) in equilibrium, (iii) initially in equilibrium but frozen downstream of a realistic freezing position. A sudden freezing criterion is outlined and an approximate model is described of the vibrational relaxation in NH_3-H_2-N_2 mixtures. In Chapter Five the details of four computer models of resistojet nozzle performance are given. After describing the general calculation procedure the four models are outlined. This is followed in Chapter Six by a presentation and discussion of the results of these models. Finally, the thesis is summarised and the major conclusions which are drawn from this study are listed in Chapter Seven.

Chapter Two Analysis of Nozzle Performance

2.1 Introduction

A performance analysis is necessary in order to quantify the loss processes which are considered to occur in the resistojet nozzle. We start by considering the idealised flow discussed in Chapter 1, where the available propellant enthalpy is converted entirely into jet energy; by introducing the various loss mechanisms a mathematical model of the nozzle performance is obtained. The loss processes considered in the present study arise from :

1. frozen chemical rate processes,
2. freezing of the propellant vibrational energy modes,
3. incomplete expansion,
4. viscous flow,
5. radial component of exhaust velocity,

and are introduced to the model in this order. In the real situation the loss processes cannot strictly be divorced from each other, so that the following analysis must be regarded only as a convenient form of accountancy.

2.2 Performance Analysis of Individual Losses

2.2.1 Ideal Performance

As an ideal performance case the following situation is defined: the flow is considered to be one-dimensional, to be in complete equilibrium through a nozzle of infinite area ratio, and to suffer no losses through viscous and radial flow. The ambient pressure at exit is taken to be zero. From the energy equation for steady non heat-conducting flow, the specific enthalpy available for conversion to kinetic energy is

$$\frac{1}{2} V_j^2 = h_T - h_j \qquad (2.1)$$

The flow presented to the nozzle can consist of a single species or a mixture of species resulting from the decomposition of the propellant in the heater. In the case of a dissociated mixture of n species, the specific enthalpy at temperature T is

$$h = \frac{1}{\bar{M}} \sum_{i=1}^{i=n} X_i \left(\int_{T_o}^{T} c^o_{p,i}\, dT + \left[\Delta H^o_f(T_o) \right]_i \right) \tag{2.2}$$

where $\left[\Delta H^o_f(T_o) \right]_i$ is the standard heat of formation of the i^{th} species at temperature T_o, taken in this work as 298^oK. Thus eq. (2.1) becomes

$$\frac{1}{2} V_j^2 = \frac{1}{\bar{M}_T} \left\{ \sum_{i=1}^{i=n} X_i \left(\int_{T_o}^{T} c^o_{p,i}\, dT + \left[\Delta H^o_f(T_o) \right]_i \right) \right\}_T$$

$$- \frac{1}{\bar{M}_j} \left\{ \sum_{i=1}^{i=n} X_i \left(\int_{T_o}^{T} c^o_{p,i}\, dT + \left[\Delta H^o_f(T_o) \right]_i \right) \right\}_j \tag{2.3}$$

In the ideal situation the chemical rate processes remain in equilibrium through the nozzle and the jet temperature, $T_j = 0$ †. The available specific enthalpy is then

$$\frac{1}{2} V_j^2 = \frac{1}{\bar{M}_T} \left\{ \sum_{i=1}^{i=n} X_i \left(\int_{T_o}^{T} c^o_{p,i}\, dT + \left[\Delta H^o_f(T_o) \right]_i \right) \right\}_T$$

$$- \frac{1}{\bar{M}_R} \left\{ \int_{T_o}^{o} c^o_p\, dT + \left[\Delta H^o_f(T_o) \right] \right\}_R \tag{2.4}$$

where R denotes the recombined state. When only one species is present, eq. (2.4) simplifies to

$$\frac{1}{2} V_j^2 = \frac{1}{\bar{M}} \int_o^{T_T} c^o_p\, dT \tag{2.5}$$

---

† It is convenient to express exhaust properties such as velocity and temperature in terms of their effective jet values, so that the available enthalpy and jet velocity can be simply related through expressions equivalent to eq. (2.1). Only when the nozzle is infinite are exhaust and effective jet conditions identical.

The jet power is defined as

$$P_j = \frac{1}{2} \dot{m} V_j^2 \tag{2.6}$$

and in the ideal situation all the available enthalpy is regained at the nozzle exit, i.e. $P_j = P_g$. Under equilibrium conditions the mass flow is choked at the nozzle throat, and mass continuity gives

$$\dot{m} = \pi R^{*2} \rho^* u^* \tag{2.7}$$

The thrust is simply

$$F = \dot{m} V_j \tag{2.8}$$

2.2.2 Frozen Chemical Rate Processes

Introducing the first assumption that the propellant composition, produced by the heater, remains constant during expansion through the nozzle means that there is a reduction in jet power. The available specific enthalpy is

$$\frac{1}{2} V_{jC}^2 = \frac{1}{\bar{M}_T} \sum_{i=1}^{i=n} \left(X_i \int_0^{T_T} c_{p,i}^o \, dT \right) \tag{2.9}$$

where the jet temperature $T_{jC} = 0$, and subscript C denotes frozen chemical rate processes. With chemistry frozen, choking again occurs at the throat and relations equivalent to eqs. (2.6) to (2.8) become

$$P_{jC} = \frac{1}{2} \dot{m}_C V_{jC}^2 \tag{2.10}$$

$$\dot{m}_C = \pi R^{*2} \rho_C^* u_C^* \tag{2.11}$$

$$F_C = \dot{m}_C V_{jC} \tag{2.12}$$

It follows that the jet power loss due to frozen chemistry is

$$P_C = P_j - P_{jC} \tag{2.13}$$

A measure of the jet power loss when chemistry is frozen is given by the efficiency

$$\eta_C = \left(\frac{V_{jC}}{V_j} \right)^2 \tag{2.14}$$

For the case where only one chemical species is present, energy is not invested in chemistry and by definition $\eta_C = 1$.

2.2.3 Frozen Vibrational Relaxation Processes

In Chapter 4 three models of the relaxation of the propellant vibrational energy modes are examined. They correspond to the cases where the vibrational energy modes :

(1) remain in equilibrium with the translational energy modes throughout the nozzle;

(2) are in equilibrium down to a realistic freezing position, but make no further contribution to the jet energy beyond this point, i.e. vibrational relaxation is frozen;

(3) are frozen throughout the nozzle.

The nozzle performance analysis of the previous section corresponds to case (1), where by definition there is no loss in the available specific enthalpy due to freezing of the vibrational energy modes. Examining the case where freezing can occur in the nozzle, i.e. case 2, it is implied that there is a further loss in jet power. The available specific enthalpy is

$$\frac{1}{2} V_{jCF}^2 = \frac{1}{\bar{M}_T} \sum_{i=1}^{i=n} X_i \left(\int_{T_{fp}}^{T_T} c_{p,i}^o \, dT + (c_{p,i}^o)_F \, T_{fp} \right) \tag{2.15}$$

where T_{fp} is the static temperature corresponding to the freezing position. Subscript F denotes frozen vibrational rate processes, so that $(c_{p,i}^o)_F$ is the molar heat capacity due to the translational and rotational energy modes only. Again the jet temperature $T_{jCF} = 0$.

In the vibrational nonequilibrium model (case 2), an approximation to the freezing position is used when freezing occurs in the convergent section or in the immediate vicinity of the nozzle throat. Under these

circumstances freezing is arbitrarily delayed to a position downstream of the nozzle throat, with little loss in accuracy. This is done in order to avoid difficulties in satisfying mass continuity, and a further discussion can be found in section 4.2.3. Then with vibrational equilibrium in the convergent section the mass flow rate is $\dot{m}_C$, as in eq. (2.11). The expressions for jet power and thrust are

$$P_{jCF} = \frac{1}{2} \dot{m}_C V_{jCF}^2 \tag{2.16}$$

$$F_{CF} = \dot{m}_C V_{jCF} \tag{2.17}$$

and an efficiency accounting for the frozen vibrational energy loss is defined as

$$\eta_F = \left(\frac{V_{jCF}}{V_{jC}} \right)^2 \tag{2.18}$$

When vibrational rate processes are assumed to be frozen throughout the nozzle, as in case (3), the available specific enthalpy becomes

$$\frac{1}{2} V_{jCF}^2 = \frac{T_T}{\bar{M}_T} \sum_{i=1}^{i=n} X_i \left(c^o_{p,i}\right)_F \tag{2.19}$$

Choking still occurs at the throat and the mass flow rate is now

$$\dot{m}_{CF} = \pi R^{*2} \rho^*_{CF} u^*_{CF} \tag{2.20}$$

The expressions for P_{jCF} and F_{CF} are modified by substituting $\dot{m}_{CF}$ for $\dot{m}_C$.

2.2.4 Incomplete Expansion

The next step in the analysis is the introduction of a finite nozzle, which implies that the jet temperature is no longer zero at exit from the nozzle. In other words the process of converting the theoretically available enthalpy to directed jet energy is not complete, as energy remains in the propellant translational, rotational, vibrational and chemical modes. Since chemical and vibrational energy can be unavailable from previous

considerations, the incomplete expansion loss is dependent upon the propellant rate processes as well as the nozzle area ratio.

Allowing for incomplete expansion, the expressions corresponding to eqs. (2.9), (2.15) and (2.19) are

equilibrium:
$$\frac{1}{2} V_{jCE}^2 = \frac{1}{\bar{M}_T} \sum_{i=1}^{i=n} X_i \left(\int_{T_{jCE}}^{T_T} c_{p,i}^o \, dT \right) \tag{2.21}$$

equilibrium - frozen:
$$\frac{1}{2} V_{jCFE}^2 = \frac{1}{\bar{M}_T} \sum_{i=1}^{i=n} X_i \left(\int_{T_{fp}}^{T_T} c_{p,i}^o \, dT + (c_{p,i}^o)_F (T_{fp} - T_{jCFE}) \right) \tag{2.22}$$

frozen:
$$\frac{1}{2} V_{jCFE}^2 = \frac{(T_T - T_{jCFE})}{\bar{M}_T} \sum_{i=1}^{i=n} X_i \, (c_{p,i}^o)_F \tag{2.23}$$

where subscript E denotes incomplete expansion. Relations (2.21) to (2.23), obtained from an energy equation equivalent to eq. (2.1), cannot be evaluated at this stage since the effective jet temperature T_{jCFE}, or T_{jCE}, is undefined. To avoid unnecessary repetition in the remainder of this analysis, only the case where vibrational energy is frozen throughout the nozzle is examined.

The mass flow rate remains unchanged at $\dot{m}_{CF}$ and as before the jet power and thrust are defined

$$P_{jCFE} = \frac{1}{2} \dot{m}_{CF} V_{jCFE}^2 \tag{2.24}$$

$$F_{CFE} = \dot{m}_{CF} V_{jCFE} \tag{2.25}$$

An efficiency accounting for the energy loss due to incomplete expansion is defined as

$$\eta_E = \left(\frac{V_{jCFE}}{V_{jCF}} \right)^2 \tag{2.26}$$

Examination of the momentum equation applied at the exit plane gives

$$F_{CFE} = \rho_{eCFE} \, u^2_{eCFE} \, \pi R^2 + p_{eCFE} \, \pi R^2 \tag{2.27}$$

in which a pressure term, not apparent in eq. (2.25), appears explicitly. The notation eCFE refers to isentropic flow conditions at the nozzle exit. Using continuity of mass and an equation of state

$$p = \hat{\rho} RT \tag{2.28}$$

eq. (2.27) can be written as

$$F_{CFE} = \dot{m}_{CF} \, u_{eCFE} \left(1 + \frac{1}{\gamma_{CF} \, M^2_{eCFE}}\right) \tag{2.29}$$

Comparing eqs. (2.25) and (2.29) the effective jet velocity is defined in terms of the exit conditions as

$$V_{jCFE} = u_{eCFE} \left(1 + \frac{1}{\gamma_{CF} \, M^2_{eCFE}}\right) \tag{2.30}$$

The exhaust velocity and Mach number are related to exhaust temperature T_{eCFE}, which in turn is a function of the nozzle area ratio, $\varepsilon = \frac{A_{ex}}{A^*}$. Expressions relating T_e and A/A^* are developed in section 4.2, so that by equating (2.23) and (2.30) a jet temperature may be defined. However, this step is unnecessary since the important performance variable, the effective jet velocity, V_{jCFE}, can be obtained from the momentum equation without resorting to eq. (2.23).

2.2.5 Viscous Flow

The presence of viscous flow complicates the analysis. The approach adopted in this work, presented in the next chapter, considers the flow to consist of two parts - an inviscid core and a viscous boundary layer. A major assumption made is that the chemical and vibrational relaxation processes are constant across the radial plane of the nozzle. Thus no recombination is considered to occur in the boundary layer or on the hot nozzle surface. Similarly the vibrational temperature across the boundary layer is assumed to be identical to the freestream vibrational temperature,

whereas vibrational temperature in the boundary layer should follow the static temperature if vibrational processes are in equilibrium in the inviscid core, and should tend to this behaviour if the core is vibrationally frozen. The reasons for the assumption of frozen chemistry have been previously discussed in Chapter One, where it was shown to be a fair approximation for the situation considered here. However, the assumption regarding vibrational relaxation in the boundary layer is not realistic, but, as demonstrated in the next chapter, is unavoidable with similar solutions of the laminar boundary layer equations.

A momentum balance at the exit plane gives the following relation for thrust:

$$F_{CFEV} = \rho_{eCFEV}\, u^2_{eCFEV}\, \pi\, (R-\delta_d)^2 + 2\pi \int_{R-\delta_d}^{R} \rho u^2 r dr + p_{eCFEV}\, \pi R^2 \qquad (2.31)$$

where $\delta_d = \delta \cos \alpha$, is the boundary layer thickness in the radial plane (see Figure 2), and subscript V denotes viscous flow. The usual boundary layer approximation that there is no pressure gradient across the boundary layer is employed.

Applying continuity at any station in the nozzle gives

$$\dot{m}_{CFV} = \rho_{eCFV}\, u_{eCFV}\, \pi (R-\delta_d)^2 + 2\pi \int_{R-\delta_d}^{R} \rho u r dr \qquad (2.32)$$

The notation eCFV refers to inviscid core conditions within the nozzle, and eCFEV to conditions in the core at the nozzle exit plane. Mass continuity may also be expressed in terms of the boundary layer displacement thickness, so that

$$\dot{m}_{CFV} = \rho_{eCFV}\, u_{eCFV}\, \pi (R - \delta^* \cos \alpha)^2 \qquad (2.33)$$

To simplify the nomenclature the subscripts CFEV are dropped in eqs. (2.34) and (2.35). Using eq. (2.32) in (2.31) the thrust becomes

$$F = \dot{m} u_e - 2\pi \int_{R-\delta_d}^{R} \rho u (u_e - u) r dr + p_e\, \pi R^2 \qquad (2.34)$$

Rearranging eq. (2.34) with the aid of eq. (2.33), the thrust can be expressed as

$$F = \dot{m} u_e \left\{ 1 - \frac{R^2}{(R-\delta^* \cos\alpha)^2} \left[\frac{2}{R^2} \int_{R-\delta_d}^{R} \frac{\rho u}{\rho_e u_e} \left(1 - \frac{u}{u_e} \right) r dr - \frac{1}{\gamma M_e^2} \right] \right\} \tag{2.35}$$

It should be noted that, with the addition of viscous flow to the analysis, no assumption has been made regarding the position at which choking occurs in the nozzle.

In a similar manner to eq. (2.25) thrust can be expressed in terms of an effective jet velocity, so

$$F_{CFEV} = \dot{m}_{CFV} V_{jCFEV} \tag{2.36}$$

and comparing eqs. (2.35) and (2.36)

$$V_{jCFEV} = \left[u_e \left\{ 1 - \frac{R^2}{(R-\delta^* \cos\alpha)^2} \left[\frac{2}{R^2} \int_{R-\delta_d}^{R} \frac{\rho u}{\rho_e u_e} \left(1 - \frac{u}{u_e} \right) r dr - \frac{1}{\gamma M_e^2} \right] \right\} \right]_{CFEV} \tag{2.37}$$

The effective jet power is now

$$P_{jCFEV} = \frac{1}{2} \dot{m} V_{jCFEV}^2 \tag{2.38}$$

and an efficiency accounting for the velocity defect due to viscous flow is defined as

$$\eta_V = \left(\frac{V_{jCFEV}}{V_{jCFE}} \right)^2 \tag{2.39}$$

The efficiency accounting for the mass defect due to viscous flow, i.e. the discharge coefficient, is simply

$$C_D = \frac{\dot{m}_{CFV}}{\dot{m}_{CF}} \tag{2.40}$$

2.2.6 Radial Flow

So far in the analysis no consideration has been given to the fact that the exhaust velocity may have components in the axial and radial

directions. Only the axial component contributes to the jet velocity and to account for the loss due to radial flow requires an integration of the velocity components across the exit plane. In general this loss is small, particularly so in the case of flows with thick boundary layers as found in resistojet nozzles. It is therefore not thought worthwhile to account fully for the radial flow loss; although the following analysis has some theoretical justification it cannot be regarded as completely rigorous.

Reverting to an ideal case with no viscous flow, eq. (2.27) can be written, using mass continuity, as

$$F_{CFE} = \dot{m}_{CF}\ u_{eCFE} + p_{eCFE}\ \pi R^2 \tag{2.41}$$

The flow at the nozzle exit can be regarded as a segment of a spherical source flow, and it can be shown for such a flow[46] that the thrust can be expressed as

$$F_{CFED} = \dot{m}_{CF}\ u_{eCFE} \left(\frac{1 + \cos \alpha}{2} \right) + p_{eCFE}\ \pi R^2 \tag{2.42}$$

where α is the nozzle wall angle at the exit plane.

The effect of a viscous boundary layer is to reduce the effective nozzle radius to one less than geometric. By subtracting the boundary layer displacement thickness from the geometric radius an effective radius and therefore effective nozzle geometry can be defined, i.e. $R_{effective} = R - \delta^* \cos \alpha$. Considering the flow at the effective nozzle exit also to be a segment of a spherical source flow allows a similar treatment to the inviscid case. Comparing eqs. (2.35), (2.41) and (2.42) an approximate expression for the thrust with allowance for the radial flow loss is

$$F_{CFEVD} = \dot{m}_{CFV} \left[u_e \left\{ \left(\frac{1 + \cos\alpha_e}{2} \right) - \frac{R^2}{(R-\delta^* \cos\alpha)^2} \cdot \left(\frac{2}{R^2} \int_{R-\delta_d}^{R} \frac{\rho u}{\rho_e u_e} \left(1 - \frac{u}{u_e} \right) r\,dr - \frac{1}{\gamma M_e^2} \right) \right\} \right]_{CFEV} \tag{2.43}$$

where α_e is the effective nozzle angle at exit.

The relations for effective jet velocity and power are

$$V_{jCFEVD} = \left[u_e \left\{ \left(\frac{1 + \cos\alpha_e}{2} \right) - \frac{R^2}{(R-\delta^* \cos\alpha)^2} \left(\frac{2}{R^2} \int_{R-\delta_d}^{R} \frac{\rho u}{\rho_e u_e} \left(1 - \frac{u}{u_e} \right) r dr - \frac{1}{\gamma M_e^2} \right) \right\} \right]_{CFEV} \tag{2.44}$$

$$P_{jCFEVD} = \frac{1}{2} \dot{m}_{CFV} V_{jCFEVD}^2 \tag{2.45}$$

Finally, an efficiency accounting for the radial flow loss is

$$\eta_D = \left(\frac{V_{jCFEVD}}{V_{jCFEV}} \right)^2 \tag{2.46}$$

Thus to summarise, efficiencies η_C, η_F, η_E, η_V and η_D accounting for the velocity defect due to the individual loss processes have been defined in eqs. (2.14), (2.18), (2.26), (2.39) and (2.46), and a discharge coefficient, C_D accounting for the mass defect due to viscous flow in eq. (2.40).

2.3 Overall Nozzle Performance Parameters

Thrust, F_{CFEVD}, and mass flow rate, $\dot{m}_{CFV}$, are the dimensional variables which essentially describe the overall nozzle performance. Individually they provide little information regarding the efficiency of the nozzle or the properties of the propellant, but the ratio of the two, i.e. thrust per unit mass flow rate, or effective jet velocity.

$$V_{jCFEVD} = \frac{F_{CFEVD}}{\dot{m}_{CFV}} \tag{2.47}$$

is a useful characteristic of performance. Jet velocity is more usually expressed in terms of a specific impulse

$$I_{sp} = \frac{V_{jCFEVD}}{g_o} \tag{2.48}$$

and although reflecting nozzle efficiency it is primarily a function of the propellant specific enthalpy.

More dependent on the nozzle performance is the thrust coefficient; a dimensionless factor defined by

$$C_T = \frac{F_{CFEVD}}{p_T A^*} \tag{2.49}$$

Noting that the overall nozzle velocity defect is defined by

$$\eta_N = \left(\frac{V_{jCFEVD}}{V_j} \right)^2 \tag{2.50}$$

or simply the product of the individual efficiencies

$$\eta_N = \eta_C \ \eta_F \ \eta_E \ \eta_V \ \eta_D \tag{2.51}$$

then using eqs. (2.47), (2.8), (2.50) and (2.40) the thrust coefficient can be expressed as

$$C_T = \left(\frac{\dot{m}_{CF}}{\dot{m}} \right) \left(\frac{F}{p_T A^*} \right) \left(\eta_N \right)^{\frac{1}{2}} C_D \tag{2.52}$$

A frequently used parameter characterising the mass defect is the C^* efficiency

$$\eta_{C^*} = \frac{\dot{m}_{CFV}}{\dot{m}} = \frac{\dot{m}_{CF}}{\dot{m}} \ C_D \tag{2.53}$$

Effects on mass flow rate of freezing the chemical and vibrational rate processes are small and $\dot{m}_{CF}/\dot{m}$ closely approximates to unity. In comparison, the mass defect due to viscous flow, C_D, can be considerably less than unity at the Reynolds numbers typical of resistojet operation. Thus the use of C_D is preferred to η_{C^*} in eq. (2.52). The second term in eq. (2.52) is the ideal thrust coefficient and is dependent on the plenum temperature and choice of propellant; for the propellants considered, i.e. NH_3, H_2, CH_4 and CO_2, over the temperature range from 300 to 2000^{o}K, its value can vary between 1.8 and 2.2. The third term in eq. (2.52) represents the

nozzle velocity defect. It is apparent that the thrust coefficient is a function of several, sometimes conflicting, trends and consideration of this factor alone can cloud understanding of the nozzle performance.

To characterise the overall resistojet nozzle performance attention will be confined mainly to :

(1) nozzle efficiency, η_N, a measure of the velocity defect

(2) discharge coefficient, C_D, a measure of the mass defect

and (3) specific impulse, I_{sp}, a measure of the propellant performance.

Finally, an estimate of the electric power required by the resistojet is necessary. The actual performance of the resistojet heater is not modelled in this work. It is assumed that $\eta_H = 1$ in which case the required power per unit mass flow is the difference between the ideal jet specific enthalpy ($P_j = P_g$) and the specific enthalpy inherent in the propellant at entry to the heater. Thus

$$P_{e\ell} = \frac{1}{2} \dot{m}_{CFV} \left\{ V_j^2 - h_{pr} \right\} \tag{2.54}$$

where

$$h_{pr} = \frac{1}{\bar{M}_{pr}} \left\{ \sum_{i=1}^{i=n} X_i \left(\int_{T_o}^{T} c^o_{p,i} \, dT + \left[\Delta H^o_f \, (T_o) \right]_i \right) \right\}_{pr} \tag{2.55}$$

where pr denotes propellant conditions at inlet to the heater and $T_{pr} = 300^oK$. $P_{e\ell}$ is only an approximation to the resistojet power requirement, but as far as the nozzle performance is concerned it can be thought of as the effective electric power transferred to the propellant.

3.1 Introduction

As shown in Chapter One, primarily for reasons of computational efficiency it is convenient to assume that the effects of viscosity and heat conduction are confined to a boundary layer in resistojet nozzle flows. Additional simplifying assumptions were also noted: (1) that the flow is a continuum so that the condition of no slip applies at the nozzle surface, and (2) that an adiabatic wall is a good approximation to the thermal condition of a resistojet nozzle.

A number of methods are available in the literature which can be used to calculate the formation of a compressible boundary layer (for instance, see Ref. 47, ch. 9). At the start of the research the approach of Murch et al[41] was followed. This was based on Cohen and Reshotko's approximate method for the compressible laminar boundary layer with heat transfer and arbitrary pressure gradient. For a number of reasons (described later) Murch's approach was found to be unsatisfactory, even for an adiabatic wall, and recourse had to be made to Cohen and Reshotko's original method. This is an extension to compressible flows of Thwaites correlation technique for calculating incompressible laminar boundary layers. In an equivalent manner to Thwaites, the two-dimensional boundary layer equations were expressed in terms of correlation parameters which were related to the wall shear, the surface heat transfer and the freestream velocity. The evaluation of these quantities was then carried out by utilising similar solutions of the laminar boundary layer equations previously determined by Cohen and Reshotko[48]. A modification of Cohen and Reshotko's method which has been successfully applied to the present resistojet nozzle flow investigation is reported in detail in Reference 37, and a summary of the model is presented in section 5.3.

This preliminary model influenced the way in which later, more

rigorous, theory was developed and some of the points raised during its development are discussed here. A source of some difficulty in the application of Cohen and Reshotko's theory to the resistojet problem is that the similar solutions on which the correlation parameters were based had been determined only for values of the pressure gradient parameter, β , up to 2. The pressure gradients found in resistojet nozzle flow fields are highly favourable, in general, with values of β considerably in excess of 2, so that extrapolation of the correlation parameters beyond $\beta = 2$ was necessary. Murch et al[41] surmounted the problem by fitting quadratics to the correlations of Cohen and Reshotko, thus securing extrapolations beyond $\beta = 2$. Such an extrapolation is difficult to justify since it is easily seen that a quadratic does not give the correct rate of change of curvature. Edwards and Jansson[37] used graphical extrapolation (see Fig. 22) to obtain new values of the correlation parameters beyond $\beta = 2$ which led to performance predictions which agreed well with experiment. This agreement was to an extent fortuitous since the correlation extensions were not theoretically justified. Thus this first model emphasised the need for similar solutions of the laminar boundary layer equations over a wider range of conditions than was to be found in the literature. Further, since results obtained with this model were encouraging it was decided to pursue the similar solutions approach, and all boundary layer models reported in this thesis are based on similar solutions.

In the next section a background to the contents of this chapter is provided by a review of the more important references on similar solutions. The equations relevant to compressible, axisymmetric laminar boundary layer flow are examined in section 3.3, and they are manipulated into a form in which the similarity concept can be applied. The mathematical conditions imposed by the assumption of similarity and the boundary layer parameters required in the performance analysis are

derived in section 3.4. In the final section similar solutions for some cases of interest in resistojet nozzle flows are presented.

3.2 A Literature Review of Similar Solutions

The boundary layer equations for two-dimensional, incompressible flow over a flat plate represent the conservation of mass and the conservation of momentum. They may be written as

$$\frac{\partial u}{\partial x} + \frac{\partial v}{\partial y} = 0 \tag{3.1}$$

$$u \frac{\partial u}{\partial x} + v \frac{\partial u}{\partial y} = \nu \frac{\partial^2 u}{\partial y^2} \tag{3.2}$$

where the boundary conditions are

$$y = 0 : \quad u = v = 0 \quad , \quad y \to \infty \quad : \quad u \to u_e \tag{3.3}$$

Under certain circumstances, by using a transformation of variables, derivatives of the dependent variables become separable and the governing equations reduce from partial differential equations to ordinary differential equations. This technique was first employed on equations (3.1) and (3.2) by Blasius (see Ref. 49, p. 126). Using the transformation

$$\eta = y\left(\frac{u_e}{\nu x} \right)^{\frac{1}{2}}$$

and introducing a stream function

$$\psi = (\nu x u_e)^{\frac{1}{2}} f(\eta)$$

where $f(\eta)$ denotes a dimensionless stream function, Blasius reduced equations (3.1) and (3.2) to the ordinary differential equation

$$ff'' + 2f''' = 0 \tag{3.4}$$

where $'$ denotes differentiation with respect to η.

Equation (3.4) is of significance since it leads to the first example of a similar solution in laminar boundary layer theory. The solution of equation (3.4) is similar in the sense that the velocity profiles, u(x,y), at different stations, x, are identical in the transformed plane and differ only by scaling factors in u and y in the x-y plane. No physical or mathematical approximations beyond those already used in deriving the boundary layer equations are necessary in the derivation of the Blasius equation so that the solution of this equation is exact.

Falkner and Skan[50] have considered two-dimensional, incompressible laminar boundary layers where pressure gradients were present in the external flow. In this case the momentum equation becomes

$$u \frac{\partial u}{\partial x} + v \frac{\partial u}{\partial y} = - \frac{1}{\rho} \frac{dp}{dx} + \nu \frac{\partial^2 u}{\partial y^2} \tag{3.5}$$

In a similar manner to Blasius they obtained an ordinary differential equation, which can be written

$$f''' + \frac{2m}{m-1} (1 - f'^2) + ff'' = 0 \tag{3.6}$$

Provided that the freestream velocity obeys a power law of the form

$$u_e \propto x^m$$

where m is a constant, solutions of equation (3.6) are also similar and exact. Solutions of the Falkner-Skan equation for a range of values of $\beta = 2m/(m-1)$ from - 0.1988 up to 2.4 have been obtained by Hartree[51].

Necessary steps in the derivation of similar solutions for compressible flows are the Illingworth-Stewartson transformations. In independent examinations of the two-dimensional, laminary boundary layer on an isothermal surface, Stewartson[52] and Illingworth[53] used transformations of the form $\xi = \xi(x)$ and $\eta = \eta(x,y)$ to transform a compressible flow in the x-y plane to an equivalent incompressible flow in the ξ-η plane, subject to the fluid property assumptions of unit Prandtl number

and a linear viscosity-temperature relation. Removal of the density, ρ, serves two purposes: (i) it reduces the number of variables and (ii) it facilitates solution of the transformed problem by existing incompressible solutions.

Another transformation which is required in the application of similar solutions to axisymmetric flows is that due to Mangler. In a study of incompressible boundary layers on axisymmetric bodies Mangler (see Ref. 49, p. 235) showed that such flows can be reduced to an equivalent two-dimensional problem again by transformations of the form $\xi = \xi(x)$ and $\eta = \eta(x,y)$. It is noted that a combination of the Illingworth-Stewartson and Mangler transformations, usually referred to as the Lees-Dorodnitsyn transformations (see eqs. 3.22 and 3.23), reduces the axisymmetric, compressible boundary layer to an equivalent two-dimensional, incompressible flow. A fuller discussion of these transformations can be found in Ref. 54.

For compressible flows an additional relation representing the conservation of total energy is necessary to describe the boundary layer. The two-dimensional compressible laminar boundary layer equations now become

$$\frac{\partial}{\partial x}(\rho u) + \frac{\partial}{\partial y}(\rho v) = 0 \tag{3.7}$$

$$\rho u \frac{\partial u}{\partial x} + \rho v \frac{\partial u}{\partial y} = -\frac{dp}{dx} + \frac{\partial}{\partial y}\left(\mu \frac{\partial u}{\partial y}\right) \tag{3.8}$$

$$\rho u \frac{\partial H}{\partial x} + \rho v \frac{\partial H}{\partial y} = \frac{\partial}{\partial y}\left\{\frac{\mu}{Pr}\frac{\partial H}{\partial y} + \mu\left(1 - \frac{1}{Pr}\right)\frac{\partial}{\partial y}\left(\frac{u^2}{2}\right)\right\} \tag{3.9}$$

where the total enthalpy per unit mass, $H = h + \frac{u^2}{2}$.

There have been several attempts to derive similar solutions for compressible flow and of the earlier work the previously mentioned study of Cohen and Reshotko[48] is notable. They examined the flow over an isothermal surface of a model fluid with Prandtl number of unity and a linear viscosity-temperature relation. For the general case with heat

transfer occurring between the fluid and surface the total temperature of the fluid is no longer uniform, so that solution of the energy equation is not trivial and an additional similar variable based on the total enthalpy is required. Applying the Stewartson-Illingworth transformations to equations (3.7) to (3.9) Cohen and Reshotko obtained two coupled ordinary differential equations, which can be written

$$f''' + \beta(1 + S - f') + ff'' = 0 \qquad (3.10)$$

$$S'' + fS' = 0 \qquad (3.11)$$

where f is again a dimensionless stream function such that $f' = u/u_e$ and S is a dimensionless total enthalpy function, $S = H/H_T - 1$. Solutions were obtained by Cohen and Reshotko for a range of heat transfer conditions, with the wall temperature varying from zero to twice the stagnation temperature.

Of the more recent similar solutions for a general gas with Prandtl number not unity and various viscosity-temperature laws, those due to Dewey and Gross[55] are noteworthy. Solutions of the similar boundary layer equations for values of Prandtl number, Pr, extending from 0.5 to 1.0, and ω, the exponent in a viscosity-temperature law (of the form $\mu = AT^{\omega}$) equal to 0.5, 0.7 and 1.0, were obtained over a wider range of pressure gradients than hitherto. They have also examined fairly rigorously the restrictions imposed by similarity.

A final point which should be noted, is that in most compressible flows for which similar solutions have been obtained, the concept of similarity is no longer physically exact, as it is in incompressible flows, but is a mathematical approximation necessary to reduce the partial differential equations to ordinary differential equations. This point is examined in more detail later.

3.3 The Boundary Layer Equations

In nozzle flows where the boundary layer is thick, as it is in resistojet nozzles, the radial dependences accounting for transverse curvature have been demonstrated to be an important consideration in the growth of the boundary layer.[30] The governing equations of the laminar boundary layer in curvilinear coordinates, which include first-order transverse curvature, developed by Probstein and Elliott[56] can be written :-

Conservation of mass,

$$\frac{\partial}{\partial x}(\rho u r) + \frac{\partial}{\partial y}(\rho v r) = 0 \tag{3.12}$$

Conservation of momentum,

in x-direction
$$\rho u \frac{\partial u}{\partial x} + \rho v \frac{\partial u}{\partial y} = -\frac{\partial p}{\partial x} + \frac{1}{r}\frac{\partial}{\partial y}\left(\mu r \frac{\partial u}{\partial y}\right) \tag{3.13}$$

in y-direction
$$\frac{\partial p}{\partial y} = 0 \tag{3.14}$$

Conservation of total energy,

$$\rho u \frac{\partial H}{\partial x} + \rho v \frac{\partial H}{\partial y} = \frac{1}{r}\frac{\partial}{\partial y}\left\{ r \left[\frac{\mu}{Pr}\frac{\partial H}{\partial y} + \mu\left(1 - \frac{1}{Pr}\right)\frac{\partial}{\partial y}\left(\frac{u^2}{2}\right) \right] \right\} \tag{3.15}$$

In the derivation of equation (3.15) it is assumed that Lewis number,

$Le = \dfrac{\rho D_{12} c_p}{k} = 1$, i.e. the magnitudes of the diffusion and conduction terms in the thermal energy equations are identical.

Additional relations come from:-

The equation of state

$$p(x,y) = p_e(x) = \rho_e \hat{R} T_e = \rho \hat{R} T \tag{3.16}$$

and a viscosity-temperature relation, not explicitly defined at this stage,

$$\mu = \mu(T) \tag{3.17}$$

The coordinate system used is shown in Fig. 2, where

$$r(x,y) = R(x) - y \cos \alpha \tag{3.18}$$

In the original derivation[56] of the governing equations, the assumption that $\delta/R_c << 1$ was made concerning longitudinal wall curvature, i.e. that the boundary layer thickness was much less than the nozzle wall radius of curvature. In the present study such an assumption can be criticised in the vicinity of the nozzle throat, where the local radius of curvature is small, in those cases when the boundary layer occupies a substantial portion of the throat. However this will only occur at Reynolds numbers where the other boundary layer approximations are so severely strained that the validity of the whole approach is in question.

To extend the work to thick boundary layers, a stream function, $\psi(x,y)$, may be introduced which satisfies continuity :

$$\left.\begin{aligned} \frac{\partial \psi}{\partial x} &= - \rho v r \\ \frac{\partial \psi}{\partial y} &= \rho u r \end{aligned}\right\} \tag{3.19}$$

so that equations (3.13) and (3.15) become

$$\frac{\partial \psi}{\partial y}\frac{\partial u}{\partial x} - \frac{\partial \psi}{\partial x}\frac{\partial u}{\partial y} = - r \frac{dp_e}{dx} + \frac{\partial}{\partial y}\left(\mu r \frac{\partial u}{\partial y}\right) \tag{3.20}$$

$$\frac{\partial \psi}{\partial y}\frac{\partial H}{\partial x} - \frac{\partial \psi}{\partial x}\frac{\partial H}{\partial y} = \frac{\partial}{\partial y}\left\{ r\left[\frac{\mu}{Pr}\frac{\partial H}{\partial y} + \mu\left(1 - \frac{1}{Pr}\right)\frac{\partial}{\partial y}\left(\frac{u^2}{2}\right)\right]\right\} \tag{3.21}$$

Applying now a modification of the Lees-Dorodnitsyn transformations[54],

$$\xi = \int_0^x \rho_w \mu_w u_e R^2 \, dx \tag{3.22}$$

$$\eta = \frac{\rho_e u_e}{(2\xi)^{\frac{1}{2}}} \int_0^y \frac{\rho}{\rho_e} r \, dy \tag{3.23}$$

the independent variables may be transformed from x and y to ξ and η. The modifications are, firstly in the y to η transformation, where r is kept under the integral, so that r/R is not constrained to be unity and a thin boundary layer is not necessarily assumed; secondly the reference viscosity refers to the wall rather than the freestream conditions.

The following operators should be noted

$$\left(\frac{\partial}{\partial y}\right) = \frac{\rho u_e r}{(2\xi)^{\frac{1}{2}}}\left(\frac{\partial}{\partial \eta}\right) \tag{3.24}$$

$$\left(\frac{\partial}{\partial x}\right) = \rho_w \mu_w u_e R^2\left[\left(\frac{\partial}{\partial \xi}\right) + \left(\frac{\partial \eta}{\partial \xi}\right)\left(\frac{\partial}{\partial \eta}\right)\right] \tag{3.25}$$

Further, a non-dimensional stream function is defined by

$$f(\xi,\eta) = \frac{\psi(\xi, \eta)}{(2\xi)^{\frac{1}{2}}} \tag{3.26}$$

such that

$$\frac{u}{u_e} = \frac{\partial f}{\partial \eta} \tag{3.27}$$

and introducing a non-dimensional total enthalpy function,

$$g(\xi, \eta) = \frac{H}{H_e} \tag{3.28}$$

After the application of equations (3.22) to (3.28) and after some manipulation, equations (3.20) and (3.21) become

$$\frac{\partial}{\partial \eta}\left\{\frac{\rho\mu}{\rho_w\mu_w}\left(\frac{r}{R}\right)^2\frac{\partial^2 f}{\partial \eta^2}\right\} + \frac{2\xi}{u_e}\frac{\partial u_e}{\partial \xi}\left\{\frac{\rho_e}{\rho} - \left(\frac{\partial f}{\partial \eta}\right)^2\right\} + f\frac{\partial^2 f}{\partial \eta^2} = 2\xi\left(\frac{\partial f}{\partial \eta}\frac{\partial^2 f}{\partial \xi \partial \eta} - \frac{\partial^2 f}{\partial \eta^2}\frac{\partial f}{\partial \xi}\right) \tag{3.29}$$

$$\frac{\partial}{\partial \eta}\left\{\frac{\rho\mu}{\rho_w\mu_w}\left(\frac{r}{R}\right)^2\left[\frac{1}{Pr}\frac{\partial g}{\partial \eta} + \frac{u_e^2}{H_e}\left(1 - \frac{1}{Pr}\right)\frac{\partial f}{\partial \eta}\frac{\partial^2 f}{\partial \eta^2}\right]\right\} + f\frac{\partial g}{\partial \eta} = 2\xi\left(\frac{\partial f}{\partial \eta}\frac{\partial g}{\partial \xi} - \frac{\partial g}{\partial \eta}\frac{\partial f}{\partial \xi}\right) \tag{3.30}$$

Equations (3.29) and (3.30) are now the general non-similar equations, equivalent forms of which have been used by Jaffe, Lind and Smith[57] for external flows, and by Whitfield[58] for nozzle flows. The equations constitute a pair of coupled partial differential equations and as such can

be solved by finite difference techniques. As in the case of Rae's slender channel program[43,45] solution on a digital computer of the non-similar equations is extremely time consuming. A particularly useful technique in the reduction of the complexity of the problem is the assumption, if it is justified, of local similarity, so that equations (3.29) and (3.30) become a pair of coupled ordinary differential equations. In this case it is assumed that the derivatives with respect to ξ of the boundary layer dependent variables are small compared to the corresponding η-derivatives, so that the right hand side of equations (3.29) and (3.30) can be neglected. Those terms on the left hand sides which are functions of ξ are assumed to take their local values, and the boundary layer equations are considered as ordinary differential equations in η, with ξ as a parameter.

The concept of local similarity infers that at every streamwise station the boundary layer adjusts to changes in the geometric and thermodynamic boundary conditions, and is identical in all essential respects to the similar boundary layer whose "history" includes the local boundary conditions. A strong case for the use of similar solutions in some non-similar flows is made by Evans[59]. In his work on incompressible laminar boundary layers he used a series expansion of the non-similar stream function, $f(\xi, \eta)$, of the form

$$f(\xi,\eta) = f_o(\eta) + \xi f_1(\eta) + \xi^2 f_2(\eta) + \cdots$$

where $f_o(\eta)$ is the first-order similar stream function and the higher-order functions $f_i(\eta)$ $(i = 1, \ldots, n)$ make a decreasing contribution to $f(\xi,\eta)$. In particular for more favourable pressure gradients it was shown that the first-order similar solution is by far the most important contribution, so that $f(\xi,\eta)$ can be usefully approximated by $f_o(\eta)$. Evans results show that, for a pressure gradient parameter, β, equal to unity, the dimensionless shear stress at the wall, $f''(o)$, resulting from

the first-order similar solution contributed over 95% of the full non-similar value of $f''(o)$. This contribution increased with increasing pressure gradient. Local similarity is assumed in this work, and its application to resistojet nozzle flows is discussed further in section 5.4.

3.4 The Similar Boundary Layer Equations

3.4.1 Derivation of Equations

The ordinary differential equations resulting from the assumption of similarity in equations (3.29) and (3.30) are

$$\left[\frac{\rho\mu}{\rho_w\mu_w}\left(\frac{r}{R}\right)^2 f''\right]' + \frac{2\xi}{u_e}\frac{du_e}{d\xi}\left\{\frac{\rho_e}{\rho} - f'^2\right\} + ff'' = 0 \qquad (3.31)$$

$$\left[\frac{\rho\mu}{\rho_w\mu_w}\left(\frac{r}{R}\right)^2\left\{\frac{g'}{Pr} + \frac{u_e^2}{H_e}\left(1 - \frac{1}{Pr}\right) f'f''\right\}\right]' + fg' = 0 \qquad (3.32)$$

where (') denotes differentiation with respect to η.

Remembering that f and g are non-dimensional stream and enthalpy functions (defined by eqs. 3.26 and 3.28), the boundary conditions are:

(1) At the wall

(i) No mass flux, $f(o) = 0$

(ii) No slip condition, $f'(o) = 0$

(iii) Dimensionless shear stress, $f''(o) =$ constant

(iv) Either (a) with heat transfer $g(o) = H(o)/H_e$ and $g'(o) =$ constant

Or (b) for adiabatic wall $g(o) =$ constant and $g'(o) = 0$ (3.33)

(2) At the outer edge of the boundary layer

$$\left.\begin{aligned} &\text{(i)} \quad f'(\infty) = 1 \\ &\text{(ii)} \quad f''(\infty) = 0 \\ &\text{(iii)} \quad g(\infty) = 1 \\ &\text{(iv)} \quad g'(\infty) = 0 \end{aligned}\right\} \tag{3.34}$$

The inner boundary conditions $f''(o)$ and either $g'(o)$ or $g(o)$ are initially unknown and must be found as part of the solution.

In order for similar solutions of equations (3.31) and (3.32) to exist the following conditions are necessary :

(1) $$\frac{2\xi}{u_e}\frac{du_e}{d\xi}\left(\frac{\rho_e}{\rho} - f'^2\right) = F(\eta)$$

(2) $$\frac{\rho\mu}{\rho_w\mu_w} = \lambda(\eta)$$

(3) $$\left(\frac{r}{R}\right)^2 = G(\eta)$$

(4) $$Pr = Pr(\eta)$$

As pointed out by Hayes and Probstein[60] similarity is a mathematical state. In general, not all of the individual conditions (1) to (4) can be physically satisfied simultaneously, and it is necessary to determine when the assumption of similarity is correct or reasonable.

Examining the first condition, which using equation (3.16), can be written as

$$\frac{2\xi}{u_e}\frac{du_e}{d\xi}\left(\frac{\rho_e}{\rho} - f'^2\right) = \frac{2\xi}{u_e}\frac{du_e}{d\xi}\left(\frac{T}{T_e} - \frac{u^2}{u_e^2}\right) \tag{3.35}$$

we need to express T/T_e in terms of the similar variables f and g. For an isenthalpic flow the energy equation for the external flow is simply $H_T = H_e$. (It is appropriate at this point to note that in the Class B

similar equation, which is presented in section 3.5.2, in order to satisfy some of the restrictions required for similarity it is necessary to introduce a distribution of heat sources and heat sinks in the external flow. In this case the flow is no longer isenthalpic and the energy equation can be written

$$H_T + q = H_e \tag{3.36}$$

where $q = q(\xi)$ represents the rate of heat generation in the external flow.) Quite generally, for a thermally and calorically perfect gas (c_p = constant), the energy equation can be written

$$H_e = c_p T_e + \frac{u_e^2}{2} \tag{3.37}$$

In the boundary layer $H = c_p T + \frac{u^2}{2}$

so that T/T_e can be expressed

$$\frac{T}{T_e} = \frac{H - \frac{u^2}{2}}{H_e - \frac{u_e^2}{2}} \tag{3.38}$$

Then eq. (3.35) becomes

$$\frac{2\xi}{u_e}\frac{du_e}{d\xi}\left[\frac{\rho_e}{\rho} - f'^2\right] = \frac{2\xi}{u_e}\frac{du_e}{d\xi}\left[\frac{H - \frac{u^2}{2}}{H_e - \frac{u_e^2}{2}} - \frac{u^2}{u_e^2}\right]$$

$$= \frac{2\xi}{u_e}\frac{du_e}{d\xi}\frac{H_e}{H_e - \frac{u_e^2}{2}}\left(\frac{H}{H_e} - \frac{u^2}{u_e^2}\right)$$

$$= \frac{2\xi}{u_e}\frac{du_e}{d\xi}\frac{T_{e,T}}{T_e}\left(g - f'^2\right) \tag{3.39}$$

where $T_{e,T}$ and T_e are the freestream total and static temperatures respectively. When the flow is isenthalpic ($q = 0$) $T_{e,T}$ is identical to T_T, but when $q = q(\xi)$, $T_{e,T}$ becomes a variable. If

$$\frac{2\xi}{u_e}\frac{du_e}{d\xi}\frac{T_{e,T}}{T_e} = \beta \tag{3.40}$$

is constant, the expression becomes

$$\frac{2\xi}{u_e}\frac{du_e}{d\xi}\left(\frac{\rho_e}{\rho} - f'^2\right) = \beta(g - f'^2) = F(\eta) \tag{3.41}$$

giving the required condition. β is referred to as the pressure gradient parameter. Thus the first condition is satisfied subject to the restrictions that

(i) specific heat of fluid, c_p = constant

(ii) pressure gradient parameter, β = constant.

The second required condition is

$$\frac{\rho\mu}{\rho_w\mu_w} = \lambda(\eta)$$

A viscosity-temperature law of the form

$$\mu = AT^{\omega} \tag{3.42}$$

is adopted, where A and ω are constants, then in a manner similar to Dewey and Gross[55] one obtains

$$\frac{\rho\mu}{\rho_w\mu_w} = \left(\frac{T}{T_w}\right)^{\omega-1} = \left(\frac{T_{e,T}}{T_w}\frac{T}{T_{e,T}}\right)^{\omega-1}$$

Now

$$\frac{T}{T_{e,T}} = \frac{H - \frac{u^2}{2}}{H_e} = g - \frac{u_e^2}{2H_e}f'^2$$

so that

$$\frac{\rho\mu}{\rho_w\mu_w} = \left[\frac{T_{e,T}}{T_w}\left(g - \frac{u_e^2}{2H_e}f'^2\right)\right]^{\omega-1}$$

With the restrictions that

(i) the ratio of freestream stagnation to wall temperature,

$T_{e,T}/T_w$ = constant

(ii) hypersonic parameter, $\sigma = u_e^2/H_e$ = constant

(iii) exponent in a power law viscosity-temperature relation (eq. 3.42), ω = constant.

$$\frac{\rho\mu}{\rho_w\mu_w} = \left[\frac{T_{e,T}}{T_w}\left(g - \sigma f'^2\right)\right]^{\omega-1} = \lambda(\eta) \qquad (3.43)$$

The restriction c_p = constant is also implicit in this relation

The third condition that $\left(\frac{r}{R}\right)^2 = G(\eta)$ can be satisfied in two ways :

(a) Restricting consideration to a thin boundary layer the approximation $r = R$ can be used, in which case $G = 1$.

(b) Using eq. (3.18) and substituting for r in eq. (3.23)

$$\eta = \frac{\rho_e u_e}{(2\xi)^{\frac{1}{2}}}\int_o^y \frac{\rho}{\rho_e}(R - y\cos\alpha)dy$$

Differentiating, rearranging and integrating

$$\frac{(2\xi)^{\frac{1}{2}}}{\rho_e u_e}\int_o^\eta \frac{\rho_e}{\rho}\,d\eta = \int_o^y (R - y\cos\alpha)dy$$

$$= Ry - \frac{y^2\cos\alpha}{2}$$

Substituting for y from eq. (3.18)

$$\frac{(2\xi)^{\frac{1}{2}}}{\rho_e u_e}\int_o^\eta \frac{\rho_e}{\rho}\,d\eta = \frac{R^2 - r^2}{2\cos\alpha}$$

So

$$\left(\frac{r}{R}\right)^2 = 1 - \frac{2(2\xi)^{\frac{1}{2}}\cos\alpha}{\rho_e u_e R^2}\int_o^\eta \frac{\rho_e}{\rho}\,d\eta \qquad (3.44)$$

But from eq (3.39)

$$\frac{\rho_e}{\rho} = f'^2 + \frac{T_{e,T}}{T_e}(g - f'^2)$$

so eq. (3.44) becomes

$$\left(\frac{r}{R}\right)^2 = 1 - \frac{2(2\xi)^{\frac{1}{2}} \cos\alpha}{\rho_e u_e R^2} \left\{ \int_o^\eta f'^2 d\eta + \frac{T_{e,T}}{T_e} \int_o^\eta (g - f'^2) d\eta \right\} \tag{3.45}$$

Thus with the restrictions that

(i) the transverse curvature parameter,

$$\Theta = \frac{2(2\xi)^{\frac{1}{2}} \cos\alpha}{\rho_e u_e R^2} \tag{3.46}$$

is constant

and (ii) the ratio of the freestream stagnation to static temperature, $T_{e,T}/T_e$ is constant, we have

$$\left(\frac{r}{R}\right)^2 = 1 - \Theta \left\{ \int_o^\eta f'^2 d\eta + \frac{T_{e,T}}{T_e} \int_o^\eta (g - f'^2) d\eta \right\} = G(\eta) \tag{3.47}$$

Again it is necessary for c_p to be constant to obtain this third required condition.

The final condition concerning similarity in Prandtl number is not examined in detail since only the case, Pr = constant, (in particular Pr = 1.0 and 0.7) is of interest. The case Pr = constant $\neq$ 1 requires that in eq. (3.32) u_e^2/H_e is constant, or in other words

$$\sigma = \text{constant}$$

With all these conditions satisfied the similar boundary layer equations resulting from eqs. (3.31) and (3.32) are

$$\left[\lambda G f'' \right]' + \beta(g - f'^2) + f f'' = 0 \tag{3.48}$$

$$\left[\lambda G \left\{ \frac{g'}{Pr} + 2\sigma \left(1 - \frac{1}{Pr}\right) f' f'' \right\} \right]' + f g' = 0 \tag{3.49}$$

where f and g are the dependent variables, λ and G are additional variables which can be expressed in terms of f and g, and β, Pr and σ

are constants. The boundary conditions are as in eqs. (3.33) and (3.34) together with the additional conditions

$$\lambda(o) = G(o) = 1$$

The solution of the full similar boundary layer equations (eqs. 3.48 and 3.49) constitutes a complex problem. However, it is not physically possible to satisfy all the mathematical restrictions at one time, and some simplification results by restricting the analysis to physical flows which are approximately similar. Dependent upon the assumptions made about the fluid properties, various classes of similar boundary layer equations can be defined. Some cases of interest are presented in section 3.5. To conclude this section the boundary layer parameters required in the performance analysis are derived.

3.4.2 Boundary Layer Parameters

The displacement thickness, which is a measure of the mass flow defect, is defined for axisymmetric flow as

$$\int_o^{\delta^*} 2\pi\, r\, \rho_e\, u_e\, dy = \int_o^{\infty} 2\pi\, r(\rho_e\, u_e - \rho u)dy \tag{3.50}$$

substituting for r in the left hand side of eq. (3.50) and integrating we obtain

$$\int_o^{\delta^*} 2\pi\, r\, \rho_e\, u_e\, dy = 2\pi\, \rho_e\, u_e \left[R\delta^* - \frac{\cos\alpha\, \delta^{*2}}{2} \right] \tag{3.51}$$

The right hand side of eq. (3.50) can be transformed with the aid of eq. (3.23)

$$\int_o^{\infty} 2\pi\, r(\rho_e\, u_e - \rho u)dy = 2\pi(2\xi)^{\frac{1}{2}} \int_o^{\eta_\infty} \left(\frac{\rho_e}{\rho} - \frac{u}{u_e} \right) d\eta \tag{3.52}$$

where η_∞ is taken to be that value of η for which $\left|\frac{u}{u_e} - 1\right| \leq 10^{-5}$.

Finally by equating the right hand sides of eqs. (3.51) and (3.52) we obtain a quadratic in δ^*, the appropriate solution of which is

$$\delta^* = \frac{R}{\cos\alpha}\left[1 - \left\{1 - \frac{2\cos\alpha\,(2\xi)^{\frac{1}{2}}}{\rho_e u_e R^2}\int_0^{\eta_\infty}\left(\frac{\rho_e}{\rho} - f'^2\right)d\eta\right\}^{\frac{1}{2}}\right] \qquad (3.53)$$

The positive square root term in the quadratic is ignored since this represents an equivalent external flow. Introducing the transverse curvature parameter (eq. 3.46) and substituting for ρ_e/ρ, eq. (3.53) becomes

$$\delta^* = \frac{R}{\cos\alpha}\left[1 - \left\{1 - \theta\left(\frac{T_{e,T}}{T_e}\int_0^{\eta_\infty}(g - f'^2)d\eta - \int_0^{\eta_\infty} f'(1-f')d\eta\right)\right\}^{\frac{1}{2}}\right] \qquad (3.54)$$

Similarly the momentum thickness is a measure of the momentum deficit due to the boundary layer and is defined by

$$\int_0^{\theta} 2\pi\, r\, \rho_e\, u_e^2\, dy = \int_0^{\infty} 2\pi\, r\, \rho(u_e u - u^2)dy \qquad (3.55)$$

In an analogous manner to the derivation of δ^* we obtain

$$\theta = \frac{R}{\cos\alpha}\left[1 - \left\{1 - \theta\int_0^{\eta_\infty} f'(1 - f')d\eta\right\}^{\frac{1}{2}}\right] \qquad (3.56)$$

The boundary layer overall thickness, δ, is taken to be that value of y for which $u/u_e = 0.995$, and can be defined from eqs. (3.23) and (3.18) as

$$\int_0^{\delta}(R - y\cos\alpha)dy = \frac{(2\xi)^{\frac{1}{2}}}{\rho_e u_e}\int_0^{\eta_\infty}\frac{\rho_e}{\rho}\,d\eta \qquad (3.57)$$

where η_e is that value of η for which $f' = \frac{u}{u_e} = 0.995$. Upon integration eq. (3.57) becomes

$$\delta = \frac{R}{\cos\alpha}\left[1 - \left\{1 - \theta\left(\int_0^{\eta_e} f'^2 d\eta + \frac{T_{e,T}}{T_e}\int_0^{\eta_e}(g - f'^2)d\eta\right)\right\}^{\frac{1}{2}}\right] \qquad (3.58)$$

Equations (3.54), (3.56) and (3.58) include the effects of transverse curvature and are the appropriate expressions for the case of a thick boundary layer. For the thin boundary layer case these equations reduce to

$$\delta^* = \frac{R\,\Theta}{2\cos\alpha}\left[\frac{T_{e,T}}{T_e}\int_0^{\eta_\infty}(g-f'^2)d\eta - \int_0^{\eta_\infty} f'(1-f')d\eta\right] \tag{3.59}$$

$$\theta = \frac{R\,\Theta}{2\cos\alpha}\int_0^{\eta_\infty} f'(1-f')d\eta \tag{3.60}$$

$$\delta = \frac{R\,\Theta}{2\cos\alpha}\left[\frac{T_{e,T}}{T_e}\int_0^{\eta_e}(g-f'^2)d\eta + \int_0^{\eta_e} f'^2 d\eta\right] \tag{3.61}$$

Using eqs. (3.18), (3.23) and (3.46), the integral appearing in the thrust and jet velocity relations (see eqs. 2.35 and 2.37) can be expressed for the general case as

$$\frac{2}{R^2}\int_{R-\delta_d}^{R}\frac{\rho\,u}{\rho_e\,u_e}\left(1-\frac{u}{u_e}\right)rdr = \Theta\int_0^{\eta_e} f'(1-f')d\eta \tag{3.62}$$

Additional parameters which are of interest in the boundary layer analysis are the skin friction coefficient and the heat transfer at the nozzle wall. The skin friction coefficient is defined by

$$c_f = \frac{\mu_w\left(\frac{\partial u}{\partial y}\right)_w}{\frac{1}{2}\rho_e\,u_e^2} \tag{3.63}$$

and using eqs. (3.24) and (3.27) this can be written

$$c_f = \frac{2\,\rho_w\,\mu_w\,R}{(2\xi)^{\frac{1}{2}}\,\rho_e}\,f''(o) \tag{3.64}$$

Finally, the heat transfer at the wall is given by

$$q_w = -\,k_w\left(\frac{\partial T}{\partial y}\right)_w \tag{3.65}$$

which, using eqs. (3.24), (3.28) and (3.37), becomes

$$q_w = -\,\frac{\rho_w\,\mu_w\,u_e\,R\,H_e\,g'(o)}{(2\xi)^{\frac{1}{2}}\,Pr} \tag{3.66}$$

3.5 Similar Solutions

Of the various types of laminar viscous flow which are represented by the similar boundary layer equations, attention is confined here to four classes of similar equations which can be used to model resistojet nozzle flow. For convenience these equations, which are special cases of the general similar equations, eqs. (3.48) and (3.49), are designated Class A,B, C and D. Before proceeding to the similar solutions it is necessary to examine the pertinant gasdynamic conditions and the various approximations which can be made to them.

The nozzle flow is an extremely rapid expansion of a high temperature gas from a relatively low pressure plenum into a vacuum. As a consequence of the low stagnation pressure (order of one atmosphere) and the hot nozzle surface, where the wall temperature approximates to the plenum temperature, the boundary layer is thick, tending to occupy the whole of the divergent section at low Reynolds numbers. As a consequence of the high plenum temperature the gas is vibrationally excited at entrance to the nozzle. During expansion the static temperature in the inviscid core falls and the degree of excitation may be reduced through equilibration of the vibrational energy with translational energy. In the boundary layer (i.e. in the radial direction) the opposite process can occur. At any station in the nozzle the static temperature across the boundary layer increases from that of the inviscid core to the higher temperature of the nozzle wall. The vibrational temperature will tend to follow this behaviour, so that propellant specific heat is a function of distance from the nozzle wall. However, the similar boundary layer equations as formulated here, are valid only for a constant specific heat and one is forced to use the approximation that at a given station specific heat is constant across the boundary layer, and equal to that of the inviscid core.

The situation regarding the thermal condition of the wall is, as pointed out in Chapter One, of some importance to the nozzle performance. A realistic, and convenient approximation is to assume that the nozzle wall is adiabatic, i.e. no heat transfer occurs. For the gases considered (NH_3, CH_4, CO_2, H_2 and N_2) over the temperature range from 300° to 3000°K the Prandtl number lies between 0.74 and 0.69. Similarly the viscosity-temperature exponent, ω , lies between 0.90 and 0.65 for all the gases except NH_3, where ω decreases from 1.10 at 300°K to 0.90 at 3000°K. (See Fig. 3 and section 3.5.4). A reasonable physical approximation, which produces considerable simplification of the similar equations, is to take the values of Pr and ω to be unity. This approximation is used in the Class A, B and C similar equations. In Classes A and B the wall is assumed to be adiabatic. Similar solutions with the thin boundary layer approximation $G = r/R = 1$ are examined in Class A, and in Class B the thin boundary layer constraint is relaxed by allowing $G = G(\eta)$, i.e. transverse curvature effects are included. In the third class of equations, C, again with $Pr = \omega$, $C = 1$, the intention is to examine the effect of a modest amount of heat transfer from the nozzle wall to the propellant flow. Solutions of these equations represent the case where the gas recovery temperature is less than the wall temperature. Such a situation can occur in pulsed resistojet operation when the stagnation temperature attained by the propellant during heating can be less than the stagnation temperature. Finally, Class D similar equations examine the effects of using more realistic approximations to Prandtl number and the exponent of the viscosity-temperature relation, in particular some solutions are presented for $Pr = \omega = 0.7$. The case examined is that of an adiabatic wall, and it follows for Prandtl number less than unity that the recovery temperature is less than the stagnation temperature.

3.5.1 Class A Solutions (Falkner-Skan equation)

Making the following approximations regarding fluid properties and the flow:

(i) Prandtl number, $Pr = 1$

(ii) Viscosity-temperature exponent, $\omega = 1$

(iii) Thin boundary layer approximation, $G = 1$

(iv) Total enthalpy profile, $g = 1$, which together with $Pr = 1$ implies that the wall is adiabatic,

produces considerable simplification and a decoupling of the momentum and energy equations. The similar equation resulting from these approximations in eqs. (3.48) and (3.49) is

$$f''' + \beta(1 - f'^2) + ff'' = 0 \qquad (3.67)$$

This is a form of eq. (3.6), the Falkner-Skan equation. The boundary conditions are

$$f(o) = f'(o) = 0, \quad f''(o) = \text{constant and } f'(\infty) = 1.$$

Restrictions necessary for similarity are

(i) c_p = constant

(ii) β = constant

For an isenthalpic flow, $q = 0$ in eq. (3.35), therefore $T_{e,T} = T_T$ and since $g = 1$, $T_w = T_T$, i.e. the wall temperature is identical to the stagnation temperature. The physical situations for which the above restrictions hold must now be examined. The implication of the form of the pressure gradient parameter in eq. (3.40) is that the external velocity gradient is given by

$$\frac{du_e}{d\xi} = \frac{\beta}{2} \frac{u_e}{\xi} \frac{T_e}{T_T}$$

In the original work of Falkner and Skan[50] the flow considered was

incompressible, so $T_e = T_T$ = constant and the potential flow required for similarity was

$$u_e = A\xi^{\beta}$$

where A and β are constants. For such a flow similarity between different stations is exact.

In the case of compressible nozzle flow when T_e is a variable, the potential velocity cannot be expressed explicitly in terms of ξ, so that in general similarity is not exact. There are two physical situations for which similarity is exact, one is that in which there is a stagnation point for the inviscid flow, when $T_e \to T_T$ and $u_e \to 0$; the other occurs when the potential velocity is constant, in which case the pressure gradient is zero, corresponding in the present study to the hypersonic limit when the freestream Mach number is very large. Thus, apart from some limited physical situations, eq. (3.67) and its restrictions are not exact, and solutions of this equation together with the assumption of local similarity are used only as a means to an end, i.e. the approximate modelling of viscous flow in a resistojet nozzle.

Eq. (3.67) constitutes mathematically a non-linear two-point boundary value problem where it is required to obtain profiles for f, f' and f'' as a function of η. Hartree[51] has obtained solutions to this equation for values of pressure gradient parameter, β, up to 2.4. However, as noted earlier, the velocity gradients found in resistojet nozzles are extremely large, with β varying typically from 2. to 8. in the nozzle divergent section. Evans[59] has produced solutions for large β, but for values of β greater than unity he uses a different similar variable, which is effectively 1/f, and his similar solutions are not compatible with the present formulation.

Solutions of eq. (3.67) for $0 \leq \beta \leq 10$, were derived in this study using a fourth order Runge-Kutta integration technique. The two point boundary value problem was treated as an initial value problem,

where the unknown boundary condition $f''(o)$ was obtained by satisfying the outer boundary conditions with convergence criteria, $(1-f'(\infty)) \leq 10^{-5}$ and $f''(\infty) \leq 10^{-5}$. It should be mentioned that Dewey and Gross[55] have produced a few solutions for values of β between 2. and 5., but values of $f''(o)$ are quoted only to three decimal places. Further they note that convergence was difficult for cases involving β greater than 2. In most of these cases they relaxed the convergence criteria to 10^{-3}. No such difficulties were experienced in this work. Details of the mathematical techniques employed in the derivation of the present similar solutions are given in Appendix A.

In section 3.4.2 it was shown that five integrals of the velocity and total enthalpy profiles are required. They are :-

$$P_1 = \int_o^{\eta_\infty} (g - f'^2)d\eta \tag{3.68}$$

$$P_2 = \int_o^{\eta_\infty} f'(1 - f')d\eta \tag{3.69}$$

$$P_3 = \int_o^{\eta_e} f'^2 d\eta \tag{3.70}$$

$$P_4 = \int_o^{\eta_e} (g - f'^2)d\eta \tag{3.71}$$

$$P_5 = \int_o^{\eta_e} f'(1 - f')d\eta \tag{3.72}$$

A reduction in the number of integrals to be evaluated and subsequently used in the nozzle performance models is achieved by making the assumptions that

$$P_4 = P_1$$

$$P_5 = P_2$$

The difference between these integrals comes from the arbitrary definition of the edge of the boundary layer. In the expressions for the momentum

and displacement thickness η_∞ is taken to be the first value of η for which $f' \geq 0.99999$, whereas in the definition of the overall thickness and in the thrust integral, η_e is that value of η for which $f' = 0.995$. The approximation that η_e equals η_∞ introduces a maximum error of less than one percent in P_4 and P_5. The overall effect, which is small, is to cause an overestimate of the boundary layer thickness, δ , and an underestimate of the thrust.

Values of $f''(o)$, P_1, P_2 and P_3 for the Class A similar equation are given in Table I, and these results are illustrated in Figs. 4 to 6. In order to interpret these results it is useful to examine the momentum equation, eq. (3.13), which with the approximation that r = R can be written

$$\rho u \frac{\partial u}{\partial x} + \rho v \frac{\partial u}{\partial y} = - \frac{dp}{dx} + \frac{\partial}{\partial y} \left(\mu \frac{\partial u}{\partial y} \right)$$

This equation expresses the balance between the inertia forces on the left hand side and the pressure and viscous forces on the right hand side. At the wall the inertia forces are zero so the pressure and viscous forces must balance. With increasing distance from the wall the inertia forces increase and the shear forces must decrease, since dp/dx is constant across the boundary layer. Variation of the dimensionless shear stress, f'', in the transformed plane is shown in Fig. 4 for various values of β from 0 to 10. This figure shows that at the wall, i.e. $\eta = 0$ in the transformed plane, the gradient of the dimensionless shear stress, $f'''(o)$, is zero for $\beta = 0$, and as the pressure gradient becomes more favourable (increasing β) so $f''(o)$ increases and $f'''(o)$ becomes more negative. In other words the wall shear stress required to balance the pressure gradient becomes correspondingly larger. As a consequence of the increased value of $f''(o)$ the shear stress decreases more rapidly with favourable pressure gradient, and it follows that the inertia forces increase quicker and the boundary layer thickness in the transformed plane is diminished.

The corresponding velocity profiles are shown in Fig. 5, where it is seen that the more uniform shear stress profile for $\beta = 0$ is reflected in a more linear velocity profile. Variation of the wall shear stress and of the boundary layer integrals with the pressure gradient parameter is shown in Fig. 6. The wall shear stress, $f''(o)$ increases monotonically with β, whereas the integrals P_1, P_2 and P_3 are decreasing functions of β. From eqs. (3.59) to (3.61) it is therefore inferred that the boundary layer thicknesses in the physical plane, δ, δ^* and θ also become smaller as β is raised. Following from this last statement, a point of some significance in later applications of the Class A solutions to the resistojet problem, is that as the pressure gradient falls in the divergent section of the nozzle (see Fig. 23) so the boundary layer thicknesses increase. This is particularly noticeable in the behaviour of P_1 and P_2 for values of β below 2.

3.5.2 Class B Solutions (Modified Falkner-Skan equation including transverse curvature)

Retaining assumptions (i), (ii) and (iv) of the Class A solutions, i.e. $Pr = \omega = g = 1$, but relaxing the thin boundary layer constraint, results in a modified Falkner-Skan equation of the form

$$\left[Gf'' \right]' + \beta(1 - f'^2) + ff'' = 0 \qquad (3.73)$$

where G comes from eq. (3.47), which, with $g = 1$, can be written

$$G = 1 - \theta \left\{ \int_o^\eta f'^2 \, d\eta + \frac{T_{e,T}}{T_e} \int_o^\eta (1-f'^2) d\eta \right\} \qquad (3.74)$$

The boundary conditions are

$$f(o) = f'(o) = 0, \quad f''(o) = \text{constant}, \quad G(o) = 1 \text{ and } f'(\infty) = 1$$

Restrictions necessary for similarity are :

(i) c_p = constant

(ii) $\beta = \frac{2\xi}{u_e} \frac{du_e}{d\xi} \frac{T_{e,T}}{T_e}$ = constant

(iii) $\Theta = \dfrac{2(2\xi)^{\frac{1}{2}} \cos \alpha}{\rho_e u_e R^2} = \text{constant}$

(iv) $\dfrac{T_{e,T}}{T_e} = \text{constant}$

Let us consider the situation where the potential flow is isenthalpic, i.e. $q = 0$ in eq. (3.36), which means that $T_{e,T} = T_T = \text{constant}$ and $T_w = T_T$. It follows from restriction (iv), with $T_e = \text{constant}$, that there is only one physical situation in compressible flow for which similarity is exact, and that is at the stagnation point, when $u_e = 0$. In the more general case, restrictions (ii) and (iv) are inconsistent since a variable velocity, u_e, and a constant static temperature, T_e, cannot be maintained simultaneously. This difficulty is overcome to some extent by the introduction of a distribution of heat sources and sinks in the potential flow, i.e. $q = q(\xi)$. In this case the total enthalpy H_e is a variable, so that the freestream total temperature is variable and from restriction (iv) T_e becomes a variable. Such a situation maintains some consistency in the restrictions, but, as in the Falkner-Skan equation, in the general case it is not possible to express u_e explicitly in terms of ξ for a compressible flow. However, by patching together solutions of eq. (3.73) which are appropriate to the conditions at different stations in a resistojet nozzle, it should be possible to model approximately a viscous flow in which some account has been taken of the effects of transverse curvature.

Although it is of limited interest in the present work, it is noted that for incompressible flows T_e can be equal to $T_{e,T}$, which equals T_T for $q = 0$, since ρ_e is a constant. The conditions for similarity to be exact are then that β and Θ are constants.

Solutions of the modified Falkner-Skan equation have been obtained over the following range of conditions for β, Θ and $T_{e,T}/T_e$:-

$$0 \leq \beta \leq 10.$$

$$0 \leq \Theta \leq 0.4$$

$$1. \leq T_{e,T}/T_e \leq 8.$$

This is not a complete coverage of the conditions found in resistojet nozzles. In particular values of $T_{e,T}/T_e$ greater than 8 may be experienced in nozzles with area ratios greater than 100, but these conditions are sufficient for an approximate examination of the effects of transverse curvature on the boundary layer growth. Values of $f''(o)$, P_1, P_2 and P_3 for the Class B similar solutions are presented in Table II, where the convergence criteria used were $f''(\infty) \leq 10^{-5}$ and $(1-f'(\infty)) \leq 10^{-5}$.

It is seen in Table II that, for certain combinations of β, Θ and $T_{e,T}/T_e$, no solutions of the unknown boundary condition, $f''(o)$ could be found which satisfied all the other boundary conditions. The reasons for this will be discussed shortly. Before considering the results further it is again instructive to examine the momentum equation,

$$\rho u \frac{\partial u}{\partial x} + \rho v \frac{\partial u}{\partial y} = - \frac{dp}{dx} + \frac{1}{r} \frac{\partial}{\partial y} \left(\mu r \frac{\partial u}{\partial y} \right)$$

The differences between the Class A and B similar solutions arise from the way in which the radial dependences accounting for transverse curvature are included in the shear stress term. In the thin boundary layer approximation for axisymmetric flows $r/R = 1$, so the shear stress term is $\frac{\partial}{\partial y} \left(\mu \frac{\partial u}{\partial y} \right)$, which corresponds in the Falkner-Skan equation to f'''. The equivalent terms for a thick boundary layer are $\frac{1}{r} \frac{\partial}{\partial y} \left(\mu r \frac{\partial u}{\partial y} \right)$ and $\left[Gf'' \right]'$.

Computed profiles of the shear stress, f'', velocity, f', and the ratio of the local to geometric radius, G, for a typical case ($\beta = 2$, $\Theta = 0.2$ and $T_{e,T}/T_e = 4.$) are shown in Fig. 7. Comparison with the shear stress and velocity profiles for $\beta = 2$ in the conventional Falkner-Skan equation reveals certain differences. These all originate from the fact

that G = r/R is a decreasing function of η in the Class B solutions, whereas in the thin boundary layer case G is taken to be unity. The first point to note is that including transverse curvature produces a decrease in the wall shear stress. The mathematical reason for this can be seen by expanding $\left[Gf''\right]'$, thus

$$\left[Gf''\right]' = G' f'' + G f'''$$

At the wall, i.e. $\eta = 0$, the Class A and B similar equations can be written as

Class A, $f'''(o) + \beta = 0$

Class B, $G'(o)\, f''(o) + f'''(o) + \beta = 0$ (with $G(o) = 1$)

For the effectively planar flow of the Class A equation, the pressure gradient is balanced by the rate of change of the shear stress at the wall. In the Class B equation, transverse curvature introduces an additional negative term, the effect of which is to make $f'''(o)$ less negative and by implication to reduce the value of $f''(o)$. The physical implication is that for internal flows transverse curvature acts as an adverse pressure gradient, since the wall shear stress necessary to balance the pressure gradient is reduced. When η is a non-zero the bracketed term in the relation for G, eq. (3.74), must be considered. This term is composed of two parts;

$$\text{(i)} \quad \int_o^\eta f'^2 \, d\eta \qquad \text{and} \quad \text{(ii)} \quad \frac{T_{e,T}}{T_e} \int_o^\eta (1 - f'^2) d\eta,$$

where the second part is dominant for small η and the first part is dominant for large η . The implication of the fuller shape of the shear stress profile over the inner portion of the transformed plane is that the inertia forces are reduced in comparison to the case where transverse curvature is not included (Class A). This is to be expected with $T_{e,T}/T_e$ greater than unity, since the second term takes account, through $T_{e,T}/T_e$, of the region of reduced density and therefore of smaller inertia

forces near the wall. As η tends to η_∞ so the second term tends to zero and the first term increases at a constant rate. Thus G = r/R tends to a linear function of η . The effect of transverse curvature at large values of η is to cause a reduction in the shear stress and therefore the boundary layer thickness in the transformed plane is decreased. It follows that the velocity profile for this typical case is slightly more linear when transverse curvature is included.

Some shear stress profiles for β = 2 and 10 in the Class B similar solutions are illustrated in Fig. 8. An important feature of the results is that with increasing pressure gradient parameter the effects of transverse curvature are reduced. It is seen in Fig. 8 for β = 10 that even with the largest influence of transverse curvature (Θ = 0.3 and $T_{e,T}/T_e$ = 8.) the differences in shear stress between Class A and Class B are not large, in fact they are much the same as the typical case just discussed. The combination of large Θ and $T_{e,T}/T_e$ at lower pressure gradient parameters has a more pronounced effect. Thus for β = 2, Θ = 0.2 and $T_{e,T}/T_e$ = 8. the reduced density near the wall combined with the effects of transverse curvature produces a region of almost uniform shear stress. The transverse curvature, acting as an adverse pressure gradient, effectively offsets the increased inertia forces, and it is only by $\eta \simeq 0.5$ when G(= r/R) has decreased to 0.3 that the transverse curvature can no longer offset the increasing inertia forces and shear stress changes significantly. The corresponding velocity profile in Fig. 9 indicates that the rate of change of the inertia forces then decreases rapidly to a constant value appropriate to the freestream conditions, so that the shear stress drops off dramatically. Convergence was difficult to achieve for this particular case (β = 2, Θ = 0.2 and $T_{e,T}/T_e$), so that it lies very close to the region where solutions for f"(o) could not be obtained.

Variation of the wall shear stress with pressure gradient parameter is shown in Fig. 10 for a range of values of transverse curvature para-

meter and freestream stagnation to static temperature ratio. A notable feature is that, for given values of Θ and $T_{e,T}/T_e$ the f"(o) versus β curves are almost linearly displaced from the Class A curve. Further, the displacement of these curves is nearly linear with changes in Θ or $T_{e,T}/T_e$. The fact that solutions for f"(o) could not be obtained where both Θ and $T_{e,T}/T_e$ are large is also apparent in Fig. 10. This feature is most noticeable for low values of β . In order to examine how this comes about let us consider the curve where $\Theta = 0.2$ and $T_{e,T}/T_e = 8$. At $\beta = 10$ the shear stress and velocity profiles do not differ substantially from the Class A profiles but as the pressure gradient parameter falls several factors contribute to change this picture. Over the inner portion of the transformed boundary layer the shear stress profile becomes fuller as the adverse pressure gradient effect of transverse curvature progressively offsets the decreased favourable pressure gradient. Also the ratio of the local to geometric radii becomes smaller as η tends to η_∞. In the nearly limiting case with $\beta = 2$, which was previously described, r/R is less than 10^{-3} at η_∞. At lower values of the pressure gradient parameter r/R is negative as η tends to η_∞. This has a noticeable effect on the velocity profile in that it is no longer asymptotic to $f' = u/u_e = 1$, so that the behaviour of eq. (3.73) under these conditions is not like that of a boundary layer. A thorough examination of this phenomenon showed that there was no value of f"(o) which would produce a velocity profile that was asymptotic to f' = 1, however it was found that the velocity profile became asymptotic to a value of the velocity ratio which was less than unity. The implication of this behaviour is that for certain combinations of pressure gradient parameter, transverse curvature parameter and freestream stagnation to static temperature ratio for which no solution of f"(o) could be found, eq. (3.73) no longer describes a boundary layer flow (see Chapter Six).

The boundary layer integrals P_1, P_2 and P_3 are illustrated in Figs. 11 to 13. It is seen that the values of all three integrals are smaller than the corresponding Class A integrals, and once again the reduction in value is almost a linear function of the changes in Θ or $T_{e,T}/T_e$. The decrease in η_∞ is reflected most noticeably in the P_3 integrals. It must be emphasised that this discussion of the Class B similar solutions has been confined to the transformed plane. Consideration of how these solutions transform to the physical plane is complicated by the form of the equations for the boundary layer thicknesses (eqs. 3.54, 3.56 and 3.58), and by the η to y transformation (eq. 3.23). This is examined in Chapter Six.

3.5.3 Class C Solutions (Coupled momentum and energy equations)

Using the assumptions that

(i) Prandtl number, Pr = 1

(ii) Viscosity-temperature exponent, $\omega = 1$

(iii) The boundary layer is thin, G = 1

and allowing the total enthalpy function g to be a function of η, $g = g(\eta)$, with the boundary condition that $g(o) \neq 1$, allows one to examine heat transfer between the gas and the wall. Under these conditions eqs. (3.48) and (3.49) become

$$f''' + (g - f'^2) + ff'' = 0 \qquad (3.75)$$

$$g'' + fg' = 0 \qquad (3.76)$$

The boundary conditions are

$$f(o) = f'(o) = 0, \quad f''(o) = \text{constant}, \quad f'(\infty) = 1$$

$$g(o) = H(o)/H_e, \quad g'(o) = \text{constant}, \quad g(\infty) = 1$$

Similarity restrictions are

(i) c_p = constant

(ii) β = constant

The implication of these restrictions are identical to those of Class A except that T_w = constant $\neq T_T$. Thus similarity is exact for the cases of stagnation point flow and zero pressure gradient only; for all other cases, even when the above restrictions are obeyed, similarity is only approximately correct.

Of particular interest here is the case where heat transfer occurs from the wall to the gas. Rae[43] in his study of low density nozzle flows noted that with the wall temperature somewhat higher than the recovery temperature the boundary layer profiles hardly differed from those obtained with an adiabatic wall. This has important implications to the performance of pulsed resistojets and it was hoped that solutions of eqs. (3.75) and (3.76) with g(o) greater than unity would confirm this finding. However some difficulty was experienced in obtaining solutions of sufficient accuracy for the boundary layer integrals to be evaluated properly. The reason for this is to be found in the fact that eqs. (3.75) and (3.76) are extremely non-linear when g(o) is larger than unity, and the problem is complicated by the presence of two unknown boundary conditions, f"(o) and g'(o). A considerable number of solutions of equations equivalent to eqs. (3.75) and (3.76), for g(o) less than unity, have been presented by Cohen and Reshotko[52], Li and Nagamatsu[61] and Dewey and Gross[55]. Test cases to compare with these solutions were carried out in this work and no difficulty was experienced in obtaining accurate values of f"(o) and g'(o). To a great extent this was due to the linearity of the energy equation for g(o) < 1, specifically that g'(o) = F(g(∞)) is linear. The linearity of the energy equation has also been noted by Smith and Clutter[62]. When g(o) is larger than unity this relation is non-linear and becomes more so with increasing pressure gradient parameter.

The case examined here used the somewhat arbitrarily chosen boundary condition of g(o) equal to 1.2. At β = 0 the momentum and

energy equation are uncoupled so that the velocity profile is independent of the total enthalpy profile, and solution is straightforward. Values of $f''(o)$ and $g'(o)$ with convergence criteria on $f''(\infty)$ and $g'(\infty)$ of 10^{-5} are presented in Table III. When β is larger than zero the two equations couple and use must be made of numerical procedures such as a Newton-Raphson two-variable routine to obtain the values of $f''(o)$ and $g'(o)$. However convergence was found to be extremely slow and to reduce computing time a visual search for solutions was adopted. Again this was not particularly satisfactory and only solutions for values of β up to 3.0 are given in Table III. In order to obtain solutions the convergence criteria were relaxed considerably. Values of the boundary layer integrals were not evaluated. References 52 and 55 present some solutions with $g(o) = 2$ for values of β up to 2. Dewey and Gross[55] also note difficulty in obtaining convergence but in this respect they appear to have been more successful than the present author since convergence to 10^{-4} is reported.

As first noted by Cohen and Reshotko[52] a feature of the similar solutions when heat is transferred from the wall to the gas is that there is an overshoot in the velocity profile with favourable pressure gradients. When the freestream velocity is uniform, i.e. $\beta = 0$, the velocity profile is identical to that of the Class A solutions, but as β increases so the velocity at the edge of the boundary layer increases to a value greater than the freestream and then slowly returns to the freestream velocity as η tends to η_∞. For the relatively modest amount of wall heating obtained with $g(o) = 1.2$ the overshoot is small; the maximum overshoot found here, occurred at $\beta = 3.0$, producing a value of f' approximately equal to 1.005. However, the magnitude of the wall shear stress is noticeably larger than the adiabatic wall case (Class A). It is shown in Fig. 14 that the difference in $f''(o)$ becomes larger with increasing pressure gradient. Also drawn in this figure is the gradient

of the total enthalpy function, g'(o). In the case of an adiabatic wall with $q_w = 0$, by definition g'(o) equals zero for all values of β, but when the stagnation enthalpy at the wall is greater than the recovery temperature there must be a gradient in the total enthalpy which transfers thermal energy from the wall to the gas. It is indicated by the approximate solutions presented here that g'(o) tends to a constant value as the pressure gradient increases, and the implication from eq. (3.66) is that with other factors constant the amount of heat transferred must also tend to a constant value.

3.5.4 Class D Solutions (An adiabatic wall with realistic values for the Prandtl number and viscosity-temperature exponent)

The final class of similar solutions presented here, considers the case where the following assumptions are made:

(i) Pr = constant $\neq 1$

(ii) ω = constant $\neq 1$

(iii) G = 1, i.e. the thin boundary layer approximation.

Under these circumstances the similar equations become

$$\left[\lambda f'' \right]' + \beta(g - f'^2) + ff'' = 0 \tag{3.77}$$

$$\left[\lambda \left\{ \frac{g'}{Pr} + 2\sigma \left(1 - \frac{1}{Pr} \right) f'f'' \right\} \right]' + fg' = 0 \tag{3.78}$$

where

$$\lambda = \frac{\rho\mu}{\rho_w \mu_w} = \left[\frac{T_{e,T}}{T_w} (g - \sigma f'^2) \right]^{\omega-1}$$

For an adiabatic wall the boundary conditions of eqs.(3.77) and (3.78) are

$$f(o) = f'(o) = 0, \quad f''(o) = \text{constant}, \quad f'(\infty) = 1$$

$$g(o) = \text{constant} = g_a, \quad g'(o) = 0, \quad g(\infty) = 1$$

$$\lambda(o) = 1$$

where the subscript a denotes an adiabatic wall.

The restrictions necessary for similarity are :

(i) $c_p = \text{constant}$

(ii) $\beta = \frac{2\xi}{u_e}\frac{du_e}{d\xi}\frac{T_{e,T}}{T_e} = \text{constant}$

(iii) $\frac{T_{e,T}}{T_w} = \text{constant}$

(iv) $\sigma = \frac{u_e^2}{2H_e} = \text{constant}$

Before examining the implications of these restrictions it is useful to define the recovery factor. The total enthalpy at the wall is given by

$$H_a = h_e + r\frac{u_e^2}{2} \tag{3.79}$$

where r is the recovery factor. For the case where the total enthalpy remains constant across the boundary layer, i.e. g = 1, with Prandtl number equal to unity, the recovery factor is unity. When Prandtl number is non-unity, the total enthalpy which is recovered by an adiabatic wall is different from the freestream total enthalpy, so the recovery factor is no longer unity. Rearranging eq. (3.79), with the aid of eq. (3.37)

$$r = 1 + \frac{H_a - H_e}{u_e^2/2}$$

which can be written

$$r = 1 + \frac{g_a - 1}{\sigma} \tag{3.80}$$

In the case of an isenthalpic flow the freestream stagnation enthalpy, H_e, is identical to the stagnation enthalpy, H_T. It is therefore implied that $T_{e,T}$ equals T_T and from restriction (iii) the wall temperature T_w remains constant. From restriction (iv) it follows that u_e must also remain constant, so that once again there are only two cases for which similarity is exact, i.e. stagnation point flow ($u_e = 0$) and

constant velocity flow ($\beta = 0$). Addition of an extra degree of freedom by allowing $q = q(\xi)$ does not alleviate this situation, so that in general similarity can only be approximately correct.

Some work is to be found in the literature on similar solutions where realistic viscosity-temperature laws and values of Prandtl number have been used. The most thorough investigation for Prandtl numbers less than unity has been carried out by Dewey and Gross, and solutions for Pr = 0.5, 0.7 and 1.0, ω = 0.5, 0.7 and 1.0, and σ = 0, 0.5 and 1.0 are presented in Refs. 55 and 63. However Dewey and Gross were particularly interested in the cold wall case and gave little consideration to the adiabatic wall which is of interest here. It is shown in Fig. 3 that taking Prandtl number equal to 0.7 is a reasonable approximation for CH_4, NH_3, CO_2, H_2 and N_2. The exponent in a viscosity-temperature relation of the form, $\mu = AT^{\omega}$, shows a wider spread but a useful approximation for all the gases except NH_3 is again to take ω equal to 0.7. Ammonia is best approximated by a linear viscosity-temperature relation. The source of most of this data is based on a Lennard-Jones 6-12 potential model[84]; the viscosity data for N_2 and H_2 comes from experimental measurements[85, 86] for temperatures up to $2200^{\circ}K$.

In order to assess what differences in the boundary layer result from using more realistic values for Prandtl number and viscosity-temperature exponent, solutions of eqs. (3.77) and (3.78) have been obtained with Pr = ω = 0.7. The differences from, say, the Class A solutions should be most marked where the boundary layer is thickest, i.e. at exit from the nozzle. A useful approximation to the hypersonic parameter in this case, is to take σ equal to unity. Solutions of the Class D similar equations with Pr = ω = 0.7, σ = 1.0 for values of the pressure gradient parameter from 0. to 2. are presented in Table IV. At higher values of β the non-linearity of eqs. (3.77) and (3.78) prevented solutions being obtained for $f''(o)$ and $g(o)$. This is not too

serious a drawback since for many resistojet nozzles the pressure gradient parameter at exit is about two.

It is apparent from a comparison of the Class D and A similar equations that the balance of the inertia, pressure and viscous forces through the boundary layer must be altered. However, the shear stress profiles drawn in Fig. 15 indicate that the differences in the transport of momentum through the boundary layer are small. The difference in shape of the shear stress profiles for the Class D and A solutions is most marked at $\beta = 0$; with increasing β the pressure gradient becomes the forcing function in the similar equations so that the profiles closely resemble one another. It follows that the velocity profiles (Fig. 16) are not markedly different. An effect of the more realistic values for Pr and ω is to cause an increase in the thickness of the velocity boundary layer in the transformed plane. Since there is no additional distortion in the η to y transformations, as there is in the Class B similar equations when $r/R = G(\eta)$, it can be inferred that the velocity boundary layer thickness in the physical plane will be larger than that with $Pr = \omega = 1$.

There is a significant difference, however, in the behaviour of the total enthalpy profile (also Fig. 16). Three points are immediately obvious;

(i) the presence of a small overshoot in the total enthalpy at the edge of the velocity boundary layer,

(ii) the thickness of the thermal boundary layer is greater than that of the velocity boundary layer,

(iii) the total enthalpy function at the wall, g_a, decreases with increasing pressure gradient.

The first point is the most remarkable. It is inferred from the shape of the total enthalpy profile that thermal energy is being transported from the hotter regions near the wall ($\eta = 0$) to the colder freestream.

At the edge of the velocity boundary layer the viscous effects become negligible, but thermal conduction has not ceased so that heat is still being transported into the cold region at the edge of the freestream. In the case when Prandtl number is unity the thicknesses of the thermal and velocity boundary layers are identical, when Prandtl number is less than unity it is to be expected (see for instance, Ref. 54, p.38) that $\delta_{thermal}/\delta_{velocity} \simeq O(Pr^{-\frac{1}{2}})$. Brief calculations of these thicknesses in the transformed plane confirm that this is a good approximation in the hypersonic limit.

The third point concerning the behaviour of g_a, is illustrated in Fig. 17. It is seen from eq. (3.80) that with $\sigma = 1$ the recovery factor, r, is identical to g_a. Further it is observed that the recovery factor is only a weak function of the pressure gradient parameter. An additional effect of increased β is to cause a reduction in the dimensionless wall shear stress, $f''(o)$, from the equivalent value of the Falkner-Skan equation.

The boundary layer integrals P_4 and P_5 for the Class D solutions are included in Table IV, but, even when an overshoot occurs in the total enthalpy profile, the differences between P_1 and P_4, and P_2 and P_5 are still small. The integrals P_1, P_2 and P_3 are shown in Fig. 18, where it is seen that the most significant difference from the Class A integrals is in the increased value of

$$P_3 = \int_o^{\eta_e} f'^2 d\eta,$$

which will be reflected in an increased boundary layer thickness, δ.

4.1 Introduction

The vibrational heat capacity of the molecules can constitute a significant proportion of the stagnation enthalpy for propellants of interest in resistojet operation. There are two factors involved in determining the amount of energy invested in vibration, one is the number of vibrational modes possessed by the molecule, the second is the degree to which these are excited at a given temperature. Both factors are dependent on the particular gas; the first by the number of atoms in the molecule and its geometry, the second by the vibrational frequency of each mode. Diatomic gases, with one vibrational mode only, and large vibrational frequencies, have small vibrational heat capacities over the temperature range of interest, consequently the ratio of vibrational energy to stagnation enthalpy, $e_{v,T}/h_T$, is small; e.g. at 2000°K $e_{v,T}/h_T$ is only 0.05 for H_2 and 0.10 for N_2. Polyatomic gases, with a greater number of vibrational degrees of freedom and much smaller vibrational frequencies which are more highly excited in this temperature regime, have correspondingly larger heat capacities, so that by 2000°K $e_{v,T}/h_T$ amount to 0.39, 0.42 and 0.50 for NH_3, CO_2 and CH_4 respectively. Energy stored in the vibrational modes is potentially available for conversion to translational energy in the resistojet nozzle and in this chapter the conversion process and its effect on performance are examined.

Exchange of energy from vibration to translation is a finite rate process requiring a large number of collisions to produce equilibrium, the rate of relaxation being proportional to pressure and increasing exponentially as temperature rises. Thus for one atmosphere pressure the required number of collisons for diatomic gases is $O(10^6)$ at 300°K decreasing to less than 10^4 at 2000°K.[18] The requirements for

polyatomics are considerably less, again due to the smaller vibrational energy spacing, with the corresponding values of $O(10^3)$ to $O(10^2)$ collisions. It has already been pointed out that very high accelerations are experienced in resistojet nozzles, and rates of cooling of 10^8 ^oK/sec are typical. Consequently, if the rate of vibrational relaxation is too slow to follow the rate of temperature fall during the expansion, there is a departure from local thermodynamic equilibrium resulting in an excess of energy in the vibrational modes which is not transferred to the active degrees of freedom. In general such nonequilibrium flows exist in resistojet nozzles, where at entrance the temperature is high, the vibrational relaxation is fast and near-equilibrium is maintained, however the relaxation rates decrease rapidly as temperature and density fall through the nozzle and a relatively narrow region is found in which nonequilibrium effects predominate. Downstream of this the flow consists of a region where vibrational relaxation has effectively ceased and the vibrational processes are considered to be frozen.[16] The effect of vibrational freezing on nozzle performance is to cause a reduction in the enthalpy available for conversion to jet energy.

For diatomic gases such as N_2 and air the vibrational nonequilibrium region is predicted to occur in the vicinity of the nozzle throat.[64,65] No reference to vibrational relaxation in the expansion of a pure polyatomic gas has been found in the literature, however some experiments have been conducted with diatomic-polyatomic mixtures.[66,67] It is indicated by the vibrational temperature measurements of Sebacher et al [66] that nonequilibrium effects in the expansion of a CO_2 - N_2 mixture are spread over a broader region, with eventual vibrational freezing occurring further downstream than is the case with N_2 alone.

In the present work vibrational relaxation is considered in three ways. In the first an upper bound is set on the effects of vibrational freezing by assuming that vibrational rate processes are frozen throughout the nozzle. Since any possible chemical rate processes are also considered

to be frozen the only contributions to jet energy come from the rotational and translational degrees of freedom. In the second, the assumption that vibrational energy remains in equilibrium throughout the nozzle provides the other limiting case. However difficulties are encountered in modelling the viscous boundary layer, since, as discussed earlier in section 3.4, a necessary condition of the similar solutions is that specific heat remains constant across the boundary layer. With vibrational energy in equilibrium the temperature characterising vibration is identical to the static temperature throughout the nozzle, implying that specific heat is a variable in the radial plane; but in order to satisfy similarity the approximation must be used that at a given station the vibrational temperature across the boundary layer is constant, and equal to that of the inviscid core. The final approach attempts to model the more realistic nonequilibrium situation by using the sudden freezing approximation,[69] which makes use of the fact that the nonequilibrium region is narrow and in the limit can be regarded as a discontinuity in going from an equilibrium flow to one in which vibrational energy is frozen.

In terms of the overall nozzle performance the vibrational energy model has a great bearing on the available enthalpy and so on the actual jet velocity. At a more detailed level, it determines the potential flow properties such as temperature and velocity which must be known before the boundary layer calculation can be carried out. The next section derives relations governing the behaviour of the inviscid core temperature as a function of nozzle area ratio for the three approaches outlined above. Further consideration of the nonequilibrium flow and details of an approximate sudden freezing model are presented in section 4.3. The chapter concludes with a description of an approximate model of a NH_3 - N_2 - H_2 mixture.

4.2 Potential Flow Parameters

The nozzle flow is considered in two parts, (i) a potential core in which the fluid properties are assumed to vary in the axial direction only, and (ii) a boundary layer on the nozzle wall (to which the dissipative effects are confined) where the fluid properties are functions of both axial and radial position. By assuming that the only consequence of the boundary layer is a displacement of the effective wall position an effective inviscid flow can be defined. In the quasi one-dimensional approximation the fluid variables in the effective flow are dependent only on the axial distance down the nozzle. Using this and the assumption of steady adiabatic flow, equations relating fluid properties to nozzle geometry can be derived.

For a thermally perfect gas the second law of thermodynamics can be expressed as

$$Tds = c_p dT - \frac{dp}{\rho} \tag{4.1}$$

Using the equation of state (eq. 3.5), in the form

$$p = \rho \hat{R} T = \rho \frac{R_u}{\bar{M}} T \tag{4.2}$$

eq. (4.1) becomes

$$ds = c_p \frac{dT}{T} - \frac{R_u}{\bar{M}} \frac{dp}{p} \tag{4.3}$$

Since the effective flow is assumed to be reversible and adiabatic it is by definition isentropic, so ds = 0 and eq. (4.3) becomes

$$\frac{c_p^o}{\bar{M}} \frac{dT}{T} = \frac{R_u}{\bar{M}} \frac{dp}{p} \tag{4.4}$$

With chemical rate processes assumed to be frozen throughout the nozzle the propellant molecular weight, $\bar{M}$, remains constant. Eq. (4.4) can then be integrated from stagnation conditions to the effective conditions

(p_C, T_C) at any station in the nozzle to give

$$\int_{T_C}^{T_T} c_p^{\,o}\, dT_C = R_u \int_{p_C}^{p_T} \frac{dp_C}{p_C} \tag{4.5}$$

The energy equation for isentropic flow can be expressed as

$$c_p\, dT + u\, du = 0 \tag{4.6}$$

which, with frozen chemistry, integrates to give

$$\frac{1}{M} \int_{T_C}^{T_T} c_p^{\,o}\, dT_C = \frac{u_C^2}{2} \tag{4.7}$$

Finally mass continuity can be written

$$\dot{m}_C = \rho_C\, u_C\, A = \rho_C^*\, u_C^*\, A^* \tag{4.8}$$

Equations (4.5), (4.7) and (4.8), together with a relation linking molar heat, $c_p^{\,o}$, with temperature completely describe the problem.

4.2.1 Frozen Vibrational Energy

With the additional assumption that vibrational rate processes are frozen throughout the nozzle, $c_p^{\,o}$ becomes independent of temperature and eq. (4.5) gives the usual isentropic flow relation

$$\frac{p_T}{p_{CF}} = \left(\frac{T_T}{T_{CF}} \right)^{\gamma_{CF}/(\gamma_{CF} - 1)} \tag{4.9}$$

where the subscripts C and F denote frozen chemical and vibrational rate processes, and $\gamma_{CF} = c_{pF}^{o}/(c_{pF}^{o} - R_u)$ is the ratio of the frozen specific heats.

It follows from eq. (4.2) that

$$\frac{\rho_T}{\rho_{CF}} = \left(\frac{T_T}{T_{CF}} \right)^{1/(\gamma_{CF} - 1)} \tag{4.10}$$

For the case of $c_p^o = c_{pF}^o$ eq. (4.7) is simply

$$u_{CF} = \left[2 \frac{c_{pF}^o}{\bar{M}} (T_T - T_{CF}) \right]^{1/2} \tag{4.11}$$

Then using eqs. (4.8), (4.10) and (4.11) an area-temperature relation is obtained of the form

$$\frac{A}{A^*} = \left(\frac{\rho^* u^*}{\rho u} \right)_{CF} = \left(\frac{T^*}{T} \right)_{CF}^{1/(\gamma_{CF}-1)} \left(\frac{T_T - T_{CF}^*}{T_T - T_{CF}} \right)^{1/2} \tag{4.12}$$

The throat temperature, T_{CF}^* is obtained from the fact that at the choking position M = 1, therefore

$$u_{CF}^* = a_{CF}^* = \left[\gamma_{CF} \frac{R_u}{\bar{M}} T_{CF}^* \right]^{1/2} \tag{4.13}$$

Equating this expression to eq. (4.11) applied at the throat, gives

$$T_{CF}^* = \frac{2T_T}{\gamma_{CF} + 1} \tag{4.14}$$

Eq. (4.12) is valid for both subsonic and supersonic flow. The temperature, T_{CF}, corresponding to a given area ratio, A/A^*, can be found by using a Newton-Raphson iteration procedure, however an inherent difficulty of such procedures is that without extreme care the incorrect root can be found. In the present work an alternative procedure is used, where an arbitrary temperature distribution is specified and the corresponding distribution of area ratio is obtained from eq. (4.12). Then by using an interpolation routine the temperature distribution corresponding to the actual area ratio distribution is found.

4.2.2 Equilibrium Vibrational Energy

Allowing the vibrational processes to have an infinite rate necessitates a functional form of molar heat capacity with temperature. This is achieved by fitting tenth order polynomial approximations to

the JANAF data [19] over the temperature range 100 to 3000°K. The polynomial coefficients for H_2, N_2, NH_3, CH_4 and CO_2 are given in Table V. Using

$$c_p^o = \sum_{i=0}^{i=10} A_i T^i \tag{4.15}$$

eq. (4.5) can be integrated to give

$$\frac{p_T}{p_C} = \left[\frac{T_T}{T_C}\right]^{A_o/R_u} \exp\left\{\frac{1}{R_u} \sum_{i=1}^{i=10} \frac{A_i}{i} (T_T^i - T_C^i)\right\} \tag{4.16}$$

The density ratio is

$$\frac{\rho_T}{\rho_C} = \left[\frac{T_T}{T_C}\right]^{(A_o/R_u - 1)} \exp\left\{\frac{1}{R_u} \sum_{i=1}^{i=10} \frac{A_i}{i} (T_T^i - T_C^i)\right\} \tag{4.17}$$

Similarly eq. (4.7) becomes

$$u_C = \left[\frac{2}{\bar{M}} \sum_{i=0}^{i=10} \frac{A_i}{(i+1)} (T_T^{i+1} - T_C^{i+1})\right]^{1/2} \tag{4.18}$$

Eqs. (4.8), (4.17) and (4.18) combine to give

$$\frac{A}{A^*} = \left[\frac{T^*}{T}\right]_C^{(A_o/R_u - 1)} \left[\frac{\sum_{i=0}^{i=10} \frac{A_i}{(i+1)} (T_T^{i+1} - T_C^{*i+1})}{\sum_{i=0}^{i=10} \frac{A_i}{(i+1)} (T_T^{i+1} - T_C^{i+1})}\right]^{1/2}$$

$$\times \frac{\exp\left\{\frac{1}{R_u} \sum_{i=1}^{i=10} \frac{A_i}{i} (T_T^i - T_C^i)\right\}}{\exp\left\{\frac{1}{R_u} \sum_{i=1}^{i=10} \frac{A_i}{i} (T_T^i - T_C^{*i})\right\}} \tag{4.19}$$

By analogy with eq. (4.13)

$$u_C^* = a_C^* = \left[\gamma_C^* \frac{R_u}{\bar{M}} T_C^*\right]^{1/2} \tag{4.20}$$

and using eq. (4.18) at the choking position the following identity can

be formed

$$\zeta = 2 \sum_{i=0}^{i=10} \frac{A_i}{(i+1)} \left(T_T^{i+1} - T_C^{*i+1}\right) - \frac{\sum_{i=0}^{i=10} A_i T_C^{*i}}{\sum_{i=0}^{i=10} A_i T_C^{*i} - R_u} R_u T_C^* = 0 \quad (4.21)$$

By calculating the value of ζ for a series of values of T_C between T_T and T_{CF}^* that value of $T_C = T_C^*$ for which $\zeta = 0$ can be derived using an interpolation routine. Then the temperature-area relation of eq. (4.19) is solved in exactly the same manner as the frozen flow case.

4.2.3 Sudden Freezing Approximation to Nonequilibrium Vibrational Energy

Assuming that the region of vibrational nonequilibrium found between the near-equilibrium and frozen flow regimes can be approximated by a sudden freezing point results in some simplification of the potential flow analysis. Since the two regions being patched together at the freezing point are both isentropic the resulting flow is also isentropic and eqs. (4.5) and (4.7) are still valid. It has already been indicated in section 2.2.3 that some difficulty is experienced in satisfying mass continuity when the freezing criterion (section 4.3) is satisfied before choking has occurred, as can happen when the propellant is a single diatomic species or a diatomic mixture. In this situation the position at which choking occurs is not known a priori and an iterative process is required to calculate the mass flow rate. At the lower temperatures where the effect is noticeable the difference in mass flow rate, with vibrational rate processes in equilibrium or frozen throughout the nozzle, is small. To avoid undue complication arising from a relatively minor point, vibrational energy is assumed to remain in equilibrium to downstream of the choking position. In fact, the exact position at which vibrational freezing is allowed to occur is determined by the boundary layer calculation (see section 5.2.3.).

The flow is considered in two parts. In the first, corresponding to equilibrium flow, the temperature T_C satisfies the inequality

$$T_T \geq T_C \geq T_{fp}$$

where T_{fp} is the value of T_C at the freezing point. Expressions for T_C^* and $T_C = T_C(A/A^*)$ are identical to eqs. (4.21) and (4.19). The second part corresponds to the frozen flow region, where

$$T_{fp} > T_{CF}$$

Eq. (4.5) can now be written as

$$\int_{T_{fp}}^{T_T} c_p^o \frac{dT}{T} + c_{pF}^o \int_{T}^{T_{fp}} \frac{dT}{T} = R_u \int_{p}^{p_T} \frac{dp}{p} \tag{4.22}$$

which upon integration gives

$$\frac{p_T}{p} = \left[\frac{T_T}{T_{CF}}\right]^{(c_{pF}^o/R_u - 1)} \left[\frac{T_T}{T_{fp}}\right]^{(A_o - c_{pF}^o)/R_u} \exp\left\{\frac{1}{R_u} \sum_{i=0}^{i=10} \frac{A_i}{i} (T_T^i - T_{fp}^i)\right\} \tag{4.23}$$

The density ratio is

$$\frac{\rho_T}{\rho} = \left[\frac{T_T}{T_{CF}}\right]^{(c_{pF}^o/R_u - 1)} \left[\frac{T_T}{T_{fp}}\right]^{(A_o - c_{pF}^o)/R_u} \exp\left\{\frac{1}{R_u} \sum_{i=0}^{i=10} \frac{A_i}{i} (T_T^i - T_{fp}^i)\right\} \tag{4.24}$$

Similarly, eq. (4.7) can be written as

$$\frac{1}{\bar{M}} \left\{ \int_{T_{fp}}^{T_T} c_p^o \, dT + c_{pF}^o \int_{T_{CF}}^{T_{fp}} dT \right\} = \frac{u_{CF}^2}{2} \tag{4.25}$$

and using the form of c_p^o given in eq. (4.15) this becomes

$$u_{CF} = \left[\frac{2}{\bar{M}} \left\{ c_{pF}^o (T_{fp} - T_{CF}) + \sum_{i=0}^{i=10} \frac{A_i}{(i+1)} (T_T^{i+1} - T_{fp}^{i+1}) \right\} \right]^{1/2} \tag{4.26}$$

An area-temperature relation results from using eq. (4.8) in the form

$$\frac{A}{A^*} = \frac{\rho_C^* \, u_C^*}{\rho_{CF} \, u_{CF}} \tag{4.27}$$

and substituting for ρ_C^*, u_C^*, ρ_{CF} and u_{CF} from eqs. (4.17), (4.18), (4.24) and (4.26). Solution is facilitated in the manner previously described at the end of section 4.2.1.

4.3 Sudden Freezing Model

A considerable amount of effort has been directed towards understanding the effects of vibrational nonequilibrium in steady nozzle flows, and a number of exact calculations combining the flow equations and those for the relaxation process have been made [64,68,65,70]. These calculations have all been for diatomic gases where the fraction of the total flow energy which may be frozen in the molecular vibrations is comparatively small. In such cases it has been shown that no great loss in accuracy results from assuming that the flow equations and the vibrational rate equation are decoupled [71], but in the case of polyatomic gases where vibrational energy can amount to over half of the total energy such an approach is not valid. The fact that nonequilibrium, whether the relaxation process be molecular dissociation or vibration, is confined to a relatively narrow region has led to the sudden freezing approximation [69,72], in which the flow is considered to be in equilibrium down to a freezing point and to remain frozen from them on. By suitable choice of an empirical constant the freezing point is found to characterise the position of the region where rapid departure from equilibrium occurs.

The present work is primarily a parametric performance study, requiring the examination of a number of variables over a wide range of conditions, and in this context vibrational nonequilibrium is modelled

by the sudden freezing approximation. A more exact analysis would be useful for the polyatomic gases where vibrational nonequilibrium in nozzle flows occurs over a broader region, but owing to the considerable uncertainty in rate data for such gases this complexity is not warranted.

Isentropic relations governing temperature and nozzle geometry, obtained by patching together an upstream region of equilibrium flow and a downstream frozen equilibrium region, where the patching point is given by a freezing criterion, were deduced in section 4.2.3. It remains to derive the sudden freezing criterion.

The classical theory of Landau and Teller[73] gives a linear equation for the rate of increase of vibrational energy of a diatomic gas due to the transfer of energy from the translational and rotational degrees of freedom. With the assumptions that (i) the vibrational energy of the molecules can be represented by a simple harmonic oscillator and (ii) transfer of energy from translation to vibration is an adiabatic process, a vibrational rate equation can be written

$$\frac{de_v}{dt} = \frac{e_{v,eq}(T) - e_v}{\tau_v} \tag{4.28}$$

where e_v is the vibrational specific energy and $e_{v,eq}(T)$ is the value of e_v at equilibrium at temperature T. The vibrational relaxation time, τ_v is expressed approximately as

$$\tau_v = \frac{A}{p} \exp\left(\frac{B}{T} \right)^{1/3} \tag{4.29}$$

where A and B are empirical molecular constants. Eq. (4.29), usually referred to as the Landau-Teller equation, relates the relaxation time to the local pressure and temperature for a diatomic gas in an excitation process. Experimental confirmation of the Landau-Teller equation has been given by the large amount of relaxation data obtained from shock wave experiments, i.e. measurements of overall vibrational excitation, in which

a linear dependence of log ($p\tau_v$) with $T^{-1/3}$ is exhibited by most diatomic gases, many diatomic mixtures and several polyatomics (for example, see Refs.74, 75). On account of its simplicity the Landau-Teller treatment is often applied to more complex situations with little, or no, further theoretical justification.

A de-excitation process, such as a nozzle flow, involves an overall energy transfer which is different from that of a normal shock wave flow. It has been reported by several researchers (for example, see Refs. 76, 77, 66) that the vibrational relaxation processes in a de-excitation environment are much faster than in an excitation environment, and the deduced relaxation times are factors from 5 to 70 times faster. Various reasons have been put forward for this behaviour, such as the effects of polyatomic impurities on the relaxation process[77], or the possibility that collisional deactivation of the upper vibrational levels involves multi-quanta exchange[76]. In a study of vibrational relaxation of anharmonic oscillator molecules[78], it is shown for N_2 that the combined effects of anharmonicity and vibration - vibration de-excitation can result in a far more rapid relaxation in expansion flows where the local conditions are far from equilibrium. The situation regarding vibrational de-excitation in polyatomic gases is far from clear, but it is to be expected, as in the expansion of mixtures of N_2 - CO_2 [66,67] and N_2 - CO_2 - H_2O[68], that with several competing processes available to de-excite the upper vibrational levels vibrational relaxation will be extremely rapid. In the present circumstances the best approach seems to be to accept the form of the Landau-Teller equation for predicting relaxation behaviour, and include a factor ϕ to account for the discrepancy between excitation and de-excitation relaxation times. A modified vibrational rate equation is written

$$p\tau_v = \frac{A}{\phi} \exp\left(\frac{B}{T} \right)^{1/3} \qquad (4.30)$$

where ϕ may vary between 1 and 100.

The work of Bray [16], shows that when the flow time characterising the local rate of expansion is much larger than the vibrational relaxation time, vibrational rate processes can be considered to be in equilibrium with translation. Similarly when the local flow time is much shorter than the relaxation time vibrational energy remains constant. Nonequilibrium exists when the two characteristic times are of the same magnitude. The rate equation (4.28) can be written as

$$u_e \frac{de_v}{dz} = \frac{e_{v,eq}(T) - e_v}{\tau_v}$$

which can be rearranged to give

$$-\frac{u_e}{e_v}\frac{de_v}{dz} = \frac{1 - e_{v,eq}(T)/e_v}{\tau_v} \tag{4.31}$$

Defining a local flow time as

$$\tau_{fl} = -\left[\frac{u_e}{e_v}\frac{de_v}{dz}\right]^{-1}_{eq} \tag{4.32}$$

which is a maximum in the equilibrium limit, Bray shows, using eqs. (4.31) and (4.32), that

$$\frac{\tau_v}{\tau_{fl}} \geq 1 - \frac{e_{v,eq}(T)}{e_v}$$

Under conditions of near-equilibrium flow $\tau_v << \tau_{fl}$ and $e_v \rightarrow e_{v,eq}(T)$; in the frozen flow limit with $\tau_v >> \tau_{fl}$, e_v is constant and $\tau_{fl} \rightarrow 0$. The nonequilibrium region exists between these two limits where $\tau_v \approx \tau_{fl}$. By considering vibration to be in equilibrium with translation when $\tau_v \leq \tau_{fl}$ and to be frozen when this relation does not hold, a sudden freezing position can be defined as that point where $\tau_{fl} = \tau_v$. It is more informative physically to express this criterion in terms of the rates of expansion and of vibrational deactivation, thus Phinney [79] uses a freezing criterion which can be expressed as

$$\left| u_e \frac{de_v}{dz} \right|_{eq} = P\left(\frac{e_v}{\tau_v}\right)_{eq} \tag{4.33}$$

where P is a constant of order unity, matching the approximate criterion with more exact solutions. Here, freezing is considered to have occurred when the time rate of change of vibrational energy with rate processes in equilibrium (left hand side of eq. (4.33)) exceeds the kinetically possible vibrational energy gradient (right hand side). Introducing eq. (4.30) into (4.33) the freezing criterion can be written as

$$\left| u_e \frac{de_v}{dz} \right|_{eq} = \Phi \left(\frac{pe_v}{A \exp\left(\frac{B}{T} \right)^{1/3}} \right)_{eq} \tag{4.34}$$

where $\Phi = P\phi$. Eq. (4.34) is the form of the sudden freezing criterion which is used in this work.

The constants A and B required to fit the Landau-Teller equation to experimental relaxation times are presented in Appendix B for gases H_2, N_2, NH_3, CH_4 and CO_2. A literature survey of the vibrational rate data relevant to these gases and for various mixtures is also presented in this place.

4.4 An Approximate Model of Vibrational Relaxation in $NH_3 - H_2 - N_2$ Mixtures

At the operating temperatures found in resistojets, NH_3, is the only gas considered here which can disssociate into a mixture containing two or more vibrationally excited species. If chemical equilibrium is attained in the heater, at temperatures above 1000°K the efflux gas consists essentially of a N_2-H_2 binary mixture; however, more realistically, the chemical kinetic rate of dissociation is probably never sufficiently high for all the NH_3 to be disssociated during its rapid passage of the heater, so even at 2000°K the efflux consists of a N_2-H_2-NH_3 mixture, all three

species being vibrationally excited. In order to examine the nozzle performance in the case where finite vibrational rate processes are assumed to occur, some consideration of vibrational relaxation in mixtures is required.

In a series of shock tube experiments performed on mixtures of NO-CO, NO-N_2 and CO_2-N_2, Taylor, Camac and Feinberg[80] found that vibrational relaxation in these mixtures was controlled by rapid V-V energy exchange processes, as a consequence of which they observed dramatic reductions in the relaxation time of the slower component. These experiments indicate that the component with the faster T-V energy exchange rate initially relaxes rapidly to some fraction of its final equilibrium vibrational energy; at this point V-V processes force the two components to approach equilibrium with the same rate. Further, the vibrational temperature measurements in expanding mixtures of CO_2 and N_2, performed by Sebacher, Guy and Lee[66], show in fact that there are two separate relaxation modes. The first, corresponding to T-V energy exchange of N_2 has a longer relaxation time than the second, which corresponds to a V-V coupling between N_2 and CO_2, the energy being transferred to translation by the faster T-V process of CO_2. Multiple relaxation paths are well known for polyatomic gases, where the larger number of modes increases the chances of frequency matching and intramolecular processes such as Fermi resonance are possible [81].

Appendix B presents some information on vibrational relaxation in mixtures where H_2 is present. Moore [82] points out that vibration-rotation (V-R) energy exchange becomes important in molecules containing hydrogen atoms, and the extremely rapid vibrational deactivation of mixtures of CH_4-H_2 and N_2-H_2 must, in part, be due to this mechanism, which also must be present in the ammonia case.

The ammonia nozzle flow problem may be further complicated by the effect of chemistry in the heater on the vibrational population distribution.

The heterogeneous dissociation of ammonia on the heater wall should give rise to a distribution, characteristic of the wall temperature, since a sorption/desorption process is involved, but the homogeneous reaction in the gas phase can give rise to non-Boltzmann distributions via atom-atom recombinations. However the homogeneous reaction is about an order slower than the heterogeneous one for temperatures below 2000°K, thus only up to 10% of the N_2 and H_2 may be affected. Further the transit time of the heater is of order 1 ms. during which there will be of order 10^6 - 10^7 collisions, which are enough essentially to restore equilibrium, particularly if polyatomics are present (section 4.1). While the physics of the situation remains intriguingly complex with several possible V-V and V-R processes competing to deactivate the higher vibrational levels, as far as engineering is concerned the gas at heater exit/nozzle entrance may be taken to be in vibrational equilibrium. Of course the relaxation through the nozzle is still complex and due to the lack of experimental data and theoretical knowledge the model for the relaxation of NH_3-N_2-H_2 mixtures necessarily is crude.

The model which is proposed is intended to produce a lower bound on performance by making pessimistic approximations to the relaxation rate. The first assumption is that N_2 is de-excited via rapid H_2 vibrational-rotation-translation energy transfer processes, so it is not a rate-limiting step in the overall de-excitation process. In other words the vibrational mode of N_2 is assumed to act only as an energy store and the possibility that it may relax separately is not considered. Thus in the equilibrium limit with a N_2-H_2 mixture, the vibrational relaxation rate is identical to that of H_2. This is consistent with a worst case approximation since experimental evidence in Appendix B suggests that a N_2-H_2 mixture relaxes nearly ten times faster than pure H_2. For the more general case of a N_2-H_2-NH_3 mixture the rate of de-excitation is assumed to be determined by the behaviour of the H_2-NH_3 with N_2 making no contribution to the rate process. The equivalent H_2-NH_3 mixture is then

assumed to follow the "parallel resistance" law [83] for simple mixtures, which can be expressed as

$$(\tau_v)^{-1}_{mix} = \frac{X(H_2)}{\tau_v(H_2)} + \frac{X(NH_3)}{\tau_v(NH_3)} \qquad (4.35)$$

where the mole fractions have been normalised so that $X(H_2) + X(NH_3) = 1$. For mixtures such as CO_2-N_2 with a resonant V-V exchange process eq. (4.35) works extremely well, in an excitation environment; however, for mixtures in which H_2 is present the relaxation rate is always underestimated. Apart from some uncertainties in the NH_3 relaxation rate (reviewed in Appendix B), by making the sweeping approximations above, therefore, the lowest possible relaxation rates should be predicted and a lower bound on performance produced.

5.1 Introduction

This chapter returns to the problem which was defined in Chapter One, that of modelling the performance of resistojet nozzles on a digital computer. The requirement of the model can be stated as follows. For a given nozzle geometry, given propellant and specified nozzle input conditions, i.e. stagnation temperature, pressure and composition, it is desired to calculate the performance taking into account losses due to frozen chemical rate processes, frozen vibrational rate processes, incomplete expansion, viscous flow and radial flow at the nozzle exit. The basis of accounting for these losses in terms of jet power was presented in Chapter Two. Two sources of loss, i.e. viscous flow and the finite vibrational relaxation rate, required further consideration, which has occupied the last two chapters. Several alternative approaches for modelling both the viscous flow and the vibrational rate processes were developed so that a hierarchy of models of resistojet nozzle performance may be produced, which describe the losses with increasing degrees of complexity.

In the computation the philosophy was adopted that a common program structure would apply to all the performance models. Therefore to change from one model where, say, the boundary layer calculation is based on the Class A similar solutions, to another model using the Class B solutions, in principle requires only substitution of one segment for another. The basic calculation procedure is described in section 5.2. While a common structure runs throughout the computer models which are used here, it is not practical from the viewpoint of economy in computer storage and execution time to write programs in which the segments are interchangeable. Thus the various models are optimised for a specific purpose, so that they are distinct programs.

Four models are reported in this chapter, the main features of which are summarised below.

Model Zero is a preliminary model used to examine the magnitude of the various losses. In order to set a lower limit on performance, "worst case" approximations are made. The vibrational rate processes are considered to be frozen throughout the nozzle, and the boundary layer calculation is based on the approximate method of Cohen and Reshotko, which was introduced in section 3.1 and is described in more detail in section 5.3.

Model One differs from Model Zero only in the boundary layer calculation. Here the laminar boundary layer is represented by the "patching together" of the Class A similar solutions (section 3.5.1). The assumptions of unit Prandtl number, a linear viscosity-temperature relationship and an adiabatic wall are still retained, but the fundamental boundary layer solutions are rigorous, (section 5.4).

Model Two examines the effects on performance of allowing vibrational energy to relax through the nozzle. There are two alternatives. In the first, a freezing criterion is applied, so that some loss from frozen vibrational energy may still occur. The second alternative results from removing the freezing criterion, in which case vibrational energy remains in equilibrium throughout the nozzle. The boundary layer calculation is again based on the Class A similar solutions. A description of this model is given in section 5.5.

Model Three reverts to the assumption of frozen vibrational rate processes, but differs from Model One in that the Class B similar solutions are used in the boundary layer calculation. Therefore it is intended for a study of the effects of transverse curvature on resistojet nozzle performance. It is presented in section 5.6.

5.2 Calculation Procedure

The basic computer program consists of three main sections (see the flow diagram in Fig. 19). Details of the nozzle geometry, and of the propellant chemistry and thermodynamics, are evaluated in the first section. The second section is an iteration in which for an assumed effective geometry, the isentropic core properties and the corresponding boundary layer growth are calculated to produce a new effective geometry. This process is repeated either, a given number of times, or, until satisfactory convergence of the boundary layer-isentropic core calculation is achieved. In the final section the performance parameters are evaluated. The individual sections are now described in more detail.

5.2.1 Nozzle Geometry

The nozzle is considered in three parts :

(i) a conical convergent section, where the geometric variables which must be specified are the inlet radius, R_1, and the convergent half angle, θ_1, (see accompanying figure),

(ii) a circular throat section with radius of curvature, R_c, and throat radius, R^*, smoothly connecting the convergent section to

(iii) the divergent section where the wall shape is described by

$$R = \theta_2 z_D + a z_D^2 + b z_D^2 \qquad (5.1)$$

so that nozzles from horn through conical to bell shapes can be generated.

Obviously a higher-order series could be used, but eq. (5.1) was found to be sufficient for the present purposes. An additional variable which must be specified is the area ratio, $\epsilon = (R_2/R^*)^2$

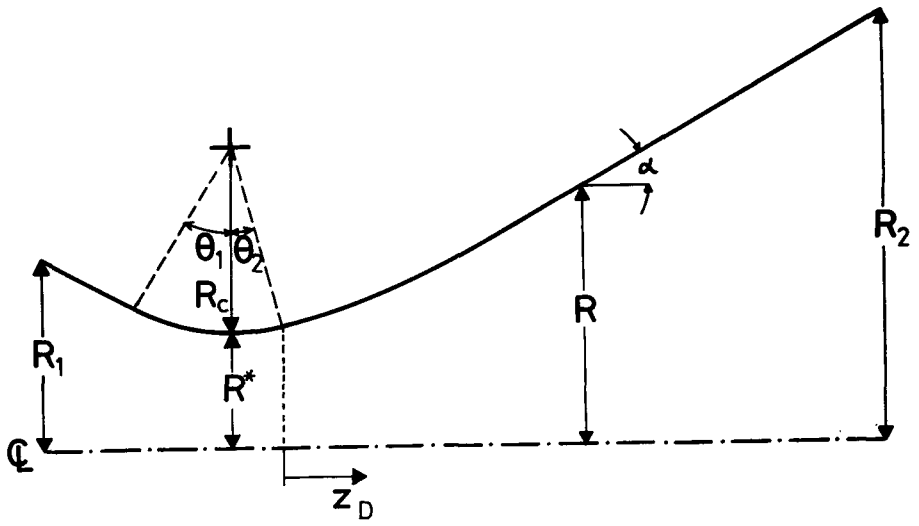

Nozzle Geometric Variables

The geometry calculation simply divides the nozzle axis into 100 equal parts, and evaluates the radius, wall position and local wall angle, α, at each of the resulting 101 stations. The station immediately upstream of the geometric throat is also determined for use later in a mass flow rate calculation.

5.2.2 Propellant Chemistry and Thermodynamics

There are two alternatives in this subsection corresponding to the cases where the propellant either dissociates during passage through the heater, or remains a single species. In the first alternative, as well as summing the contributions to the thermodynamic variables from two or more species, the program calculates the chemical composition. Of the propellants considered here, CO_2 does not dissociate at resistojet operating temperatures. Methane does dissociate, with detrimental effects on the useful resistojet life. The temperature at which carbon deposition becomes significant is a function of the heater geometry and transit time[38], but in the present work it is considered to remain a single species. The highest temperature for which results have been obtained for CO_2 and CH_4 is 2000°K. The remaining two propellants, i.e. NH_3 and H_2, dissociate without solid deposition to produce an increase in jet velocity.

It has been indicated in Chapter One that decomposition is a finite rate process, which requires kinetic data on both the gas phase and wall catalysed reactions for complete modelling. In the case of NH_3 and H_2 insufficient kinetic data is available to make good predictions and a simplifed approach is used, which considers only the end state of the reaction. The performance of NH_3 is investigated for temperatures up to 2000°K. Examination of the equilibrium constants, K_p, in the JANAF tables[19] shows that at temperatures below 2000°K the components finally present can be taken as NH_3, N_2 and H_2. Strictly at temperatures above 1200°K monatomic hydrogen is also present in the equilibrium composition, but to simplify matters it is assumed to be absent at temperatures below 2000°K. The chemical equilibrium in the heater can then be written as

$$2NH_3 \rightleftharpoons N_2 + 3H_2 \tag{5.2}$$

The mole fractions of the three species are given by

$$\left.\begin{aligned} X(NH_3) &= (1-\alpha_1)/(1+\alpha_1) \\ X(N_2) &= \alpha_1/2(1+\alpha_1) \\ X(H_2) &= 3X(N_2) \end{aligned}\right\} \tag{5.3}$$

where α_1, the degree of dissociation of NH_3 at the plenum conditions T_T and p_T is given by

$$\alpha_1 = \sqrt{\frac{4K_p}{4K_p + 2\sqrt{3}p_T}} \tag{5.4}$$

and K_p is the equilibrium constant for eq. (5.2) at T_T.

If the transit time of the heater is less than the characteristic time for decomposition, the above equilibrium calculation does not truly represent the propellant composition at the heater exit; allowance is made for the occurrence of non-equilibrium flow, by introducing a variable f in eqs. (5.3). f is taken as the mole fraction of undissociated

ammonia not included in the equilibrium calculation. Thus f equals zero for an equilibrium composition at exit, and f equals unity when NH_3 remains undissociated. Eqs. (5.3) become :

$$\left.\begin{aligned} X(NH_3) &= f + (1-f)(1-\alpha_1)/(1+\alpha_1) \\ X(N_2) &= (1-f)\alpha_1/2(1+\alpha_1) \\ X(H_2) &= 3X(N_2) \end{aligned}\right\} \qquad (5.5)$$

Hydrogen, being a propellant suitable for prime propulsion, is likely to be operated at higher temperatures than NH_3, CH_4 or CO_2, since the available electric power will be greater. A maximum temperature is taken to be 3000^oK. At temperatures below 2000^oK the simplifying assumption is made that hydrogen remains a single species. Above 2000^oK the dissociation reaction

$$H_2 \rightleftharpoons 2H \qquad (5.6)$$

should be considered. Whether any dissociation can occur in the rapid passage through the heater is doubtful, and in most of the computation H_2 is considered to remain a single species. In order to set a limit on the possible effects of dissociation, the performance with the equilibrium composition is also examined. The degree of dissociation in the equilibrium mixture is simply

$$\alpha_2 = \sqrt{\frac{K_p}{K_p + 4p_T}} \qquad (5.7)$$

and the mole fractions are

$$\left.\begin{aligned} X(H_2) &= (1-\alpha_2)/(1+\alpha_2) \\ X(H) &= 2\alpha_2/(1+\alpha_2) \end{aligned}\right\} \qquad (5.8)$$

where K_p is the equilibrium constant appropriate to eq. (5.6) at a plenum temperature of T_T.

In the remainder of this subsection the available enthalpy is evaluated for the ideal state, when no losses are incurred, and for

the case when the composition is frozen throughout the nozzle. These relations are given by eqs. (2.4) and (2.9). The corresponding mass flow rates, eqs. (2.7) and (2.11) are also calculated. The information on which these calculations are based is again taken from the JANAF tables. As previously mentioned, tenth-order polynomials for the molar heats of H_2, N_2, NH_3, CH_4 and CO_2 have been derived, and the coefficients are presented in Table V. It is seen in this table that there are two sets of coefficients for H_2. This is necessary since hydrogen is an unusual molecule in that the rotational energy is not fully excited until about 360°K. Thus over the temperature range in which the function $c_p^{\,o} = c_p^{\,o}(T)$ is required (approximately 50°K to 3000°K) there are two steps in the molar heat behaviour corresponding to the excitation of first rotational energy and then vibrational energy. It is difficult to accurately fit a polynomial to such a curve so that two polynomials are used, one for temperatures equal to, or less than 500°K, and the other for higher temperatures.

The subsection finishes by calculating the viscosity of the propellant at the plenum conditions. Viscosity data for the gases of interest is shown in Fig. 20. For the mixture of NH_3 - N_2 - H_2 the empirical formula developed by Ulybin[88] is used. This can be written

$$(\mu_{mix})_T = (\mu_{mix})_{Ref} \sum_{i=1}^{i=3} X_i \frac{(\mu_i)_T}{(\mu_i)_{Ref}} \qquad (5.9)$$

where $(\mu_{mix})_{Ref}$ is the viscosity of the mixture at a reference temperature, $(\mu_i)_T$ and $(\mu_i)_{Ref}$ are the viscosities of the i^{th} component at temperature T_T, and the reference temperature. The reference temperature is taken as 283°K. In the equilibrium mixture of H_2 and H, monatomic hydrogen is assumed to have the same viscosity as H_2. Smith[89] presents theoretical values for the viscosity of monatomic hydrogen, indicating that the viscosity of H is approximately 30% less

than that of H_2. Since the amount of monatomic hydrogen present is small, and the viscosities of H_2 and H are similar, the error involved in the above assumption is small.

5.2.3 The Boundary Layer-Isentropic Core Iteration Procedure

The second section of the program is an iteration and it is considered as a whole, rather than in subsections, so as to emphasise the fundamental features of the procedure. More complete descriptions of the various isentropic core and boundary layer subsections are given in 5.3 to 5.6.

By assuming that the only consequence of the boundary layer is a displacement of the effective wall position, an effective inviscid flow can be defined. Further assuming that the effective flow is quasi one-dimensional means that the fluid variables, such as temperature and velocity, are dependent only on the axial distance down the nozzle. The iteration starts by calculating the axial temperature distribution corresponding to a completely inviscid flow, i.e. the initial effective geometry is taken to be the actual nozzle geometry. These calculations are carried out at the 101 stations previously evaluated in program section 1 (5.2.1). The resulting pressure gradient is then calculated, from which the corresponding boundary layer growth is found at each station. At this stage all that is required in the boundary layer calculation is an estimate of the displacement thickness, δ^*. In high Reynolds number flow the boundary layer has a negligible displacement effect on the potential flow, but in resistojets where the boundary layer occupies a considerable portion of the nozzle flow field the interaction cannot be ignored. Thus a new effective geometry must be defined and the corresponding isentropic core and boundary layer calculation repeated. A new effective geometry is found by taking the average value of the old effective geometry and that resulting from displacement by the boundary

layer. In general, the new effective geometry, given by the n^{th} iteration, can be written as

$$(R_{eff})_{n+1} = \frac{1}{2}\left\{(R_{eff})_n + R - (\delta^*)_n \right\} \tag{5.9}$$

A feature of viscous nozzle flows is that the choking position is no longer necessarily coincident with the geometric throat, and its exact position is determined in the effective geometry subsection. This is found by examining the boundary layer in the throat region in more detail. In particular the effective radii at the five stations immediately upstream and five stations immediately downstream of the previous choking position (i.e. ten in all) are interpolated by a cubic spline subroutine (CSFMIE) to find the axial position for which $(R-\delta^*)$ is a minimum. This gives the new effective throat. Mass continuity at each station in the nozzle can now be satisfied so that the isentropic core properties corresponding to the new effective geometry can be recalculated.

There are a variety of ways of testing the iteration procedure for convergence. The method used here is to examine the ratio of the effective area ratio at exit to the initial inviscid area ratio, i.e. the geometric area ratio, ε. Convergence of this procedure is illustrated in Fig. 21 for a hydrogen resistojet nozzle with $\varepsilon = 25$ and plenum temperature of $1500^{o}K$ over a range of Reynolds numbers, Re_{D^*}, from 4030 down to 201. At the higher Reynolds numbers, i.e. Re_{D^*} greater than 1000, convergence to the final effective area ratio is smooth, but at lower Reynolds numbers (in this case lower plenum pressures) the process is slower and oscillatory. At the lowest Re_{D^*} convergence has not occurred after five boundary layer calculations, and increasing the number of iterations causes the process to become divergent. The reason for this lies in the fact that with a larger number of iterations the numerical errors introduced in computation are increased; in particular numerical differentiation becomes

troublesome. This is of some importance to the present results and it is examined further in the discussion of results in Chapter Six. The point which is made at this juncture is that convergence to a specified value cannot be achieved over the whole range of Reynolds numbers. Thus the approach adopted in this study is that the iteration procedure is carried out a fixed number of times rather than to a convergence criterion. A reasonable compromise is taken as three isentropic core - boundary layer - effective geometry iterations, with a fourth and final calculation of the isentropic core parameters to give mass continuity. In the final boundary layer calculation other boundary layer parameters such as the momentum thickness and overall thickness are also evaluated.

It should be noted that the available specific enthalpy when vibrational energy is frozen throughout the nozzle, or freezes in the nozzle, given in eqs. (2.19) and (2.15), is calculated at the end of the first isentropic core calculation, i.e. when the complete flow is inviscid. The jet velocity with the additional loss due to incomplete expansion, V_{jCFE}, given by eq. (2.30), is also calculated at this point.

5.2.4 Performance Parameters

In the final section of the basic program the parameters such as thrust, jet power and the various efficiencies are calculated. The required relations are all set out in Chapter Two and only a word of explanation about the radial flow loss is necessary. Account of the loss in thrust due to the radial component of exhaust velocity is given by the expression $(1 + \cos \alpha_e)/2.$, where α_e is the effective nozzle angle at exit. An estimate of α_e can be obtained from the change in the effective radius between the last two stations in the nozzle. This can be expressed as

$$\tan \alpha_e = \frac{(R-\delta^*)_{101} - (R-\delta^*)_{100}}{z_{101} - z_{100}} \qquad (5.10)$$

5.3 Model Zero

This model is described in two parts, (i) the isentropic core calculation with vibrational rate processes frozen at entrance at the nozzle, and (ii) the approximate method of Cohen and Reshotko for compressible laminar boundary layers.

5.3.1 Isentropic Core Calculation (Vibrational Energy Frozen)

The theory relevant to this situation is developed in section 4.2.1 and the order in which the isentropic core properties are evaluated in the program is given below.

(i) The temperature at the choking position, T^*_{CF}, is obtained from eq. (4.14).

(ii) The area ratios at 100 points through the subsonic section of the nozzle are calculated from eq. (4.12), which correspond to the temperatures

$$T = T_T - \frac{i}{100}(T_T - T^*_{CF}) \quad \text{where } i = 1,2 \ldots, 100$$

(iii) Using the subroutine CSFMIE (Fig. 19) the resulting 100 points in the T - A plane are interpolated to give the temperatures which correspond to the area ratio of the required equi-spaced stations in the subsonic flow.

(iv) A similar procedure to operations (ii) and (iii) is carried out in the supersonic flow. The initial temperature - area distribution is evaluated at the temperatures given by

$$T = T^*_{CF} - \frac{i}{100}(T^*_{CF} - T_T/20.) \quad \text{where } i = 1,2\ldots,100$$

(v) With the values of T_{CF} corresponding to the 101 equi-spaced stations through the nozzle, all other isentropic core properties can be evaluated. Thus the velocity, density and pressure come from eqs. (4.11), (4.10) and

(4.9). The Mach number is given by

$$M_{CF} = U_{CF} \Big/ \left[\gamma_{CF} \frac{R_u}{\bar{M}} T_{CF} \right]^{\frac{1}{2}} \tag{5.11}$$

It is noted that the temperature-area (T-A) method of evaluating the properties of a constant specific heat isentropic core differs from the conventional Mach number-area (M-A) relation which was initially used and reported in Ref. 37. The present T-A method is preferred for its accuracy and speed of calculation as the original M-A relation requires an iteration procedure, which converges very slowly as Mach number tends to unity.

5.3.2 Application of Cohen and Reshotko's Approximate Boundary Layer Method to Resistojet Nozzles

The following description of the Cohen and Reshotko boundary layer method is fairly concise. For further details the reader should consult the original paper.[42]

The fundamental relation of this approximate method is the momentum integral equation in the transformed, incompressible plane, which Cohen and Reshotko reduce to the form

$$-\tilde{u}_e \frac{d}{d\tilde{x}} \left(\frac{n}{d\tilde{u}_e/d\tilde{x}} \right) = N(n, S_w) \tag{5.12}$$

where $$N(n, S_w) = 2\left[n(H_{tr} + 2) + \ell \right] \tag{5.13}$$

The tilde notation refers to quantities in the transformed plane, thus $\tilde{u}_e$ is the freestream velocity in the $(\tilde{x}, \tilde{y})$ plane. N, known as the momentum parameter, is a function of n and S_w, which is obtained from the earlier similar solutions of Cohen and Reshotko[48] for Pr = ω = 1. S_w is a non-dimensional enthalpy function given by

$$S_w = H_w/H_T - 1.$$

n is a correlation parameter, related to the pressure gradient and ℓ is

a shear parameter. The final quantity H_{tr} is a transformed boundary layer form factor which is given by

$$H_{tr} = \delta^*_{tr}/\theta_{tr}$$

where δ^*_{tr} and θ_{tr} are the corresponding displacement and momentum thicknesses. The three quantities H_{tr}, δ^*_{tr} and θ_{tr} are all evaluated in Cohen and Reshotko's first paper.

The problem is to determine the value of the correlation parameter, n, at the particular station under consideration; once n is known, θ_{tr} and thus θ (momentum thickness in the physical plane) can be determined leading to values for δ^* and δ . An approach suggested by Cohen and Reshotko for the case of an isothermal wall, i.e. when S_w remains constant, is to assume a linear relationship between the momentum parameter, N, and the correlation number, n. This implies that

$$N = A + Bn \tag{5.14}$$

Using eq. (5.14) in eq. (5.12) results in a linear first order equation, the solution of which is

$$n = - A \, (\tilde{u}_e)^{-B} \, \frac{d\tilde{u}_e}{d\tilde{x}} \int_0^{\tilde{x}} \tilde{u}_e^{(B-1)} \, d\tilde{x} \tag{5.15}$$

Transforming to the compressible plane and converting to axisymmetric flow by application of the standard Mangler transformation the following equation is obtained

$$n = A \, \frac{u^*}{u_e} \, \frac{d\left(\frac{u_e}{u^*}\right)}{d\left(\frac{x}{L}\right)} \left(\frac{T_T}{T_e} \right)^{\left(\frac{5\gamma - 3}{2(\gamma-1)}\right)} \frac{M_e^{(1-B)}}{(R/R^*)^2} \int_0^{x/L} \left(\frac{R}{R^*} \right)^2 \left(\frac{T_e}{T_T} \right)^{\left(\frac{3\gamma - 1}{2(\gamma-1)}\right)} M_e^{(B-1)} \, d\left(\frac{x}{L}\right) \tag{5.16}$$

Provided that A and B are known the correlation parameter, n, can be determined in terms of the inviscid core conditions at any station in the nozzle. The momentum thickness, θ , is obtained from

$$\theta^2 = - \left(\frac{T_e}{T_w}\right) \left(\frac{T_e}{T_T}\right) \frac{n \mu_w L}{\rho_e u^*} \frac{d\left(\frac{x}{L}\right)}{d\left(\frac{u_e}{u^*}\right)} \tag{5.17}$$

When the wall is assumed to be adiabatic, for Pr = 1 it is implied that $T_w = T_T$, $\mu_w = \mu_T$ and $S_w = 0$.

The displacement thickness is given by

$$\delta^* = \theta \left[\frac{T_T}{T_e} (H_{tr} + 1) - 1 \right] \tag{5.18}$$

and the boundary layer thickness

$$\delta = \theta \left[\frac{\delta_{tr}}{\theta_{tr}} + \left(\frac{T_T}{T_e} - 1 \right) \left(H_{tr} + 1 \right) \right] \tag{5.19}$$

taken at $u/u_e = 0.995$.

The correlations of Cohen and Reshotko for $S_w = 0$, of N versus n, H_{tr} versus n, and δ_{tr}/θ_{tr} versus n are presented in Fig. 22. It is seen that there is a maximum favourable pressure gradient (negative correlation parameter) that can be dealt with by this method, which corresponds to $\beta = 2$. As already discussed the pressure gradients in resistojet nozzles are very favourable and correlations for more negative values of n are required. This was achieved by extrapolating the existing correlations graphically. It is also observed from the top graph in Fig. 22 that a linear relation for N = N(n) is a good approximation. A suitable relation is

$$N = 0.394 + 4.78n \tag{5.20}$$

which is the linear approximation at n = - 0.15. However, it was found that the choice of the tangent line had little influence on the various boundary layer thicknesses.

At a given station the sequence of operations in the boundary layer subsection are :-

(i) The correlation parameter, n, is calculated from eq. (5.16). This requires the use of subroutines

CSINT and DYDX.

(ii) Using the interpolation subroutine CSFMIE the appropriate values of H_{tr} and δ_{tr}/θ_{tr} are obtained.

(iii) The momentum and displacement thicknesses are evaluated from eqs. (5.17) and (5.18). In the final boundary layer calculation (i.e. third iteration) the overall boundary layer thickness, given by eq. (5.19), is also calculated.

(iv) Since these boundary layer thicknesses are all normal to the nozzle wall, the interpolation subroutine is again used to give the corresponding thicknesses in the radial plane (see Fig. 2).

Finally, the integral in the thrust relation (eq. 2.35) can be evaluated upon the assumption of a linear velocity profile. It can be shown (see Ref. 37) that an approximate expression for this integral is

$$\frac{2}{R^2}\int_{R-\delta_d}^{R}\frac{\rho u}{\rho_e u_e}\left(1-\frac{u}{u_e}\right)rdr=\frac{2\theta}{R}K_1 \tag{5.21}$$

where

$$K_1=1-\frac{\delta}{R}\left\{\frac{\phi\ \ln\left(\frac{\phi+1}{\phi-1}\right)-\phi^2\ \ln\left(\frac{\phi^2}{\phi^2-1}\right)-1}{\ln\left(\frac{\phi^2}{\phi^2-1}\right)-\phi\ \ln\left(\frac{\phi+1}{\phi-1}\right)+2}\right\} \tag{5.22}$$

and

$$\phi=\frac{2\,C_{pF}\,T_T}{u_e^{\,2}} \tag{5.23}$$

5.4 Model One

In this model the vibrational rate processes are again assumed to be frozen, but the boundary layer calculation is based on the Class A

similar solutions which were developed in Chapter Three.

Similar solutions can be applied to a general non-similar flow by using the concept of local similarity. To paraphrase Hayes and Probstein (Ref. 60, p.313), the applicability of this technique relies essentially on the condition that the freestream flow properties vary sufficiently slowly with the x-dependent variable ξ (eq. 3.22). Provided that this is the case the full non-similar equations (eqs. 3.29 and 3.30) can justifiably be approximated by ordinary differential equations in η, in which ξ appears only as a parameter (eqs. 3.31 and 3.32). Thus in the application of local similarity to the present problem, the flow is assumed to be similar in the vicinity of a given station in the nozzle. For the values of the ξ-dependent parameters, such as the pressure gradient and transverse curvature parameters, appropriate to that station the boundary layer can be predicted by using the previously determined similar solutions of section 3.5. By assuming that the flow at each station throughout the nozzle is locally similar the boundary layer development can then be approximated by connecting (or "patching together") these similar solutions.

In the Class A similar equation, i.e. the Falkner-Skan equation (eq. 3.67), only the pressure gradient parameter, β , is ξ-dependent. Variation of β in a typical resistojet nozzle is shown in Fig. 23. It is seen that β changes appreciably through the nozzle, in which case the assumption of local similarity is only a crude approximation. Therefore, the modelling of the boundary layer development by successive patching of the similar solutions, appropriate to each station, is not theoretically valid. In spite of this, justification for the use of similar solutions in this study is to be found in the good agreement with other experimental and theoretical results, given in Chapter Six.

The order in which the boundary layer calculation is applied at each station is as follows.

(i) The x-coordinate is transformed through the use of eq. (3.22),

$$\xi = \int_0^x \rho_w \mu_w u_e R^2 \, dx$$

(ii) The pressure gradient is determined from eq. (3.40), which can be written as

$$\beta = \frac{2\xi}{u_e} \frac{du_e}{d\xi} \frac{T_T}{T_e}$$

(iii) Hence, the appropriate values of P_1 and P_2 (also P_3 in the third iteration) can be obtained by interpolation of the values presented in Table I.

(iv) The transverse curvature parameter is evaluated from eq. (3.46),

$$\Theta = \frac{2(2\xi)^{\frac{1}{2}} \cos \alpha}{\rho_e u_e R^2}$$

(v) The displacement thickness is calculated from eq. (3.59), which can be written as

$$\delta^* = \frac{R \Theta}{2 \cos \alpha} \left[\frac{T_T}{T_e} P_1 - P_2 \right]$$

In the final iteration the momentum and overall boundary layer thickness are also determined. Eqs. (3.60) and (3.61) can be expressed

$$\theta = \frac{R \Theta}{2 \cos \alpha} P_2$$

$$\delta^* = \frac{R \Theta}{2 \cos \alpha} \left[\frac{T_T}{T_e} P_1 + P_3 \right]$$

(vi) Finally, the corresponding thicknesses in the radial plane are derived by interpolation.

5.5 Model Two

In this model the effects on performance of allowing vibrational rate processes to relax in the nozzle flow are examined with the theory which has been described in sections 4.2.2 and 4.5. The boundary layer calculation is exactly as described in Model One.

First, the calculation procedure for the sudden freezing approximation of nonequilibrium flow is outlined.

(i) The temperature at the choking position, T_c^*, is determined from the identity given in eq. 4.21.

(ii) The temperature distribution in the subsonic flow is evaluated by obtaining an arbitrary temperature-area distribution from eq. (4.19), where the temperatures are specified by

$$T = T_T - \frac{i}{100}(T_T - T_c^*) \qquad (i = 1, 2 \ldots, 100)$$

Then the unknown temperatures corresponding to the required area ratios at the equi-spaced stations on the nozzle axis can be determined by interpolation.

(iii) For the first five stations in the supersonic flow it is assumed that vibrational energy remains in equilibrium. Why this is done is explained shortly. The temperature at these stations is then determined in a similar manner to step (ii).

(iv) At each station downstream of this an initial, equi-temperature difference, temperature-area distribution is defined with eq. (4.19), from which the unknown temperature for the required area ratio can be obtained.

(v) The freezing criterion given by eq. (4.34) is applied. When this is satisfied, i.e. when the rate of change of vibrational energy with rate processes in equilibrium exceeds the kinetically possible rate, vibrational freezing is assumed to have occurred, so that the molar heat, c_p^o, becomes a constant.

(vi) The required temperature-area distribution in the remainder of the nozzle is then derived by interpolating an initial, equi-temperature difference, temperature-area distribution given by eq. (4.27).

(vii) Values for velocity, density and the other isentropic core variables are derived from the relevant relations given in sections 4.2.2 and 4.2.3.

It is necessary to assume that vibrational rate processes remain in equilibrium in the vicinity of the throat, in order that no discontinuities are obtained in the displacement thickness in this region. Although the flow variables such as velocity and temperature (from eqs. 4.26 and 4.27) are continuous functions at the patching point, i.e. the freezing position, the gradients of these variables must be discontinuous. It follows that there is a discontinuity in the rate of change of the displacement thickness at the freezing position. If this is allowed to occur at any of the 10 stations which are used in the determination of the choking position, the subsequent calculation of the mass flow rate can be disturbed. This assumption has little or no effect on the performance of the polyatomic propellants, where the vibrational energy is a significant fraction of the total internal energy, since, in general, freezing does not occur until well into the supersonic flow (see Chapter Six). In the case of the diatomic propellants it can markedly delay freezing. However the vibrational energy content is small in this case, and the effect on performance is negligible.

Second, the calculation procedure for the case where vibrational energy remains in equilibrium throughout the nozzle is obtained by simply removing the freezing criterion. In this case steps (v) and (vi) in the above list are not used.

5.6 Model Three

This model makes use of the Class B similar solutions to examine the nozzle performance, when some account is taken of the effects of transverse curvature in the boundary layer development. It is assumed that vibrational energy is frozen at entrance to the nozzle, so that the isentropic core calculation is as described in section 5.3.1.

In a like manner to Model One the Class B similar solutions are patched together to approximate the boundary layer growth through a resistojet nozzle. The same reservations must be made regarding the applicability of solutions of the modified Falkner-Skan equation, as were noted with the straightforward Falkner-Skan equation. It is seen from section 3.5.2 that there are three ξ-dependent parameters in the Class B equation (eq. 3.73) - the pressure gradient parameter, transverse curvature parameter and freestream stagnation to static temperature ratio. The variations of β, Θ and T_T/T_e in a typical resistojet nozzle flow are shown in Fig. 23. It is assumed in the patching of the Class B solutions that the freestream stagnation temperature, $T_{e,T}$, is identical to the plenum stagnation temperature T_T. This factor combined with the other reservations means that the boundary layer model can account only very approximately for the effects of transverse curvature. However, it is interesting to see what are the differences between this model and Model One, where the boundary layer solutions are essentially for planar flow and conversion to axisymmetric flow is achieved with the standard Mangler transformation.

The calculation procedure follows that described in section 5.4. For completeness it is outlined below.

(i) The transformation from x to ξ is carried out with eq. (3.22).

(ii) The pressure gradient parameter, β, and the transverse curvature parameter, Θ, are calculated from eqs. (3.40) and (3.46).

(iii) At each station, for the known values of β, Θ and T_T/T_e, the integrals P_1 and P_2 (later P_3 also) are obtained by interpolation of Table II. The fact that these integrals are almost linear with changes in Θ and T_T/T_e, for the region in which solutions were obtained, results in some simplification of the interpolation procedure.

(iv) The displacement thickness is obtained from eq. (3.53) which, using the definitions for P_1 and P_2, can be written as

$$\delta^* = \frac{R}{\cos \alpha} \left[1 - \left\{ 1 - \Theta \left(\frac{T_T}{T_e} P_1 - P_2 \right) \right\}^{\frac{1}{2}} \right]$$

The momentum and overall boundary layer thicknesses come from eqs. (3.56) and (3.58), and can be expressed as

$$\theta = \frac{R}{\cos \alpha} \left[1 - \left\{ 1 - \Theta P_2 \right\}^{\frac{1}{2}} \right]$$

$$\delta = \frac{R}{\cos \alpha} \left[1 - \left\{ 1 - \Theta \left(\frac{T_T}{T_e} P_1 + P_3 \right) \right\}^{\frac{1}{2}} \right]$$

(v) These thicknesses are converted to the radial plane.

Chapter Six Results and Discussion

6.1 Introduction

The models of resistojet nozzle performance which were described in the previous chapter have been programmed in FORTRAN IV, and results have been obtained, on an ICL 1907 digital computer, for NH_3, CH_4, CO_2 and H_2 over a wide range of plenum conditions and nozzle geometries. The results, and discussion of their significance, fall into three parts; (i) an examination of the predictions of the four models for one resistojet nozzle geometry over a matrix of plenum conditions, (ii) an examination of the variation in performance with different nozzle geometries, and (iii) a comparison with published results for the experimental performance of resistojet motors, and for other related nozzle experiments.

Predictions of Models Zero, One, Two and Three for a nominal nozzle geometry are presented in section 6.2. The main purpose of this section is to quantify the individual efficiencies, and to gain an insight into the gasdynamics of resistojet nozzle flows. Obviously, this depends on the approximations used in the various models so that, to an extent, the discussion is a comparative one. The results of the models are considered in the following order :

(i) Model Zero, serves as an introduction to the results and quantifies the various possible losses.

(ii) Model One, in which the Class A similar solutions are employed, is used almost exclusively for an examination of the viscous flow losses. Since vibrational rate processes are assumed to be frozen, the discussion concentrates mainly on the results for hydrogen, where this assumption is reasonable.

(iii) Model Two, which allows vibrational relaxation to occur, is used to examine the problem of vibrational freezing more closely. It is therefore concerned mainly with the losses suffered by CH_4, CO_2 and NH_3.

(iv) Model Three, employing the Class B similar solutions, is again concerned with the viscous flow losses. Comparison is made with the results of Model One in order to ascertain what effect first-order transverse curvature has on the boundary layer development.

It is found that the predictions of the different boundary layer models differ, although the trends are similar. The results of Model One (i.e. boundary layer calculation based on the Class A similar solutions) are the most pessimistic, and this model is used to examine the variation in performance with different nozzle geometries. These results are presented in section 6.3.

In section 6.4 comparisons of the predictions of Models One and Two are made with experimental results which have been reported in the literature. It was remarked previously that a number of difficulties are encountered in accurately measuring resistojet performance. The way in which these factors affect comparisons between experiment and theory is also discussed.

The overall performance parameters such as specific impulse and thrust coefficient are not discussed at length, however, extensive tabulations of the performance figures obtained with Model Two for hydrogen, methane, carbon dioxide and ammonia for the nominal nozzle geometry are presented in Table VI.

6.2 Nominal Nozzle Geometry

In order to examine the differences between the predictions of

the four performance models and to gain an understanding of the physics of resistojet nozzle flow, computation was first carried out for a fixed nozzle geometry with a conical divergent section of 25 : 1 area ratio. The geometric parameters (see figure on page 104) are defined :-

R_1 = 2.0 mm

θ_1 = 60^o.

R_c = 2.0 mm

R^* = 0.5 mm

θ_2 = 20^o.

ε = 25.

a = b = 0.

Calculations were performed at 25 points in the following matrix of plenum conditions:

p_T (kNm^{-2})	200.	100.	50.	25.	10.
T_T (^oK)	300.	500.	1000.	1500.	2000.

6.2.1 Predictions of Model Zero

To recapitulate, the main features of this model are that (i) vibrational rate processes are assumed to be frozen throughout the nozzle and (ii) the boundary layer calculation is based on the approximate method of Cohen and Reshotko. Although the boundary layer calculation is not strictly justified, the results obtained with this model are useful since they give the relative magnitudes of the component losses, therefore enabling an assessment to be made of the processes which should be examined further. To avoid undue repetition, only results for NH_3 and H_2 are presented. The individual losses arising from frozen flow, viscous flow and so forth are now examined in turn.

(i) Frozen chemical rate processes

At temperatures below 2000^oK, NH_3 is the only propellant which is

considered to dissociate during passage through the heater. In order to set a limit on the maximum loss which results from the non-recovery of dissociation energy in the nozzle flow, the performance with the NH_3 "equilibrium" composition is studied. Under equilibrium conditions NH_3 dissociates almost completely between 300 and 500°K to produce a diatomic mixture of N_2 and H_2. This causes a dramatic decrease in the efficiency accounting for the frozen chemistry loss, η_c, as is shown in Fig. 24a. At higher temperatures the fraction of the electric power going into dissociation energy decreases in comparison to the power required actually to raise the temperature, so that η_c increases. The case illustrated is for a plenum pressure of 50 kNm^{-2}. In the equilibrium limit the composition is significantly dependent on pressure (pressure range, 10 to 200 kNm^{-2}) only at temperatures between 300 and 500°K, the effect of lowering the pressure is to favour dissociation, and vice versa. Dissociation has two effects on the overall nozzle performance, one is to decrease the nozzle efficiency through η_c, and the other is to increase the exhaust velocity through the reduced molecular weight.

(ii) Frozen vibrational rate processes

The loss in jet power arising from the assumption of freezing vibrational energy at entrance to the nozzle is illustrated in Fig. 24b, in terms of the efficiency, η_F. As temperature is raised the fraction of the total internal energy which is invested in the vibrational modes increases, therefore η_F falls. For undissociated NH_3 the potential loss is large, with a 22% reduction in the ideal jet power at 1000°K, increasing to 39% at 2000°K. However, the frozen vibrational energy loss decreases as NH_3 dissociates, so that in the equilibrium limit, when it is essentially a diatomic mixture there is only a 6% reduction in jet power at T_T = 2000°K. The vibrational energy loss in pure H_2 is even smaller than equilibrium NH_3, with $\eta_F \simeq 0.95$ at 2000°K.

It is noted from Fig. 24b that η_F for H_2 is greater than unity at temperatures below 1000^oK. This is a consequence of the assumption made in Model Zero of a constant ratio of specific heats, $\gamma_{CF} = 1.4$ (i.e. $c^o_{pCF} = 6.9545$), which implies that the translational and rotational modes are fully excited, and that the vibrational mode is not active. At temperatures below 360^oK the two rotational degrees of freedom of H_2 are less than fully excited and with decreasing temperature the molar heat decreases, therefore the ratio of the specific heats increases. At approximately 50^oK only the lowest rotational energy level of the H_2 molecule is occupied so that it behaves effectively as a monatomic molecule with only three translational energy modes excited. Thus in summing the contributions from the internal energy modes from T_T to 0^oK, the assumption that $\gamma = \gamma_{CF} = 1.4$ causes an overestimate of the available enthalpy and therefore of the jet velocity (c.f. eqs. 2.19 and 2.9).

An inference from the behaviour of the frozen flow losses of NH_3 according to Model Zero, is that the chemical and vibrational energy losses are inversely coupled. In the equilibrium limit the frozen vibrational energy loss is small and frozen chemistry losses are large, whereas when NH_3 remains undissociated the chemistry loss is non-existant but the vibrational energy loss is large.

(iii) Incomplete expansion loss.

Clearly this is a function of the nozzle geometry, since the amount of energy which is retained in the active internal energy modes should decrease as the area ratio becomes larger. It is also dependent on the number of active degrees of freedom. Thus in Model Zero, with the vibrational processes frozen, there are five active degrees of freedom (three translational and two rotational) for a diatomic molecule, which for the nominal geometry ($\varepsilon = 25.$) gives an efficiency accounting for the incomplete expansion loss, $\eta_E = 0.8816$. For a non-

linear polyatomic such as NH_3 there are three rotational degrees, giving a total of six active degrees of freedom so that the incomplete expansion loss is larger, with $\eta_E = 0.8353$ for an area ratio of 25 : 1.

(iv) Viscous flow loss

The losses arising from the dissipative effects of viscosity and heat conduction are manifest in two ways. The first is as a velocity defect with a consequent reduction in the jet velocity and jet power, and the second is as a mass defect, which although not affecting the jet velocity or nozzle efficiency, η_N, causes a reduction in thrust since the mass flow rate is reduced.

There are two causes of the velocity defect, (i) displacement of the potential core by the viscous boundary layer reduces the effective nozzle area ratio and (ii) skin friction on the nozzle surface causes a momentum deficit in the boundary layer flow. Viscous flow losses are dependent on both the plenum temperature and pressure and are usually correlated against Reynolds number. The velocity defect, η_V, is illustrated in Fig. 25a as a function of the throat diameter Reynolds number, $Re_{D*} = 2\rho^* u^* R^*/\mu_T$. It is seen that η_V is strongly dependent on Reynolds number, with the loss increasing as Re_{D*} decreases. (Re_{D*} falls when T_T is raised and/or p_T is lowered.) As Reynolds number falls the boundary layer thickens; for hydrogen at $Re_{D*} \simeq 14000$. the boundary layer overall thickness is only 20% of the nozzle radius at the exit plane, but by $Re_{D*} \simeq 250$, $(\delta/R)_{ex} \simeq 0.75$, i.e. 94% of the nozzle exit area is occupied by a viscous "boundary layer" and only 6% is a potential core. To a lesser extent η_V is dependent on the propellant, in particular on the ratio of the frozen specific heats, γ_{CF}. For clarity the results for equilibrium NH_3 have not been included in Fig. 25, but for all temperatures in the matrix of plenum conditions, except 300^oK at which little dissociation occurs, the velocity defect coincides with the $\eta_V - Re_{D*}$ line for H_2. At a

given Re_{D*} the velocity defect is greater for $NH_3(\gamma_{CF} = 4/3)$ than for $H_2(\gamma_{CF} = 7/5)$. This difference arises from the predicted pressure gradient at the nozzle exit being less favourable for a polyatomic molecule such as NH_3. It follows that for a given Re_{D*} the boundary layer momentum thickness is greater with ammonia and therefore the velocity defect is larger. The difference in the velocity defect caused by skin friction is offset to a minor extent by the behaviour of the displacement thickness, since, for a given Re_{D*}, δ^* is slightly smaller (approximately 4%) in the case of ammonia. This information suggests that the form factor, equal to δ^*/θ, is dependent on the propellant specific heat ratio. The boundary layer theory used in Model Zero predicts, that for the nominal geometry over the range of Re_{D*} from 10^4 down to 300, the form factor at nozzle exit decreases from approximately 16. to 10. when the propellant is H_2. In the case of NH_3 the corresponding values are $\delta^*/\theta \simeq 12.$ at $Re_{D*} = 10^4$ and $\delta^*/\theta \simeq 8.5$ at $Re_{D*} = 300$.

The result that the displacement thickness is smaller for NH_3 at a given Reynolds number is also reflected in the variation of the discharge coefficient with Re_{D*}, which is presented in Fig. 25b. The difference is small and the two lines for H_2 and NH_3 are practically coincident. At $Re_{D*} = 10^4$ the discharge coefficient is approximately 0.96 and by $Re_{D*} = 10^2$ it falls to $C_D \simeq 0.72$. Values for η_V below $Re_{D*} \simeq 300$ are not presented in Fig. 25a since the flow is predicted to be completely viscous at exit from the nozzle. Although, according to its definition, there is still an effective inviscid core, the results obtained under these conditons are not consistent with those obtained at slightly higher Reynolds numbers.

(v) Radial flow loss

The final non-ideality to be considered is inversely coupled to the viscous flow loss, and in particular it is related to the

development of the displacement thickness at the nozzle exit. For the nominal geometry, the loss in jet velocity due to radial flow is small. Thus at $Re_{D*} = 10^4$ the efficiency accounting for the radial flow loss, η_D, is approximately 0.96, and as the boundary layer thickens with decreasing Re_{D*}, η_D increases so that at $Re_{D*} = 300$, η_D equals 0.985.

The overall nozzle efficiency, η_N, is illustrated as a function of plenum temperature in Fig. 26a for the case where the plenum pressure is 50 kNm^{-2}. It is immediately apparent that the overall efficiency of equilibrium NH_3 is dominated by the frozen chemistry loss. However the equilibrium limit is not a realistic case since kinetic considerations (section 1.3.2) indicate that little or no dissociation is likely to occur at temperatures below about 1000°K. When NH_3 remains undissociated the dominant loss is caused by the assumption of frozen vibrational rate processes. The incomplete expansion loss is also substantial ($\eta_F \simeq 0.84$), as is the velocity defect caused by viscous flow, which is most severe at the highest temperatures, and lowest pressures. At 300°K the overall nozzle efficiency with undissociated NH_3 is $\eta_N \simeq 0.75$, but this falls with increasing temperature, and by $T_T = 2000$°K, $\eta_N \simeq 0.42$. Using hydrogen as the propellant results in a far greater efficiency, since the potential vibrational energy loss is considerably smaller. Here, the dominant loss processes are incomplete expansion and viscous flow. Again η_N falls as temperature is raised, from 0.82 at 300°K to 0.68 at 2000°K.

In Chapter Two it was pointed out that the thrust coefficient, defined by eq. (2.52), does not provide a great deal of information about the overall nozzle efficiency. However, it is an important design parameter, in that it relates the plenum pressure and throat area to the resulting thrust. The variation of thrust coefficient,

corresponding to Fig. 26a, is shown in Fig. 26b. It is noted from eq. (2.52) that C_T is proportional to C_D, so that the thrust coefficient exhibits a strong Re_{D*} dependence.

6.2.2 Predictions of Model One

In this model the laminar boundary layer calculation is based on the Class A similar solutions, i.e. solutions of the Falkner-Skan equation. Since these solutions are valid over a wider range of favourable pressure gradients than those used in the Cohen and Reshotko method of Model Zero and are still computationally economic, they are used to examine the viscous flow losses in the nominal nozzle more closely. Results have been obtained for H_2, NH_3 (both the equilibrium and undissociated cases), CH_4 and CO_2 for the basic matrix of plenum conditions.

Before discussing the boundary layer results, the losses due to frozen vibrational energy and incomplete expansion are briefly described. The frozen chemistry loss with equilibrium NH_3 was outlined in section 6.2.1 and is not discussed further. As in the case of undissociated NH_3, the loss arising from the freezing of vibrational energy at nozzle entrance can be substantial with CH_4 or CO_2 as the propellant. The behaviour of the frozen flow efficiency, η_F, as a function of plenum temperature is illustrated in Fig. 27. The $\eta_F - T_T$ curves for H_2 and NH_3 of Fig. 24b are also included for completeness. It is seen from the curves for CO_2 and CH_4 that even at 1000^oK, over 30% of the potential jet power is locked up in vibrational energy. This value increases with temperature, so that by 2000^oK the loss is over 42% with CO_2 and over 50% with CH_4. Fig. 27 demonstrates that the vibrational modes of the CO_2 molecule are excited at comparatively low temperatures, and vibrational freezing could produce a 7% loss in jet power even at 300^oK. This "worst case" examination of the possible losses which could result from the freezing of vibrational

energy emphasises that at high temperature a large fraction of the total internal energy of polyatomic molecules is invested in vibration. Hence the need for a more accurate assessment of this loss, which is given in Model Two. The incomplete expansion loss suffered with CH_4 as the propellant, with vibrational energy frozen, is identical to that of NH_3, i.e. $\eta_E = 0.8353$ for a nozzle area ratio of 25 : 1. Carbon dicxide, unlike CH_4 and NH_3 which are non-linear polyatomics with three rotational degrees of freedom, is a linear molecule with only two rotational degrees. Therefore the incomplete expansion loss of CO_2 is the same as H_2 when there is no vibrational relaxation, i.e. $\eta_E = 0.8816$ for $\varepsilon = 25$.

In the remainder of this section the predictions of the boundary layer growth and the viscous flow losses, which are produced with the calculation procedure outlined in section 5.4, are examined. The efficiency accounting for the velocity defect, η_V, is shown as a function of Re_{D^*} in Fig. 28. As in Model Zero, i.e. the modified Cohen and Reshotko theory, the results of Model One give two distinct curves corresponding to $\gamma_{CF} = 1.4$ (H_2, CO_2 and equilibrium NH_3) where the curve is composed of over 80 points, and $\gamma_{CF} = 1.33^{\bullet}$ (NH_3 and CH_4) where there are over 50 points on the curve. It is observed in the case with $\gamma_{CF} = 1.4$ that the velocity defect increases rapidly when Re_{D^*} falls below 250. The same behaviour is found with $\gamma_{CF} = 1.33^{\bullet}$ for Re_{D^*} below 200. Calculations, additional to the basic matrix, were carried out at $T_T = 1500^{o}K$ for p_T between 25. and 10. kNm^{-2} in order to clearly define the drop-off region. At the lowest pressures ($Re_{D^*} \simeq 10^2$) it was found that the isentropic core-boundary layer iteration procedure produced an unacceptably large value for the displacement thickness in the divergent section so that the effective radius predicted by eq. (5.9) was negative, in which case the computation was abandoned. The conditions at which this occurs therefore lie

outside the range of applicability of the present model. At Reynolds numbers above $Re_{D*} \simeq 150$ the results were found to lie on consistent lines and they are included in Fig. 28. The prediction of a rapid drop-off in efficiency is obviously of some importance to resistojet nozzle performance and the validity of the prediction will be examined shortly.

The $\eta_V - Re_{D*}$ curve for $\gamma_{CF} = 1.4$, of Model Zero, is included in Fig. 28 in order to compare the two boundary layer calculations. It is seen that down to $Re_{D*} \simeq 400$ there is close agreement between the two methods. However this is fortuitous, since the boundary layer thicknesses at the nozzle exit predicted by the modified Cohen and Reshotko theory are some 25 to 30% larger than those given in Model One. This factor is offset by the different expressions used for the thrust integral, since the approximate relation used in Model Zero (eq. 5.21) predicts a considerably larger thrust than the "exact" relation of Model One (eq. 3.62). By chance, the two differences cancel out to give nearly the same answers.

Explanation of the differences in η_V (which relates to the velocity defect) for different ratios of frozen specific heats can be found from an examination of the boundary layer theory of section 3.4. The crucial factor in the boundary layer development is the pressure gradient parameter, β, which from eq. (3.40) can be written

$$\beta = \frac{2\xi}{u_e} \frac{du_e}{d\xi} \frac{T_T}{T_e}$$

It can be deduced from the temperature-area relationship of eq. (4.12) that, when the propellant has a lower specific heat ratio, γ_{CF}, a given area ratio produces a higher freestream static temperature, T_e (T_{CF} in eq. 4.12). In other words, for a given nozzle the conversion of internal energy to kinetic energy is less efficient when the propellant is NH_3 or CH_4, than is the case for CO_2 or H_2. It follows for NH_3 and CH_4 that at any station in the nozzle, the ratio of the

stagnation to static temperature, T_T/T_e, is smaller and, since the quantity, $\frac{2\xi}{u_e}\frac{du_e}{d\xi}$, does not vary significantly with γ_{CF}, the pressure gradient parameter is also smaller. Thus for a given Reynolds number the boundary layer integrals, P_1 to P_3, are larger (see Fig. 6), which in turn affects the boundary layer thicknesses. The difference is most marked in the momentum thickness, defined by eq. (3.60) as

$$\theta = \frac{R\,\Theta}{2\cos\alpha}\,P_2$$

and for a typical case with $Re_{D^*} \simeq 2000$, the momentum thickness is approximately 16% greater with $\gamma_{CF} = 4/3$ than with $\gamma_{CF} = 7/5$. The boundary layer overall thickness is also larger (typically 2%), but as found with Model Zero the displacement thickness is smaller for $\gamma_{CF} = 4/3$. At $Re_{D^*} \simeq 2000$, $\delta^*(\gamma_{CF} = 7/5)$ is approximately 6% larger than $\delta^*(\gamma_{CF} = 4/3)$. Examining eq (3.59), which can be written as

$$\delta^* = \frac{R\,\Theta}{2\cos\alpha}\left[\frac{T_T}{T_e}\,P_1 - P_2\right]$$

it is inferred that the increase in the value of P_1 for $\gamma_{CF} = 4/3$, is more than compensated by the decrease in T_T/T_e and the increase in P_2. The overall effect of the changes in δ^* and θ for different γ_{CF} is to increase the velocity defect incurred with NH_3 and CH_4. It is noted that there is a pressure term, $p_e\,\pi\,R^2$, in the thrust relation of eq. (2.34). The effect of viscous flow on the importance of this term is not large, and it will be considered in the discussion of the displacement effect which follows shortly.

The mass flow defect, in the form of a discharge coefficient, is shown in Fig. 29 for the nominal geometry over the range of Re_{D^*} from 35,000 to below 200. It has just been noted that the displacement thickness at the nozzle exit is larger for a given Re_{D^*} when $\gamma_{CF} = 1.4$. At the throat this still holds but the differences are small, so that $C_D(\gamma_{CF} = 1.4)$ is only slightly smaller than $C_D(\gamma_{CF} = 1.33^{\circ})$. The

boundary layer affects the position at which choking occurs, so that it is not necessarily conincident with the geometric throat as it is defined to be in the inviscid flows which are considered here. However the effect is small; at $Re_{D*} = 10^4$ the choking position is shifted downstream of the throat by $0.02R^*$, this increases slightly as Re_{D*} falls and by $Re_{D*} = 200$ the downstream movement is approximately $0.1R^*$.

Displacement of the inviscid core by the boundary layer produces a smaller effective flow area. This is particularly noticeable in the divergent section (see Fig. 33), and although there is a reduction in the effective throat area the overall result is a reduction in the equivalent inviscid area ratio. This increases the static temperature distribution along the nozzle centre line, which in turn reduces the velocity. The distribution of the stagnation to static temperature ratio along the nozzle axis is shown in Fig. 30 for hydrogen at a plenum temperature, $T_T = 1500^oK$. In the ideal inviscid flow the static temperature falls fairly uniformly through the divergent section to reach 250^oK at the nozzle exit. Viscosity and heat conduction in the boundary layer modify this picture, so that T_e decreases less rapidly. At a plenum pressure of $200kNm^{-2}$ ($Re_{D*} = 2015$), the temperature of the inviscid core at exit has only decreased to 310^oK, and as Re_{D*} falls with decreasing pressure the static temperature increases, so that by $Re_{D*} = 201$, T_e at exit has only fallen to 410^oK. This increase in static temperature means that the static pressure at the exit plane is also higher than in an inviscid flow. It follows that the pressure term in the thrust relation is somewhat larger, thus somewhat offsetting the velocity defects due to the momentum deficit and the displacement effect of the boundary layer.

Radial velocity profiles through the nozzle are shown in Fig. 31 for a nominal case, i.e. the nominal geometry, $T_T = 1500^oK$ and

p_T = 50 kNm^{-2}, with hydrogen as the propellant. The Reynolds number based on throat diamter corresponding to these plenum conditions is Re_{D*} = 504. First a few words of explanation are necessary before the profiles are discussed. The ordinate of this figure is u/V_{jCFE}, where u is the local velocity in the x-direction and V_{jCFE} is an ideal jet velocity which takes into account the losses from frozen chemistry, frozen vibrational energy and incomplete expansion. The abscissa is y cos α/R, where y is the distance normal to the nozzle wall and α is the local wall angle. These velocity profiles were obtained from a separate similar solutions program which basically integrated a form of eq. (3.61), which can be written

$$y = \frac{R\,\theta}{2\cos\alpha}\left[\frac{T_T}{T_e}\int_o^\eta (1-f'^2)d\eta + \int_o^\eta f'^2 d\eta\right] \qquad (6.1)$$

It should be noted that the profiles were transformed from the plane normal to the wall into the radial plane simply by multiplying by cos α, whereas in the nozzle programs the boundary layer thicknesses in the radial plane were obtained more correctly by interpolation. Finally, the jet velocity V_{jCFE} differs from the exhaust velocity when the flow is inviscid since there is an additional pressure term in the definition of V_{jCFE} (eq. 2.30). It is seen from Fig. 31 that in the convergent section and in the throat section down to station 30 (z/z_L = 0.29), the inviscid core occupies over 80% of the nozzle radius at each station. In the main divergent section the boundary layer develops quite rapidly, giving $\delta/R \simeq 0.5$ at the nozzle exit. In other words, Model One predicts that the boundary layer occupies three-quarters of the cross-sectional area at the nozzle exit for Re_{D*} = 504.

It is seen from the slope of the velocity profiles at the nozzle wall that the wall shear stress increases through the convergent section of the nozzle and reaches a maximum just downstream of the throat. It is found in Fig. 23 that the maximum pressure gradient

parameter, β, and therefore maximum wall shear stress, occurs at $z/z_L = 0.33$. Downstream of this the pressure gradient drops off rapidly with a consequent reduction in the slope of the velocity profile. Two sources of velocity defect can be deduced from the shape of the exit velocity profile ($z/z_L = 1.$). They are

(i) A defect in the inviscid core velocity due to the displacement effect.

(ii) A velocity defect in the boundary layer, which is manifest as the momentum thickness.

It is apparent that the boundary layer momentum deficit causes the largest loss in jet velocity.

Velocity profiles at the nozzle exit for plenum pressures of 50, 25 and 20 kNm^{-2} are shown in Fig. 32. The propellant is hydrogen. It was pointed out earlier that in the boundary layer calculation of Model One the important factor in determining the boundary layer development is the pressure gradient parameter, β. Values of β at the nozzle exit for the three cases illustrated in Fig. 32 and for $p_T = 200$ and 100 kNm^{-2} are listed below.

$p_T (kNm^{-2})$	Re_{D*}	β_{exit}	η_V
200	2015	2.65	0.919
100	1007	2.42	0.888
50	504	2.19	0.845
25	252	1.70	0.780
20	201	1.11	0.713

It is seen from this table that β_{exit} falls almost linearly with $\log_{10}(Re_{D*})$ for Re_{D*} down to 504, but decreases rapidly at lower Reynolds numbers. It follows that the value of the momentum thickness integral,

$P_2 = \int_0^{\eta_\infty} f'(1-f')d\eta$, increases rapidly for values of β_{exit} less than 2., with a corresponding decrease in η_V. It was noted in section 5.2.3 (also see Fig. 21) that convergence of the boundary layer-inviscid core iteration procedure was not achieved at $Re_{D^*} = 201$, so that the predictions for this case are not completely satisfactory. Reasonable convergence was not achieved after three iterations (i.e. four isentropic core and three boundary layer calculations) since the changes in effective geometry between iterations are still large. Improvement was not forthcoming by increasing the number of iterations since numerical errors were introduced which caused the procedure to diverge. Whitfield[58], in a study of low density wind-tunnel nozzle flows which was similar in several respects to the present study, also experienced calculation difficulties when the boundary layer was very thick. He attributed the source of these errors to the form of the Lees-Dorodnitsyn transformations, and in particular to the ξ-x relation (eq. 3.22). In the present study numerical errors are introduced into the pressure gradient parameter by the differential, $du_e/d\xi$. Numerical differentiation magnifies any round-off errors in the values of u_e and ξ between each station, and with an increasing number of iterations the errors build up so that the iteration procedure ultimately diverges. As Re_{D^*} falls an increasingly large part of the nozzle flow field is occupied by the viscous flow, and the importance of the boundary layer calculation becomes correspondingly greater.

Under circumstances where the boundary layer is very thick, Whitfield and Lewis[30] have used an initial effective geometry which is less than the actual nozzle geometry. This technique has been applied in a few cases in the present study. Results obtained here with a modified initial geometry were similar to those found with the usual procedure for Reynolds numbers down to 250, with the predicted boundary layer thicknesses, and therefore velocity defect, being slightly greater.

However for Re_{D*} below 250 (specifically Re_{D*} = 201) it was found that the drop-off in η_V was not as rapid as shown in Fig. 28, although once again satisfactory convergence was not achieved. It is inferred that, for the nominal geometry, the predictions of the boundary layer method of Model One are valid down to at least Re_{D*} = 250. Below this Reynolds number, although results are given, they are very tentative. Thus, use of the present boundary layer method at the lowest Reynolds numbers is not completely satisfactory but the predictions are indicative of the large losses due to viscous flow which are expected under these conditions. As has already been said in section 1.5.2., at these low Reynolds numbers the validity of assuming a boundary layer is doubtful and only calculations based on the Navier-Stokes equations are strictly correct. However, the present results show how far a purely boundary layer approach can be taken.

The growth of the boundary layer displacement thickness through the nozzle, over the range of Re_{D*} from 2015 down to 201 is illustrated by Fig. 33. It is noticed that δ^*/R reaches a minimum well in front of the throat. In the region just downstream of the throat the displacement thickness develops quickly under the influence of the rapid decrease in pressure gradient (see Figure 23). The change in δ^*/R with Reynolds number is most noticeable in the convergent portion of the nozzle, and in the divergent section although δ^*/R increases as Re_{D*} falls the effect is not so marked. Thus at the nozzle exit at Re_{D*} = 2015, δ^*/R equals 0.24 causing the effective exit area to be reduced to 58% of the geometric area. The corresponding figures at Re_{D*} = 201 are δ^*/R = 0.4, or an effective exit area of 36% of the original. On account of the differential growth of δ^*/R the effective area ratio does not change so markedly with Reynolds number, although the effective value is considerably less than the geometric area ratio of 25 : 1. Thus at Re_{D*} = 2015, the effective area ratio is 15.5 : 1 and by Re_{D*} = 201 it decreases to approximately 11 : 1.

The coefficient of skin friction along the nozzle surface, c_f, defined by eq. (3.64), corresponding to the above range of Re_{D*} is shown on a semi-log scale in Fig. 34. In the convergent section c_f falls rapidly, levelling off in the region of the throat. When the pressure gradient falls sharply in the divergent section there is a decrease in skin friction, but as β levels off and the changes in density and velocity become smaller c_f tends to a constant value. Remembering that Fig. 34 is on a semi-log scale it is seen that there is a large increase in the skin friction coefficient at the lower Reynolds numbers.

The earlier discussion of the change in the momentum and displacement thickness with γ_{CF} suggests, as in Model Zero, that the form factor, δ^*/θ, is dependent on the type of propellant. The variation in δ^*/θ at the nozzle exit for the cases of γ_{CF} = 7/5 and 4/3 is illustrated in Fig. 35a as a function of Re_{D*}. It is seen that for a given Reynolds number the form factor is considerably larger for the "diatomic" propellants; up to 30% larger at $Re_{D*} = 10^4$, and about 20% larger at Re_{D*} = 200. In Fig. 35b the variation of the form factor through the nominal nozzle is shown as a function of the centre-line Mach number for H_2 and NH_3 at plenum conditions of $T_T = 1500^oK$ and $p_T = 50kNm^{-2}$. In the subsonic flow δ^*/θ increases only slightly from 2.06 at $M_e = 0.2$ to approximately 2.7 at $M_e = 1$. In the supersonic flow, however, the form factor changes substantially. Although the momentum thickness increases considerably in the supersonic flow (typically by a factor of five between the throat and nozzle exit), the increase in the displacement thickness is far greater (typically a factor of 25). This is a consequence of the hot nozzle wall, which causes the gas density near the wall to be significantly lower than in the freestream. Thus at the exit δ^*/θ reaches a value of 10. in the case of NH_3, and nearly 12. in the case of H_2. Examination of

eqs. (3.59) and (3.60) reveals that, for the Class A similar solutions, the form factor can be written

$$\frac{\delta^*}{\theta} = \frac{T_T}{T_e} \frac{P_1}{P_2} - 1. \qquad (6.2)$$

Strictly, therefore δ^*/θ is a function of T_T/T_e and β, however the variation of P_1/P_2 with β is not large, e.g. $P_1/P_2 = 3.58$ at $\beta = 0.$ and 3.02 at $\beta = 10.$, so that the behaviour of the form factor in the nozzle is dominated by the freestream static temperature. Thus if the form factor were plotted against T_T/T_e the two curves for different γ_{CF} in Fig. 35b would collapse to one curve.

To summarise the viscous flow losses predicted by Model One:

(i) For a given nozzle, the mass and velocity defects are dependent on the throat diameter Reynolds number. These losses become severe at low Re_{D^*}.

(ii) The velocity defect is caused by a momentum defect in the boundary layer and by a reduction in the inviscid core velocity due to the displacement effect.

A final point concerns the radial flow losses, this is illustrated in Fig. 36 as a function of Re_{D^*}. Since, for a given Re_{D^*}, the displacement thickness obtained at the nozzle exit is larger in the case of $\gamma_{CF} = 7/5$ it follows that the radial flow loss is reduced in comparison to $\gamma_{CF} = 5/3$; therefore η_D is more nearly equal to unity. It is seen however that the difference between the two cases is small.

6.2.3 Predictions of Model Two

Model Two is used to investigate the effects of vibrational relaxation on resistojet nozzle performance, by employing the realistic freezing criterion which was described in section 4.3. The results are discussed in two parts; firstly for the single species CH_4, CO_2 and H_2, and secondly for NH_3 where the problem of vibrational relaxation is

complicated by dissociation. Before these are examined, two points about the model are noted.

A rate parameter, Φ, was introduced in the freezing criterion given by eq. (4.34). This parameter is the product of two terms, P and ϕ , where P is a constant of order unity, matching the approximate sudden freezing criterion with more exact solutions, and ϕ is a factor accounting for the discrepancy between excitation and de-excitation rates. It was noted in section 4.3 that ϕ varies typically between 1 and 100. With $\Phi = 1$ it is assumed that vibrational processes in the nozzle flow relax at the same rate as those observed in shock tube measurements. A reasonable upper bound on the de-excitation rates is thought to be given by $\Phi = 100$. In Model One, vibrational energy was frozen at the nozzle entrance, i.e. it was assumed that the equilibrium rate of change of vibrational energy was always greater than the kinetically possible rate. The results of Model One therefore correspond to $\Phi = 0$. Simply removing the freezing criterion from the program produces the other limiting state where vibrational energy remains in equilibrium throughout the nozzle, in which case $\Phi = \infty$. The second point concerns the position in the nozzle at which vibrational energy is allowed to freeze. To simplify the mass flow calculation it was assumed that freezing was not considered to occur until five stations downstream of the geometric throat. Subsequent computation showed this to be a sensible condition (see below). For the nominal geometry where the throat corresponds to $z/z_L \cong 0.26$, this means that vibrational freezing is not allowed to occur until $z/z_L \gtrsim 0.31$.

Variation in the frozen flow efficiency, η_F, for H_2, CO_2 and CH_4 is shown in Fig. 37 as a function of the plenum temperature, at a constant plenum pressure of 50 kNm^{-2}, for values of $\Phi = 0$, 1 and 100. In the case of carbon dioxide, with $\Phi = 1$, it is found that freezing occurs at $z/z_L = 0.31$; below 1500^{o}K it is constrained to occur here,

and for higher temperatures it occurs spontaneously at this station. A similar behaviour is exhibited by methane for $\Phi = 1$, although for temperatures above $1000^{o}K$ the freezing point moves downstream and at $2000^{o}K$ freezing occurs at $z/z_L = 0.39$. The effect of vibrational relaxation is to reduce the frozen flow losses, but it is seen from Fig. 37 that although there is some improvement between $\Phi = 0$ and 1, the frozen vibrational losses are still greater than 30% of η_F at $2000^{o}K$. However, the situation in CH_4 and CO_2 flows changes dramatically at $\Phi = 100$. At the highest temperatures, where the rates are fastest, it is predicted that vibration will remain in equilibrium throughout the nominal nozzle, in which case $\eta_F = 1$. In the intermediate temperature range, i.e. 500 to $1500^{o}K$, some loss from vibrational freezing is still incurred, typically giving a 5% reduction in η_F. It is noted that when $\Phi = \infty$, η_F is defined to be unity at all temperatures.

Using Model One, where $\Phi = 0$, it was shown that the maximum possible vibrational loss suffered by H_2 was small, since the vibrational content and the degree of excitation were small. Using Model Two, not unexpectedly it is found that the vibrational loss is even smaller, and with $\Phi = 100$, $\eta_F \simeq 0.98$ at $2000^{o}K$. At temperatures above $1000^{o}K$ the freezing criterion is satisfied at $z/z_L = 0.31$ to 0.32, but at lower temperatures with $\Phi = 100$, and for all temperatures with $\Phi = 1$, freezing is constrained by the program to occur at $z/z_L = 0.31$. Therefore the results for H_2 with $\Phi = 1$ and 100 are virtually identical.

The results of Model One (section 6.2.2) indicated that the reduction in static temperature between the plenum and nozzle exit, achieved by a given nozzle, is smaller for a propellant which has a larger number of active degrees of freedom. This phenomenon is also observed in the results of Model Two, and is illustrated in Fig. 38 with axial temperature profiles in CH_4 and CO_2 flows, for different values of Φ, for the nominal case where $T_T = 1500^{o}K$ and $p_T = 50 kNm^{-2}$. These profiles were obtained from the final isentropic core calculation,

so that they include the influence of the viscous boundary layer. With increasing Φ, freezing is delayed so that more active degrees of freedom are, or have previously been, available to contribute to kinetic energy. It follows from the potential flow relations of Chapter Four that the freestream static temperature at any station is increased, or in other words, the temperature ratio, T_T/T_e, is decreased. For a polyatomic propellant there is a large difference in the axial static temperature distribution between vibrationally frozen ($\Phi = 0$) and equilibrium flow ($\Phi = \infty$). This is most noticeable at the nozzle exit; e.g. for the CH_4 case illustrated in Fig. 38, with $\Phi = 0$ the static temperature in the inviscid core at exit, $(T_e)_{ex}$, is $405^{\circ}K$, but with $\Phi = \infty$, $(T_e)_{ex}$ is doubled to $810^{\circ}K$.

Figure 38 further emphasises that correct modelling of vibrational relaxation is extremely important in predicting the performance of resistojets which employ polyatomic propellants. However, due to the lack of relaxation data for de-excitation flows, it is only possible to present likely limiting cases with $\Phi = 1$ and 100; even within these limits there is considerable difference in temperature distributions and in the frozen flow losses.

Although the vibrational energy loss is smaller when relaxation occurs it does not follow that the full benefits are reflected in the jet power. As just discussed, $(T_e)_{ex}$ increases when vibrational energy equilibrates, so that the fraction of the available internal energy (rotational and translational), which is not converted to kinetic energy, also increases. This means that the incomplete expansion loss is increased. The change in the efficiency account for the incomplete expansion loss, η_E, with the rate parameter, Φ, is tabulated below for the nominal CO_2 and CH_4 cases.

Variation in the Incomplete Expansion Loss of CH_4 and CO_2 with Vibrational Relaxation (Plenum conditions: $T_T = 1500^oK$, $p_T = 50\ kNm^{-2}$)

Φ	$\eta_E(CO_2)$	$\eta_E(CH_4)$
0.	0.8816	0.8353
1.	0.8784	0.8247
100.	0.7649	0.6735
∞	0.7500	0.6735

It is apparent that the large increase in the frozen flow efficiency, η_F, between $\Phi = 1$ and 100, is offset to an extent by the decrease in η_E. Further, the incomplete expansion loss is dependent on the plenum temperature, and increases with T_T. An extreme case is obtained with CH_4 at 2000^oK with $\Phi = 100$, when η_E equals 0.61. It should be noted that all the results so far presented are for an area ratio of 25 : 1, so that the variation in the incomplete expansion loss is a result of changes in the gasdynamics of the flow and is not due to changes in the nozzle geometry.

The possible improvement in performance due to the equilibration of vibrational energy is further offset by an increase in the viscous flow loss. Since T_T/T_e at a given station is smaller when vibrational energy relaxes in the nozzle flow, it follows that the pressure gradient parameter, β, is also smaller. Consequently the velocity defect due to viscous flow is increased. The variation in the efficiency accounting for the viscous flow velocity defect, η_V, is shown in Fig. 39 for both CH_4 and CO_2, as a function of Re_{D^*} for values of $\Phi = 0$, 1, 100 and ∞. The Reynolds number variation is obtained by plotting the results for the temperature range 300 to 2000^oK. It is seen that the velocity defect is most severe at the highest temperatures, which in the case of

a constant plenum pressure (50 kNm^{-2}) corresponds to the lowest Reynolds numbers. The results for given values of T_T and Φ over a range of p_T produce a family of approximately parallel η_V - Re_{D*} curves. Examination of the following table of results for CH_4, at plenum conditions of 1500^oK and 50 kNm^{-2}, reveals several changes in the boundary layer structure at the nozzle exit when Φ varies between 0 and 100.

Variation in the Boundary Layer at Nozzle Exit with Vibrational Relaxation

Φ	Re_{D*}	δ_{ex} (mm)	δ^*_{ex} (mm)	θ_{ex} (mm)	$(M_e)_{ex}$
0	1064.	1.127	0.679	0.067	4.04
1.	996.	1.202	0.658	0.084	3.90
100(∞)	996.	1.305	0.530	0.126	3.11

The most striking change is in the momentum thickness, θ_{ex}, which nearly doubles in value between the case where vibrational energy is completely frozen (Φ = 0) and where it remains in equilibrium throughout the nozzle (Φ = 100). Since the loss in jet velocity is dependent on θ_{ex} it follows that there is a substantial decrease in η_V with increasing Φ (see eqs. 2.44 and 3.62). The opposite effect is seen to occur in the displacement thickness, i.e. δ^*_{ex} decreases as vibrational energy equilibrates. The mathematical reasons for the changes in θ and δ^* with T_T/T_e have been discussed in section 6.2.2, and the physical implications are now described. With vibrational energy in equilibrium the freestream static temperature is higher, therefore the temperature difference across the boundary layer is smaller and the density at the nozzle wall is more comparable to the freestream density. It follows that (i) the mass flow in the boundary layer is higher when vibrational energy relaxes (particularly when the flow is supersonic),

therefore the displacement thickness is smaller; and (ii) the region of the greatest velocity defect at the nozzle wall corresponds to an increased density, so that the momentum defect is increased. The effect of Φ on the form factor, δ^*/θ, is pronounced; with $\Phi = 0$ $(\delta^*/\theta)_{ex} \simeq 10.$, but with $\Phi = 100$, $(\delta^*/\theta)_{ex} \simeq 4$. Thus the shape of the velocity profile is much fuller when vibrational energy is in equilibrium.

It is emphasised that these predictions are based on similar solutions of the laminar boundary layer equations, in which it is assumed that the propellant specific heat remains a constant at any station. They can therefore only be taken as an indication of the effects of vibrational relaxation on the boundary layer development.

Calculation of the frozen vibrational efficiency, η_F, is carried out in the first isentropic core calculation, i.e. it corresponds to the loss suffered in a completely inviscid flow and is not affected by the subsequent boundary layer calculations. However, the boundary layer can have a significant effect on the freezing position, since it increases the freestream temperature and therefore decreases the rate of change of vibrational energy in the expansion. Any change in the freezing position is felt in the boundary layer calculation and in the estimation of the viscous flow loss. If the freezing criterion is satisfied well into the supersonic inviscid flow, then the presence of the boundary layer will further delay freezing. Thus for CH_4 at $1000^{o}K$ with $\Phi = 100$, freezing occurs at $z/z_L = 0.77$ in the inviscid flow, and after the final boundary layer calculation the freezing position is shifted downstream to $z/z_L = 0.92$. However when freezing in the inviscid flow occurs in the vicinity of the throat, the subsequent boundary layer calculations have little or no effect on the freezing position.

Vibrational equilibrium has a small effect on the mass defect due to viscous flow. It is observed that there is a slight improvement in the discharge coefficient, which is consistent with the behaviour noted

in section 6.2.2, where $C_D(\gamma_{CF} = 4/3)$ was greater than $C_D(\gamma_{CF} = 7/5)$. The maximum increase is less than half of one per cent of C_D at the lowest Reynolds numbers.

So far we have considered vibrational relaxation for plenum conditions where the temperature has been varied, and the pressure held constant. However, the rate of vibrational relaxation is directly proportional to pressure (see eq. 4.34), so that it is to be expected that changes in plenum pressure will also affect vibrational freezing. The dependence of the frozen flow efficiency, η_F, on the plenum pressure is particularly noticeable in the case of CH_4 and the effect is illustrated in Fig. 40 for temperatures of 1000, 1500 and 2000^oK; the rate parameter is unity. At 1000^oK, for plenum pressures of 25 and 50 kNm^{-2} freezing occurs just downstream of the throat at z/z_L = 0.31, and η_F therefore remains constant. With further increases in p_T, the kinetic rate becomes sufficiently fast for a downstream movement of the freezing position. The result is an increase in the frozen flow efficiency which is essentially linear with $\log_{10}(p_T)$. At higher temperatures the downstream movement is even more pronounced. Thus at plenum conditions of 2000^oK and 25 kNm^{-2} freezing is predicted to occur at z/z_L = 0.34, which gives η_F = 0.60, but by increasing the pressure to 200 kNm^{-2} freezing is delayed to z/z_L = 0.59, giving η_F = 0.74. This is a substantial change. It follows from the previous discussion that the losses from incomplete expansion and viscous flow will partly counteract any changes in the frozen flow loss.

It is apparent that vibrational relaxation produces a considerable complication of the flow structure in resistojet nozzles where the propellant is a polyatomic, such as methane or carbon dioxide. In Model One where vibrational energy was frozen throughout the nominal nozzle, for a given propellant the losses due to frozen flow, incomplete

expansion and viscous flow were independent of one another. This is not the case in Model Two, where there is a strong coupling between η_F, η_E and η_V. It has been demonstrated that the losses are dependent on the amount of energy invested in vibration as well as the rate of vibrational relaxation, which in turn is dependent on the plenum pressure and temperature.

The result of these conflicting factors on the overall performance of CH_4 and CO_2 is shown in Fig. 41, which is a graph of specific impulse versus plenum temperature for various values of Φ. It is seen that the closer one gets to fully equilibrium flow the higher the specific impulse. The maximum improvement in performance from $\Phi = 0$ to $\Phi = \infty$ is found at 2000^oK where a 15% increase in I_{sp} is predicted for both CH_4 and CO_2. At lower temperatures where the vibrational content is smaller, the difference in performance is less marked. Vibrational relaxation in H_2 resistojet nozzles has only been briefly mentioned, since the effect on performance is a minor one. This is substantiated by the following figures. At 2000^oK and 50 kNm^{-2}, with $\Phi = 0$, the specific impulse is predicted by Model One to be 653 seconds, while Model Two predicts $I_{sp} = 660$ seconds when $\Phi = 100$, which is only a one per cent difference. Thus the results for H_2 of Models One and Two are very similar.

Turning now to the predictions of Model Two for ammonia, the problem of vibrational relaxation is complicated by dissociation in the resistojet heater, so that a mixture of several vibrationally excited species is present in the nozzle flow. It was assumed that, for temperatures below 2000^oK, the dissociated mixture consisted of three species - NH_3, N_2 and H_2 - and a plausible model of the vibrational relaxation in such a mixture was developed in section 4.4.

The results of Model Two for the equilibrium and undissociated cases are presented in Fig. 42, for the plenum pressure of 50 kNm^{-2}.

Let us first examine the equilibrium limit, i.e. f = 0 in eq. (5.5). At temperatures above 500°K the mixture consists essentially of H_2 and N_2, and it was seen for this case in Model One with $\Phi = 0$, that the vibrational energy loss was small. The results of Model Two with the realistic value of $\Phi = 1$ indicate that η_F does not differ signficantly from unity (even at 2000°K $\eta_F \simeq 0.98$). Next examining the undissociated case (f = 1.), it is noted that most of the computation was carried out with the rate equation which exhibits the usual temperature dependence, i.e.

$$p\tau_v = 2.46 \times 10^{-17} \exp(152.6/T)^{1/3} \text{ atm.sec.} \qquad \underline{\text{Rate eq. 1}}$$

It is seen from Fig. B.2 in Appendix B, that the rates predicted by this equation are extremely fast, particularly at high temperatures, so it is not surprising to find that substantial equilibration of vibrational energy is predicted by Model Two. Figure 42 shows that the loss in the frozen flow efficiency, η_F, of undissociated ammonia is found to be small using rate equation 1 with $\Phi = 1$. With $\Phi = 100$ it is predicted that, at plenum temperatures above 1000°K, vibration remains in equilibrium with translation throughout the nominal nozzle. A curve for undissociated NH_3 for $\Phi = 100$ is not included in Fig. 42 since η_F does not vary significantly from unity in any case. The alternative rate equation for pure NH_3, based on the experimental data of Bass and Winter (see Appendix B), is

$$p\tau_v = 1.78 \times 10^{-7} \exp(-28.85/T)^{1/3} \text{ atm.sec.} \qquad \underline{\text{Rate eq. 2}}$$

This has a different temperature dependence to the first equation, i.e the rate decreases with increasing temperature. Using this equation with $\Phi = 1$, it is found that at temperatures above 1000°K freezing occurs in the range of z/z_L from 0.7 to 0.8. It is seen from Fig. 42 that the result is a decrease in η_F, which is largest at 2000°K where $\eta_F \simeq 0.88$. However, using rate equation 2 with $\Phi = 100$ it is found

that the flow remains in equilibrium for the whole temperature range. Although there are differences in the results obtained with these two, very different, rate equations, the results are notable for both showing that the vibrational energy loss suffered in undissociated NH_3 nozzle flows is small.

Calculations have also been carried out for partially dissociated mixtures for values of f, the mole fraction of NH_3 which is not included in the equilibrium calculation, equal to 0.2, 0.4, 0.6 and 0.8. The form of the "parallel resistance" law (eq. 4.35), which was used in the approximate model of vibrational relaxation in NH_3-N_2-H_2 mixtures (section 4.4), is such that the relaxation time of the mixture corresponds to that of the fastest component, i.e. NH_3. This holds for all the ammonia mixtures considered here, except f = 0 at temperatures above 500°K when NH_3 is only a trace species. The computations show that the losses from finite rate vibrational processes are small for partially dissociated mixtures; in fact, the $\eta_F - T_T$ curves are intermediate between the equilibrium and undissociated limits. Thus it is concluded that the vibrational energy loss in ammonia resistojets is small.

Vibrational relaxation in NH_3 has the same effect on incomplete expansion and viscous flow losses as was described earlier for CH_4 and CO_2. Since the degree of relaxation in ammonia is substantial it follows that the incomplete expansion and viscous flow efficiencies will be markedly lower than the predictions of Model One. These differences will be most acute when f = 1., i.e. when ammonia remains undissociated. In the following table the efficiencies accounting for the losses due to frozen vibration, incomplete expansion and viscous flow, and the overall nozzle efficiency, which are predicted by Models One (Φ = 0) and Two (Φ = 1), are compared.

Comparison of Predictions of Models One and Two for NH_3

($f = 1$, $p_T = 50\ kNm^{-2}$)

$T_T(^oK)$	η_F		η_E		η_V		η_N	
	$\Phi = 0$	$\Phi = 1$	$\Phi = 0$	$\Phi = 1$	$\Phi = 0$	$\Phi = 1$	$\Phi = 0$	$\Phi = 1$
300.	0.992	0.997	0.835	0.835	0.954	0.953	0.758	0.766
500.	0.951	0.980	0.835	0.833	0.931	0.926	0.702	0.733
1000.	0.815	0.975	0.835	0.803	0.887	0.854	0.564	0.652
1500.	0.717	1.000	0.835	0.740	0.858	0.799	0.474	0.576
2000.	0.652	1.000	0.835	0.697	0.830	0.755	0.417	0.513

It may be seen that there are large differences in the individual efficiencies between the two models, which are most prominent at the highest temperatures. However, the effect of vibrational relaxation on the overall nozzle efficiency is beneficial. This is illustrated in terms of specific impulse in Fig. 43, for both the undissociated and equilibrium cases. Three points are made about this figure. Firstly, differences in specific impulse predicted by Models One and Two are small in the equilibrium limit ($f = 0$), and of the order of 10% for undissociated NH_3 ($f = 1$) at temperatures above 1500^oK. Secondly, it is seen that the two rate equations and different values of the rate parameter used in Model Two (i.e. $\Phi > 0$), produce very similar specific impulses for undissociated NH_3. Finally, Model Two predicts up to 30% difference in specific impulse between the equilibrium and undissociated cases.

Dissociation of NH_3 is obviously advantageous for the resulting increase in specific impulse. Whether it is achieved in resistojets is dependent on the kinetics of the decomposition and on the heater design. As seen in the discussion of Model Zero, dissociation causes a considerable decrease in the overall nozzle efficiency, since electric

power going into dissociation energy is not subsequently recovered by recombination in the nozzle expansion. Results obtained with Model Two for the variation in nozzle efficiency with differing degrees of dissociation are shown in Fig. 44. At temperatures below 1400°K it is seen that a maximum nozzle efficiency is given by the undissociated (f = 1.) case. At higher temperatures η_N is maximised with the partially dissociated mixtures, and by 2000°K the most efficient use of the nozzle is with the equilibrium mixture. It is apparent from Figs. 43 and 44 that the performance of ammonia resistojets is dominated by the chemical kinetics occurring in the heater flow.

To summarise the main performance implications of Model Two for the nominal nozzle :

(i) Frozen vibrational energy loss in the cases of NH_3 and H_2 is small. For CH_4 and CO_2, an upper limit on vibrational rates (Φ = 100) indicates that substantial vibrational equilibration occurs, but with a lower limit (Φ = 1) the losses are still large.

(ii) Any improvements in the frozen flow efficiency, η_F, due to vibrational relaxation are partly offset by increased incomplete expansion and viscous flow losses.

(iii) The overall effect of vibrational equilibration is to increase the nozzle efficiency and specific impulse.

Results of Model Two for the nominal geometry are presented in Table VI for the following cases :-

(a) Undissociated hydrogen for the range of plenum temperatures from 300 to 3000°K, and equilibrium hydrogen for T_T from 2000 to 3000°K.

(b) Methane for T_T from 300 to 2000°K.

(c) Carbon dioxide for T_T from 300 to 2000°K.

(d) Undissociated and equilibrium ammonia for the temperature range 300 to 2000°K.

The rate parameter, Φ, is equal to unity in all cases except for H_2, where for T_T greater than 500°K Φ equals 100 and for temperatures below this $\Phi = \infty$. A few cases for hydrogen with the equilibrium composition are included in Table VI (a) although this limit is not thought to be realisable in resistojet operation. For the purpose of calculating the freezing position in the equilibrium hydrogen mixture it is assumed, without further justification, that the vibrational relaxation of the mixture is identical to pure H_2.

6.2.4 Predictions of Model Three

Briefly recapitulating, the boundary layer calculation used in this model is based on solutions of a modified Falkner-Skan equation, which includes the radial dependences accounting for transverse curvature (i.e. the Class B similar solutions of section 3.5.2). The assumption was made that vibrational energy was frozen throughout the nozzle ($\Phi = 0$), so that an indication of the effects of transverse curvature on resistojet performance can be gained by comparing the results of Models Three and One. The computation carried out with Model Three has not been so extensive as the previous models due partly to the increased execution time, of the order of 200 seconds compared to 25 seconds need by Model One, and partly to a lack of overall project time. Thus results have been obtained only for hydrogen.

It was noted in section 3.5.2 that it was not possible to obtain solutions of the modified Falkner-Skan equation (eq. 3.73) over the complete range of dimensionless parameters β, Θ and T_T/T_e. This point is of some importance not only in the interpretation of the results but also in their derivation, as will now be explained. The boundary layer calculation procedure, given in section 5.6, consists mainly of interpolating the integrals P_1 to P_3 of Table II. However, the interpolation

routine CSFMIE also extrapolates quite efficiently, so that the boundary layer thicknesses can be evaluated for combinations of the pressure gradient parameter, transverse curvature parameter and total to static temperature ratio for which there are no solutions of the similar equation, eq. (3.73). Thus some care is necessary in obtaining the results, particularly for the lower values of β, and the higher values of Θ and T_T/T_e. This combination of conditons is found in the nominal nozzle at the exit plane, when Re_{D*} is low, (see Fig. 23). The results presented here correspond to the range of Reynolds numbers, Re_{D*}, from 2015 to 252. In order to verify the validity of these results for $Re_{D*} < 504$, separate similar solutions of eq. (3.73) were obtained for the combinations of β, Θ and T_T/T_e pertinent to the conditions at the exit plane.

The first point about the results of Model Three is that the boundary layer growth in the convergent and throat section is almost identical to the prediction of Model One. Thus the discharge coefficient, which characterises the subsonic and transonic flow, is found to be only 0.1% larger with Model Three over the range of Re_{D*} from 252 to 2015. It can therefore be concluded that transverse curvature has an insignificant effect on the flow in the convergent and throat section. This is attributed to the fact that T_T/T_e approximates to unity in these sections, so that the dimensionless wall shear stress, f"(o), is almost the same as that predicted by Model One (see Fig. 10).

In the divergent section the temperature ratio T_T/T_e increases considerably, and, combined with a falling pressure gradient, causes differences in the predictions of the two models. These differences are most pronounced at the nozzle exit, and the boundary layer thicknesses at this station are compared in Fig. 45. It is seen that the overall boundary layer thickness and the displacement thickness are predicted to be larger (of the order of 3%), when transverse

curvature is included. This is not a large difference, particularly since the similar solutions and the equations for the boundary layer thicknesses are quite different. However the effect of transverse curvature causes a considerable decrease in the momentum thickness, of the order of 20%. The differences in θ are smallest at the highest Reynolds numbers and increase with falling Re_{D*} when the boundary layer thickens. It was noted in section 6.2.2 that decreasing Reynolds number causes the pressure gradient parameter and the total to static temperature ratio to decrease. Thus at $Re_{D*} = 2015$, the values of β and T_T/T_e at the nozzle exit are 2.65 and 4.9 respectively, whereas at $Re_{D*} = 252$, $\beta = 1.70$ and $T_T/T_e = 3.9$. Decreasing Re_{D*} has the opposite effect on the transverse curvature parameter, Θ , so that $\Theta = 0.15$ at $Re_{D*} = 2015$ and $\Theta = 0.25$ at $Re_{D*} = 252$. This change has a significant influence on the boundary layer development and especially on the form factor δ^*/θ. In Model One, the form factor decreases from approximately 13.6 to 10.6 in this Reynolds number range, whereas the comparable figures for Model Three (i.e. including transverse curvature) are 16. and 14.3 respectively. It is worth examining the definitions of the boundary layer thicknesses to see where this difference comes from. Using eqs. (3.59) and (3.60) the form factor in the boundary layer theory of Model One can be written

$$\frac{\delta^*}{\theta} = \frac{T_T}{T_e}\,\frac{P_1}{P_2} - 1 \qquad (6.2)$$

and in Model Three, from eqs. (3.53) and (3.56), we can write

$$\frac{\delta^*}{\theta} = \frac{1 - \left\{1 - \Theta\left(\frac{T_T}{T_e}P_1 - P_2\right)\right\}^{\frac{1}{2}}}{1 - \{1 - \Theta P_2\}^{\frac{1}{2}}} \qquad (6.3)$$

Thus in Model One, eq. (6.2) can be expressed

$$\frac{\delta^*}{\theta} = F(\beta, T_T/T_e)$$

and similarly in Model Three, eq. (6.3) is

$$\frac{\delta^*}{\theta} = F(\beta, T_T/T_e, \Theta)$$

It is apparent that the form factor is independent of the transverse curvature parameter in Model One, but in Model Three δ^*/θ is intimately dependent on Θ.

In reducing the momentum thickness, transverse curvature causes the velocity defect due to viscous flow to be reduced. The efficiency accounting for this loss, η_V, is shown for Models One and Three in Fig. 46. It is observed that the difference between the two models is considerable and this is most noticeable at the lowest Reynolds numbers. However, an interesting point is that for values of Re_{D*} below 250, the combinations of β, Θ and T_T/T_e found in the vicinity of the nozzle exit lie in the region where solutions of the modified Falkner-Skan equation could not be obtained. This is also the region in which a rapid drop-off in η_V is observed in Model One. Although it may be a coincidence, the two distinct models <u>both</u> suffer from computational difficulties when they are applied to the nominal nozzle at Re_{D*} below approximately 250. The fact that both boundary layer models are unsatisfactory implies that a calculation procedure based on the full Navier-Stokes equations must be used at these conditions.

While it is stressed that the analysis and application of the similar solutions of the modified Falkner-Skan equation have been far from rigorous, there are several interesting implications about the effects of transverse curvature on the boundary layer development in resistojet nozzles. The results of what is essentially a first-order perturbation of conventional thin boundary layer theory show that:

(i) Transverse curvature has little effect on subsonic nozzle flow.

(ii) The effects on the overall and displacement thicknesses are minor ones.

(iii) However, including transverse curvature causes a marked reduction in the momentum thickness and consequent velocity defect due to viscous flow.

6.3 Variation of Nozzle Geometry

It was shown for the nominal geometry in the previous section that the various loss mechanisms are dependent on one another. This is particularly so in the case of the polyatomic propellants where the losses due to frozen vibrational energy, incomplete expansion, viscous flow and radial flow are all coupled. When we consider which model should be used to examine the variation in performance with changes in the nozzle geometry it is apparent that Model Two, which allows vibrational relaxation, will produce extremely complicated results. In order to achieve some simplification, apart from discussing the incomplete expansion loss suffered by polyatomic propellants with vibrational energy in equilibrium, H_2 is used as the propellant in this section. The assumption of frozen vibrational energy is reasonable in this case so that Model One is employed. It is accepted that Model One is not the most sophisticated model which has been developed in this work, however the fact that it is computationally economical allows examination of a wide range of variables. The changes in performance due to variations of the nozzle geometry are dependent on the viscous flow, so that further simplification is achieved, without loss in generality, by using a plenum temperature of $1500^{o}K$ and allowing pressure to be the only plenum variable. The nozzle geometry consists conceptually of three parts: the convergent, throat and divergent sections. They are considered in that order. Unless otherwise stated the remaining geometric variables which describe

the nozzle are identical to the nominal geometry. Values of these variables are listed at the beginning of section 6.2.

(i) Convergent section

It is generally accepted that the shape of the convergent section of a convergent-divergent nozzle has little effect on the nozzle performance. Changes in the shape of the convergent section were not investigated thoroughly, but the few results that were obtained confirm this statement. Only the effect of the initial wall angle, θ_1, was investigated in any detail. Using an inlet radius of 2.5 mm, the convergent half angle was varied from 15 to 90^o in steps of 15^o, for a plenum pressure of 50 kNm^{-2} (i.e. Re_{D*} = 504). With increasing θ_1 it was found that there was a slight, but consistent, increase in the efficiency accounting for the viscous flow velocity defect, η_V, from 0.839 with $\theta_1 = 15^o$ to 0.843 with $\theta_1 = 90^o$. The changes in the discharge coefficient were negligible.

While changes in the shape of the convergent section are predicted to have little effect on performance, it should be appreciated that these findings depend on the assumption that stagnation conditions exist at the nozzle entrance plane. In actual fact the gas will have a finite velocity at exit from the heater, and the velocity profile may be fully viscous. The form of this profile and the shape of the convergent section may therefore be important to resistojet performance. However, the effects of a starting profile cannot be assessed with the models used in this study.

(ii) Throat section

There are two variables in the throat geometry; they are the radius of curvature, R_c and the throat radius R^*. The effects of the radius of the wall curvature on performance were investigated for values of R_c from 0.5 mm to 4.0 mm, i.e. R_c/R^* from 1. to 8., for Re_{D*} from 16000. down to 150. Decreasing R_c produces a more favourable pressure

gradient at the throat, so that the boundary layer thickness is reduced. Thus the displacement thickness is also smaller, and it follows that the discharge coefficient, C_D, is larger. The variation of the discharge coefficient with throat diameter Reynolds number is illustrated in Fig. 47. At the highest Re_{D^*} the differences in C_D with R_c/R^* are small, e.g. at $Re_{D^*} = 10^4$ there is less than a 2% decrease in C_D between $R_c/R^* = 1.$ and 8. At the lower Reynolds numbers the differences are more pronounced, e.g. at $Re_{D^*} = 250$, $C_D = 0.883$ with $R_c/R^* = 1$ which decreases to 0.806 with $R_c/R^* = 8.$ This predicted change in the discharge coefficient with the ratio of R_c to R^* is confirmed by experiment, as will be discussed in section 6.4. The radius of curvature affects not only the discharge coefficient but also the velocity defect due to viscous flow, as represented by η_V. This effect is again most pronounced at low Re_{D^*}. At $Re_{D^*} = 252$, η_V equals 0.754 with $R_c/R^* = 8.$, but with $R_c/R^* = 1.$ η_V increases to 0.786.

The second variable is the throat radius, R^*. It was shown in the last section that for a given propellant the velocity defect due to viscous flow is dependent only on Re_{D^*} (see Fig. 28). Since Re_{D^*} is defined as $Re_{D^*} = \rho^* u^* R^*/\mu_T$, it would appear at first sight that changes in η_V with R^* may be deduced directly from this graph. However, as will be shown shortly, the viscous flow loss is dependent not only on Re_{D^*} but also on the nozzle area ratio, and in particular on the Reynolds number based on wall length, defined by $Re_L = \frac{\rho^* u^* L}{\mu_T}$. Thus Fig. 28 can be used to predict η_V for nozzles with different throat radii only if the whole nozzle is scaled so that Re_L/Re_{D^*} remains a constant.

(iii) Divergent section

This is the most important part of the convergent-divergent nozzle. Attention is first given to conical divergent shapes, where the two

variables are area ratio, ε, and divergent half angle, θ_2.

(a) Area ratio, ε.

It was shown in the discussion of Model One (section 6.2.2) that with vibrational energy frozen the incomplete expansion efficiency, η_E, for a given nozzle, was dependent only on the ratio of the frozen specific heats, γ_{CF}. In order to determine the magnitude of this loss over a wide range of area ratios, a simple program based on eqs. (2.26), (2.30), (4.11) and (4.12) was written to calculate the area ratio and resulting η_E required to achieve a given exit temperature. The results are illustrated in Fig. 48a for the cases of a monatomic gas ($\gamma_{CF} = 5/3$), a diatomic or linear polyatomic gas ($\gamma_{CF} = 7/5$) and a non-linear polyatomic gas ($\gamma_{CF} = 4/3$) over the range of ε from 1 to 1000. As previously noted, the incomplete expansion loss increases with the complexity of the propellant molecule; and from Fig. 48a it is seen, not unexpectedly, that the loss decreases with increasing area ratio.

We are also aware from section 6.2.3 that vibrational relaxation can significantly influence η_E. This dependence is strongest when vibrational energy is in equilibrium, and in order to set a limit on the incomplete expansion loss an additional program, based on eqs. (2.26), (2.30), (4.18) and (4.19), was written to evaluate the behaviour of η_E for this situation. With vibrational relaxation the incomplete expansion loss is no longer independent of the plenum temperature, so that η_E is a function of the area ratio, the propellant properties and the plenum temperature. The results for H_2 and NH_3 are shown in Fig. 48b. In the case of H_2 vibrational relaxation makes little difference in η_E from the $\gamma_{CF} = 1.4$ curve, and only results for $T_T = 2000^oK$ are shown. The curve is truncated at $\varepsilon \simeq 200$ since the temperature at the exit plane equals 100^oK, which was the minimum temperature considered. The results for NH_3 (undissociated) show

considerable differences from the frozen case where $\gamma_{CF} = 4/3$, particularly at the higher temperatures. Thus with a plenum temperature of 1000°K (at which temperature little dissociation of NH_3 is likely in resistojets) an area ratio of 10 : 1 produces an incomplete expansion efficiency of 0.71. Increasing ε causes some improvement, but even with $\varepsilon = 100$, η_E increases only to 0.87. These figures contrast sharply with the incomplete expansion loss for a monatomic where η_E equals 0.94 at $\varepsilon = 10$, and 0.99 at $\varepsilon = 100$. For completeness the $\eta_E - \varepsilon$ curves for CO_2 and CH_4 are shown in Figs. 48c and 48d. It is therefore emphasised that the use of polyatomic propellants in resistojet motors incurs a severe penalty in the form of large incomplete expansion losses, if vibrational equilibrium is maintained throughout the nozzle.

Although an increased area ratio produces improvements in the incomplete expansion the benefits in the jet velocity are countered by the increased viscous flow loss. An increase in ε, keeping R^* constant, produces a larger surface area and it follows that the momentum defect is increased. The effect of changes in the nozzle area ratio on the overall nozzle performance were investigated with Model One for a range of plenum pressure, therefore Re_{D^*}, for area ratios from 4 to 800 : 1. The results for η_V, the velocity defect due to viscous flow, are shown in Fig. 49. It is seen that, for a given Re_{D^*}, η_V decreases as ε is raised. Also the rapid drop-off in η_V which was found with the nominal geometry ($\varepsilon = 25$) is exhibited by other nozzles at different Re_{D^*}. (It may be remembered that with the nominal geometry at $Re_{D^*} = 201$ convergence of the isentropic core-boundary layer iteration procedure was not completely satisfactory, and the results under these conditions were regarded as tentative. The same reservations must also be made for the other geometries where the drop-off is very steep.) In the nominal nozzle this occurred when the pressure gradient parameter, β, fell below a value of about two.

With larger area ratios this occurs at higher plenum pressures and therefore higher Reynolds numbers, and the result is the behaviour shown in Fig. 49. It can be seen that the velocity defect, η_V, is dependent on the throat diameter Reynolds number and the nozzle area ratio. Since the change in ε represents a change in the nozzle wall length, it is more useful to correlate η_V as a function of Re_{D^*} and Re_L, where Re_L is a Reynolds number based on the wall length. The ratios of Re_L to Re_{D^*} are included alongside the values of ε in Fig.49. Thus the η_V curves can then be applied to other nozzle geometries for which R^* is not necessarily equal to 0.5 mm, provided that $Re_L/Re_{D^*} = L/2R^*$ remains constant.

It is apparent that variation of the nozzle area ratio causes a coupling of the incomplete expansion and viscous flow loss, and this in turn affects the radial flow loss. The overall nozzle performance corresponding to Fig. 49 is shown in Fig. 50, in terms of an efficiency, $\eta = (\eta_E \ \eta_V \ \eta_D)^{\frac{1}{2}}$, which is simply the ratio of the specific impulses, $I_{spCFEVD}$ to I_{spCF}. At the smallest area ratios there is a distinct improvement in efficiency by increasing ε from 4 to 10, since the improvements in incomplete expansion outweigh the viscous flow penalty. This is also true for the larger area ratios at higher Re_{D^*}, but as Reynolds number decreases the drop-off in the viscous flow efficiency when $\beta_{ex} \simeq 2.$ more than offsets the improvements in η_E, so that there is a rapid decrease in the overall efficiency. An envelope drawn around these curves would represent an optimum performance. It is stressed, however, that this is not a true optimum as only the area ratio has been varied while the divergent shape and the half angle, θ_2, have been held constant.

The information presented in Fig. 50 has been re-interpreted in Fig. 51a, where contours of constant efficiency have been drawn on a graph of Re_L versus Re_{D^*}. First a word of explanation is necessary. Examining the line $\eta = 0.90$ in Fig. 50 it can be seen that a nozzle

with $\varepsilon = 25$ corresponds to $Re_{D^*} \simeq 4000$. With increasing area ratio the Reynolds number, required to achieve this efficiency, falls and reaches a minimum at $Re_{D^*} \simeq 1200$ when the area ratio lies between 100 and 200. Further increases in ε cause the required Re_{D^*} to rise, and by $\varepsilon = 800$, Re_{D^*} is required to be approximately 5000. In order that the optimum area ratio can be evaluated more precisely it is necessary to draw a graph either of Re_L versus Re_{D^*}, as in Fig. 51a, or of ε versus Re_{D^*}. The former was chosen since the discussion is then not restricted to a nozzle with $R^* = 0.5$ mm. The $\eta = 0.9$ contour in Fig. 51a corresponding to the increase in ε just described starts at $Re_{D^*} \simeq 4000$, moves to the left and reaches a minimum Reynolds number (Re_{D^*}) for which this efficiency can be achieved at $Re_{D^*} \simeq 1200$; this point corresponds to the "optimum" ε. With increasing ε the viscous flow loss predominates and the constant efficiency contour moves to the right. The line joining the minimum Re_{D^*} points can now easily be drawn. It is seen that this "optimum" efficiency line is essentially linear on a $\log_{10} Re_L$ versus $\log_{10} Re_{D^*}$ plot. This is redrawn in Fig. 51b on the original axes of η and Re_{D^*}. An experimental "optimum" $I_{spCFEVD}/I_{sp}$ curve determined by Halbach[90] is included for comparison. This figure is discussed further in section 6.4, but at this stage it is noted that there is encouraging agreement.

Finally, it is seen in Fig. 51a that no contours are found on the left hand side of the diagonal. The implication is that the model cannot be used to predict the performance of nozzles where the nozzle design and plenum conditions produce values of Re_L and Re_{D^*} which lie within this region.

(b) Divergent Half Angle, θ_2.

Still restricting the discussion to conical nozzles, the next geometric variable to be considered is the initial wall angle of the

divergent section, θ_2, which for a conical shape is the wall angle throughout the divergent section. The effect of θ_2 on the nozzle performance essentially involves trading off the viscous flow loss against the radial flow loss. The changes in performance were first investigated for the nominal nozzle, changing only θ_2, for the range of Re_{D*} from 16000 down to approximately 100; the divergent angle was varied from 5 to 40°. Variation of the nozzle efficiency, $\eta = (\eta_E \eta_V \eta_D)^{\frac{1}{2}}$, is shown in Fig. 52, which is a plot of θ_2 versus Re_{D*} on which lines of constant η have been drawn. It is seen that changes in the divergence angle can significantly affect the nozzle efficiency. The nozzle performance is dominated by the viscous losses at small divergence angles, but with increasing θ_2 the nozzle becomes shorter for a given ε and the viscous loss is less severe. However the radial flow increases in significance and at large θ_2 this loss is dominant. Thus there is an intermediate region in which the combined viscous flow-radial flow loss is minimised; or, put another way, for a given Re_{D*} an optimum value of θ_2 exists which maximises the efficiency, η. At $Re_{D*} = 10^4$, the optimum divergence angle for a nozzle of 25 : 1 area ratio is approximately 12°, and with decreasing Reynolds number the boundary layer thickens and the optimum θ_2 increases, so that at $Re_{D*} = 200$, $(\theta_2)_{optimum}$ is almost 40°.

A similar investigation of the variation in performance with divergence angle was carried out for $\varepsilon = 100$ and 400. The resulting optimum θ_2 curves are shown in Fig. 53. Superimposed on this figure are contours of constant efficiency, $\eta = I_{spCFEVD}/I_{spCF}$. It is seen that for a given Re_{D*} the optimum half angle increases with ε, however the differences in $(\theta_2)_{optimum}$ with ε are not large. The reasons for this can be found by examining the component losses for the different area ratios for the case where $(\theta_2)_{optimum} = 20^{\circ}$. The relevant information is tabulated below.

ε	Re_{D*}	η_E	η_V	η_D	$\eta = (\eta_E \eta_V \eta_D)^{\frac{1}{2}}$
25.	1700.	0.882	0.910	0.976	C.885
100.	2650.	0.932	0.917	0.980	0.915
400.	4400.	0.960	0.928	0.983	0.936

The decisive factor in the similarity of the $(\theta_2)_{optimum} - Re_{D*}$ curves is the viscous flow efficiency, η_V. It is seen from Fig. 49 that the Reynolds numbers at which $\theta_2 = 20^o$ is optimum, i.e. Re_{D*} in the above table, are situated in the region where there are no major differences in η_V between different area ratios. The relative boundary layer thickness, at the nozzle exit increases with ε as evidenced by η_D, but the combined effect is that the optimum curves are very similar for different area ratios.

It should be remembered, however, that these results are the product of a quasi one-dimensional theory and for this reason the results for larger divergent angles can be criticised.

(c) Variation in Shape of the Divergent Section

The previous observation that there are gains to be made in the nozzle efficiency by increasing the divergence angle at lower Reynolds numbers suggests that performance benefits are also to be obtained by using a horn divergent shape. This suggestion was briefly examined for a nozzle of 100 : 1 area ratio. The relation used to describe the shape of the divergent section is given by eq. (5.1), which is

$$R = \theta_2 z_D + a z_D^2 + b z_D^3$$

All the geometries so far discussed have used a conical shape where $a = b = 0$. To produce variations in the divergent shape, geometries

were considered where the parameter b was again set to zero but with a non-zero. The values of a which were used, are 5, 10, 15,25 and 50 and the resulting shapesof the divergent section, with $\theta_2 = 20^o$ (0.3491 rads), are shown in Fig. 54. The resulting performance figures, in terms of the specific impulse ratio are shown in Fig. 55. At the highest Reynolds numbers where the viscous effects are smallest the conical shape (a = 0) produces the most efficient nozzle. The horn nozzles are penalised by large radial flow losses, e.g. at $Re_{D*} = 8060$ with a = 50, $\eta_D = 0.847$ compared to η_D of 0.968 with a = 0. Decreasing Re_{D*} reduces the radial flow loss. Thus it is seen from Fig. 55 that with decreasing Re_{D*}, nozzles with larger values of a become more efficient in comparison to those with smaller a. At the lowest Reynolds numbers the nozzle with a = 50 is the most efficient, although the radial flow loss is still substantial the divergence of the nozzle wall allows the effective inviscid core to occupy a larger portion of the nozzle flow field.

The following points summarise the main findings concerning the variation in performance with resistojet nozzle geometry :-

(i) The convergent section has little influence on performance.

(ii) Decreasing the ratio of R_c to R^* increases the discharge coefficient and, to a lesser extent, reduces the viscous flow velocity defect. The improvements are most significant at low Re_{D*}.

(iii) Since the viscous flow, mass and velocity defects are strong functions of the throat diameter Reynolds number, it follows that these losses are dependent on the throat radius, R^*.

(iv) Substantial losses from incomplete expansion are found for all nozzles employing polyatomic propellants, when

vibrational equilibrium is maintained throughout the nozzle.

(v) The viscous flow velocity defect is shown to be dependent on two Reynolds numbers, based on the throat diameter and wall length respectively.

(vi) For conical nozzles of given divergence angle the optimum area ratio increases with Re_{D*}.

(vii) The optimum divergence angle in conical nozzles increases as Re_{D*} is lowered. However, the optimum is not a strong function of area ratio.

(viii) At lower Reynolds numbers, horn shaped nozzles offer considerable performance benefits.

6.4 Comparison with Experiment

The crucial test of any theoretical model is how its predictions compare with experimental measurements. Although a considerable amount of experimental work has been done on resistojet motors, there is not a lot of data in the literature which can be regarded as reliable. This is caused mainly by the small size and low thrust levels of resistojets, so that it is extremely difficult, physically, to monitor much more than the gross performance quantities of thrust and mass flow rate. Even these parameters are only obtained accurately when extreme care is taken (for instance see Ref. 93). As mentioned in Chapter One, the fact that perfect vacua cannot be maintained in space simulation chambers causes additional complication, since the ambient pressure of the vacuum chamber interacts with the low density viscous nozzle flow with adverse effects on the resistojet performance. This was clearly demonstrated in the work of Yoshida et al [7], who measured a specific impulse of 539 seconds from a hydrogen resistojet at a vacuum chamber pressure of 300 microns, but as the chamber pressure

was lowered the specific impulse improved markedly to reach nearly 670 seconds at a pressure of one micron. It is for this reason that much of the early data on resistojet performance is considered unreliable. On account of their small size† detailed flow measurements, such as the velocity and density profiles at the nozzle exit, have never been taken. Finally, even such basic properties as plenum temperature and pressure are difficult to measure directly and are often inferred from other information.

As comparisons of thrust and mass flow rates reveal very little about the structure of the flow and the nature of the loss processes found in resistojet nozzles, resort has to be made to other experimental data in which some, if not all, of the losses are found. The first experimental comparison is with the work of Tang[91], who has made extensive measurements of the discharge coefficient in small ($R^* \simeq 0.25$mm) convergent-divergent nozzles at a stagnation temperature of 300^oK. This work was an experimental and theoretical investigation of the dependence of C_D on the throat geometry (R_c/R^*) for the gases H_2, N_2, Ar and He. In the theoretical part of his study, Tang derived closed-form, analytic solutions for the discharge coefficient as a function of Reynolds number and throat geometry, which he obtained from the Falkner-Skan equation for values of β = 1, 2 and infinity. However it is the experimental aspect of this work which is of primary interest, as Tang's results are very consistent and it is possible to draw fair mean lines through his data. Comparisons of the results for the four gases over the range of Re_{D^*} from 100 to 20000. with the predictions of Model One for a nozzle with R^* = 0.258 mm and R_c/R^* = 2.18 is shown in Fig. 56a. First it is noted that the experimental results for He and Ar are coincident. The corresponding theoretical curve (γ_{CF} = 5/3) is found to give a consistently higher

† For example, the exit diameter of the nozzles used by Yoshida et al is typically 2.7 mm.

value of discharge coefficient, although the maximum difference is only of the order of 2%. In the case of H_2 and N_2, Tang's experimental results do not produce coincident lines as is predicted by Model One with $\gamma_{CF} = 7/5$. The measured N_2 curve again lies below the predicted curve, although the maximum difference is less than 1%. However the comparison between experiment and theory for H_2 is very favourable. At the lowest Reynolds numbers the two curves are coincident, but as Re_{D^*} increases the difference also increases, which is contrary to what one intuitively expects to happen when the boundary layer thickness decreases. The difference in the experimental C_D between H_2 and N_2 is ascribed mainly to the differing amounts of velocity slip at the nozzle surface. Next, the effects of variation in the throat geometry as measured by Tang and as predicted by Model One are compared in Fig. 56b. The test gas is N_2 and the geometries considered are the previous case with $R_c/R^* = 2.18$ and another with a sharper throat where $R_c/R^* = 1$. It was predicted in section 6.3 that reductions in the throat radius of curvature cause an improvement in the discharge coefficient, and Tang's data confirms this behaviour as is shown in Fig. 56b. The agreement between prediction and measurement is seen to be good, and the little difference that there is at low Reynolds numbers is attributed to the neglect in the theory of the terms accounting for longitudinal curvature.

Mention was made in Chapter One of the investigations of Rae[43] and Rothe[28] on viscous low-density nozzle flows. The former was a theoretical study which employed the slender channel approximation to the Navier-Stokes equations, to examine the viscous flow in various nozzles for Reynolds numbers below $Re_{D^*} \simeq 660$. (See footnote on page 28). In the second work, Rothe used an electron beam to obtain radial density and temperature profiles at several stations in two conical nozzles, at Reynolds numbers comparable to those studied by Rae. The nozzles were comparatively small, with $R^* = 1.25$ and 2.5 mm, and $\varepsilon = 66$.

Nitrogen was used as the test gas at a stagnation temperature of 300°K. The main interest of these studies was in the existence at Re_{D^*} less that 50 of a supersonic "bubble" inside the nozzle divergent section, with a subsequent shock-free viscous transition to subsonic flow. This phenomenon lies outside the predictive capabilities of the present boundary layer models, however Rothe reports on an experiment with $Re_{D^*} = 633$ which the present models can handle. Predications of Model One for the centreline density and temperature distributions in this case are compared to Rothe's measurements and Rae's predictions in Figs. 57a and 57b. The present results are seen to compare favourably with those of Rae, although both sets of theoretical curves differ from Rothe's experimental data. It must be pointed out that the modelling of the nozzle geometry in the present computation was not exact since the throat shape which was used here differed from the experimental geometry. The actual throat radius of curvature was 0.64 mm giving $R_c/R^* = 0.51$, which is a very sharp throat. In most cases reported in this thesis the calculations were carried out at 101 equi-spaced stations along the nozzle axis. Using such a procedure with Rothe's geometry produced an ill-defined throat section, and sensible results were not obtained. Attempts to alter the step-size were not successful in this particular case, and the difficulty was overcome by modifying the geometry to give $R_c/R^* = 2$. Although the effects of this difference on the boundary layer growth in the divergent section are only small, the two theoretical predictions are not strictly comparable.

A better example is to be found from the experiments of Yevseyev[92] on the flow of air through a nominally inviscid Mach 6 nozzle from a plenum temperature of 300°K. In this nozzle the throat radius was 5 mm and $R_c/R^* \simeq 13.4$, so that the throat section did not present a problem. The plenum pressure was somewhat lower at 500 Nm^{-2}, which gives a throat diameter Reynolds number of 660 and is therefore comparable to Rothe's

case. In fact Yevseyev's data was used by Rae as his original test case. Comparison of Yevseyev's measured centreline Mach number distribution with the predictions of Rae and with Model One are shown in Fig. 58a. The agreement of the present predictions with Yevseyev's data is seen to be good, and is considerably better than the predictions of Rae taken from Ref. 43. However, further examination of Yevseyev's data indicates that this agreement must, to an extent, be fortuitous, since Rae's model predicts the velocity profiles more accurately. Comparison of the predicted velocity profiles of Rae and of Model One with Yevseyev's velocity measurements for the station $z/R^* = 11.1$ is given in Fig. 58b. It is seen that the no slip condition which is assumed in the present work differs considerably from Rae's prediction of $u_w/u_e \simeq 0.15$. This assumption largely offsets the increased velocity defect at the edge of the boundary layer which is predicted by Rae. Nevertheless, it is remarkable that the boundary layer/inviscid core model succeeds as well as it does at such low Reynolds numbers.

Turning now to the prediction of resistojet performance, a useful starting point is the previously discussed hydrogen resistojet of Yoshida et al[7]. This resistojet is composed of a concentric tube heater and a conical nozzle with an area ratio of 32.6 : 1. Yoshida estimated the plenum temperature by two methods, (i) using an optical pyrometer sighted on the rear wall of the heating element and (ii) using an overall energy balance. It is inferred from Ref. 7 for the case where the specific impulse was measured to be 668.6 seconds that the plenum temperature, T_T, lay between 1800 and 1900^oK. No mention is made of the plenum pressure, but an examination of the results of Model One for a range of plenum pressures indicates that p_T must have been of the order of 170 kNm^{-2}. It is noted that the supply pressure was approximately 340 kNm^{-2}, so it is implied that an

extremely large pressure drop occurred in the heater. Computation was carried out with Models One and Two for p_T = 170 kNm^{-2} and T_T = 1800 and 1900°K. The other nozzle geometric variables were θ_2 = 22°, R^* = 0.2365 mm and it was assumed that R_c/R^* = 1. Comparison of the results is shown below.

Comparison of Predictions of Models One and Two with H_2 Resistojet of Yoshida

	Measured	T_T=1800°K (Re_{D^*} = 640)			T_T=1900°K (Re_{D^*} = 600)		
		Φ = 0	Φ= 100	Φ = ∞	Φ = 0	Φ= 100	Φ = ∞
$\dot{m}(gs^{-1})$	0.00688	0.00688	0.00683	0.00683	0.00668	0.00662	0.00662
F(m N)	45.1	43.3	43.5	43.6	43.3	43.4	43.5
I_{sp}(s)	668.6	641.9	649.6	651.6	658.1	666.9	670.5
η_{Res} or η_N	0.597	0.731	0.748	0.753	0.723	0.743	0.751
P_{el}(W)	218.8	157.4	156.2	156.2	163.9	162.6	162.6

Since there is some uncertainty in the plenum conditions, in particular in the value of p_T, it follows that the comparison between Yoshida's measurements and the present predictions is only approximate. Of the parameters presented in the above table the specific impulse is the least affected by the plenum pressure, being essentially a function of temperature, with the pressure exerting a secondary influence through the Reynolds number dependence of the viscous flow velocity defect. It is seen from Fig. 28 that, for a similar nozzle geometry, η_V is not critically dependent on Reynolds number for Re_{D^*} of the order of 600. Thus comparison of the specific impulse is the most meaningful. The comparison is seen to be good, and it is again noted that the rate parameter, Φ, has only a small influence on the theoretical performance of hydrogen. The comparisons of η_{Res} with η_N and of P_{el}

are not so meaningful since losses from the heater contribute to the experimental figures.

An experiment in which the influence of the heater should have a lesser bearing on the overall efficiency is reported by Murch and Krieve[15], who have developed a vortex heater which they claim gives very low thermal losses for temperatures below 1200°K. Using this design Murch and Krieve have measured the performance of NH_3, CH_4 and CO_2 for heater temperatures up to 2000°K. The amount of hot metal surface in the heater is very small so that it is expected that little catalytic decomposition of the propellants will occur. In fact when using CH_4 Murch and Krieve found no measurable deposition of solid carbon at heater temperatures below 1900°K. In order to compare with these experiments computation was carried out with Model Two, with $\Phi = 1$, for a range of plenum temperatures using the stated nozzle dimensions of $R^* = 0.216$ mm, $\varepsilon = 40$; it was assumed that $\theta_2 = 20°$ and $R_c/R^* = 2$. Comparisons of the results for NH_3, CH_4 and CO_2 are shown in Figs. 59 to 61. First examining the performance predictions for ammonia, it is seen from Fig. 59a that the mean curve of electric power per unit thrust plotted against specific impulse, taken from the data of Murch and Krieve, is matched extremely well by the undissociated (f = 1) curve predicted by Model Two for a plenum pressure of 145 kNm^{-2}. Comparison of the measured resistojet efficiency, η_{Res}, with the predicted nozzle efficiency, η_N, for f = 1, shown in Fig. 59b is also seen to be good. Results of Model Two for the equilibrium limit (f = 0) are also included in these figures and it is seen that even at high temperatures there is little resemblance between the f = 0 curves and the experimental curves. It is observed that specific impulses of over 300 seconds were measured by Murch and Krieve, which suggests that either some dissociation occurred, or heater temperatures well in excess of 2000°K were achieved.

Comparison of the methane performance parameters is shown in

Fig. 60. It is seen that the present theoretical results do not correspond as well as in the case of NH_3, although the shapes of both the P_{el}/F versus I_{sp}, and η versus I_{sp} curves are very similar. It is not readily apparent what is the cause of the significantly higher theoretical performance, but it should be mentioned that there is considerable scatter in all of the data of Murch and Krieve, in some cases as much as 20%. Finally, the carbon dioxide performance curves are shown in Fig. 61. Again the comparison is fair only, although here too the present author has some reservations about the experimental data. For instance, Murch and Krieve report a specific impulse of 68 seconds for CO_2 when it is operated cold (300^oK) which is a value greater than that produced by an ideal nozzle with no losses. However, accepting the considerable degree of uncertainty in the plenum conditions it is seen that Model Two gives a reasonable prediction of the overall performance of the polyatomic propellants for a range of plenum temperatures.

It was mentioned in the literature review of section 1.4 that the slender channel computer program of Rae has been used by Kallis, Goodman and Halbach[45] to predict the performance of resistojets. For three reasons this was a welcome addition to the literature. Firstly, it provided additional theoretical modelling of resistojet nozzle flows. Secondly, it reported experimental results for several propellants for which the vacuum chamber pressure was less than two microns. Finally, and perhaps most importantly, in relating experiment and theory Kallis et al have had to evaluate the plenum conditions, T_T and p_T. A further point is that full details of the nozzle geometry were given. These are $\theta_1 = 70^o$, $R^* = 0.2286$ mm, $R_c = 0.254$ mm and $\varepsilon = 360$. The divergent section was of a horn shape which in the present calculations was approximated by

$$R = 0.2129 z_D + 27.0 z_D^2$$

Model Two was run with Φ = 100 to compare with some of the cases reported in Ref. 45. With this geometry the stepsize was modified in the vicinity of the throat without encountering any computational difficulties. Comparison of the predictions of Model Two with the experimental results of Kallis, Goodman and Halbach, and with the predictions of the Rae program are tabulated below.

Comparison of Predictions of Model Two with Results of Kallis, Goodman and Halbach

Gas	T_T (^oK)	p_T (kNm^{-2})	Re_{D^*}	I_{sp} (s)				
				Expt.	"Rae" Model	% Diff. with Expt.	Model Two	% Diff. with Expt.
H_2	1667.	223.	893.	630.	630.	0.0	653.6	+ 3.7
H_2	777.	233.	2384.	436.	431.	- 1.1	445.2	+ 2.1
CH_4	1000.	172.	2533.	227.	206.	- 9.2	212.0	- 6.6
CO_2	1222.	213.	2890.	143.	150.	+ 4.9	138.3	- 3.3
CH_4	667.	182.	4405.	172.	168.	- 2.3	165.1	- 4.0

It is seen that in comparison to the experimental specific impulse, Model Two overestimates the performance of H_2 and underestimates for CO_2 and CH_4. The percentage difference with the experimental I_{sp} is comparable to that obtained with the "Rae" model. However it should be noted that the slender channel program used the assumption of a constant ratio of specific heats, γ. Kallis et al make the approximation that γ is equal to the value appropriate to the plenum temperature, with vibrational energy in equilibrium, and is constant throughout the nozzle. This is not physically valid and the effect on performance is to cause an increase in specific impulse over the case where vibration is in equilibrium with translation. Thus, apart from the CO_2 case, more correct modelling of the vibrational relaxation would reduce their predicted specific impulse and therefore cause an increase in the percentage

difference of the "Rae" model with experiment.

Next, the theoretical and experimental "optimum" nozzle efficiency curves which are shown in Fig. 51b are briefly discussed. The theoretical curve was obtained with Model One by deriving that area ratio which maximised $\eta = I_{spCFEVD}/I_{spCF}$ for a given Reynolds number, for the case of conical nozzles with a divergent half angle of 20^{o}. The experimental curve was derived by Halbach[90], who essentially analysed a large amount of experimental data from which he obtained a conservative optimum curve. Thus the two curves are not necessarily optimum at any point. However they are very useful indicators of the maximum nozzle efficiency as a function of Re_{D*}, and the fact that there is less than 2% difference between them for Re_{D*} ranging from 600 to 6000 substantiates the present performance predictions.

Finally, it is interesting to note that Halbach, together with Page and Short, i.e. the authors of Ref. 2, have designed a 3kW hydrogen resistojet with a nozzle area ratio of 100 : 1. Details of the preliminary testing of this resistojet at R.P.E., Westcott have been reported in Ref. 93. Although measurements have not yet been made at the design operating temperature of $2480^{o}K$, the predictions of Model Two using a vibrational rate parameter, $\Phi = 100$, are found to compare very favourably with the performance estimates of Halbach et al. These performance predictions are listed below, without further comment.

Predicted Performance of RPE Resistojet (T_T = 2480°K, p_T = 304 kNm^{-2}, Re_{D^*} = 2100)

	Estimated Performance (Ref. 93)	Model Two Predictions
$\dot{m}$ (gs^{-1})	0.0806	0.0822
F (N)	0.652	0.655
V_j (kms^{-1})	8.09	7.97
P_j (kW)	2.64	2.61
η_C		1.000
η_F		0.991
η_E		0.931
η_V		0.902
η_D		0.983
η_N	0.810	0.818

Chapter Seven Summary Discussion

This thesis has been concerned with the theoretical prediction of resistojet performance; in particular it identifies the various energy loss processes, and models the gasdynamics of the nozzle flow. It was shown in Chapter One that a complex, interacting situation exists in the nozzle flow, so that a number of assumptions were made in the analysis to make the problem more tractable. For the sake of computational economy an inviscid core/viscous boundary layer model was assumed, and an important portion of this work has been devoted to the development of similar solutions of the laminar boundary layer equations, where the boundary conditions at the nozzle wall were that of no slip and an adiabatic wall. These solutions were then used to represent the boundary layer development. The nozzle flow was assumed to be quasi one-dimensional, and vibrational relaxation of the propellant was modelled by assuming that at a given station in the nozzle the specific heat was constant.

A hierarchy of computer programs have been developed which describe the gasdynamics with varying degrees of sophistication. The effects of the major variables (propellant, temperature, pressure, degree of dissociation, vibrational rate and nozzle design) were examined using the appropriate computer program. It was found that, even in the simplified situations considered here, the various energy loss processes were intimately coupled; for example vibrational relaxation leads to increased losses from viscous flow and incomplete expansion. It was also shown that the performance of ammonia resistojets is significantly affected by propellant decomposition, but in order to accurately model the performance, more complete kinetic data of the NH_3 dissociation is required. Further it is noted that there is little vibrational relaxation data in the literature for the polyatomic gases - NH_3, CH_4 and CO_2 - in a de-excitation environment.

The agreement of calculations based on solutions of the Falkner-Skan equation with experimentally measured boundary layers is reasonable, even when the boundary layer is thick, thereby justifying the approach. Overall resistojet performance parameters have been compared with experiment and with the semi-empirical estimates of Halbach. Again the agreement is satisfactorily good. Predictions of the present performance models are also found to compare favourably with alternative theoretical predictions based on Rae's slender channel model. An important advantage of the computer programs reported in this work is that they are very economical. For instance, the best program (Model Two) requires 80 seconds per case on an ICL 1907 computer, whereas the modified Rae program used by Kallis et al typically takes 900 seconds per case on a CDC 6500 computer - a computer which is approximately ten times faster.

Although the present results compare favourably with a range of experiments, in view of the assumptions made, it must be accepted that this agreement is in parts fortuitous. Thus it is recognised that the basic model (inviscid core/viscous boundary layer) is inappropriate when the flow is essentially viscous throughout the nozzle, which in typical resistojet nozzles occurs for Re_{D*} of the order of a few hundreds. It is in this region that the slender channel approach is most applicable and where the inclusion of slip velocity is essential. However, the agreement of the present models with experiment over the region of Reynolds numbers of practical interest in resistojet applications ($500 \lesssim Re_{D*} \lesssim 5000$) has been shown to be satisfactory. Finally, the fact that considerable difficulties are experienced in the experimental determination of resistojet performance, means that the computationally economical models developed here are of considerable use in resistojet design.

The major conclusions of this study are as follows :

1. The five energy loss processes considered to occur in resistojet nozzle flows, are all potentially important. Depending on the propellant, the losses from frozen chemistry and finite vibrational relaxation rate may be dominant. Losses from incomplete expansion, viscous flow and radial flow are coupled and they can be traded-off against each other to produce an optimum nozzle.

2. It has been demonstrated that the basic approach, in which the flow is separated into an inviscid core and a viscous boundary layer, provides an adequate description of most resistojet nozzle flows except near the onset of viscous closure; this limit is a function of two Reynolds numbers based on the throat diameter and the wall length.

3. Representation of the laminar boundary layer by the patching together of similar solutions of the Falkner-Skan equation, leads to predictions which agree quite well with experiment.

4. According to the solutions of the modified Falkner-Skan equation the influence of transverse curvature on the boundary layer development is significant only in the supersonic region of the nozzle, where the effect is to somewhat reduce the boundary layer momentum thickness and therefore decrease the velocity defect due to viscous flow. However the overall effect on resistojet nozzle performance is relatively small, so that use of the ordinary Falkner-Skan equation, which is better justified theoretically, is considered to be satisfactory for the purpose of resistojet performance prediction.

5. The results show that the losses due to finite vibrational rate processes in the polyatomic propellants are very dependent on the relaxation rates of such gases in a de-excitation environment.

6. Vibrational relaxation in the polyatomic propellants significantly affects the losses due to incomplete expansion and viscous flow.

7. Performance predictions obtained with Model Two, i.e. the model which is found to compare best with experiment, are tabulated for H_2, CH_4, CO_2 and NH_3 for the nominal geometry over a range of plenum conditions.

8. The models presented here will be of considerable help in the design of resistojet nozzles and in the theoretical prediction of resistojet performance.

REFERENCES

1. Jahn, R.G. — "Physics of Electric Propulsion", McGraw-Hill (1968)

2. Page, R.J., Halbach, C.R. and Short, R.A. — "Three kW concentric tubular resistojet performance", AIAA Paper No. 66-224 (1966)

3. Jack, J.R. — "Theoretical performance of propellants suitable for electrothermal jet engines", ARS J 31, 1685 (1961)

4. Howard, J.M. — "The resistojet", ARS J 32, 961 (1962)

5. Ferrara, J.D. — "A method for calculating steady-state thrust and flow-rate levels for Mariner 4 type attitude control nitrogen gas jets", NASA-CR-100070 (1969)

6. Jackson, F.A. — "An operational electrothermal propulsion system for spacecraft reaction control", AIAA Paper No. 66-213 (1966)

7. Yoshida, R.Y. et al — "Resistojet thruster life tests and high vacuum performance", NASA-CR-66970 (1970)

8. Lord, W.T., Donovan,A. and Savage, A. — "Electrothermal propulsion by resistojets", Ninth European Space Symposium. (1969)

9. Pisciotta, A. and Eusanio, E. — "Subsystem analysis for a MORL resistojet control system", AIAA Paper No. 67-712 (1967)

10. Lord. W.T. and Parkinson, R.C. — "Two-stage (resistojet-ion motor) transfer of communications satellites", AIAA Paper No. 70-1116 (1970)

11. Parkinson, R.C. — "The use of mixed-thruster electric propulsion with Thor-Delta 2910 as a launcher for large communications satellites", Paper presented by B.I.S. Meeting on Rocket Propulsion, April 1972.

12. Edwards, I. and Jansson, R.E.W. — "Performance of low-thrust ammonia resistojets", Southampton University, AASU Report No. 307 (1971)

13. Porter, J. — "Satellite attitude and orbital control systems based on hydrazine or ammonia", RAE Tech Memo Space 128 (1969)

14. Greco, R.V. and Charhut, D.E. — "Resistojet systems for manned space applications", AIAA Paper No. 69-255 (1969)

15. Murch, C.K. and Krieve, W.F. — "Electrothermal thruster performance with biowaste propellants", AIAA Paper No. 70-1161 (1970)

16. Bray, K.N.C. — "Chemical and Vibrational Nonequilibrium in Nozzle Flows", Ch. 3 of "Nonequilibrium Flows". Vol. 1, part 2 (ed. P.P. Wegener) Marcel Dekker (1970)

17. Page, R.J. and Short, R.A. — "Definition of resistojet control system for MORL", Vol. V NASA CR-66604 (1968)

18. Herzfeld, K.F. and Litovitz, T.A. — "Absorption and Dispersion of Ultrasonic Waves", Academic Press (1959)

19. Stull, D.R. et al — "JANAF Thermochemical Tables", Dow Chemical Co.

20. Sawyer, R.F. — "The homogeneous gas phase kinetics of reactions in the hydrogen-nitrogen tetroxide propellant system", AFOSR Sci. Rep. No. 66-0855 (1966)

21. Michel, K.W. and Wagner, H. — "The pyrolysis and oxidation of hydrazine behind shock waves", 10th Symp. on Combustion, p. 353 (1965)

22. Logan, R. and Kemball, C. — "The catalytic decomposition of ammonia on evaporated metal films", Trans. Faraday Soc. 56, 144 (1960)

23. Miles, G.A. — "An investigation of the catalytic dissociation of ammonia", Allison Technical Data Report RN 65-47 (1965)

24. Perroud, P. et al — "Forced convection of ammonia. Part Two: Gaseous ammonia at very high wall temperatures", CEA-R-3728 (1969)

25. Lewin, R. and Jansson, R.E.W. — "Environmental facility for measurements on low-thrust ammonia resistojets", Paper presented at BIS Meeting on Rocket Propulsion, April 1972.

26. Halbach, C.R. — "Ten mlb. biowaste resistojet performance", AIAA Paper No. 71-687 (1971)

27. Myerson, A.L. and Wyatt, W.S. — "Atom formation rates behind shock in hydrogen and the effect of added oxygen", J. Chem. Phys. 49, 425 (1968)

28. Bahn, G.S. — "Chemical kinetics. Detailed compilation of reaction rate information for the H-O-N system", Pyrodynamics 5, 49 (1967)

29. Rothe, D.E. — "Experimental study of viscous low-density nozzle flows", Cornell Aero. Lab., CAL No. AI-2590-A-2 (1970)

30. Whitfield, D.L. and Lewis, C.H. — "Analysis of boundary layers in low density hypersonic axisymmetric nozzles, including the effects of displacement, first-order transverse curvature, velocity slip and temperature jump", AIAA Paper No. 69-653 (1969)

31. Jonath, A.D. "Gasdynamic problems in low pressure microthrust engines", Astro. Acta. 11, 348 (1965)

32. Schaaf, S.A. and Chambré, P.L. "Flow of Rarefied Gases". Section H of "Fundamentals of Gas Dynamics" (ed. H. W. Emmons) (1958)

33. Milligan, M.W. "Nozzle characteristics in the transition regime between continuum and free molecular flow", AIAA J 2, 1088 (1964)

34. Kolin, I. "Thermodynamic Atlas", Longmans (1967)

35. Wegener, P.P. "Gasdynamics of Expansion Flows with Condensation, and Homogeneous Nucleation of Water Vapour". Ch. 4 of "Nonequilibrium Flows", Vol. 1, part 1 (ed. P.P. Wegener) Marcel Dekker (1969)

36. Brainherd, J.J. and Levinsky, E.S. "Viscous and nonviscous nonequilibrium nozzle flows", AIAA J 1, 2474 (1963)

37. Edwards, I. and Jansson, R.E.W. "Gasdynamics of resistojets : initial modelling and preliminary results", Southampton University, AASU Report No. 304 (1971)

38. Gaubatz, W.A., James, N.E. and Page, R.J. "Nonequilibrium effects in biowaste thruster performance", AIAA Paper No. 71-688 (1971)

39. Ferguson, H. "Electrothermal engine research and development", NASA-CR-54104 (1964)

40. Jeffries, N.P. and Cumbers, L.L. "Computer program for calculation of laminar boundary layer in a supersonic nozzle", General Electric Report TIS R65-SD3007 (1965)

41. Murch, C.K. et al "Low-thrust nozzle performance", AIAA Paper No. 68-91 (1968)

42. Cohen, C.B. and Reshotko, E. "The compressible laminar boundary layer with heat transfer and arbitrary pressure gradient", NACA Rep. No. 1294 (1956)

43. Rae, W.J. "Some numerical results on viscous low-density nozzle flows in the slender-channel approximation", AIAA Paper No. 69-654 (1969)

44. Williams, J.C. "Viscous compressible and incompressible flow in slender channels", AIAA J 1, 186 (1963)

45. Kallis, J.M., Goodman, M., and Halbach, C.R. "Viscous effects on biowaste resistojet nozzle performance", AIAA Paper No. 72-450 (1972)

46. Hill, P.G. and Peterson, C.R. "Mechanics and Thermodynamics of Propulsion", p. 359, Addison-Wesley (1965)

47. Curle, N. "The Laminar Boundary Layer Equations", O.U.P. (1962)

48. Cohen, C.B. and Reshotko, E. "Similar solutions for the compressible laminar boundary layer with heat transfer and pressure gradient", NACA Rep. 1293 (1956)

49. Schlichting, H. "Boundary Layer Theory", McGraw-Hill (1968)

50. Falkner, V.M. and Skan, S.W. "Some approximate solutions of the boundary layer equations", ARC, R & M No. 1314 (1930)

51. Hartree, D.R. "On an equation occurring in Falkner and Skan's approximate treatment of the boundary layer", Proc. Cambridge Phil. Soc. 33, 223, (1937)

52. Stewartson, K. "Correlated incompressible and compressible boundary layers", Proc. Roy. Soc. A, 200, 84 (1949)

53. Illingworth, C.R. "Steady flow in the laminar boundary layer of a gas", Proc. Roy. Soc. A, 199, 533 (1949)

54. Dorrance, W.H. "Viscous Hypersonic Flow", p. 26, McGraw-Hill (1962)

55. Dewey, C.F. and Gross, J.F. "Exact Similar Solutions of the Laminar Boundary Layer Equations", pp. 317-446 of "Advances in Heat Transfer", Vol. 4, Academic Press (1967)

56. Probstein, R.F. and Elliott, D. "The transverse curvature effect in compressible axially symmetric laminar boundary-layer flow", J. Aero. Sci. 23, 208 (1956)

57. Jaffe, N.A., Lind, R.C. and Smith, A.M.O. "Solution to the binary diffusion laminar boundary-layer equations with second-order transverse curvature", AIAA J 5, 1563 (1967)

58. Whitfield, D.L. "Theoretical and experimental investigation of boundary layers in low density hypersonic axisymmetric nozzles", AEDC-TR-68-193 (1968)

59. Evans, H.L. "Laminar Boundary Layer Theory", Addison-Wesley (1968)

60. Hayes, W.D. and Probstein, R.F. "Hypersonic Flow Theory", Academic Press (1959)

61. Li, T.Y. and Nagamatsu, H.T. "Similar solutions of compressible boundary layer equations", J.Aero.Sci. 22, 607 (1955)

62. Smith, A.M.O. and Clutter, D.W. "Machine calculation of compressible laminar boundary layers", AIAA J 3, 639 (1965)

63. Dewey, C.F. and Gross, J.F. "Similar solutions of the laminar boundary-layer equations with variable fluid properties", Fluid Dynamics Transactions 2, 529 (1965)

64. Anderson, J.D. "A time-dependent analysis for vibrational and chemical nonequilibrium nozzle flows", AIAA J 8, 545 (1970)

65. Stollery, J.L. and Park, C. "Computer solutions to the problem of vibrational relaxation in hypersonic nozzle flows", JFM 19, 113 (1964)

66. Sebacher, D.I., Guy, R.W. and Lee, L.P. "Vibrational energy transfer in expanding mixtures of N_2 and CO_2 as measured by an electron beam." NASA TN D-6445 (1971)

67. Rosser, W.A., Wood, A.D. and Gerry, E.T "Deactivation of vibrationally excited CO_2 (ν_3) by collisions with CO_2 or N_2", J. Chem. Phys. 50, 4996 (1969)

68. Anderson, J.D. "Time-dependent analysis of population inversion in an expanding gas", Phys. Fluids 13, 1983 (1970)

69. Bray, K.N.C. "Atomic recombination in a hypersonic wind-tunnel nozzle", JFM 6, 1 (1959)

70. Emanuel, G. and Vincenti, W.G. "Method for calculation of the one-dimensional nonequilibrium flow of a general gas mixture through a hypersonic nozzle", AEDC-TDR-62-131 (1962)

71. Phinney, R. "Nondimensional solutions of flows with vibrational relaxation", AIAA J 2, 240 (1964)

72. Musgrove, P.J. and Appleton, J.P. "On molecular vibrational relaxation in the flow of a chemically reacting gas", Southampton University, AASU Report No. 183

73. Landau, L. and Teller, E. Physik.Z. Sowjetunion 10, 34 (1936)

74. Millikan, R.C. and White, D.R. "Systematics of vibrational relaxation", J. Chem. Phys. 39, 3209 (1963)

75. Taylor, R.L. and Bitterman, S. "Survey of vibrational relaxation data for processes important in the CO_2-N_2 laser system", Revs of Modern Physics 41, 26(1969)

76. Hurle, I.R., Russo, A.L. and Hall, J.G. "Spectroscopic studies of vibrational non-equilibrium in supersonic nozzle flows", J. Chem. Phys. 40, 2076 (1964)

77. Von Rosenberg, C.W., Taylor, R.L. and Teare, J.D. "Vibrational relaxation of CO in nonequilibrium nozzle flows", J. Chem. Phys. 48, 5731 (1968)

78. Bray, K.N.C. "Vibrational relaxation of anharmonic oscillator molecules : relaxation under isothermal conditions", J. Phys. B. (Proc. Phys. Soc.), Ser. 2, Vol. 1, 705 (1968)

79. Phinney, R. "Criterion for vibrational freezing in a nozzle expansion", AIAA J 1, 496 (1963)

80. Taylor, R.L., Camac, M. and Feinberg, R.M. "Measurements of vibration - vibration coupling in gas mixtures", 11th Symp. on Combustion, p. 49 (1966)

81. Herzberg, G. "Molecular Spectra and Molecular Structure", Vol. II, Ch. 2, Van Nostrand (1966)

82. Moore, C.B. "Vibration-rotation energy transfer", J. Chem. Phys. 43, 2979 (1965)

83. Stevens, B. "Collisional Activation in Gases", Pergamon Press (1967)

84. Svehla, R.A. "Estimated viscosities and thermal conductivities of gases at high temperatures", NASA TR R-132 (1962)

85. Dawe, R.A. and Smith, E.B. "Viscosities of the inert gases at high temperatures", J. Chem. Phys. 52, 693 (1970)

86. Guevara, F.A., McInteer, B. and Wageman, W. "High temperature viscosity ratios for hydrogen, helium, argon and nitrogen", Phys. of Fluids 12, 2493 (1969)

87. Burch, L.G. "High temperature viscosities of polar gas mixtures : ammonia and methylamine", Ph.D. Thesis St. Louis University. U.M. 68-14061 (1968)

88. Ulybin, S.A. "Temperature dependence of the viscosity of rarefied gas mixtures", High Temperature 2, 526 (1964)

89. Smith, F.J. "Calculations of higher order collision integrals for use in the determination of transport coefficients of high temperature gases", NASA CR-103703 (1969)

90. Halbach, C.R. Appendix to Volume II, "Resistojet control system analysis; definition of a resistojet control system for MORL", NASA CR-66601 (1968)

91. Tang, S.S.-pu "Discharge coefficients for critical flow nozzles and their dependence on Reynolds numbers", Ph.D. Thesis, Princeton University, U.M. 70-8394 (1969)

92. Yevseyev, G.A. "Experimental investigation of flow of rarefied gas", AN SSSR, Izvestiya, Mekhanika 3, 172 (1965). Translation in AF, FTD, MT-67-22. AD 662 502 (1967)

93. Donovan, J.A., Lord, W.T. and Sherwood, P.J. "Fabrication and preliminary testing of a 3kw hydrogen resistojet", AIAA Paper No. 72-449 (1972)

Appendix A Discussion of Mathematical Techniques Used in Solving the Similar Boundary Layer Equations

The similar boundary layer equations, such as eq. (3.67) or eqs. (3.77) and (3.78), constitute a non-linear two-point boundary value problem in which either one or two of the inner boundary conditions are unknown. The crux of the solution of these equations lies in determining the correct unknown boundary conditions. There are various ways of achieving this, of which two are mentioned here. The first method is termed quasilinearisation, and an account of the application of this approach to solving the Falkner-Skan equation has been given by Radbill[1]. In essence this method simply linearises the original differential equations, however it is pointed out by Nachtsheim and Swigert[2] that several difficulties can be experienced with quasilinearisation, of which the most significant is the fact that the solution can become badly determined. This, added to the complex formulation of the method makes quasilinearisation unattractive. An alternative, which was used here, is to treat the similar equations as an initial value problem[3]. In this method guess values are used for the unknown initial conditions and the ordinary differential equations are integrated until quantities such as velocity and shear stress become asymptotic at large η. Integration is carried out for several trial values of the unknown boundary conditions and the correct value is obtained by interpolation.

This method is also not without its difficulties. These can be illustrated by considering the Falkner-Skan equations (eq. 3.67). The first point concerns the initial guess value of $f''(o)$ which is the unknown boundary condition in the Falkner-Skan equation. If this initial guess is too large then the boundary layer profiles such as the velocity profile tend to infinity with large values of η; if it is too small then the velocity ratio will reach a maximum which is less than

unity and then decrease. Thus there is a restricted range of values about the required $f''(o)$ which can be used to obtain the correct initial condition. The second point is concerned with the method for which the acceptable guess values of $f''(o)$ are then interpolated. Smith and Clutter[4], in an examination of the laminar boundary layer equations, used a shooting technique in which the previous guess values of $f''(o)$ were fitted by linear, quadratic or cubic curves in the $f''(o) - f'(\infty)$ plane. These curves were then used to predict the value of $f''(o)$ which would produce $f'(\infty) = 1$. Integration was then carried for the new value of $f''(o)$ and the process was repeated until convergence was achieved. These techniques have been used in this study, but were found to be satisfactory only when the ordinary differential equations were not excessively non-linear, i.e. for small values of the pressure gradient parameter. A far more attractive technique is the Newton-Raphson iteration method (ref. 5, p. 447). This method was used here for the Class A and B similar equations, and is briefly described. A guess value of $f''(o)$ which was known to be less than the required value was used to start the calculation, and the similar equation was then integrated until a maximum in $f'(\eta)$ was reached; this value was assumed to be $f'(\infty)$. The guess value of $f''(o)$ was then perturbed and the process repeated. This formed the pre-requisite for use of the Newton-Raphson equation, which for the present problem can be written

$$f''(o)_{k+1} = f''(o)_k - (f'(\infty)_k - 1.)/(d(f'(\infty)_k - 1.)/df''(o)_k)$$

where $k = 2$ for the first application of this equation. The whole integration and the Newton-Raphson process were repeated until

$$(1 - f'(\infty)_k) \leq 10^{-5}$$

and $$f''(\infty)_k \leq 10^{-5}$$

Four or five applications of the Newton-Raphson process were required

in most cases for the Class A and B equations. It was observed that when these equations were extremely non-linear (i.e. at large β), if a value of $f'(\infty)$ which was larger than unity was used in the iteration process, convergence was corrupted. To overcome this all values of $f''(o)$ for which $f'(\infty)$ was larger than unity were ignored, so that the Newton-Raphson method was used as an extrapolation procedure.

In the cases where there are two unknown boundary conditions, as in the Class C and D similar equations, a two variable Newton-Raphson procedure was used (see Ref. 5, p. 450). This method was not so successful as its one variable counterpart, and then was only relatively satisfactory for values of pressure gradient less than unity. At higher values of β convergence was very slow. The difficulty lay in the fact that the perturbation required to achieve convergence in one variable had a detrimental effect on the convergence of the other variable, so that the Newton-Raphson procedure was trying to work in opposite directions. The process converges, but does so at a decreasing rate as the correct outer boundary conditions are approached.

Actual integration of the similar equations was carried out using a fourth-order Runge-Kutta procedure (see Ref. 5, p.236). To use the Runge-Kutta method the original ordinary differential equation(s) must be reduced to a series of first-order equations. In the case of the Falkner-Skan equation four first-order equations are required, and for the Class D equations (eqs. 3.77 and 3.78) seven equations are necessary. At low values of β (less than two) the step size used was $\Delta\eta = 0.01$. Thus in solving the Falkner-Skan equation for $\beta = 0$ about 600 steps were required in going from $\eta = 0$ to $\eta = \eta_\infty$. At higher pressure gradients the step size was reduced and in general for β greater than five, $\Delta\eta = 0.001$ was used. This resulted in about 2500 steps across the boundary layer. The use of such small step sizes almost certainly accounts for the present successful integration of the

Falkner-Skan equations for β greater than two.

It is recommended procedure in the use of Runge-Kutta integration techniques to vary the step size until consistency in the results is obtained. Although thorough checks on the accuracy of the similar solutions have not been carried out, examination of the following table of solutions of the Falkner-Skan equations shows that the values of f"(o) which have been obtained should be consistent to at least six decimal places.

β	$\Delta\eta$	η_∞	f"(o)
0.	0.1	5.8	0.469 601 372
0.	0.01	5.78	0.469 601 457
0.	0.001	5.779	0.469 601 465
10.	0.01	2.46	3.675 234 01
10.	0.001	2.447	3.675 234 06

References of Appendix A

1. Radbill, J.R., AIAAJ 2, 1860 (1964)

2. Nachtsheim, P.R. and Swigert, P., NASA TN D-3004 (1965)

3. Fox, L., "Numerical Solution of Ordinary and Partial Differential Equations", Pergamon Press, (1962)

4. Smith, A.M.O., and Clutter, D.W., AIAAJ 1, 2062 (1963).

5. Hildebrand, F.B., "An Introduction to Numerical Analysis", McGraw-Hill (1956)

Appendix B Literature Survey of Relevant Vibrational Rate Data

A survey of vibrational rate data for gases used as resistojet propellants is necessary in order to obtain the empirical constants A and B of the Landau-Teller equation,

$$p\tau_v = A \exp(B/T)^{1/3} \tag{4.29}$$

required in the sudden freezing model. It should be noted that all the data presented here are obtained from shock wave experiments, therefore they are measurements of excitation rates. Of the molecules considered, N_2 and CO_2, have been extensively examined and only mean experimental lines are presented. For H_2 and CH_4, although not so widely studied, there is sufficient data in the literature to enable determination of the Landau-Teller constants with some degree of confidence. However, the available data for NH_3 is scarce, even contradictory, with recent experiments [19] indicating an unusual temperature dependence.*

Considerable experimental information is available on the rates for exchange of energy between translational and vibrational (T-V) mode of diatomic molecules, (see, for instance, Ref. 2) including N_2 which is of interest here, since along with H_2 it is a product of NH_3 dissociation. In Fig. B1, a plot of $\log_{10}(p\tau_v)$ against $T^{-1/3}$ for various single gases, two lines are presented for N_2 which are least squares fits of the experimental data of Refs. 1 and 2. Agreement between the two lines is good, and in a later survey of vibrational relaxation processes, Taylor and Bitterman[3] confirm the mean line suggested by Millikan and White[2]. This line is used to obtain the Landau-Teller constants for N_2. The other diatomic molecule of interest, H_2, has not been examined thoroughly, however the rate data that exists [4-7] does indicate a linear dependence of $\log_{10}(p\tau_v)$ with $T^{-1/3}$. The least squares line of Kiefer and Lutz[4], obtained over the temperature range 1100 to 2700°K, when extrapolated to

* A list of references used in this Appendix can be found on page 196.

lower temperatures in Fig. B1, agrees extremely well with the measurement of de Martini and Decius[5] for $p\tau_v$ (H_2) = 1.06 x 10^{-3} atm.sec. at 300°K. AT 1400°K White[6] notes that $p\tau_v$ (H_2) is less than 2.μsec.atm., a rate slightly faster than the measurements of Ref. 4. A further measurement by Gaydon and Hurle[7] confirms the general behaviour of the mean of Kiefer and Lutz, and this line is used in the present study.

For polyatomic molecules with two or more vibrational modes, vibration-vibration (V-V) energy exchange becomes important. Taylor and Bitterman [3] note that in general V-V rates are faster than the corresponding T-V process and that the rate controlling process for vibrational energy exchange in polyatomic molecules is a T-V exchange with one specific mode, and all the other modes are equilibrated by rapid inter-and/or intramolecular vibrational exchange. The mechanisms of vibrational excitation and de-excitation are clearly dependent on the V-V processes, however in application to a sudden freezing model only the rate-limiting step of energy transfer from vibration to translation is of interest. It is stressed that in the Landau-Teller theory the transition probabilities, and therefore rates, of energy exchange from V-T and T-V are identical.

Of the polyatomic molecules, carbon dioxide has been widely studied; see Ref. 3. The least squares line of Carnavale et al[8], presented in Fig. B1, agrees closely with the mean of Taylor and Bitterman's extensive survey, and is the relation adopted here. The data for CH_4 [9-13], once again, approximates to a straight line on a Landau-Teller plot. At 300°K, there is good agreement between the values given in Refs. 9, 10 and 13 for $p\tau_v(CH_4)$ of 1.9, 1.6 and 1.86 sec.atm., respectively. Eucken and Aybar[11], Richards and Sigafos[12], and Hill and Winter[13] present relaxation data of CH_4 for temperatures up to 1400°K and a sensible straight line can be drawn through the data.

Few references on vibrational relaxation of NH_3 are to be found in the literature, but such data as there is indicates very fast relaxation

with $p\tau_v < 10^{-6}$ atm.sec. at room temperature. Early measurements[14-16] were at temperatures below 400°K, with Buschmann and Schafer[15] reporting two separate relaxation times. Cottrell and McCoubrey[22] in reviewing the early work expressed some doubt over the double relaxation of Ref. 15, but these results together with two later measurements[17,18] at room temperature were, until very recently, the only data available. The measurements of Strauch and Decius[18], and Jones et al[17] at 300°K indicate extremely fast vibrational relaxation with values of $p\tau_v$ equal to 6. x 10^{-9} and 4.4 x 10^{-10} atm.sec. respectively. On the basis of these eight points, with a spread of over three decades at 300°K, a "mean" line was drawn. As found with other gases an increase in rate is predicted with elevated temperature, so much so that by 1000°K, $p\tau_v(NH_3) = 10^{-10}$ atm.sec. It was realised that extrapolation of such skant information to high temperatures must be regarded with extreme caution. The recently reported (April 1972) measurements of Bass and Winter[19] confirm this caution. Using an ultrasonic absorption technique, over the range 300 to 770°K, the inferred relaxation times increase slowly with temperature, contrary to all other findings. Relaxation times are still extremely fast with $p\tau_v < 10^{-8}$ atm.sec., but the situation regarding temperature dependence is far from resolved. At temperatures above 770°K Winter[20] notes that dissociation of NH_3 occurs, and, although composition measurements were not taken, a vibrational relaxation time of 3.5 x 10^{-9} sec. is indicated at 953°K.

The constants used in the Landau-Teller equation based on the mean lines derived in Fig. B1 (replotted in Fig. B2) are :-

	A (atm.sec.)	B($^{\circ}K^{1/3}$)
N_2	1.16 x 10^{-11}	225.4
H_2	3.9 x 10^{-10}	100.
CO_2	3.94 x 10^{-8}	32.8
CH_4	2.93 x 10^{-9}	43.3
NH_3	2.46 x 10^{-17}	152.6

In order to examine the effect on nozzle performance of the ammonia relaxation behaviour found in Ref. 19, a modified Landau-Teller equation of the form $p\tau_v = 1.78 \times 10^{-7} \exp(-28.85/T)^{1/3}$ is also used.

Included in Fig. B2 are some vibrational relaxation data for mixtures which may assist in the approximate modelling of the relaxation in NH_3-H_2-N_2 mixtures. It is pointed out[14] that vibration-rotation energy exchange becomes important in hydride-like molecules, such as CH_4 and NH_3. Therefore the measurements of Yardley, Fertig and Moore[9] with CH_4-N_2 and CH_4-H_2 mixtures are relevant. At room temperature with $X(CH_4)$ varying from 0.0225 to 0.1044 in a nitrogen diluent, vibrational relaxation times are fast, and of the same magnitude as τ_v in pure CH_4. The relaxation time for a mixture of 0.9335 CH_4 + 0.665 H_2 is faster than in CH_4 alone, with $p\tau_v$ (CH_4-H_2) = 9. x 10^{-7} atm.sec. White[21] reporting on measurements in a H_2-N_2 mixture with $X(H_2)$ = 0.02, over the temperature range 1700 to 2400°K, also finds that the mixture relaxes more quickly than either of the individual components. The data point of Winter[20] for a mixture of NH_3, N_2 and H_2 is also included in Fig. B2, and a faster relaxation, compared with the measurements for pure NH_3 of Ref. 19, is again apparent. In general, the policy throughout this work has been to underestimate rather than overestimate performance. By assuming that mixtures such as CH_4-H_2 and N_2-H_2 obey a "parallel resistance" law produces an underestimate of vibrational relaxation rates.

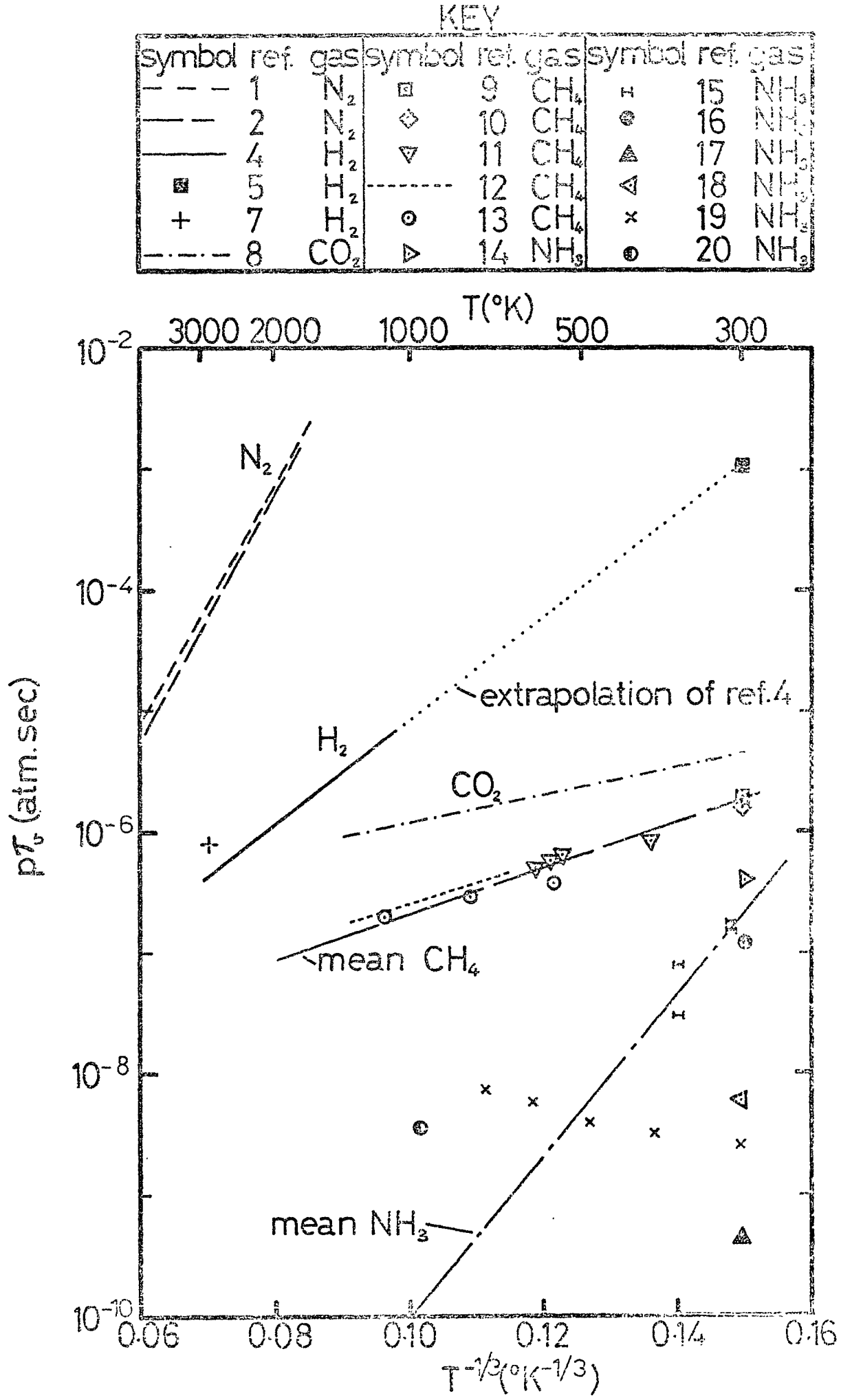

Fig.B1 Vibrational Rate Data for N_2, H_2, CO_2, CH_4, NH_3

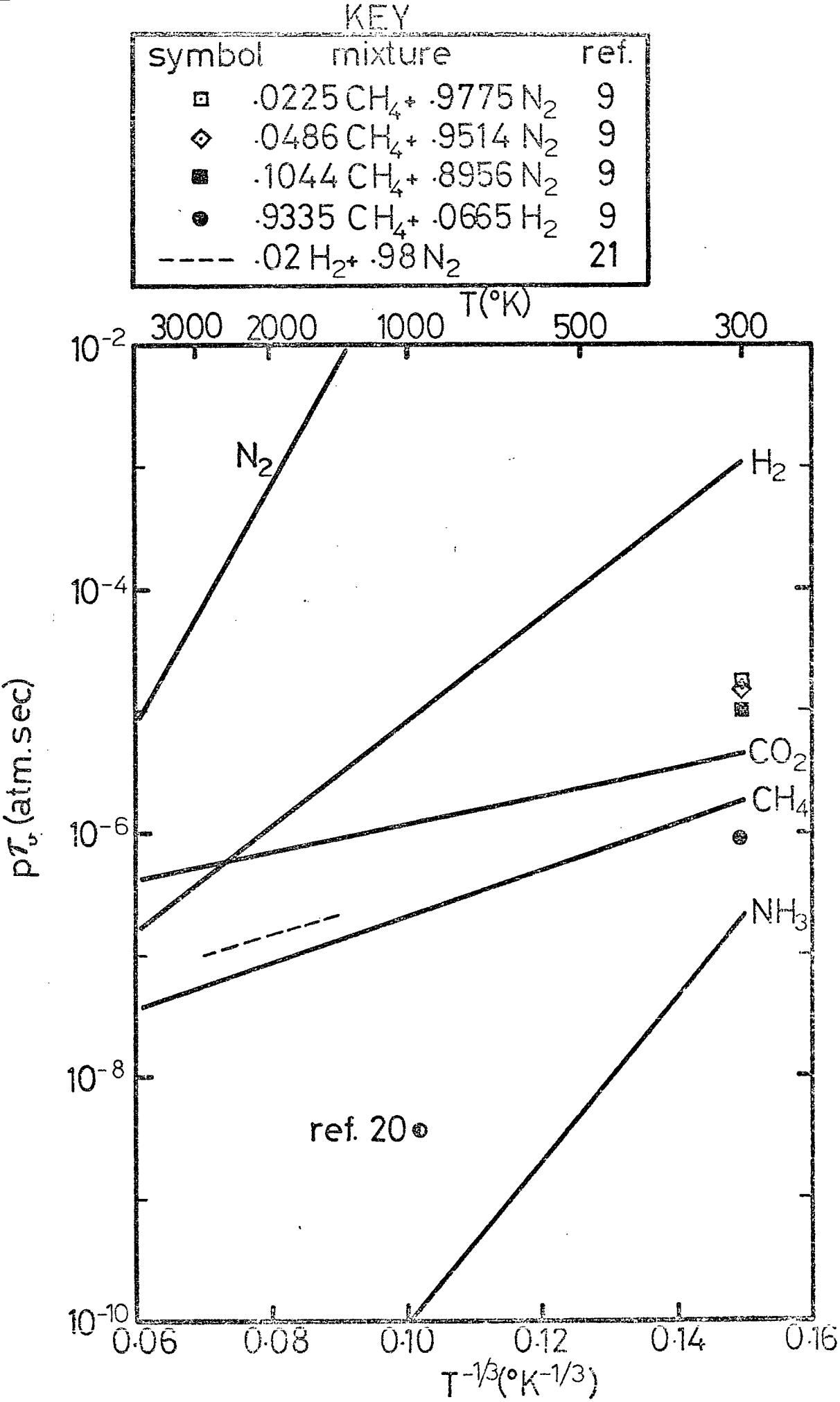

Fig.B2 Vibrational Rate Data for Mixtures

References of Appendix B

1. Hurle, I.R., J. Chem. Phys. 41, 3911 (1964)

2. Millikan, R.C. and White, D.R., J.Chem. Phys. 39, 3209 (1963)

3. Taylor, R.L. and Bitterman, S., Revs Modern Phys. 41, 26 (1969)

4. Kiefer, J.H. and Lutz, R.W., J. Chem. Phys. 44, 668 (1966)

5. de Martini, F. and Decius, J., J.Phys. Rev. Letters 17, 117 (1966)

6. White, D.R., J. Chem. Phys. 42, 447 (1965)

7. Gaydon, A.G. and Hurle, I.R., 8th Symp. on Combustion, p.309 (1962)

8. Camavale, E.H., Carey, C., and Larson, G., J. Chem. Phys. 47, 2829 (1967)

9. Yardley, J.T., Fertig, M.N. and Moore, C.B., J. Chem. Phys. 52, 1450 (1970)

10. Cottrell, T.L., MacFarlane, I.M., Read, A.W. and Young, A.H., Tr. Fara. Soc. 62, 2655 (1966)

11. Eucken, A and Aybar, S., Z. Phys. Chem. 46B, 195 (1940)

12. Richards, L.W. and Sigafos, D.H., J. Chem. Phys. 43, 492 (1965)

13. Hill, G.L. and Winter, T.G., J. Chem. Phys. 49, 440 (1968)

14. Griffith, W., J. Appl. Phys. 21, 1319 (1950)

15. Buschmann, K.F. and Schäfer, K., Z. Phys. Chem. 50B, 73 (1941)

16. Steil, O., Z. Phys. Chem. 31B, 343 (1936)

17. Jones, D.G., Lambert, J.D., Saksena, M.P. and Stretton, J.L., Tr. Fara. Soc. 65, 965 (1969)

18. Strauch, J.G. and Decius, J.C., J.Chem. Phys. 44, 3319 (1966)

19. Bass, H.E. and Winter, T.G., J.Chem. Phys. 56, 3619 (1972)

20. Winter, T.G., private communication.

21. White, D.R., J. Chem. Phys. 46, 2016 (1967)

22. Cottrell, T.L. and McCoubray, J.C., "Molecular Energy Transfer in Gases", Butterworths, London (1961)

Notation used in Tables

Tables One to Four

BETA	=	β
D2F(O)/DETA2	=	$f''(o)$
DG(O)/DETA	=	$g'(o)$
G(O)	=	$g(o)$
P1	=	P_1
P2	=	P_2
P3	=	P_3
P4	=	P_4
P5	=	P_5
TET/TE	=	$T_{e,T}/T_e$
THETA	=	Θ

Table Five

CPO	=	c_p^o

Table Six

CD	=	C_D
CT	=	C_T
DMDT	=	$\dot{m}_{CFV}$
ETAC	=	η_C
ETAD	=	η_D
ETAE	=	η_E
ETAF	=	η_F
ETAN	=	η_N
ETAV	=	η_V
F	=	F_{CFEVD}
ISP	=	$I_{spCFEVD}$
PEL	=	P_{el}
PT	=	p_T
REDST	=	Re_{D*}
TT	=	T_T

TABLE ONE CLASS A SIMILAR SOLUTIONS

BETA	D2F(0)/DETA2	P1	P2	P3
0.0	0.469601457	1.673187	0.467982	2.046813
0.1	0.587036209	1.502581	0.433848	2.007432
0.2	0.686706574	1.379174	0.406590	1.965941
0.4	0.854420103	1.206110	0.365042	1.888513
0.6	0.995835908	1.086674	0.334572	1.815769
0.8	1.120267200	0.997344	0.310201	1.748781
1.0	1.232587800	0.927084	0.290704	1.687151
1.5	1.477224100	0.800975	0.254555	1.555020
2.0	1.687218090	0.715251	0.229218	1.447560
3.0	2.043937050	0.602971	0.195221	1.283600
4.0	2.347285940	0.530644	0.172897	1.163883
5.0	2.615779440	0.479074	0.156803	1.071895
6.0	2.859213690	0.439916	0.144494	0.998547
8.0	3.292581350	0.383481	0.126632	0.887755
10.0	3.675234060	0.344054	0.114076	0.807050

TABLE TWO CLASS B SIMILAR SOLUTIONS

BETA	THETA	TET/TE	D2F(0)/DETA2	P1	P2	P3
0.	0.1	1.	0.440333646	1.619946	0.439109	1.741304
0.	0.1	4.	0.359850026	1.462587	0.359081	1.185625
0.	0.1	8.	NO SOLUTION			
0.	0.2	1.	0.409473251	1.564939	0.409473	1.437334
0.	0.2	4.	NO SOLUTION			
0.	0.2	8.	NO SOLUTION			
0.	0.3	1.	0.376607491	1.507817	0.376076	1.134154
0.	0.3	4.	NO SOLUTION			
0.	0.3	8.	NO SOLUTION			
0.	0.4	1.	NO SOLUTION			
0.	0.4	4.	NO SOLUTION			
0.	0.4	8.	NO SOLUTION			
1.	0.1	1.	1.204959550	0.909440	0.281542	1.536983
1.	0.1	4.	1.134139990	0.862154	0.258743	1.303870
1.	0.1	8.	1.031053960	0.793792	0.225068	0.965820
1.	0.2	1.	1.176692980	0.891409	0.272109	1.384213
1.	0.2	4.	1.024965120	0.790700	0.222599	0.885624
1.	0.2	8.	NO SOLUTION			
1.	0.3	1.	1.147708490	0.872937	0.262368	1.228726
1.	0.3	4.	NO SOLUTION			
1.	0.3	8.	NO SOLUTION			
1.	0.4	1.	1.117907430	0.853968	0.252269	1.070905
1.	0.4	4.	NO SOLUTION			
1.	0.4	8.	NO SOLUTION			

TABLE TWO (CONTINUED 1) CLASS B SIMILAR SOLUTIONS

BETA	THBTA	TET/TE	D2F(0)/DETA2	P1	P2	P3
2.	0.1	1.	1.659797410	0.704768	0.223789	1.348210
2.	0.1	4.	1.590224080	0.677076	0.210481	1.198350
2.	0.1	8.	1.491834800	0.638014	0.191453	0.985831
2.	0.2	1.	1.631909700	0.694113	0.218240	1.247055
2.	0.2	4.	1.486195920	0.636248	0.190082	0.931059
2.	0.2	8.	1.253770550	0.553822	0.143335	0.414807
2.	0.3	1.	1.603510320	0.683266	0.212556	1.143803
2.	0.3	4.	1.371627670	0.591468	0.167077	0.634919
2.	0.3	8.	NO SOLUTION			
2.	0.4	1.	1.574545550	0.672204	0.206720	1.038128
2.	0.4	4.	NO SOLUTION			
2.	0.4	8.	NO SOLUTION			
3.	0.1	1.	2.016615710	0.595529	0.191371	1.209846
3.	0.1	4.	1.947611560	0.575976	0.181989	1.099530
3.	0.1	8.	1.851221120	0.548701	0.168764	0.944892
3.	0.2	1.	1.988911850	0.587985	0.187451	1.134781
3.	0.2	4.	1.845785780	0.547482	0.167828	0.904204
3.	0.2	8.	1.629331200	0.486509	0.137295	0.547599
3.	0.3	1.	1.960794940	0.580331	0.183454	1.058226
3.	0.3	4.	1.736454530	0.516953	0.152354	0.692178
3.	0.3	8.	NO SOLUTION			
3.	0.4	1.	1.932229400	0.572557	0.179371	0.979985
3.	0.4	4.	NO SOLUTION			
3.	0.4	8.	NO SOLUTION			

TABLE TWO (CONTINUED 2) CLASS B SIMILAR SOLUTIONS

BETA	THETA	TET/TE	D2F(0)/DETA2	P1	P2	P3
4.	0.1	1.	2.320024010	0.524878	0.169917	1.105303
4.	0.1	4.	2.251358310	0.509773	0.162676	1.018130
4.	0.1	8.	2.156117450	0.488847	0.152556	0.896776
4.	0.2	1.	2.292431320	0.519045	0.166890	1.045853
4.	0.2	4.	2.150799240	0.487920	0.151849	0.864655
4.	0.2	8.	1.941930010	0.442150	0.129165	0.592453
4.	0.3	1.	2.264484980	0.513137	0.163811	0.985241
4.	0.3	4.	2.044240160	0.464793	0.140211	0.700283
4.	0.3	8.	NO SOLUTION			
4.	0.4	1.	2.236158690	0.507151	0.160676	0.923415
4.	0.4	4.	1.929294570	0.439891	0.127389	0.518457
4.	0.4	8.	NO SOLUTION			
5.	0.1	1.	2.588557350	0.474370	0.154373	1.023424
5.	0.1	4.	2.520120640	0.462071	0.148481	0.951386
5.	0.1	8.	2.425642560	0.445103	0.140291	0.851575
5.	0.2	1.	2.561040130	0.469616	0.151908	0.974220
5.	0.2	4.	2.420401210	0.444357	0.139723	0.825078
5.	0.2	8.	2.216102710	0.407737	0.121686	0.605109
5.	0.3	1.	2.533209550	0.464808	0.149406	0.924143
5.	0.3	4.	2.315594980	0.425759	0.130407	0.691111
5.	0.3	8.	1.969441800	0.372745	0.098748	0.308181
5.	0.4	1.	2.505044970	0.459945	0.146865	0.873202
5.	0.4	4.	2.204056750	0.405992	0.120323	0.545530
5.	0.4	8.	NO SOLUTION			

TABLE TWO (CONTINUED 3) CLASS B SIMILAR SOLUTIONS

BETA	THETA	TET/TE	D2F(0)/DETA2	P1	P2	P3
6.	0.1	1.	2.832020320	0.435943	0.142442	0.957205
6.	0.1	4.	2.763751090	0.425571	0.137476	0.895808
6.	0.1	8.	2.669823650	0.411309	0.130601	0.811113
6.	0.2	1.	2.804558210	0.431931	0.140364	0.915254
6.	0.2	4.	2.664637040	0.410685	0.130128	0.788619
6.	0.2	8.	2.463447640	0.380181	0.115166	0.604151
6.	0.3	1.	2.776812210	0.427879	0.138258	0.872627
6.	0.3	4.	2.561056360	0.395140	0.122366	0.675607
6.	0.3	8.	2.227879170	0.344761	0.096900	0.356322
6.	0.4	1.	2.748765430	0.423785	0.136122	0.829352
6.	0.4	4.	2.451774530	0.378758	0.114060	0.554392
6.	0.4	8.	NO SOLUTION			
8.	0.1	1.	3.265426930	0.380451	0.125068	0.855845
8.	0.1	4.	3.197389830	0.372557	0.121292	0.808491
8.	0.1	8.	3.104216400	0.361751	0.116092	0.743554
8.	0.2	1.	3.238040780	0.377395	0.123487	0.823452
8.	0.2	4.	3.099103350	0.361282	0.115738	0.726302
8.	0.2	8.	2.901946710	0.338349	0.104550	0.583251
8.	0.3	1.	3.210411630	0.374314	0.121888	0.790710
8.	0.3	4.	2.997150050	0.349590	0.109925	0.640325
8.	0.3	8.	2.678485940	0.312725	0.091555	0.408441
8.	0.4	1.	3.182527140	0.371205	0.120269	0.757407
8.	0.4	4.	2.890725290	0.337397	0.103791	0.549563
8.	0.4	8.	NO SOLUTION			

TABLE TWO (CONCLUDED) CLASS B SIMILALAR SOLUTIONS

BETA	THETA	TET/TE	D2F(0)/DETA2	P1	P2	P3
10.	0.1	1.	3.648105120	0.341606	0.112813	0.781052
10.	0.1	4.	3.580224070	0.335235	0.109767	0.742560
10.	0.1	8.	3.487557930	0.326486	0.105562	0.687466
10.	0.2	1.	3.620769570	0.339139	0.111537	0.754751
10.	0.2	4.	3.482486680	0.326167	0.105307	0.676161
10.	0.2	8.	3.287883700	0.307919	0.096435	0.564014
10.	0.3	1.	3.593218520	0.336653	0.110249	0.728123
10.	0.3	4.	3.381584680	0.316804	0.100665	0.606708
10.	0.3	8.	3.071139020	0.287729	0.086290	0.424228
10.	0.4	1.	3.565442270	0.334148	0.108946	0.701146
10.	0.4	4.	3.276930630	0.307100	0.095807	0.536112
10.	0.4	8.	NO SOLUTION			

TABLE THREE CLASS C SIMILAR SOLUTIONS

BETA	D2F(0)/DETA2	DG(0)/DETA	CONVERGENCE
0.0	0.469602	=0.093920	0.00001
0.5	0.991100	=0.109190	0.00020
1.0	1.338000	=0.116200	0.00100
2.0	1.854800	=0.123500	0.00200
3.0	2.260800	=0.128600	0.01000

TABLE FOUR CLASS D SIMILAR SOLUTIONS

BETA	D2F(0)/DETA2	G(0)	P1	P2	P3	P4	P5	CONVERGENCE
0.0	0.50540	0.8186	1.570670	0.502876	2.871860	1.551310	0.499298	0.00001
0.5	0.91462	0.7935	1.078670	0.371115	2.284200	1.056750	0.368768	0.00003
1.0	1.18484	0.7774	0.865623	0.311609	1.994050	0.847768	0.309620	0.00010
2.0	1.57600	0.7540	0.646024	0.253462	1.731920	0.639457	0.252067	0.00100

TABLE FIVE MOLAR HEAT CAPACITY, POLYNOMIAL COEFFICIENTS

CPO = SIGMA(A(I)*(T**I))

I	NH3	CH4	CO2	N2	H2(1)	H2(2)
0	0,849767E 01	0,686782E 01	0,786860E 01	0,650917E 01	0,470085E 01	0,258639E 01
1	-0,955406E-02	0,289340E-01	-0,251687E-01	0,644756E-02	0,307488E-01	0,412890E-01
2	0,457411E-04	-0,287314E-03	0,219303E-03	-0,355515E-04	-0,126364E-02	-0,163896E-03
3	-0,460087E-07	0,133884E-05	-0,672785E-06	0,960959E-07	0,238780E-04	0,361964E-06
4	-0,985514E-11	-0,318580E-08	0,117973E-08	-0,139870E-09	-0,229823E-06	-0,494235E-09
5	0,654969E-13	0,454925E-11	-0,130416E-11	0,124113E-12	0,132074E-08	0,439030E-12
6	-0,671761E-16	-0,413644E-14	0,937532E-15	-0,707495E-16	-0,483084E-11	-0,257720E-15
7	0,351814E-19	0,241745E-17	-0,437305E-18	0,261132E-19	0,113752E-13	0,990265E-19
8	-0,103954E-22	-0,880124E-21	0,127623E-21	-0,604330E-23	-0,167140E-16	-0,239231E-22
9	0,164688E-26	0,181759E-24	-0,211684E-25	0,797862E-27	0,139459E-19	0,329382E-26
10	-0,109104E-30	-0,162666E-28	0,152276E-29	-0,458731E-31	-0,504489E-23	-0,196994E-30

TEMPERATURE RANGE

NH3, CH4, CO2, N2 100 TO 3000 DEG,K
H2(1) 50 TO 500 DEG,K
H2(2) 500 TO 3000 DEG,K

TABLE SIX RESISTOJET PERFORMANCE PARAMETERS FOR NOMINAL NOZZLE GEOMETRY

TABLE SIX(A) HYDROGEN
UNDISSOCIATED, ETAC = 1.000

TT	PT	REDST	PEL	F	DMDT	ISP	CT	CD	ETAF	ETAE	ETAV	ETAD	ETAN
300.	200.	13830.	0.	0.2416	0.0943	261.2	1.538	0.976	1.000	0.881	0.969	0.964	0.825
300.	100.	6915.	0.	0.1190	0.0467	259.9	1.516	0.966	1.000	0.881	0.955	0.969	0.818
300.	50.	3457.	0.	0.0582	0.0230	258.0	1.483	0.952	1.000	0.881	0.937	0.973	0.806
300.	25.	1729.	0.	0.0282	0.0113	254.8	1.435	0.933	1.000	0.881	0.911	0.976	0.786
500.	200.	7591.	210.	0.2419	0.0724	340.5	1.540	0.968	1.000	0.881	0.957	0.968	0.805
500.	100.	3795.	103.	0.1184	0.0357	338.0	1.508	0.954	1.000	0.881	0.939	0.972	0.794
500.	50.	1898.	51.	0.0574	0.0175	334.1	1.462	0.936	1.000	0.881	0.915	0.976	0.775
500.	25.	949.	25.	0.0275	0.0853	328.4	1.399	0.911	1.000	0.881	0.882	0.978	0.749
1000.	200.	3271.	514.	0.2422	0.0502	492.3	1.542	0.951	1.000	0.881	0.934	0.973	0.805
1000.	100.	1636.	252.	0.1171	0.0246	486.1	1.491	0.932	1.000	0.881	0.908	0.932	0.785
1000.	50.	817.	122.	0.0558	0.0119	477.1	1.421	0.904	1.000	0.881	0.873	0.978	0.756
1000.	25.	409.	59.	0.0261	0.0057	465.5	1.331	0.869	1.000	0.881	0.831	0.978	0.720
1500.	200.	1993.	721.	0.2367	0.0401	601.6	1.507	0.938	0.996	0.881	0.916	0.976	0.784
1500.	100.	996.	351.	0.1132	0.0195	591.0	1.441	0.914	0.996	0.881	0.882	0.978	0.756
1500.	50.	498.	169.	0.0533	0.0094	577.5	1.358	0.881	0.996	0.881	0.841	0.979	0.722
2000.	200.	1402.	895.	0.2323	0.0341	695.1	1.479	0.928	0.990	0.880	0.896	0.977	0.762
2000.	100.	701.	433.	0.1101	0.0165	679.9	1.402	0.899	0.985	0.880	0.860	0.978	0.729
2000.	50.	350.	207.	0.0511	0.0079	660.4	1.302	0.859	0.982	0.881	0.811	0.981	0.688
2500.	200.	1062.	1048.	0.2290	0.0300	778.9	1.458	0.918	0.985	0.878	0.880	0.978	0.744
2500.	100.	531.	506.	0.1076	0.0145	758.0	1.370	0.886	0.978	0.879	0.838	0.978	0.705
3000.	200.	845.	1186.	0.2258	0.0269	855.0	1.438	0.909	0.987	0.876	0.862	0.978	0.728
3000.	100.	422.	570.	0.1054	0.0129	830.1	1.342	0.874	0.977	0.877	0.817	0.980	0.687

TABLE SIX(A) CONTINUED

EQUILIBRIUM COMPOSITION

TT	PT	REDST	PEL	F	DMDT	ISP	CT	CD	ETAC	ETAF	ETAE	ETAV	ETAD	ETAN
2000.	200.	1394.	998.	0.2322	0.0339	699.0	1.478	0.927	0.909	0.991	0.883	0.898	0.977	0.697
2000.	100.	695.	504.	0.1100	0.0164	685.3	1.400	0.898	0.876	0.988	0.884	0.861	0.978	0.644
2000.	50.	346.	255.	0.0510	0.0078	667.6	1.300	0.858	0.834	0.983	0.886	0.811	0.985	0.499
2500.	200.	1039.	1397.	0.2281	0.0293	794.5	1.452	0.916	0.768	0.994	0.887	0.882	0.978	0.584
2500.	100.	515.	741.	0.1071	0.0140	780.6	1.364	0.884	0.702	0.989	0.892	0.845	0.978	0.512
3000.	100.	393.	1061.	0.1038	0.0120	885.1	1.322	0.867	0.548	0.997	0.907	0.830	0.985	0.405

TABLE SIX(B) METHANE

ETAC = 1.000

TT	PT	REDST	PEL	F	DMDT	ISP	CT	CD	ETAF	ETAE	ETAV	ETAD	ETAN
300.	200.	30270.	0.	0.2598	0.2623	101.0	1.654	0.984	0.999	0.835	0.975	0.958	0.779
300.	100.	15140.	0.	0.1286	0.1303	100.7	1.634	0.978	0.999	0.835	0.965	0.962	0.774
300.	50.	7569.	0.	0.0633	0.0645	100.1	1.613	0.968	0.999	0.835	0.950	0.966	0.765
300.	25.	3784.	0.	0.0310	0.0318	99.2	1.578	0.956	0.999	0.835	0.929	0.971	0.752
500.	200.	15260.	100.	0.2569	0.1974	132.7	1.635	0.978	0.965	0.834	0.963	0.962	0.745
500.	100.	7628.	50.	0.1265	0.0978	131.9	1.611	0.969	0.965	0.834	0.947	0.966	0.736
500.	50.	3814.	24.	0.0619	0.0483	130.7	1.575	0.958	0.965	0.834	0.925	0.970	0.722
500.	25.	1907.	12.	0.0299	0.0237	128.8	1.524	0.939	0.965	0.834	0.885	0.974	0.702
1000.	200.	6433.	319.	0.2589	0.1341	196.8	1.648	0.968	0.836	0.823	0.933	0.966	0.620
1000.	100.	3217.	157.	0.1244	0.0661	191.2	1.584	0.954	0.806	0.828	0.909	0.971	0.589
1000.	50.	1608.	77.	0.0594	0.0324	186.7	1.512	0.936	0.775	0.832	0.887	0.974	0.557
1000.	25.	804.	38.	0.0280	0.0158	181.1	1.428	0.911	0.775	0.832	0.833	0.977	0.525
1500.	200.	3983.	524.	0.2640	0.1076	250.2	1.681	0.959	0.778	0.801	0.907	0.968	0.547
1500.	100.	1992.	258.	0.1254	0.0529	241.7	1.596	0.943	0.732	0.815	0.881	0.972	0.511
1500.	50.	996.	126.	0.0581	0.0258	229.7	1.481	0.920	0.688	0.825	0.833	0.976	0.461
1500.	25.	498.	61.	0.0269	0.0125	220.0	1.370	0.889	0.657	0.830	0.794	0.978	0.423
2000.	200.	2858.	710.	0.2645	0.0922	292.6	1.684	0.952	0.740	0.780	0.883	0.969	0.494
2000.	100.	1429.	348.	0.1248	0.0452	281.6	1.590	0.934	0.695	0.800	0.846	0.973	0.458
2000.	50.	714.	169.	0.0575	0.0220	267.2	1.465	0.907	0.647	0.816	0.799	0.976	0.412
2000.	25.	357.	81.	0.0261	0.0105	252.6	1.329	0.870	0.601	0.826	0.758	0.978	0.368

TABLE SIX(C) CARBON DIOXIDE

ETAC = 1.000

TT	PT	REDST	PEL	F	DMDT	ISP	CT	CD	ETAF	ETAE	ETAV	ETAD	ETAN
300.	200.	36880.	0.	0.2547	0.4339	59.9	1.621	0.986	0.973	0.880	0.980	0.958	0.804
300.	100.	18440.	0.	0.1263	0.2156	59.7	1.608	0.980	0.973	0.880	0.971	0.962	0.800
300.	50.	9220.	0.	0.0624	0.1069	59.5	1.588	0.971	0.973	0.880	0.959	0.967	0.794
300.	25.	4610.	0.	0.0306	0.0528	59.1	1.558	0.960	0.973	0.880	0.942	0.971	0.783
500.	200.	18110.	61.	0.2524	0.3281	78.4	1.607	0.980	0.898	0.879	0.970	0.962	0.737
500.	100.	9057.	30.	0.1246	0.1627	78.1	1.586	0.972	0.898	0.879	0.957	0.967	0.730
500.	50.	4528.	15.	0.0611	0.0804	77.5	1.556	0.960	0.898	0.879	0.938	0.971	0.719
500.	25.	2264.	7.	0.0297	0.0395	76.6	1.512	0.944	0.898	0.879	0.913	0.975	0.702
1000.	200.	7554.	171.	0.2505	0.2261	113.0	1.595	0.969	0.785	0.876	0.949	0.968	0.632
1000.	100.	3777.	85.	0.1213	0.1116	110.8	1.544	0.957	0.765	0.879	0.930	0.972	0.608
1000.	50.	1889.	41.	0.0587	0.5480	109.3	1.496	0.940	0.765	0.879	0.902	0.975	0.591
1000.	25.	944.	20.	0.0280	0.0267	107.1	1.428	0.916	0.765	0.879	0.864	0.978	0.568
1500.	200.	4662.	255.	0.2497	0.1822	139.8	1.590	0.961	0.737	0.873	0.931	0.970	0.582
1500.	100.	2331.	126.	0.1193	0.0896	135.8	1.520	0.946	0.707	0.877	0.909	0.974	0.549
1500.	50.	1165.	61.	0.0570	0.0438	132.6	1.451	0.925	0.697	0.878	0.875	0.977	0.524
1500.	25.	583.	30.	0.0269	0.0212	129.3	1.368	0.895	0.697	0.878	0.830	0.979	0.498
2000.	200.	3336.	325.	0.2493	0.1565	162.5	1.587	0.955	0.708	0.871	0.925	0.972	0.554
2000.	100.	1668.	159.	0.1178	0.0767	156.6	1.500	0.937	0.677	0.876	0.890	0.976	0.515
2000.	50.	834.	77.	0.0555	0.0373	151.6	1.413	0.911	0.658	0.878	0.854	0.978	0.483
2000.	25.	417.	37.	0.0260	0.0179	147.7	1.322	0.875	0.658	0.878	0.809	0.979	0.458

TABLE SIX(D) AMMONIA

UNDISSOCIATED, ETAC = 1.000

TT	PT	REDST	PEL	F	DMDT	ISP	CT	CD	ETAF	ETAE	ETAV	ETAD	ETAN
300.	200.	34500.	0.	0.2602	0.2704	98.1	1.656	0.985	0.997	0.835	0.977	0.957	0.778
300.	100.	17250.	0.	0.1289	0.1344	97.9	1.641	0.979	0.997	0.835	0.967	0.961	0.773
300.	50.	8626.	0.	0.0636	0.0666	97.3	1.619	0.970	0.997	0.835	0.953	0.966	0.766
300.	25.	4313.	0.	0.0311	0.0329	96.5	1.585	0.958	0.997	0.835	0.933	0.970	0.753
500.	200.	15280.	93.	0.2589	0.2049	128.9	1.648	0.978	0.988	0.832	0.963	0.962	0.761
500.	100.	7638.	46.	0.1274	0.1015	128.0	1.622	0.969	0.983	0.832	0.949	0.966	0.750
500.	50.	3819.	23.	0.0621	0.0501	126.5	1.583	0.956	0.980	0.833	0.926	0.970	0.733
500.	25.	1920.	11.	0.0300	0.0246	124.5	1.529	0.939	0.977	0.833	0.896	0.974	0.710
1000.	200.	5453.	267.	0.2619	0.1396	191.3	1.667	0.964	0.985	0.798	0.925	0.966	0.703
1000.	100.	2727.	131.	0.1271	0.0687	188.5	1.618	0.950	0.980	0.801	0.895	0.970	0.682
1000.	50.	1363.	64.	0.0608	0.0336	184.3	1.548	0.930	0.975	0.803	0.854	0.974	0.652
1000.	25.	682.	31.	0.0285	0.0250	178.3	1.454	0.902	0.968	0.806	0.800	0.977	0.610
1500.	200.	3137.	416.	0.2626	0.1116	239.9	1.672	0.954	1.000	0.740	0.896	0.966	0.641
1500.	100.	1569.	204.	0.1260	0.0547	234.8	1.604	0.935	1.000	0.740	0.854	0.971	0.614
1500.	50.	784.	99.	0.0593	0.0266	227.4	1.511	0.909	1.000	0.740	0.799	0.974	0.576
1500.	25.	392.	48.	0.0272	0.0128	217.3	1.387	0.874	1.000	0.740	0.728	0.976	0.526
2000.	200.	2170.	550.	0.2606	0.0953	278.7	1.659	0.945	1.000	0.697	0.871	0.968	0.587
2000.	100.	1085.	268.	0.1238	0.0466	271.1	1.576	0.923	1.000	0.697	0.820	0.972	0.556
2000.	50.	543.	130.	0.0575	0.0255	260.4	1.464	0.892	1.000	0.697	0.755	0.975	0.513
2000.	25.	271.	62.	0.0259	0.0107	250.0	1.318	0.851	1.000	0.697	0.672	0.977	0.457

TABLE SIX(D) CONTINUED

EQUILIBRIUM COMPOSITION

TT	PT	REDST	PEL	F	DMDT	ISP	CT	CD	ETAC	ETAF	ETAE	ETAV	ETAD	ETAN
300.	200.	31470.	0.	0.2601	0.2674	99.2	1.656	0.985	0.916	0.999	0.837	0.977	0.957	0.716
300.	100.	17020.	0.	0.1288	0.1323	99.3	1.640	0.979	0.886	0.999	0.838	0.967	0.961	0.689
300.	50.	8463.	0.	0.0634	0.0651	99.3	1.615	0.970	0.847	0.999	0.839	0.953	0.966	0.653
300.	25.	4199.	0.	0.0310	0.0319	99.3	1.581	0.958	0.799	1.000	0.841	0.933	0.970	0.608
500.	200.	14360.	410.	0.2530	0.1597	161.6	1.611	0.977	0.474	1.000	0.874	0.964	0.964	0.389
500.	100.	7108.	219.	0.1245	0.0771	164.6	1.585	0.967	0.452	1.000	0.877	0.955	0.969	0.370
500.	50.	3530.	112.	0.0608	0.0374	165.9	1.549	0.953	0.440	1.000	0.879	0.936	0.973	0.356
500.	25.	1758.	56.	0.0294	0.0181	165.4	1.499	0.934	0.433	1.000	0.880	0.911	0.976	0.342
1000.	200.	6061.	530.	0.2475	0.1043	242.0	1.576	0.964	0.602	1.000	0.881	0.951	0.970	0.491
1000.	100.	3030.	260.	0.1208	0.0513	240.0	1.538	0.950	0.602	1.000	0.881	0.931	0.974	0.482
1000.	50.	1515.	126.	0.0583	0.2510	236.5	1.484	0.929	0.602	1.000	0.881	0.904	0.977	0.469
1000.	25.	758.	61.	0.0277	0.0122	232.2	1.413	0.901	0.602	1.000	0.881	0.868	0.978	0.452
1500.	200.	3710.	582.	0.2432	0.0837	296.4	1.548	0.955	0.700	0.989	0.881	0.937	0.973	0.555
1500.	100.	1855.	284.	0.1178	0.0410	292.3	1.500	0.936	0.700	0.989	0.881	0.911	0.976	0.542
1500.	50.	927.	137.	0.0563	0.0199	288.0	1.433	0.910	0.700	0.989	0.881	0.878	0.978	0.524
1500.	25.	464.	66.	0.0264	0.0096	280.8	1.347	0.876	0.700	0.989	0.881	0.835	0.979	0.498
2000.	200.	2624.	638.	0.2400	0.0714	342.8	1.528	0.947	0.762	0.976	0.880	0.923	0.974	0.588
2000.	100.	1312.	311.	0.1155	0.0349	337.5	1.470	0.925	0.762	0.976	0.880	0.893	0.977	0.571
2000.	50.	656.	150.	0.0548	0.0169	331.0	1.395	0.896	0.762	0.979	0.880	0.854	0.979	0.549
2000.	25.	328.	71.	0.0254	0.0081	321.1	1.294	0.856	0.762	0.979	0.880	0.803	0.981	0.517

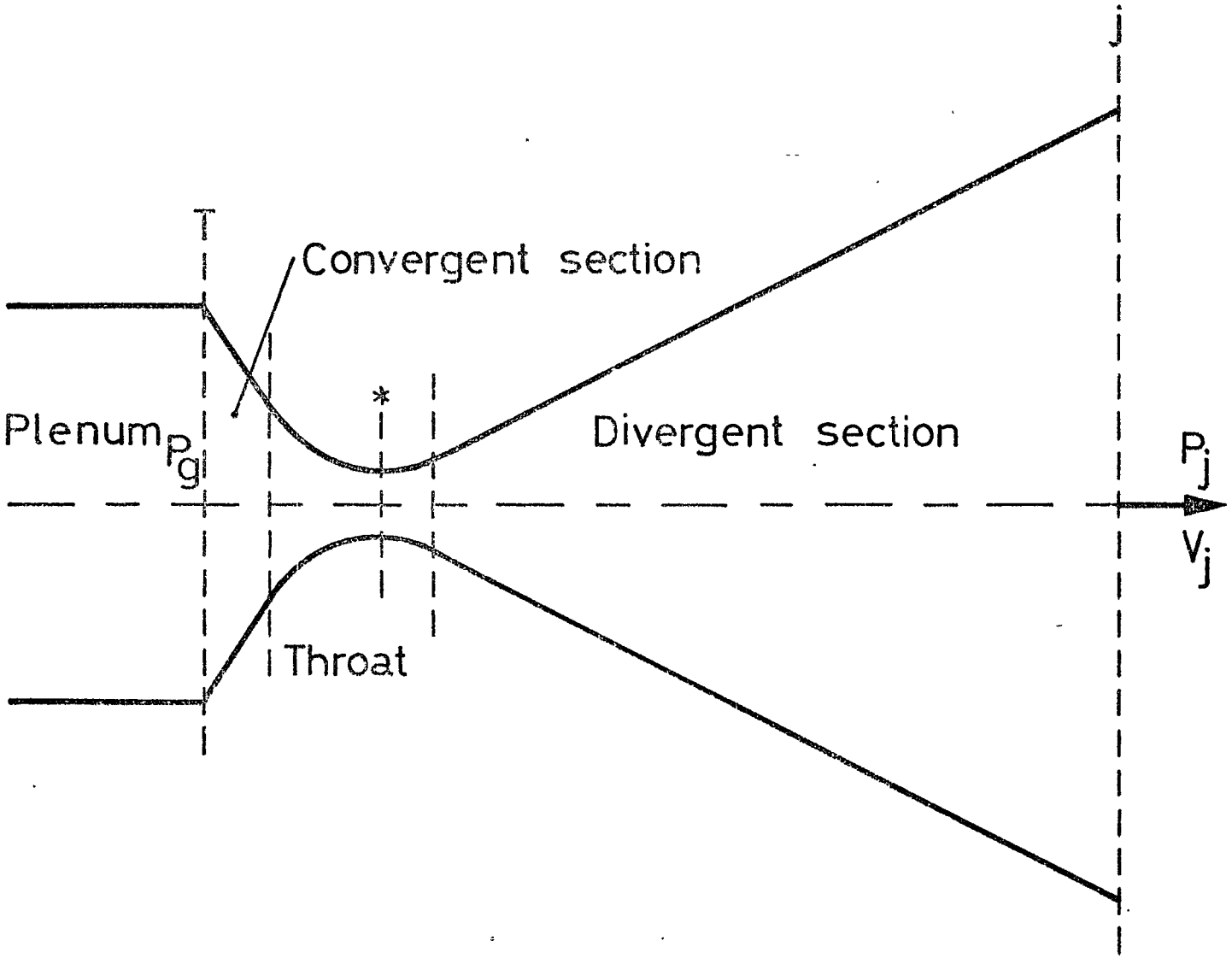

Fig.1 Nozzle Configuration

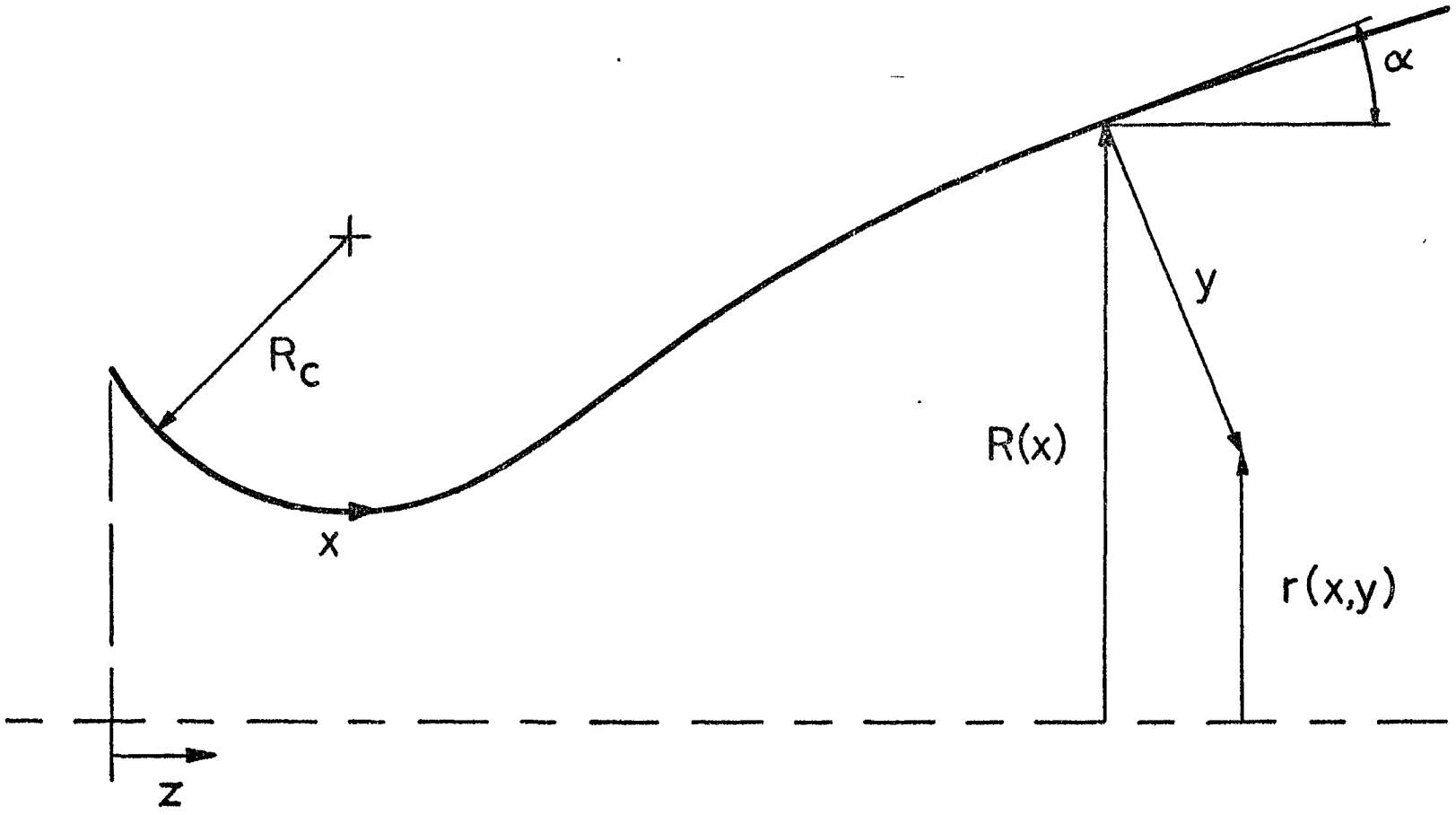

Fig.2 Coordinate System

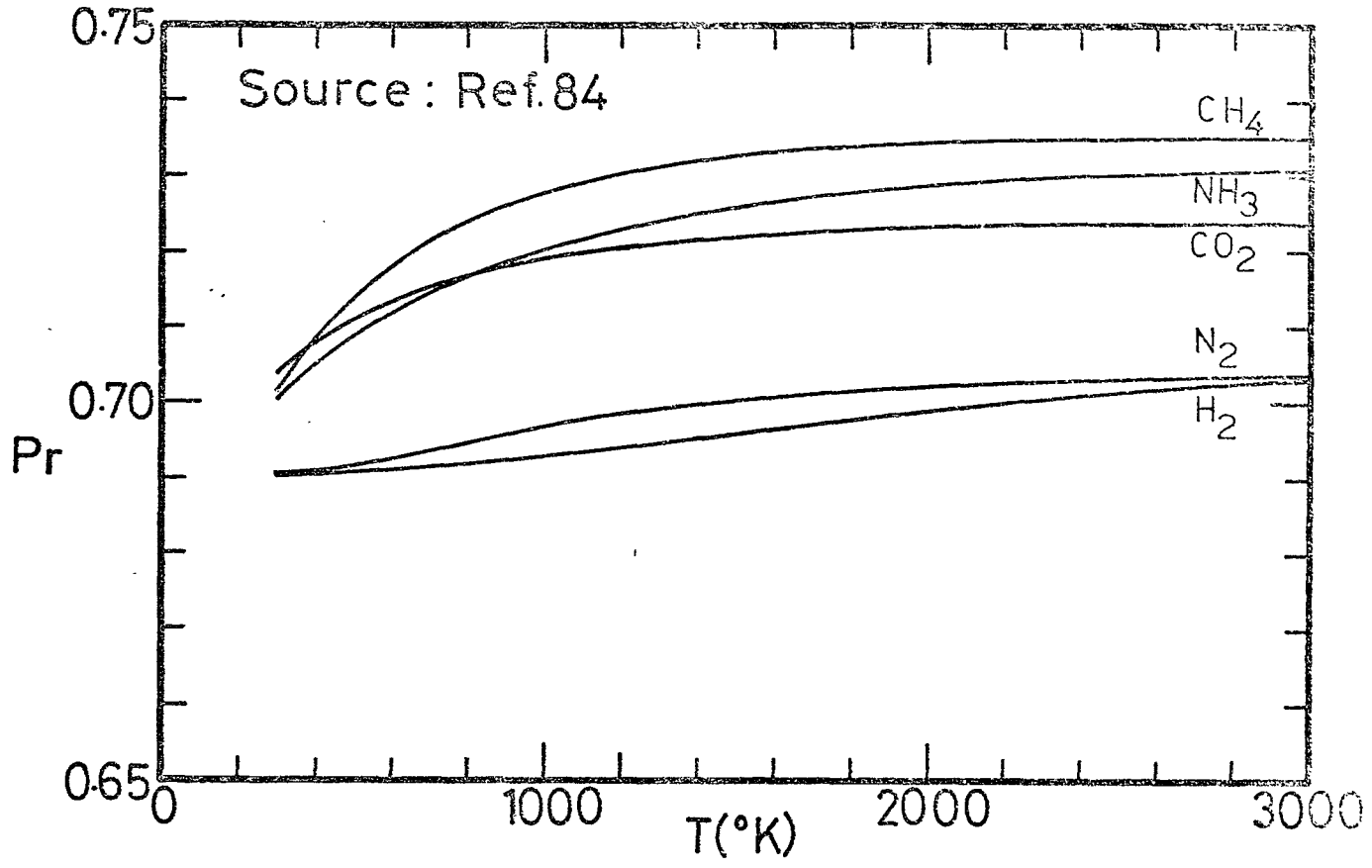

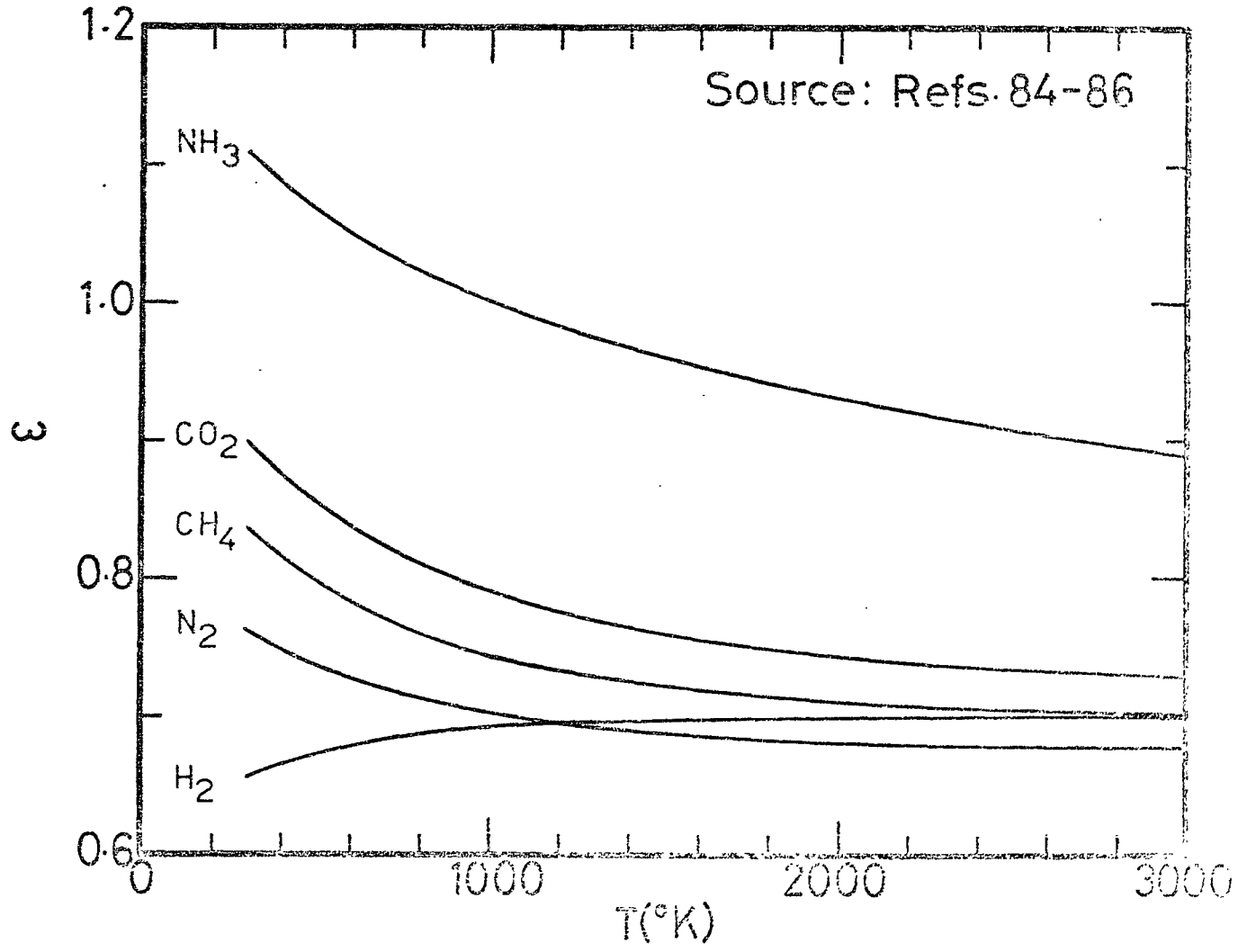

Fig.3 Variation of Prandtl Number & Viscosity Exponent

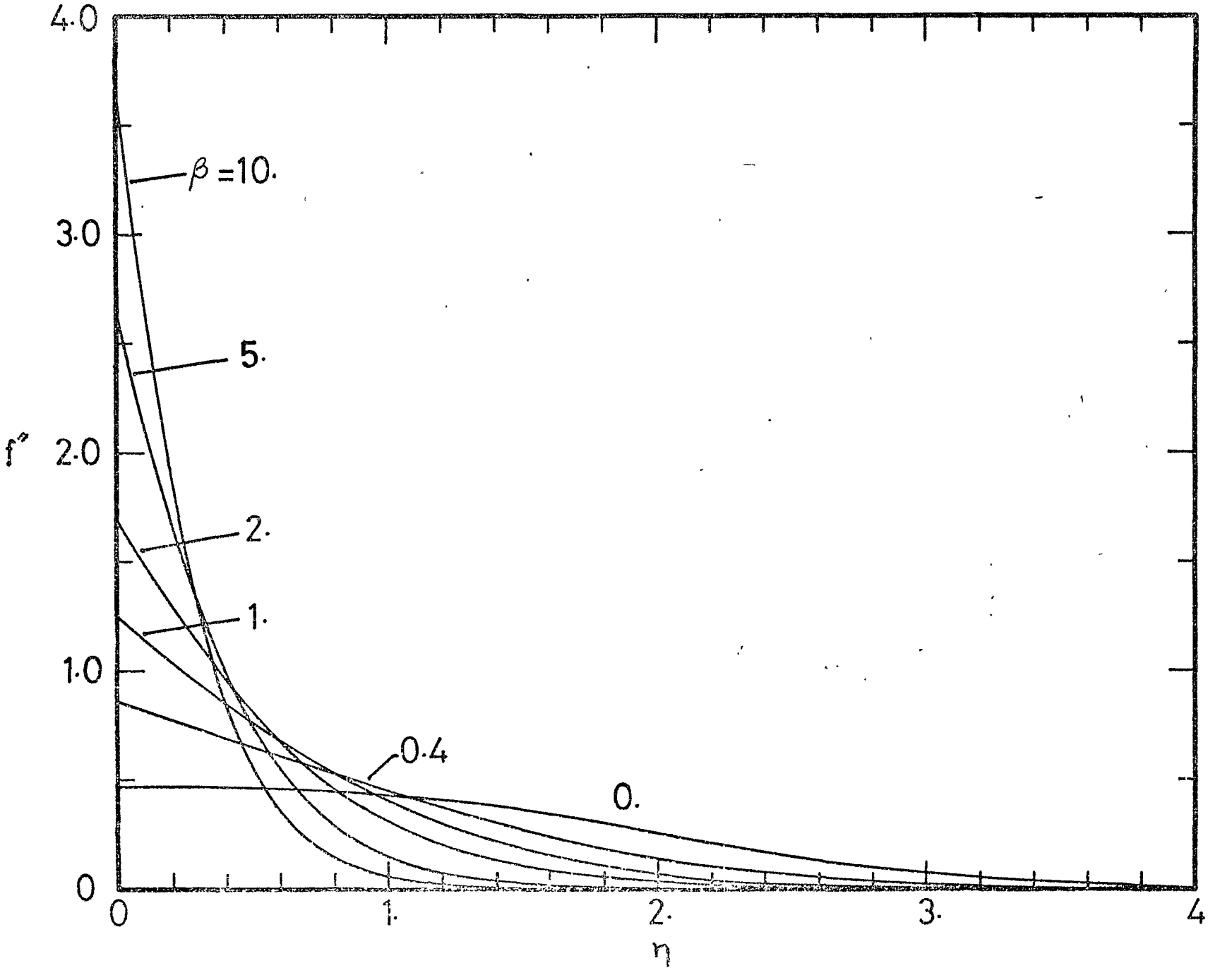

Fig.4 Shear Stress Profiles for Class A Similar Solutions

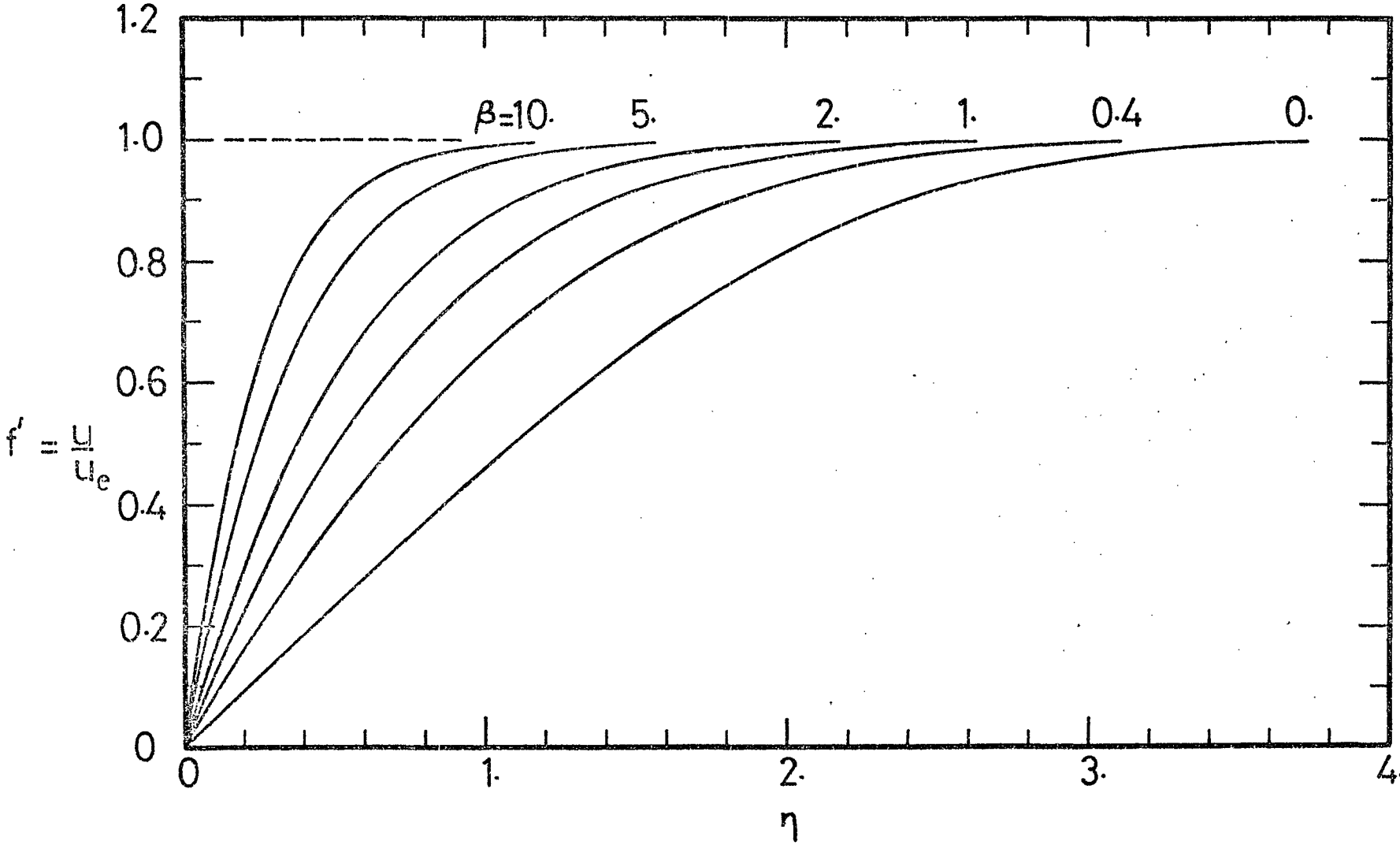

Fig·5 Velocity Profiles for Class A Similar Solutions

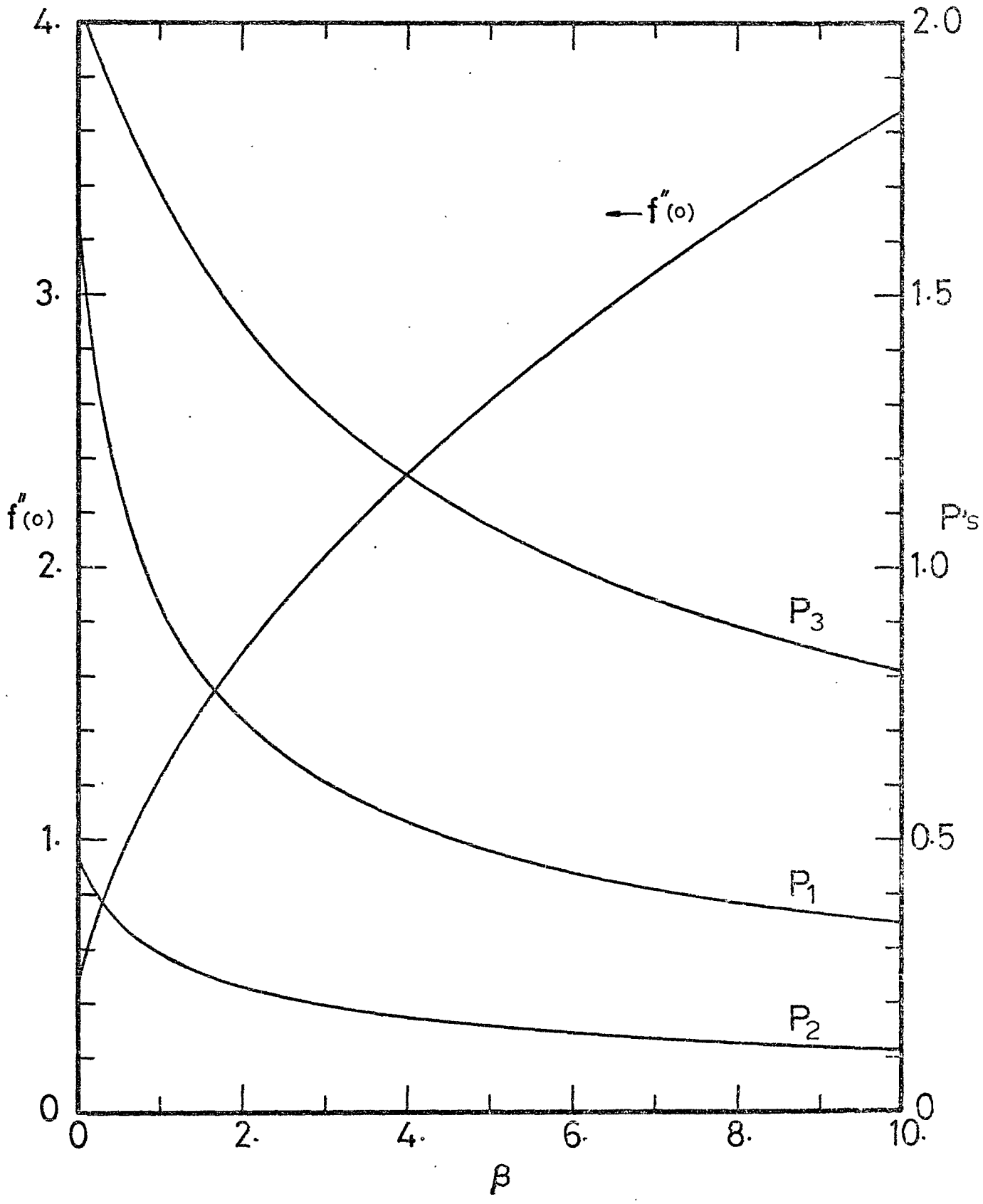

Fig.6 Variation of Dimensionless Wall Shear Stress & Boundary Layer Integrals (Class A)

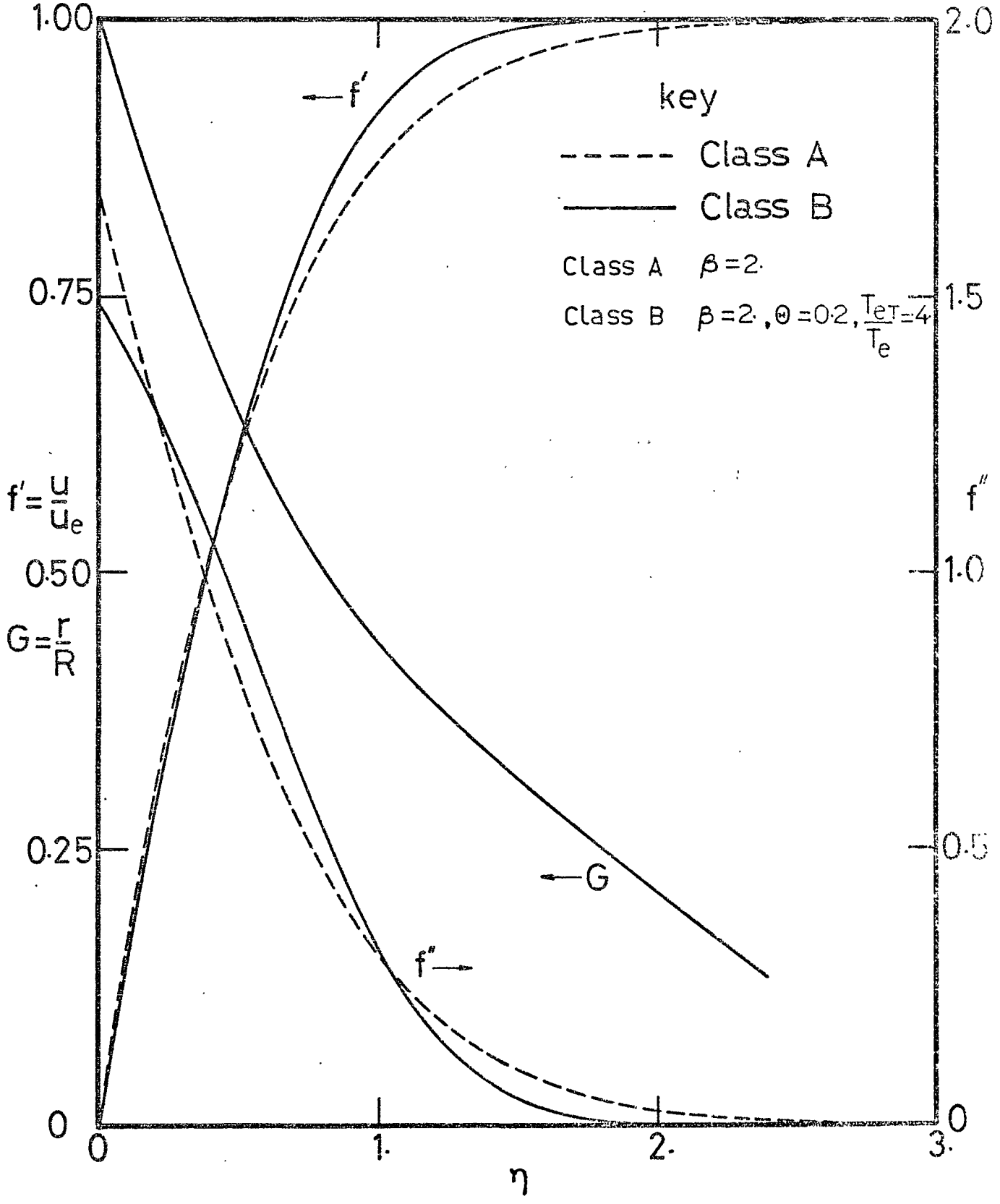

Fig·7 A Comparison of Class A & B Profiles

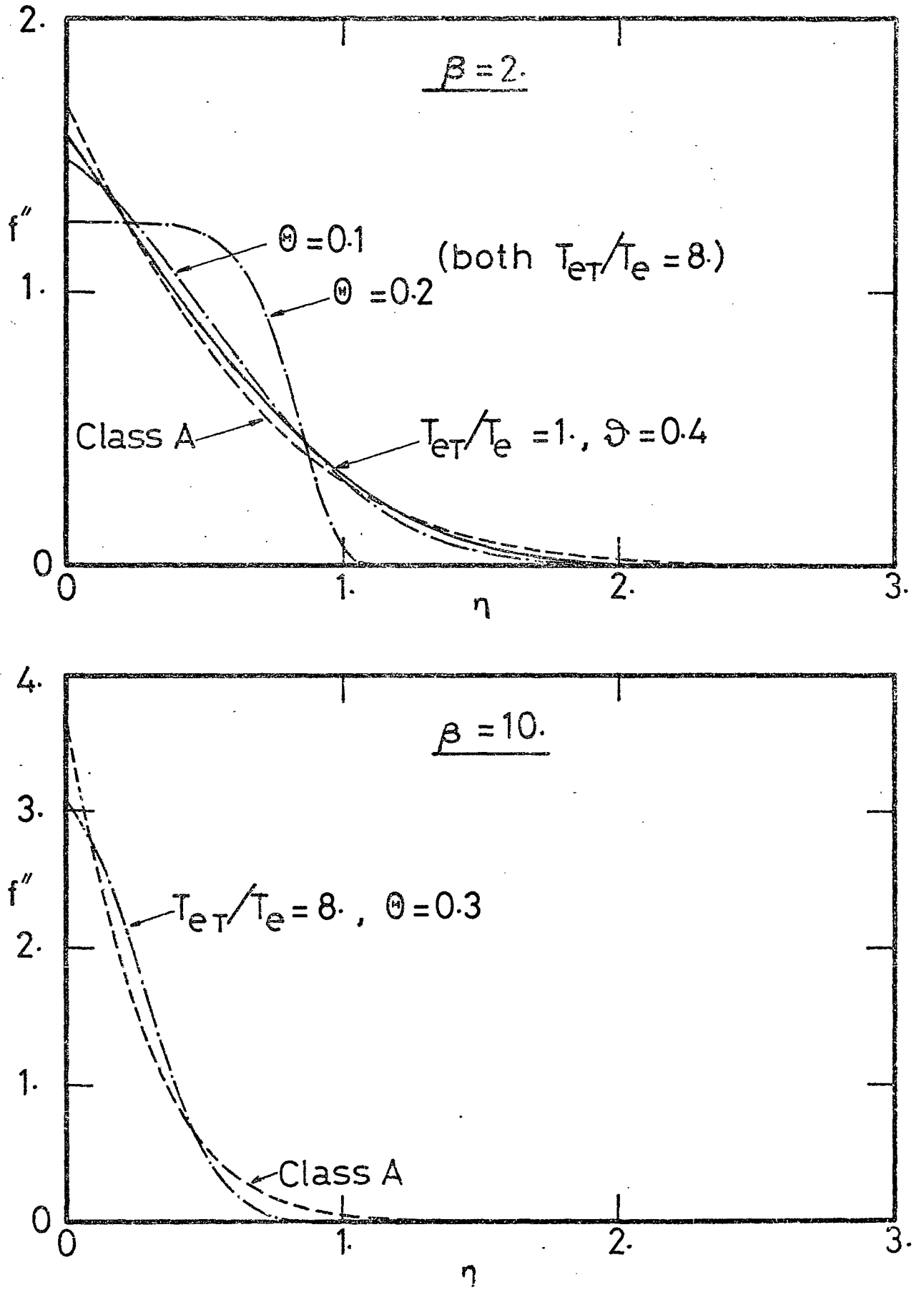

Fig. 8 Shear Stress Profiles for Class B Similar Solutions

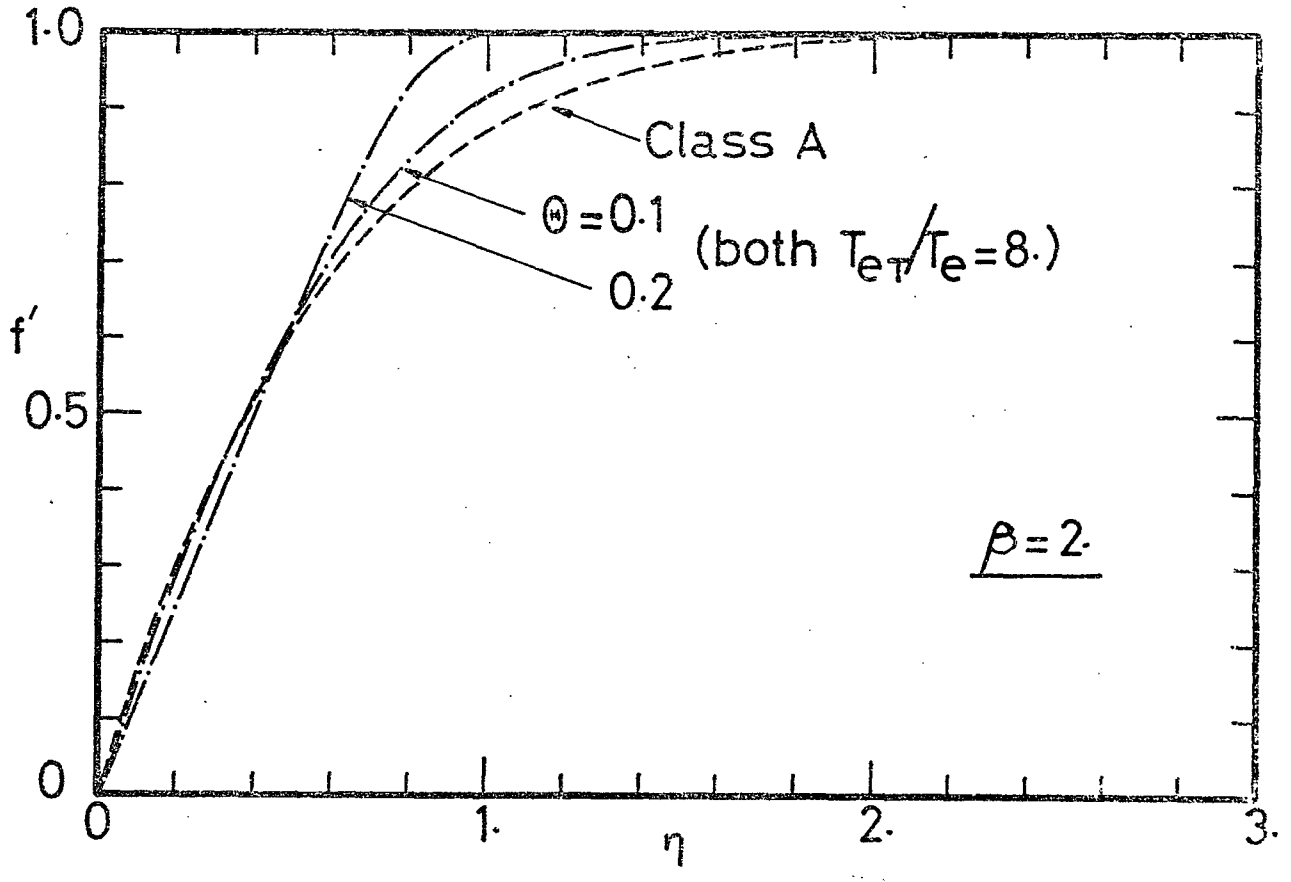

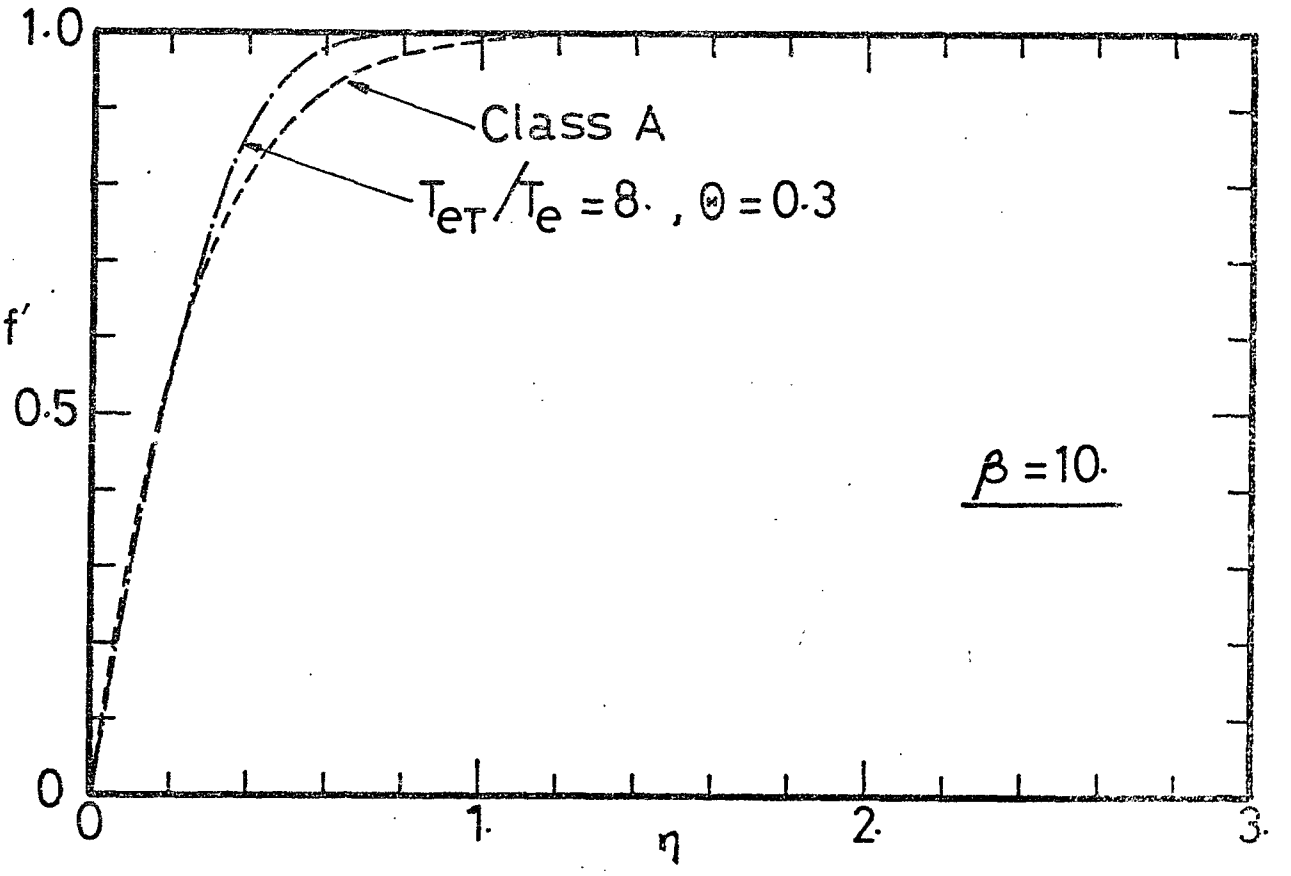

Fig. 9 Velocity Profiles for Class B Similar Solutions

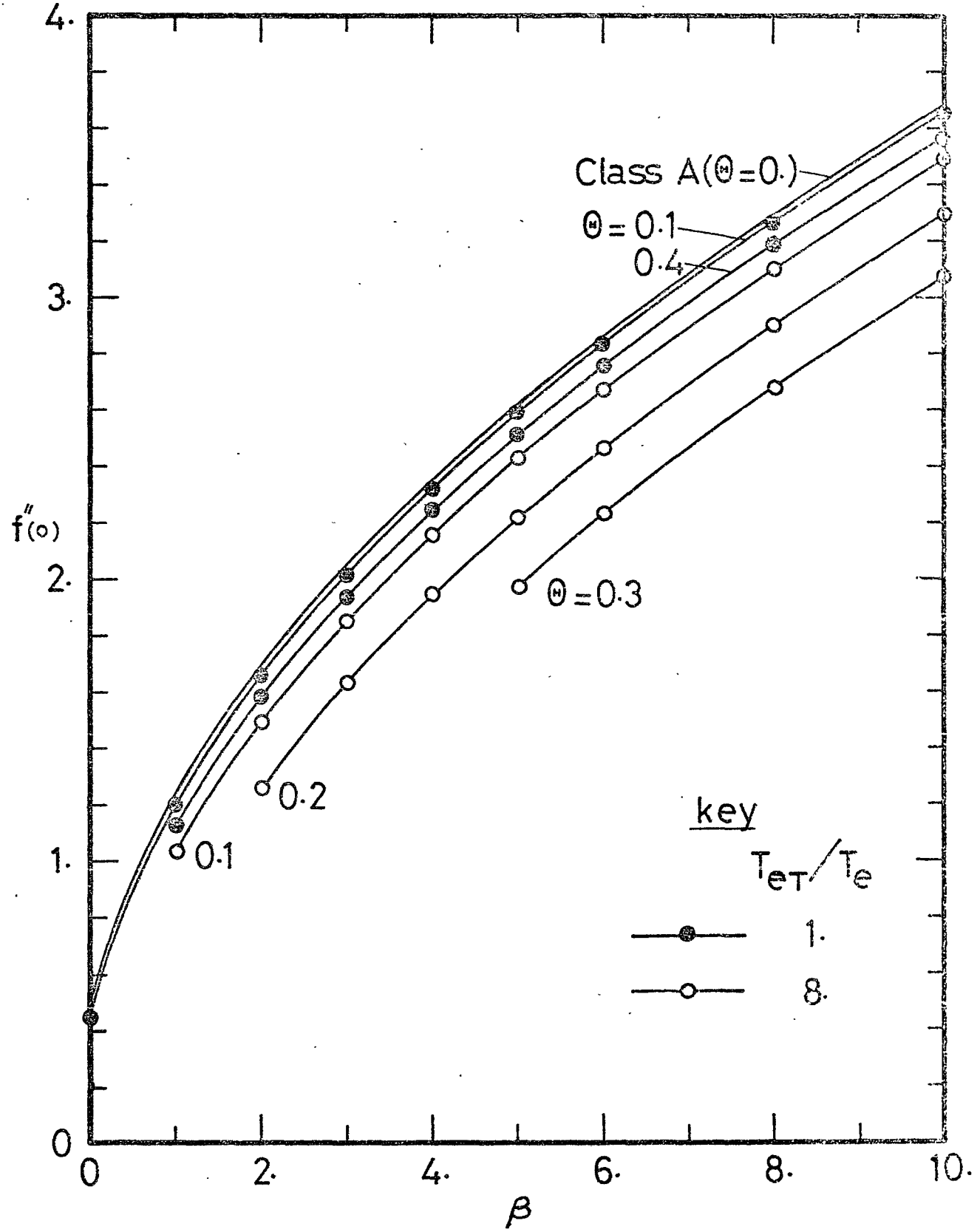

Fig.10 Variation of Wall Shear Stress, $f''(o)$ (Class B)

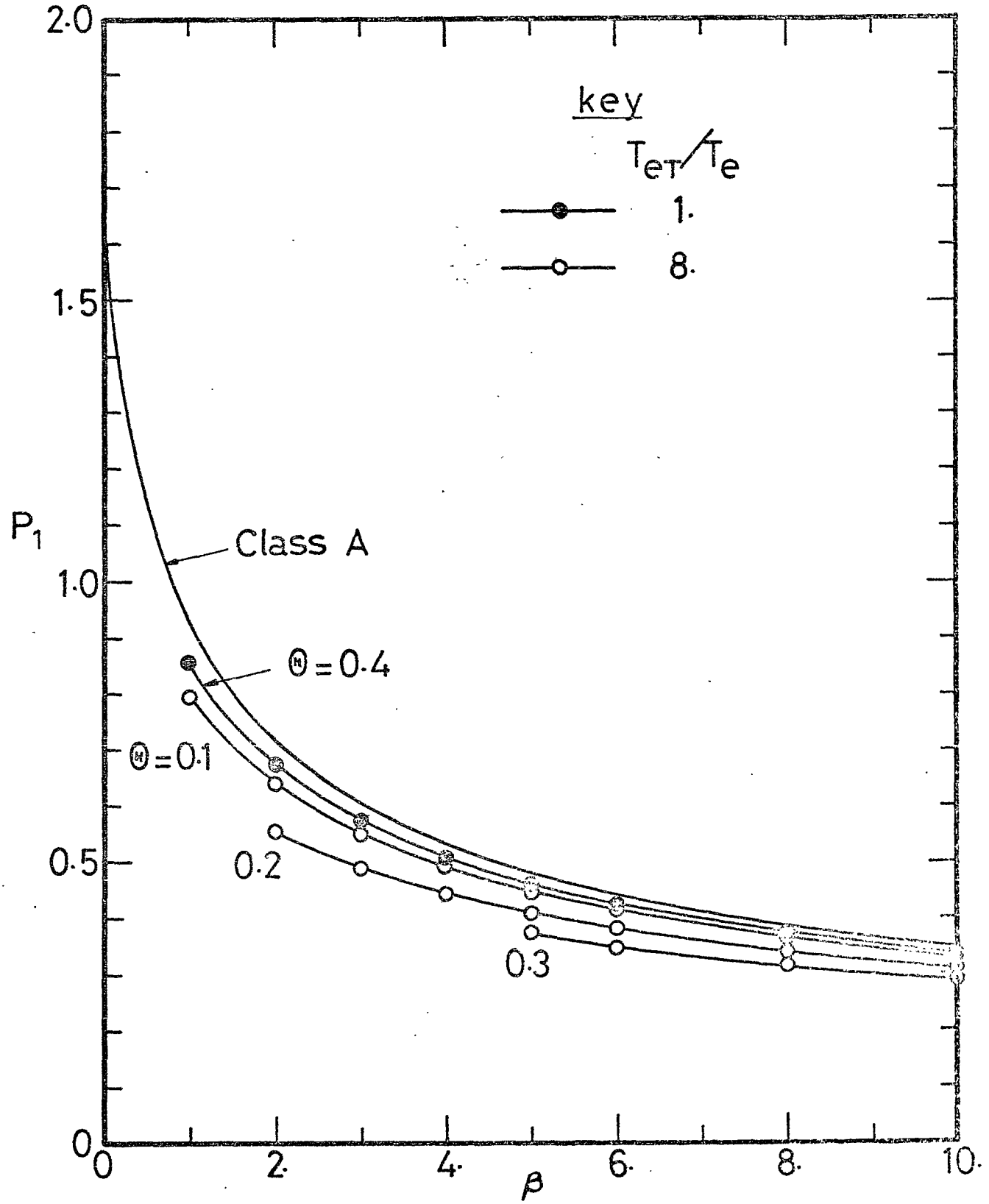

Fig·11 Variation of $P_1 = \int_0^{\eta_\infty} (1-f'^2)\,d\eta$ (Class B)

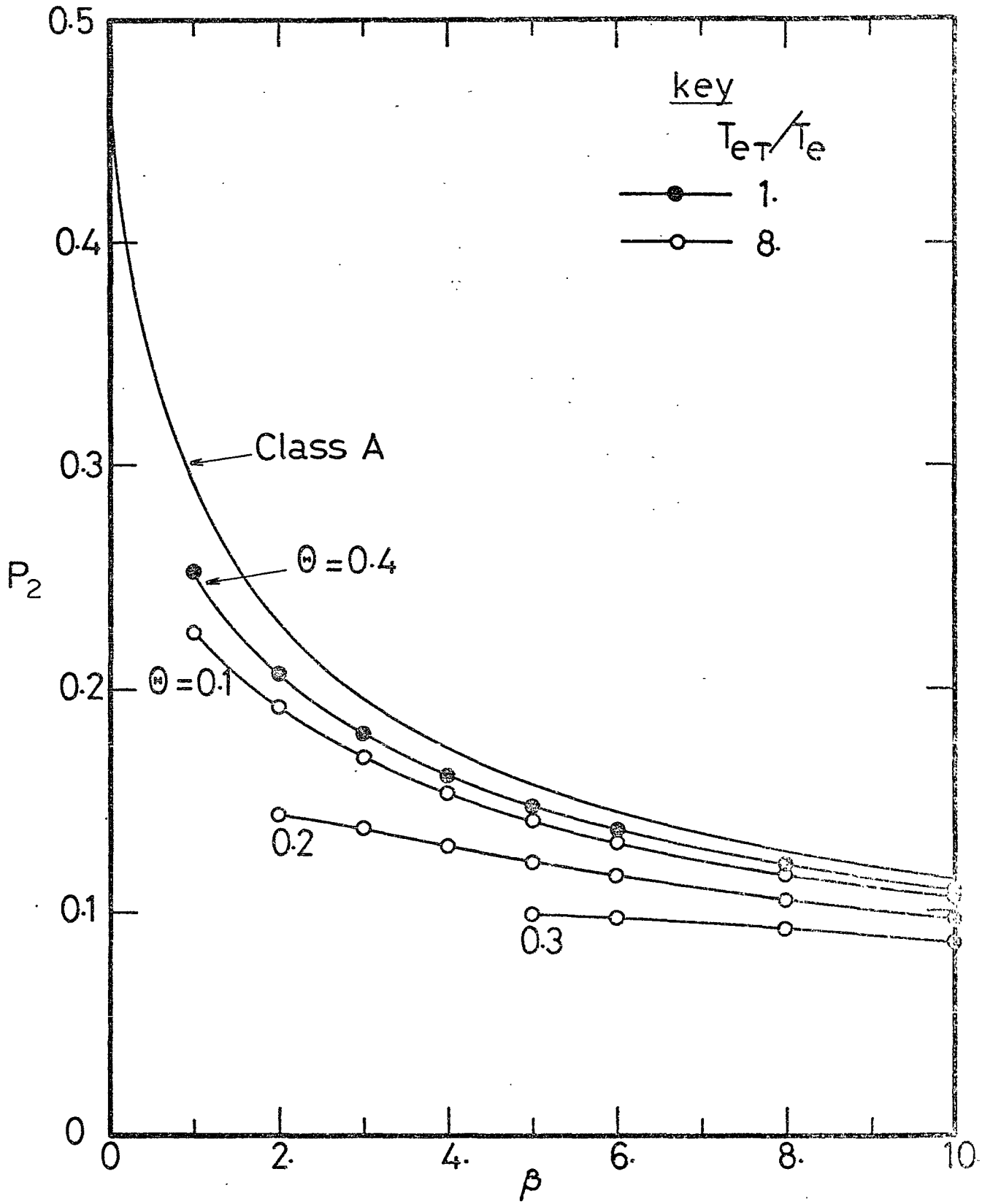

Fig-12 Variation of $P_2 = \int_0^{\eta_\infty} f'(1-f')d\eta$ (Class B)

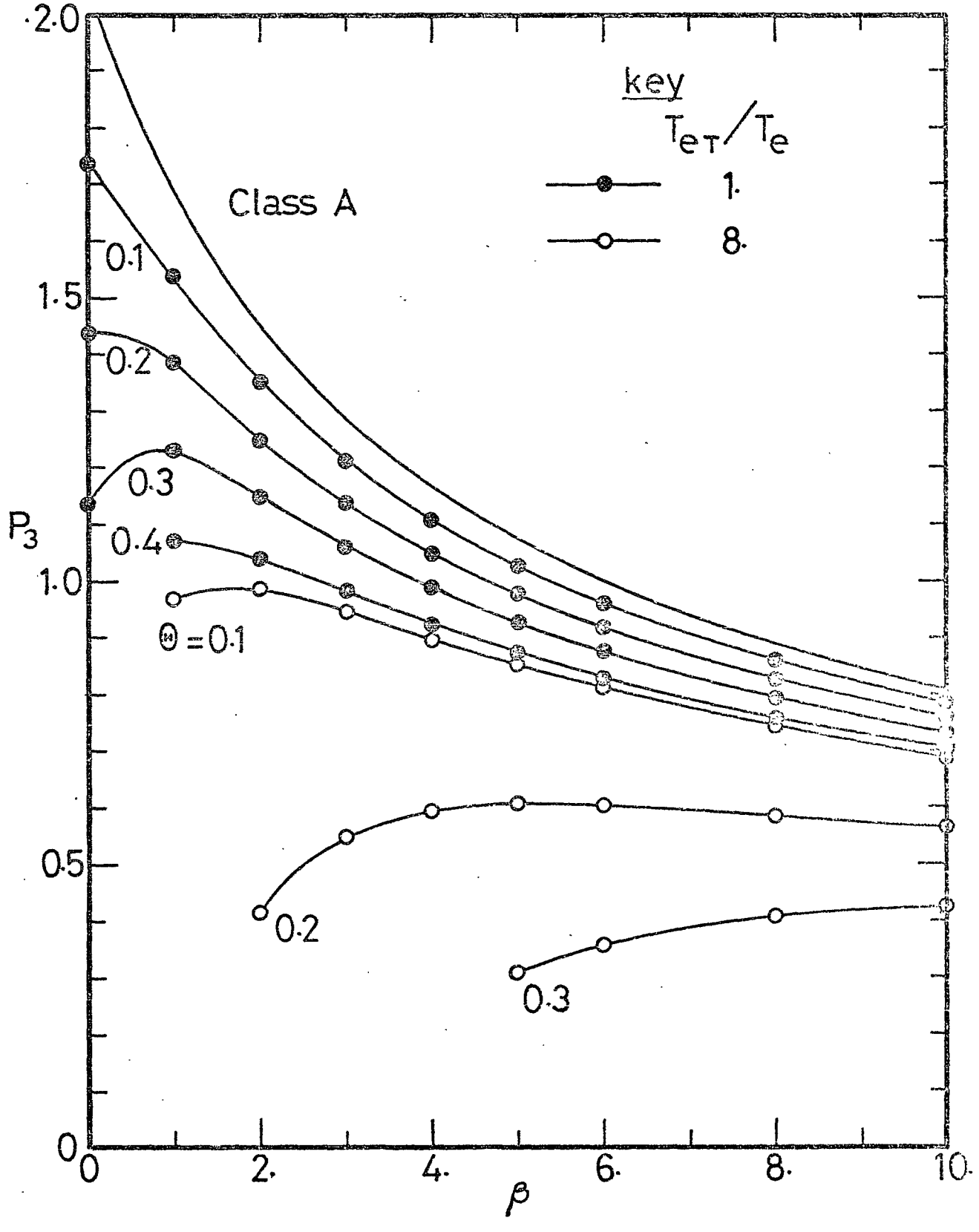

Fig-13 Variation of $P_3 = \int_0^{\eta_\infty} f'^2 d\eta$ (Class B)

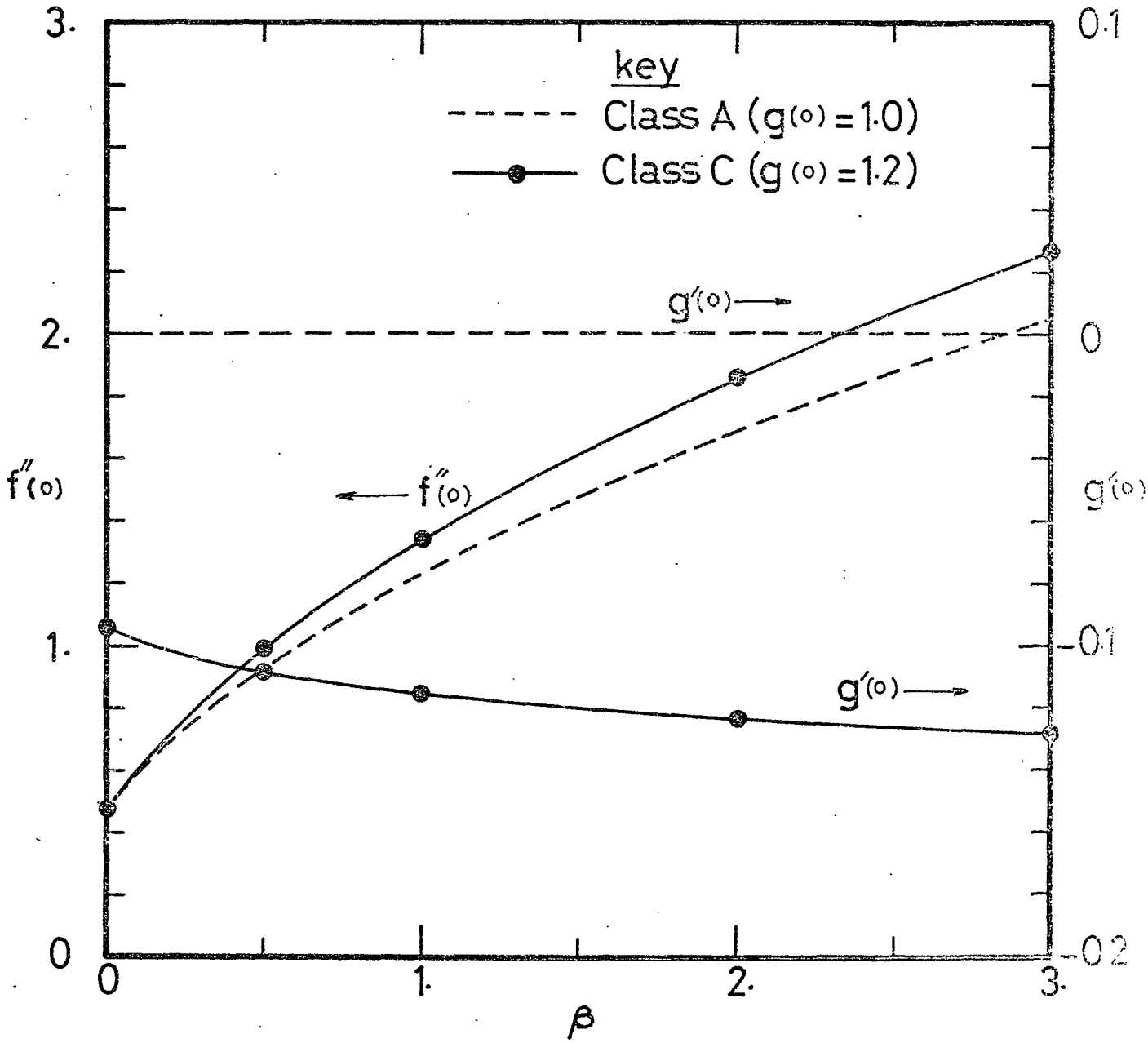

Fig·14 Shear Stress & Total Enthalpy Function Gradient at Wall (Class C)

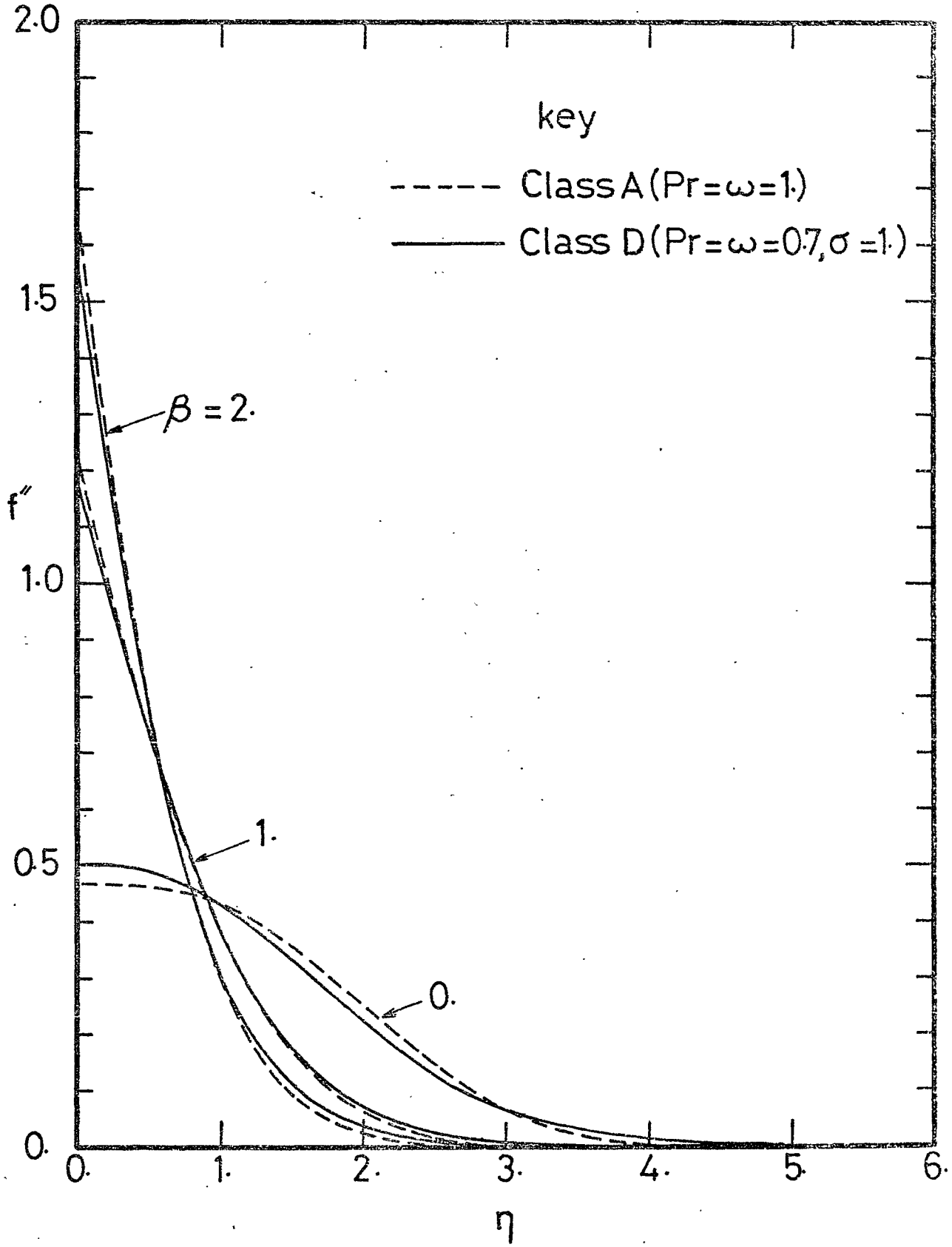

Fig.15 Comparison of Shear Stress Profiles (Class A & D)

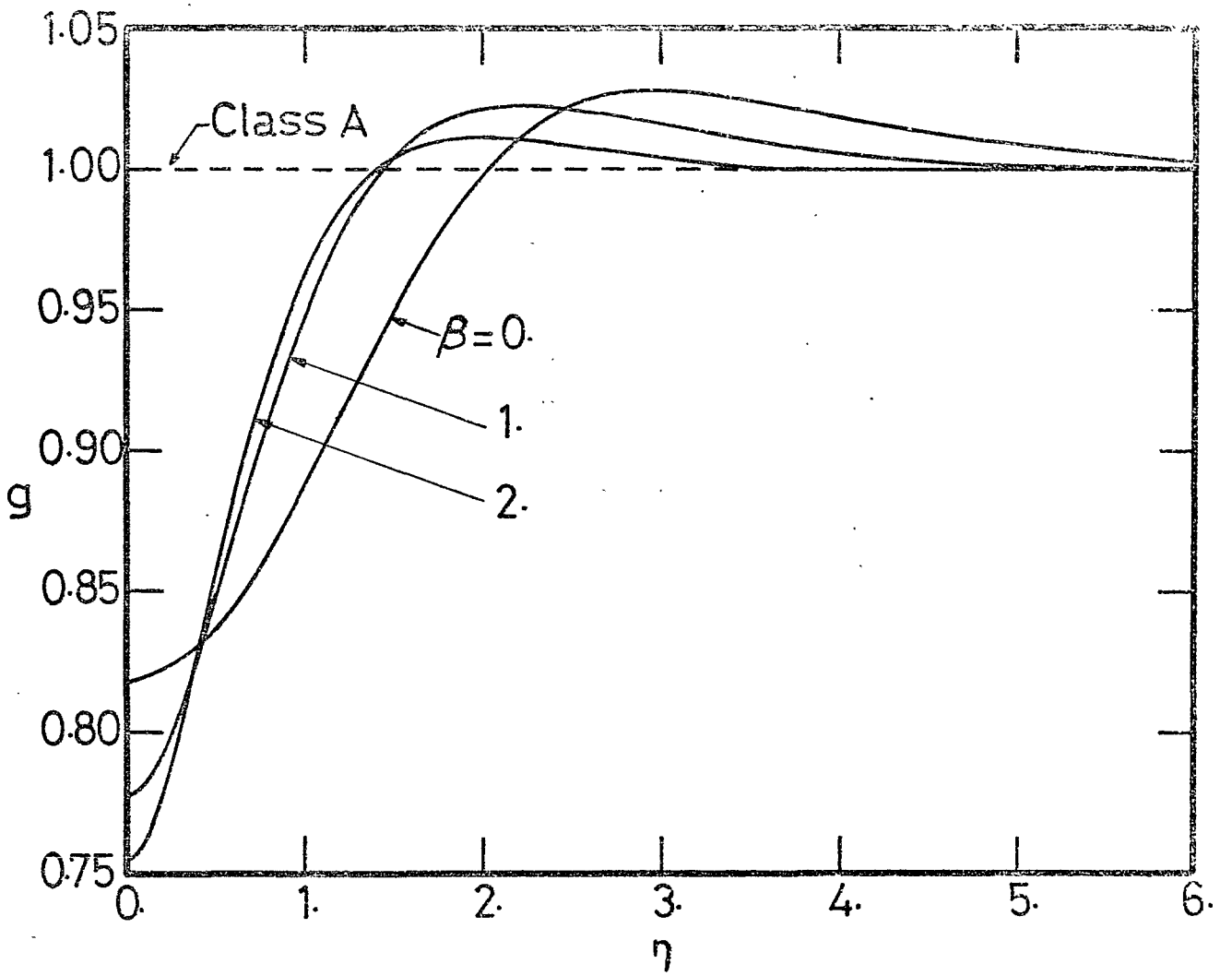

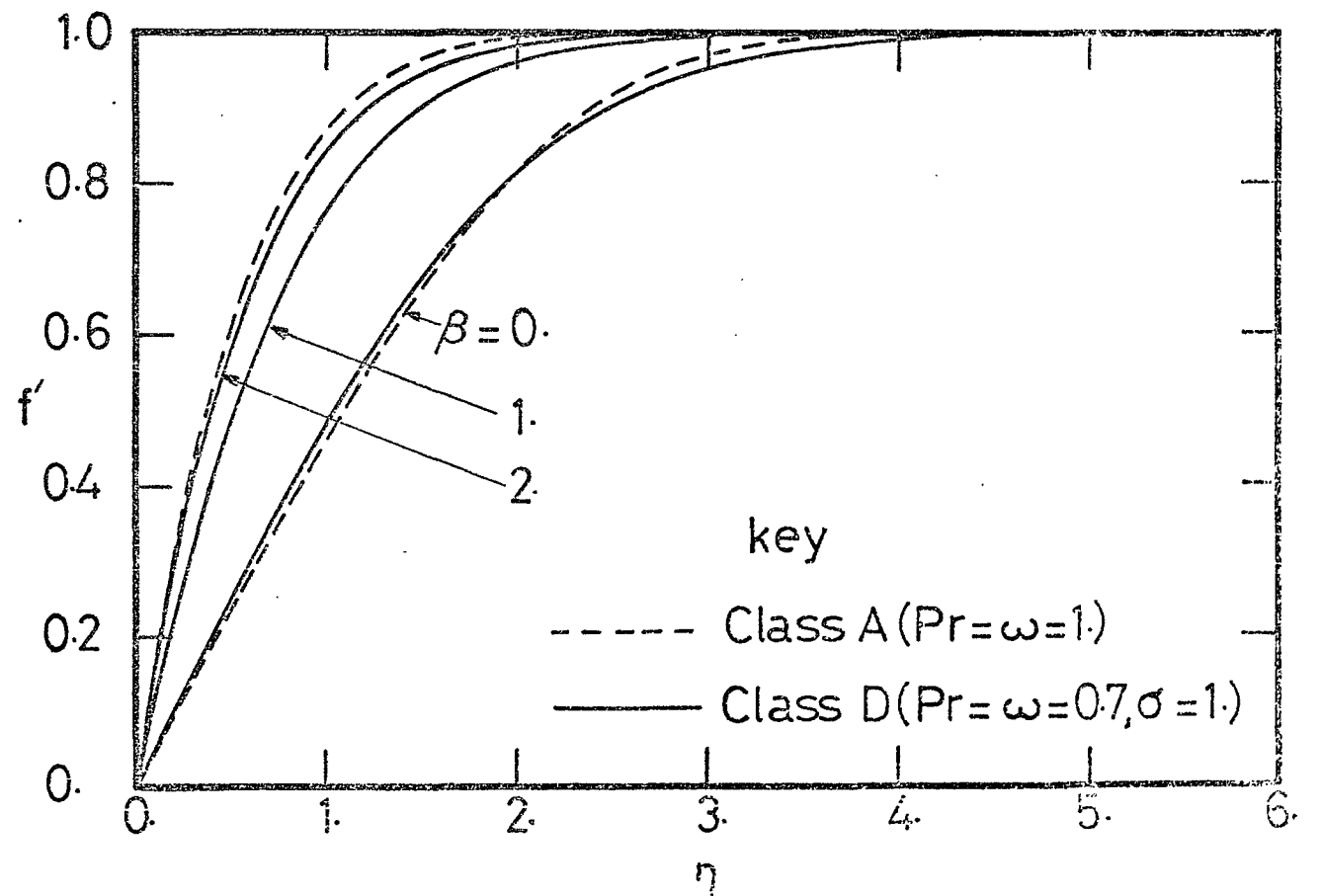

Fig·16 Total Enthalpy & Velocity Profiles (Class D)

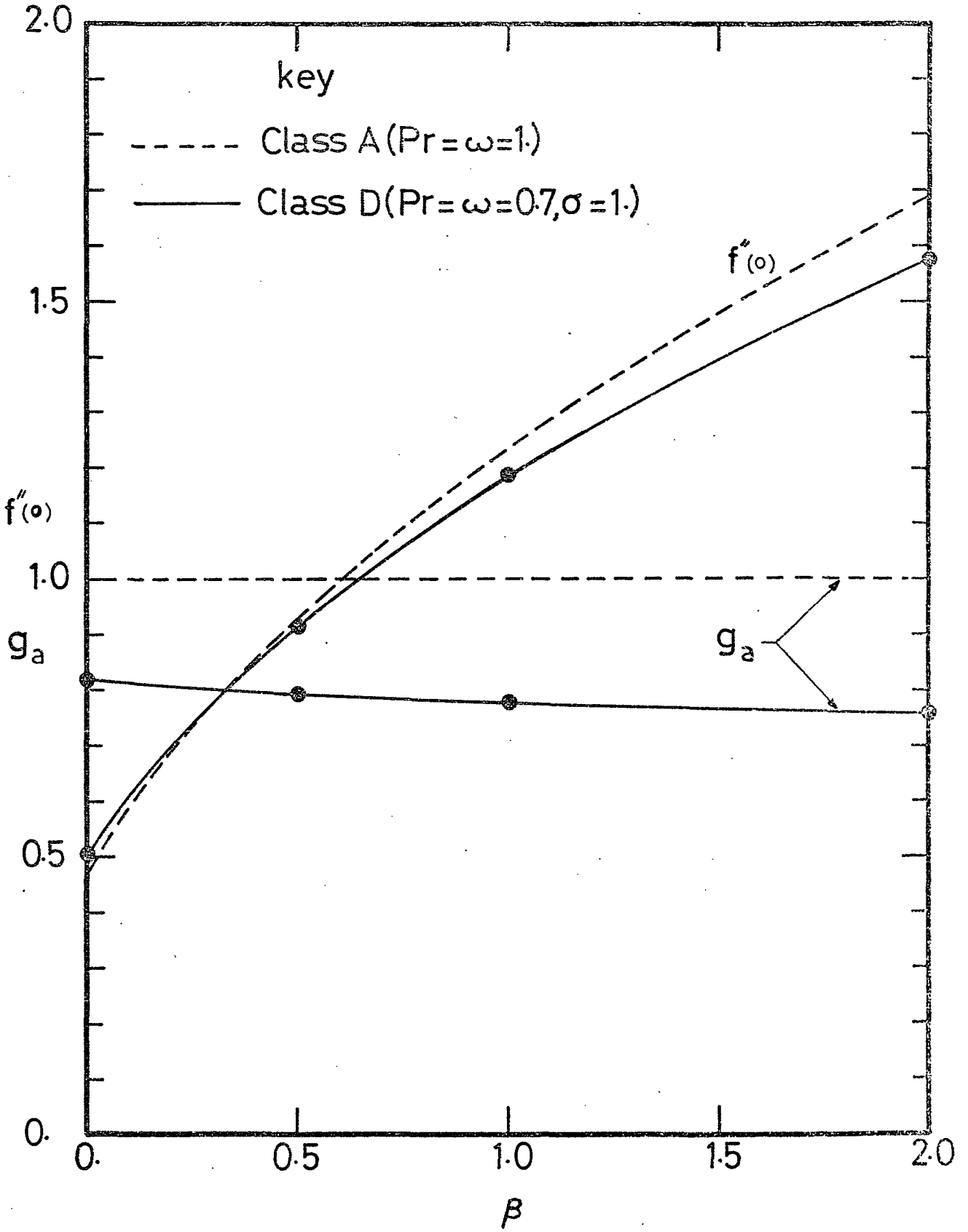

Fig.17 Shear Stress & Total Enthalpy at Wall (Class D)

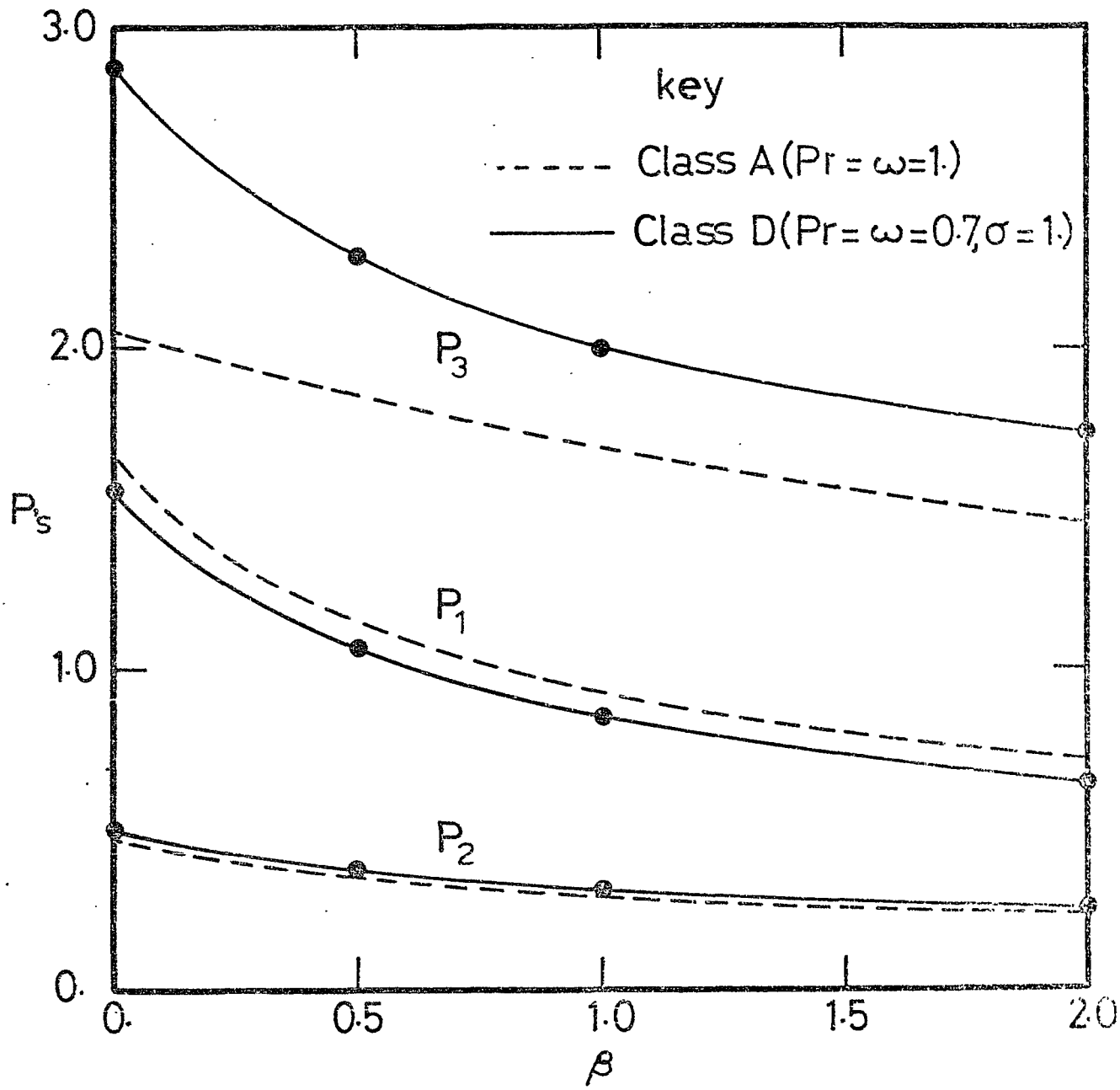

Fig·18 Boundary Layer Integrals (Class D)

Master Segment

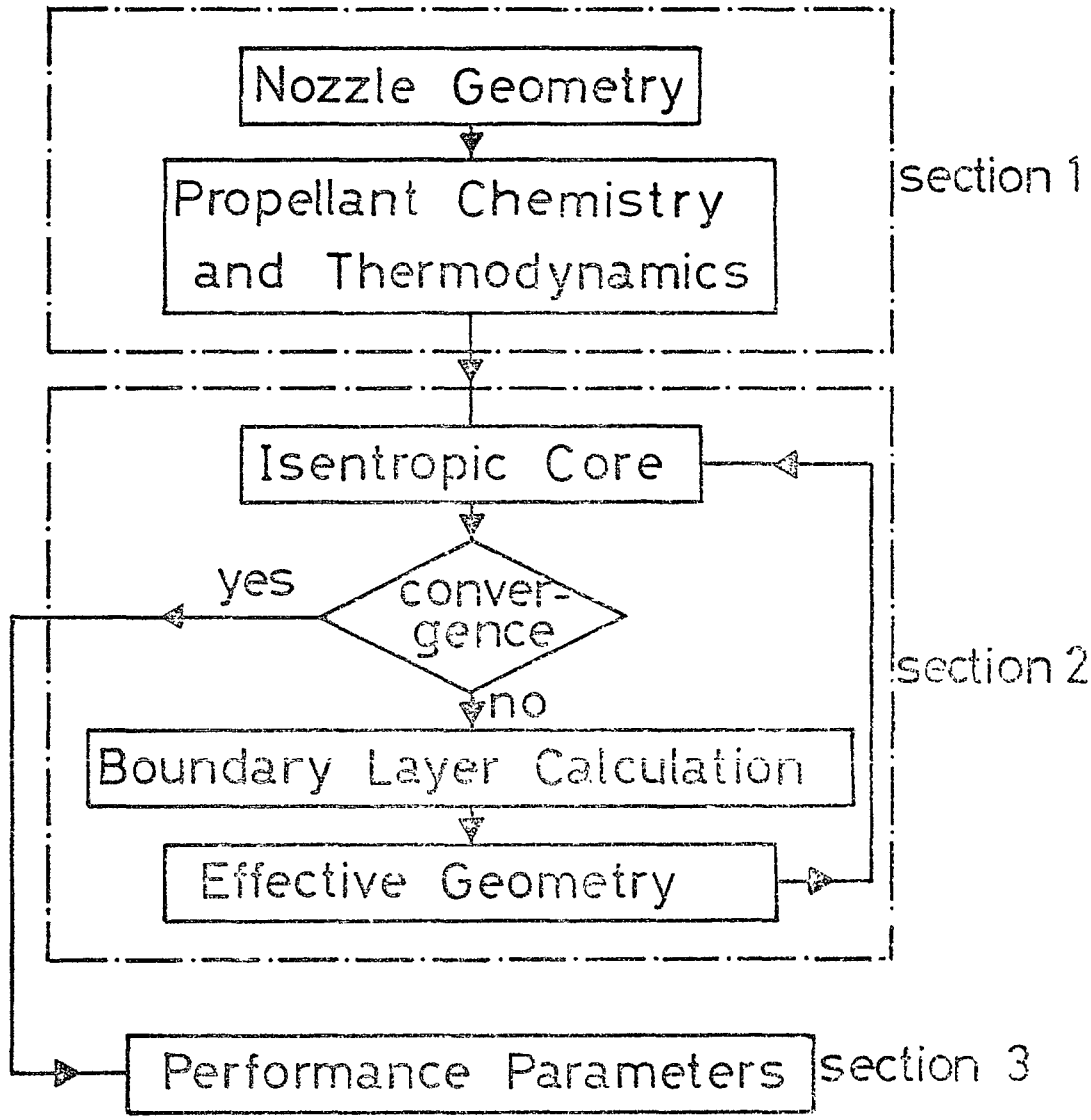

Subroutines

CSINT	cubic-spline integration
CSFMIE	cubic-spline interpolation
DYDX	three-point differentiation

Fig.19 Flow Diagram of Nozzle Programs

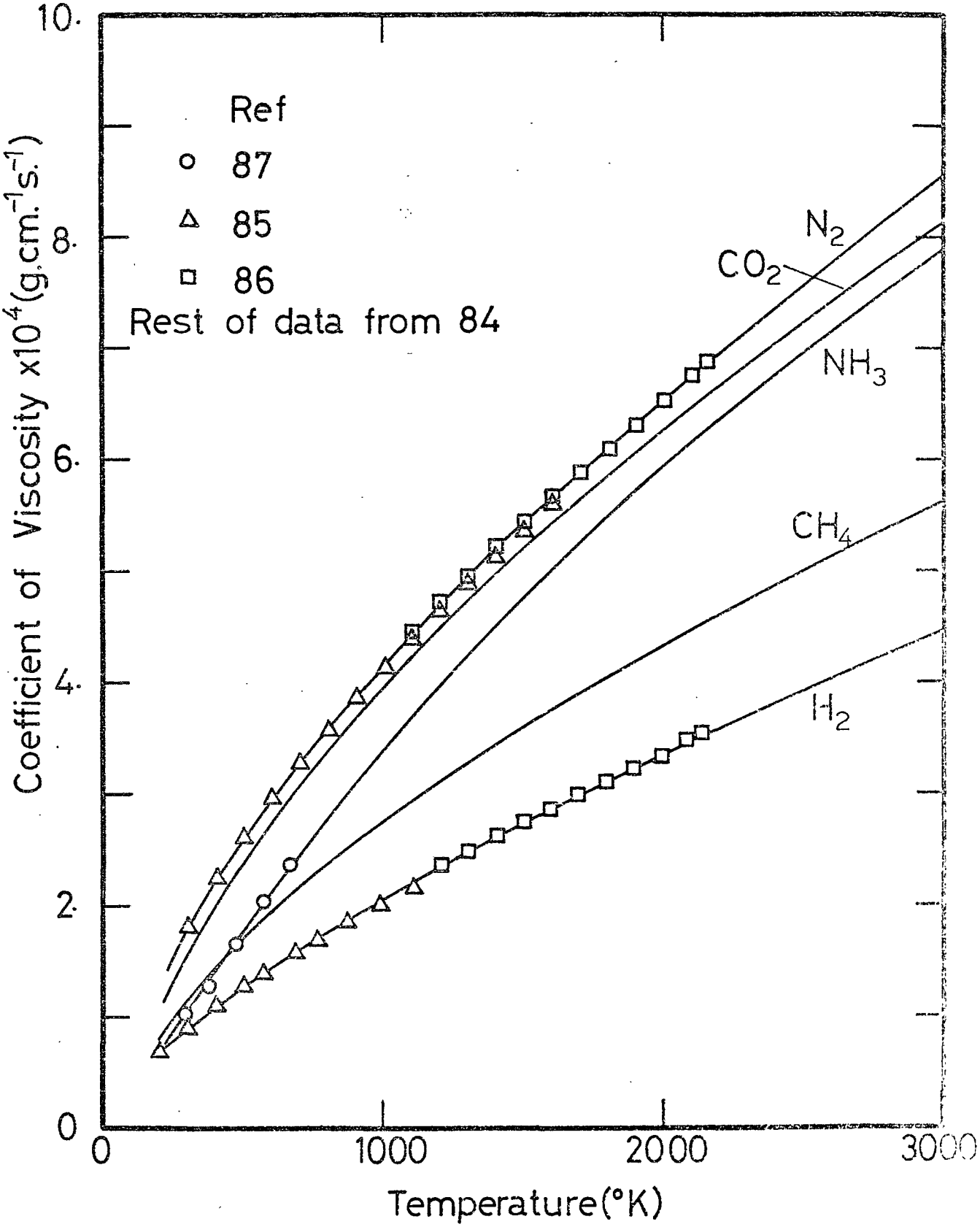

Fig.20 Viscosity Data

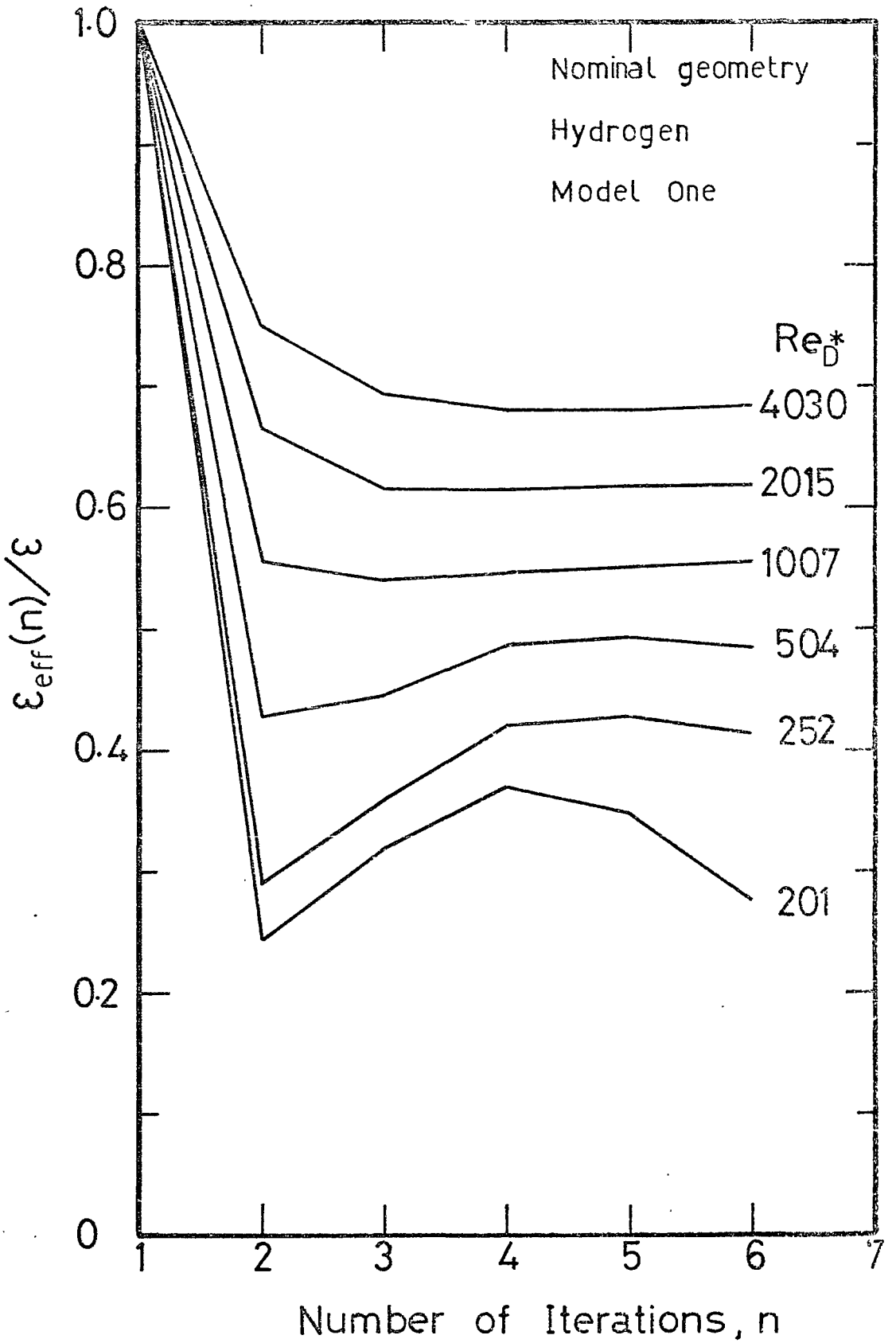

Fig.21 Convergence of Boundary Layer-Inviscid Core Iteration Procedure (Model One)

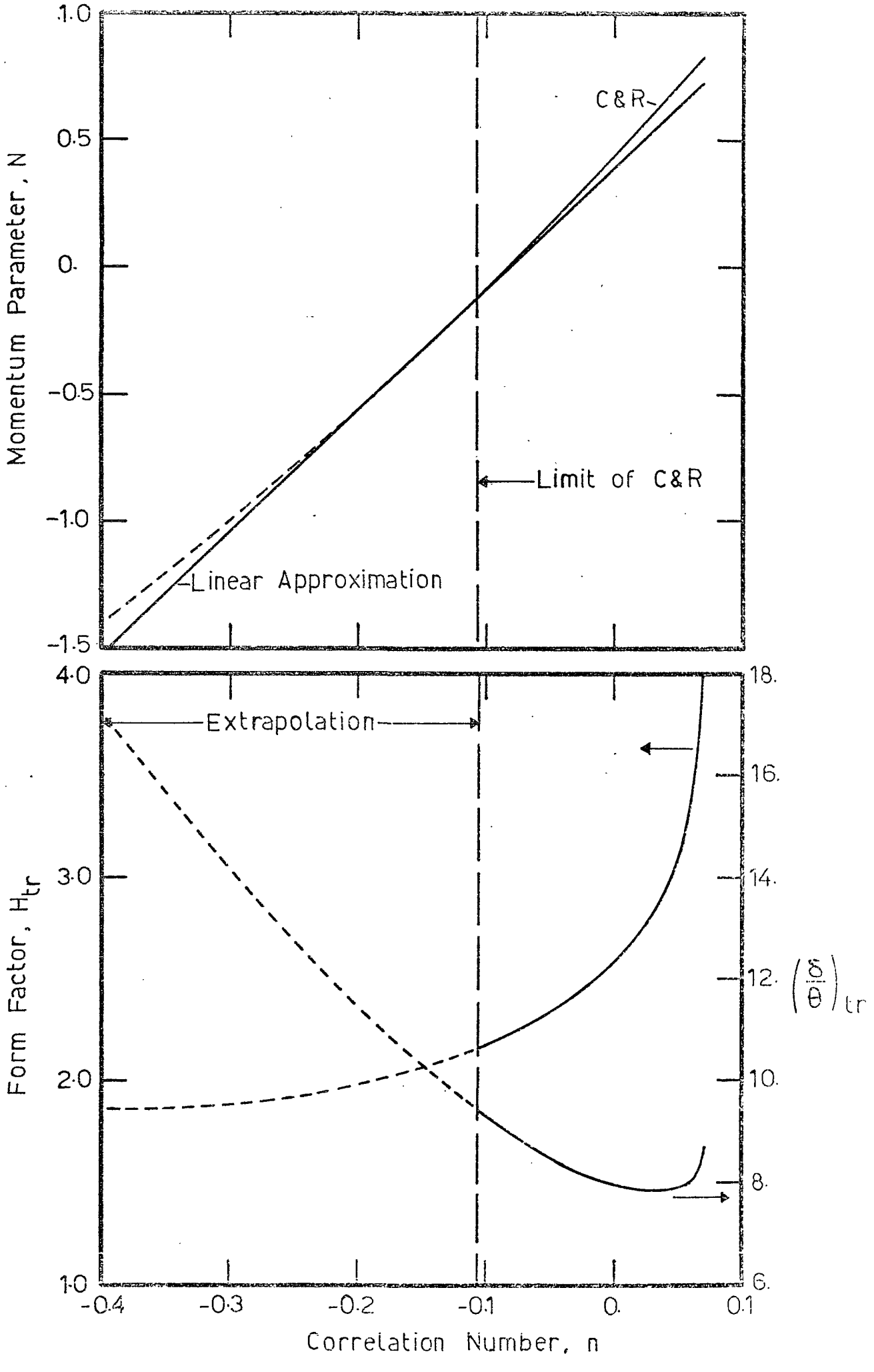

Fig 22 Correlation Parameters of Cohen & Reshotko

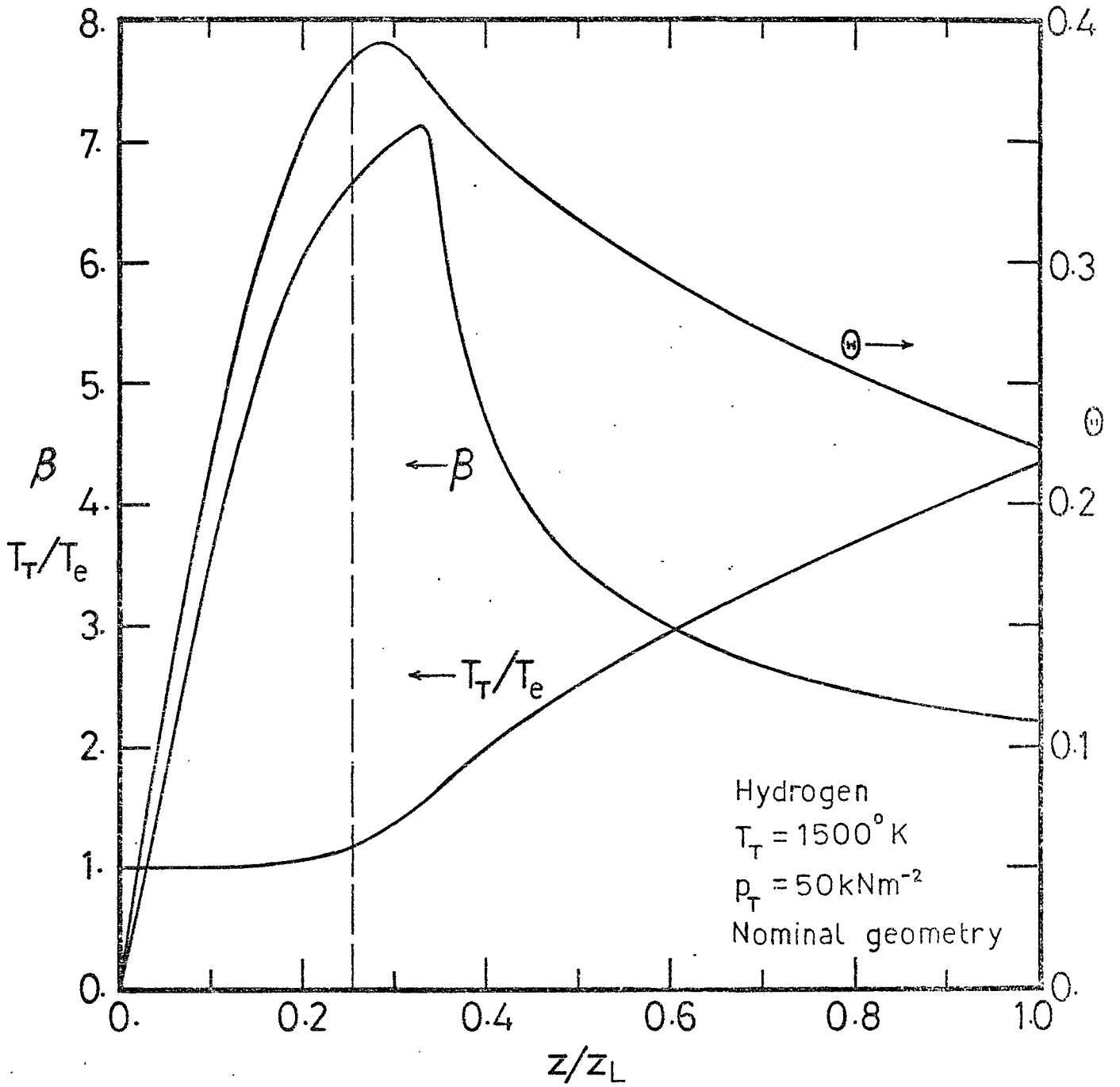

Fig.23 Variation of ξ-dependent Parameters (Model One)

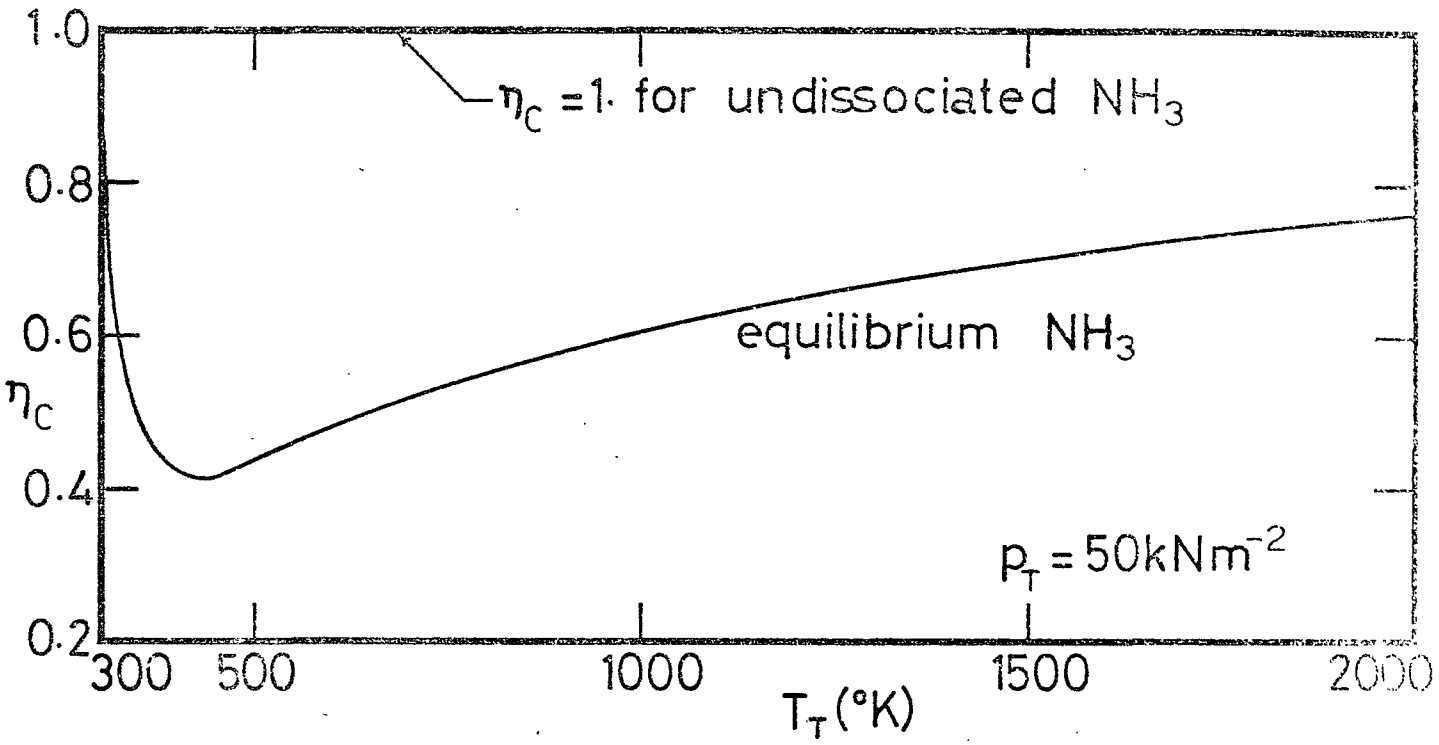

(a) Frozen Chemistry Losses

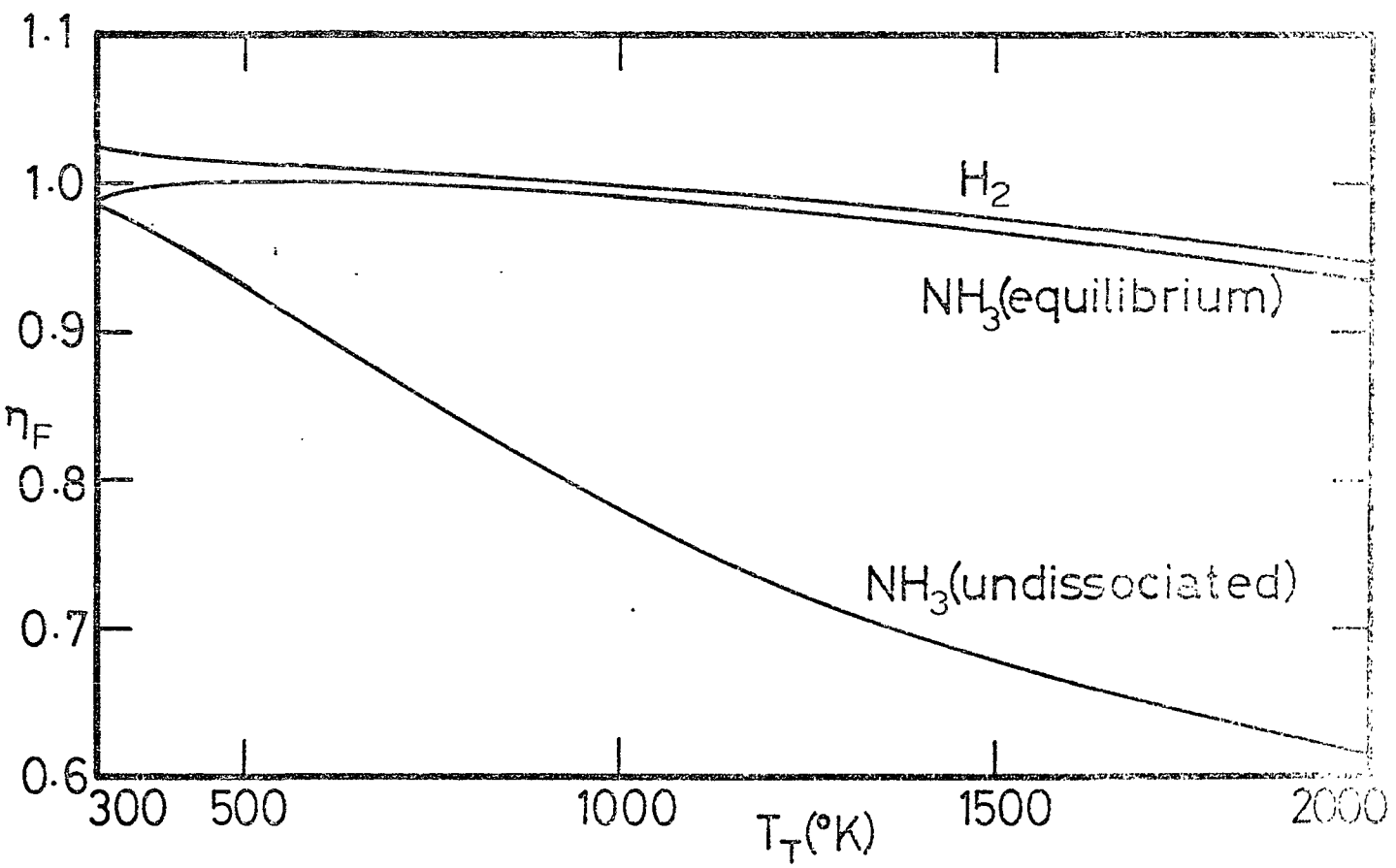

(b) Frozen Vibrational Energy Losses

Fig.24 Frozen Flow Losses(Model Zero)

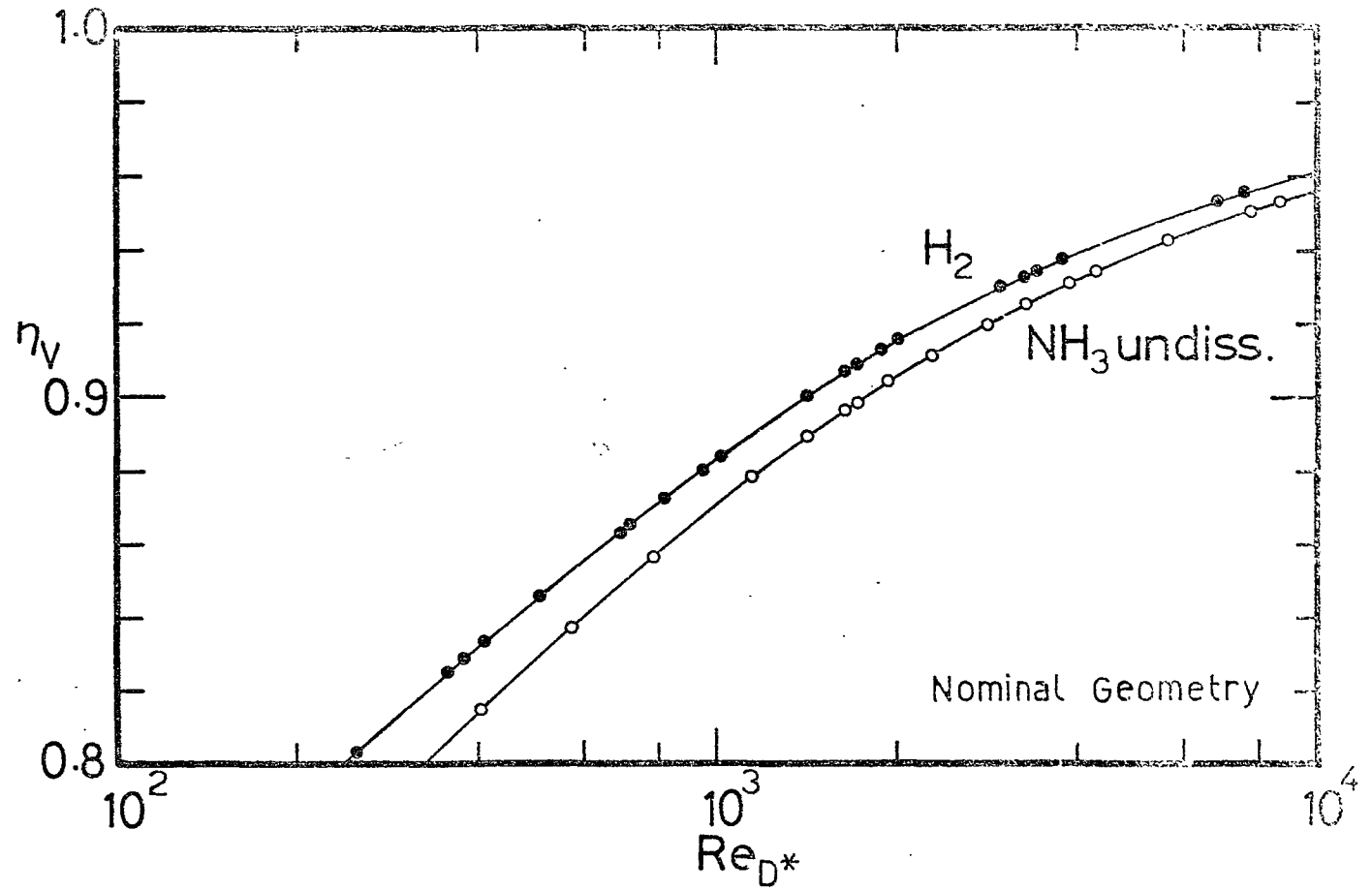

(a) Velocity Defect

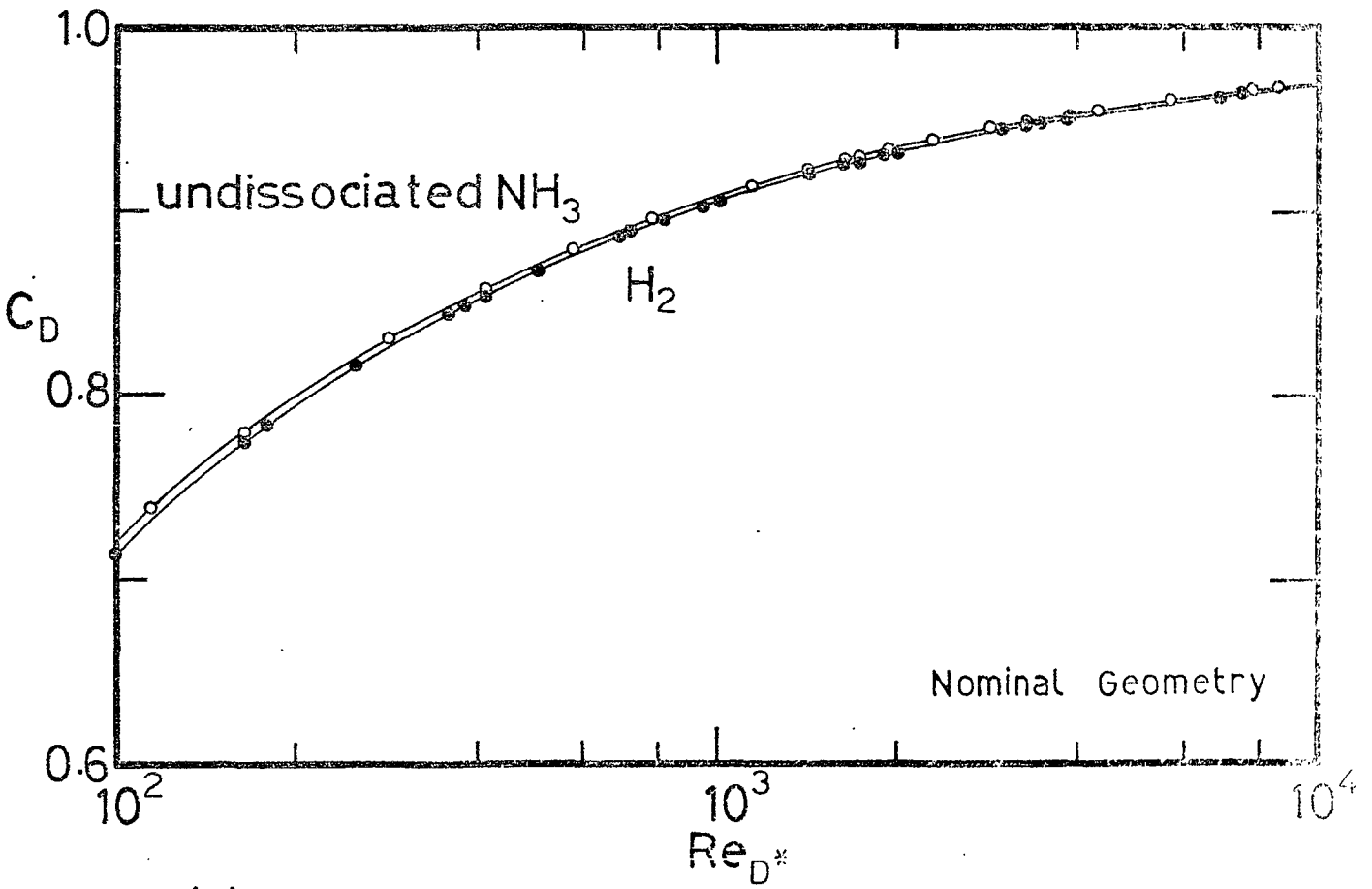

(b) Mass Defect

Fig.25 Viscous Flow Losses (Model Zero)

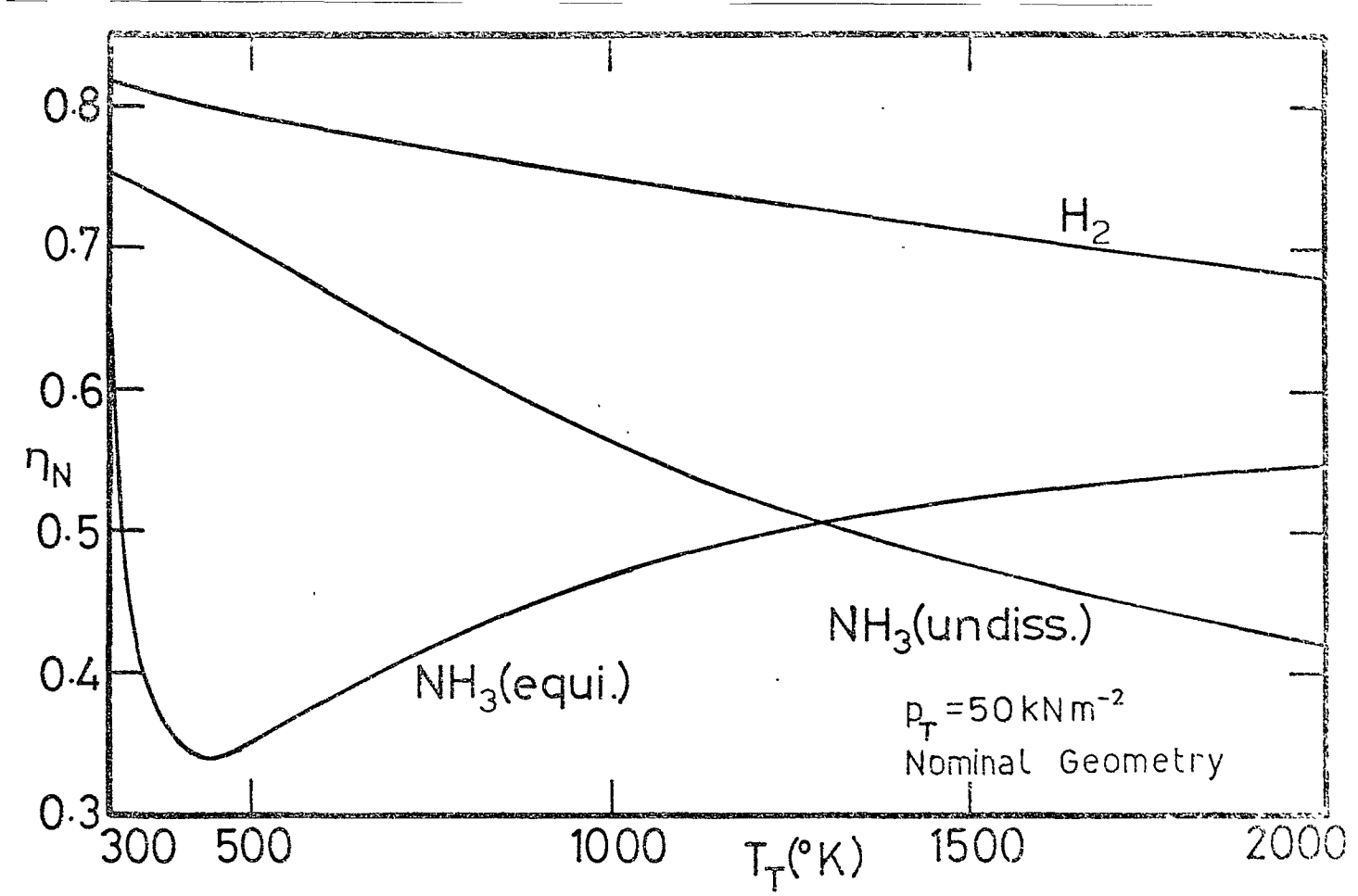

(a) Nozzle Efficiency

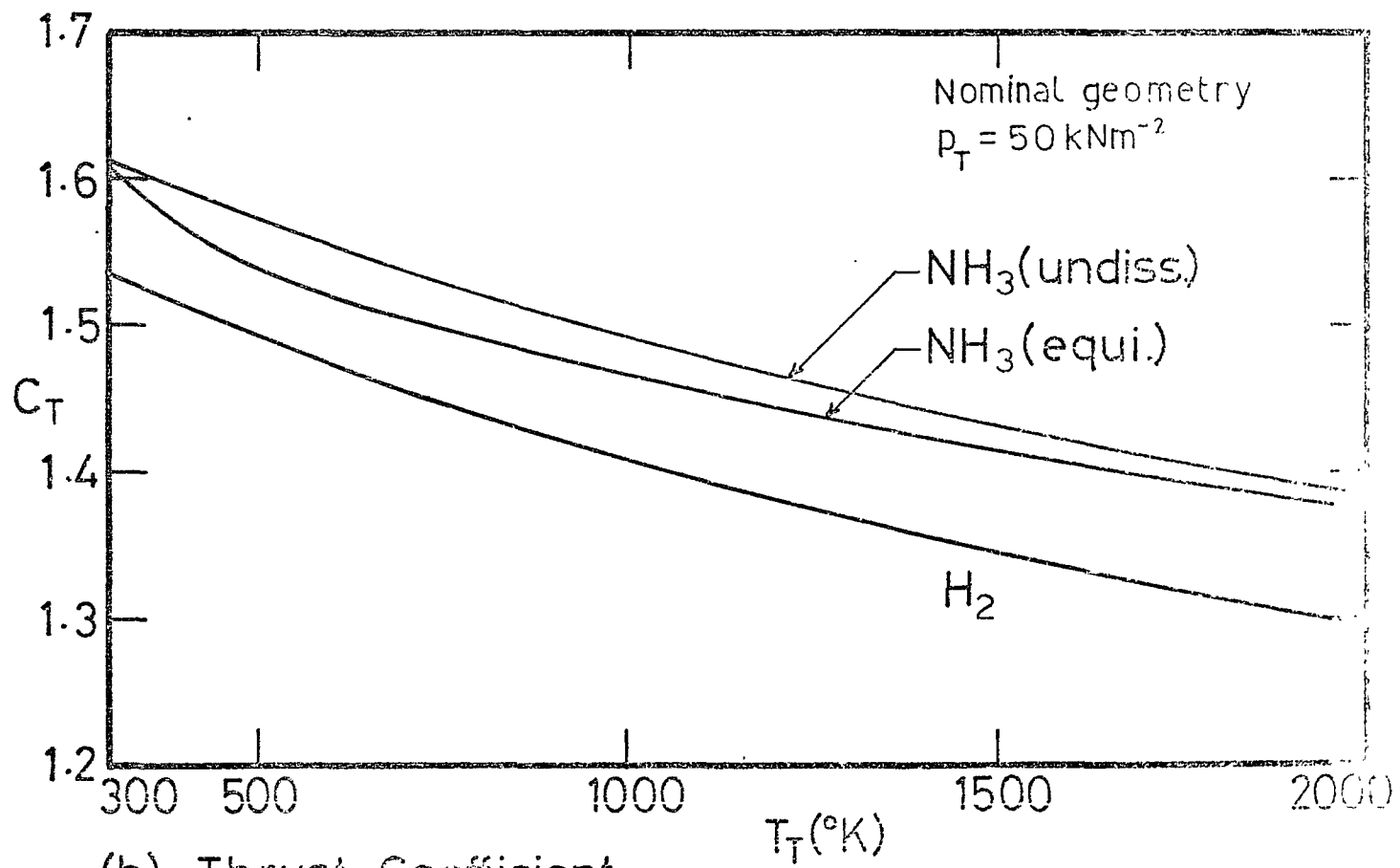

(b) Thrust Coefficient

Fig. 26 Overall Nozzle Performance (Model Zero)

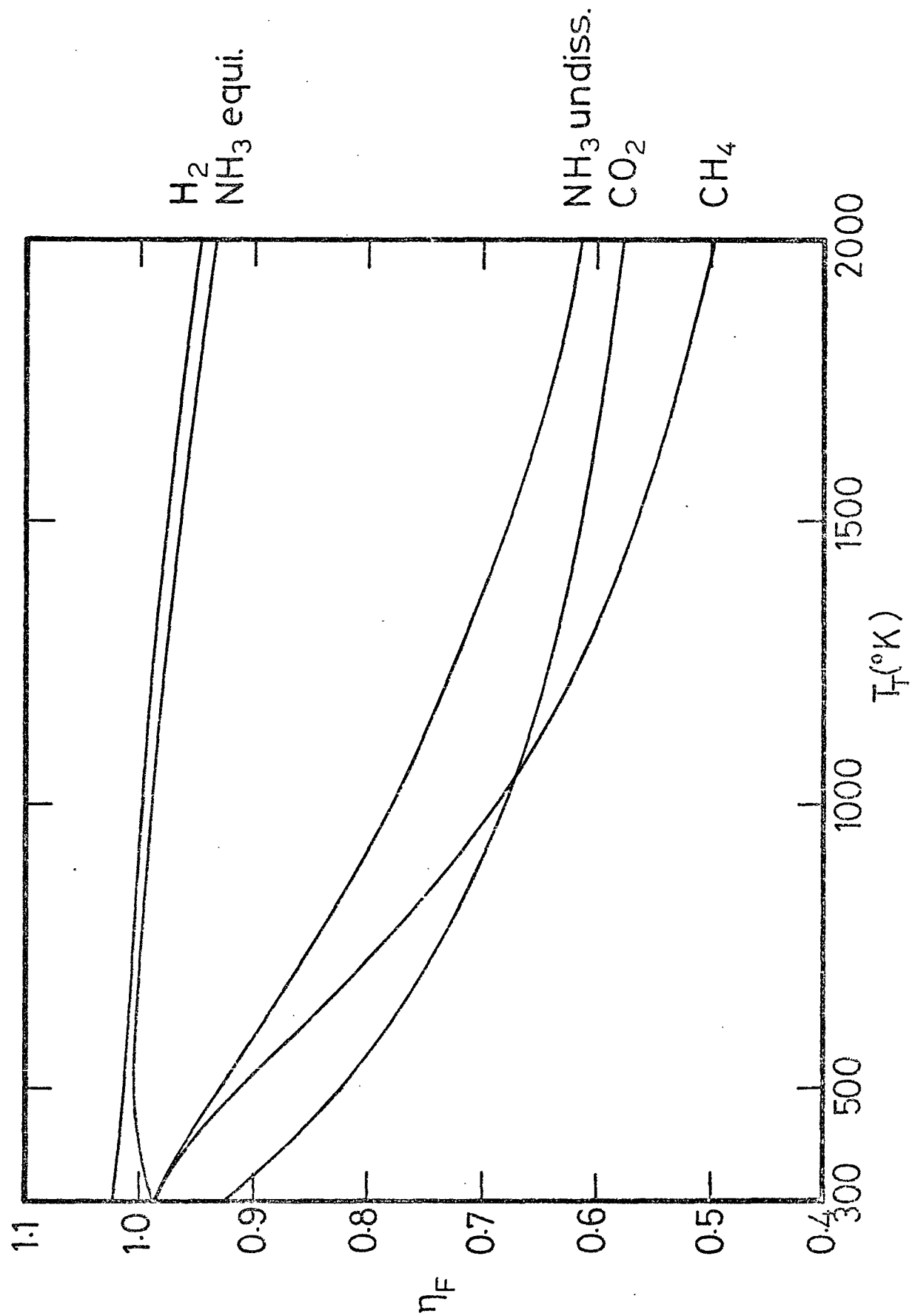

Fig.27 Frozen Vibrational Energy Loss(Model One)

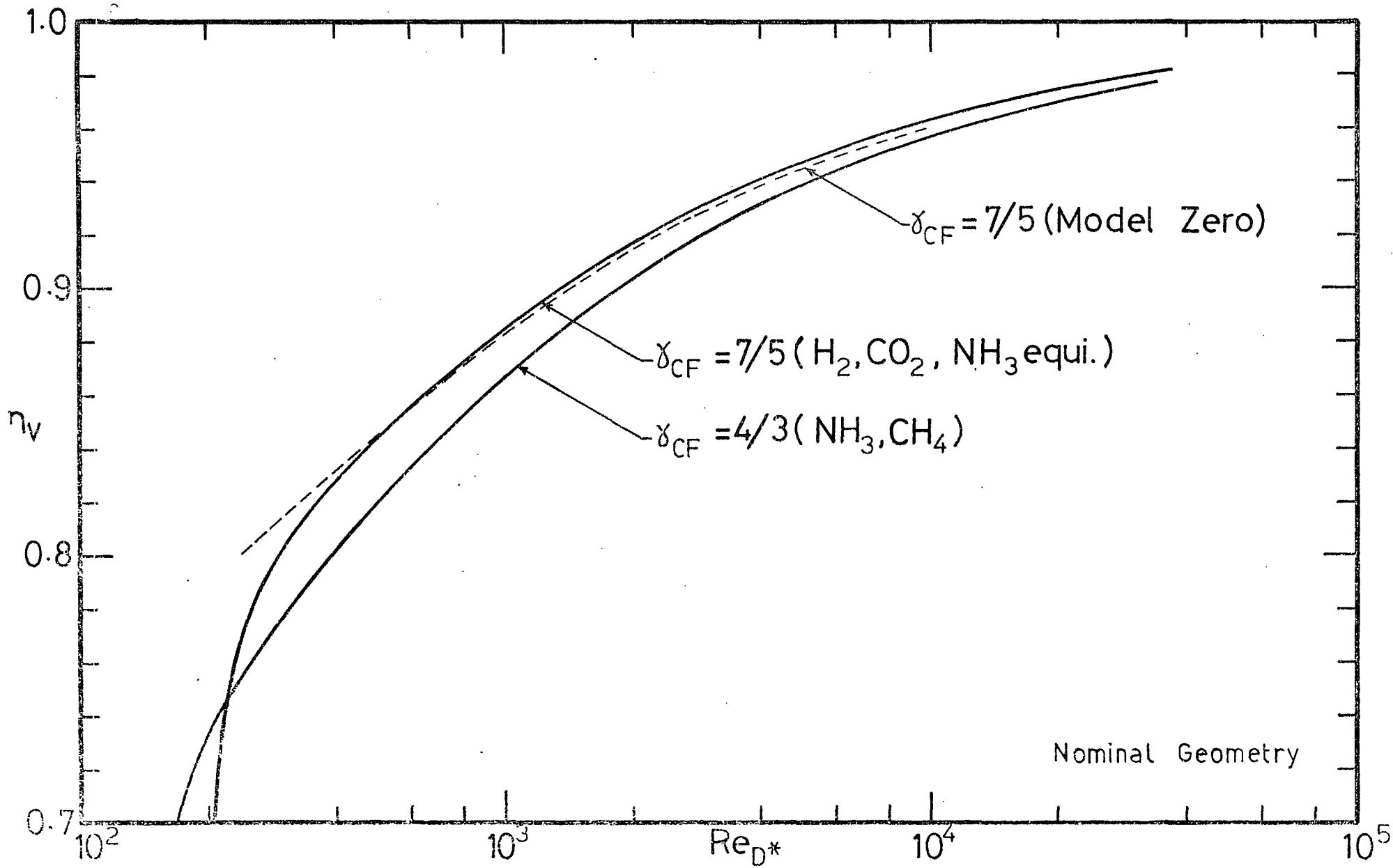

Fig.28 Velocity Defect due to Viscous Flow(Model One)

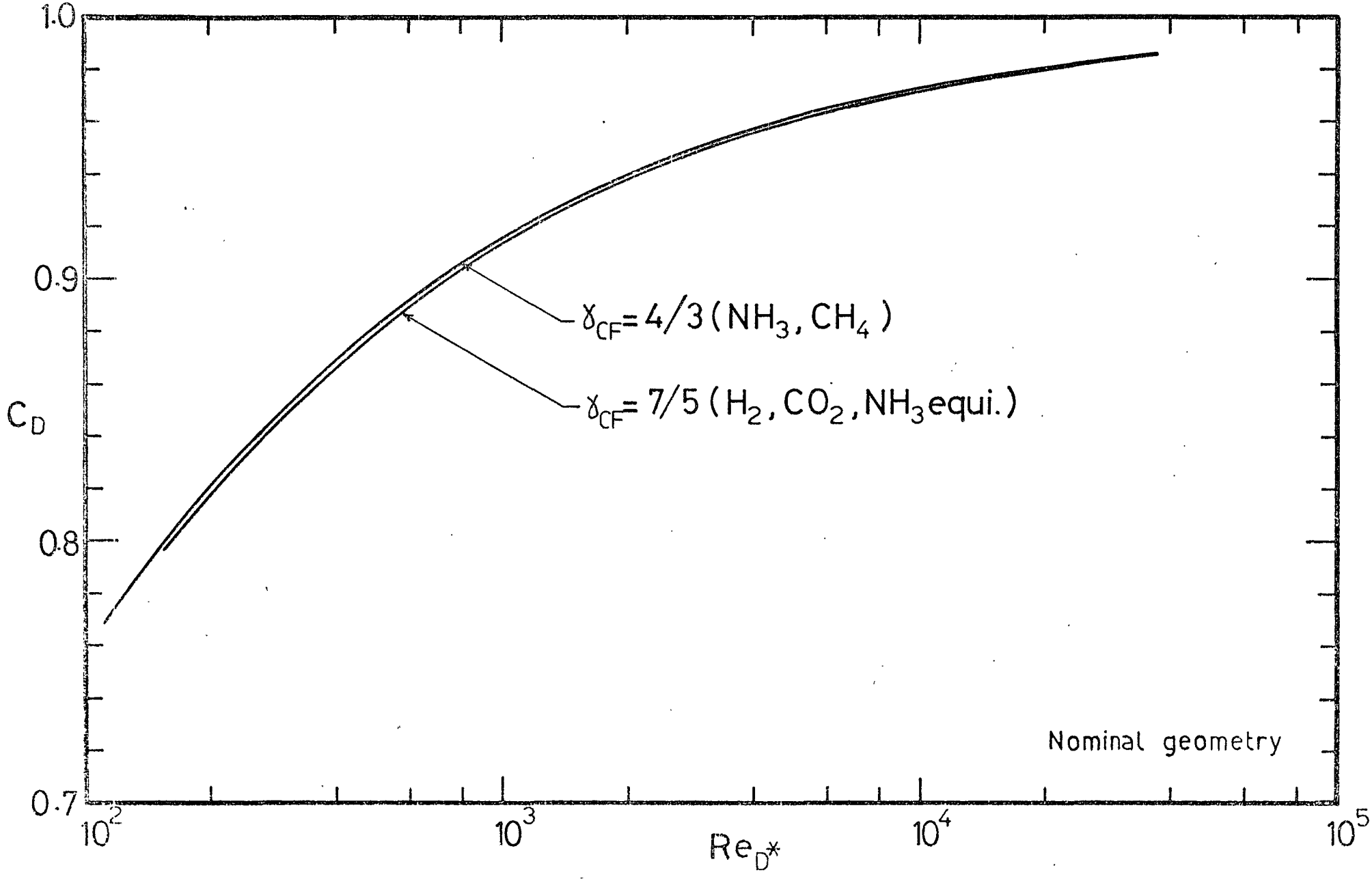

Fig·29 Discharge Coefficient (Model One)

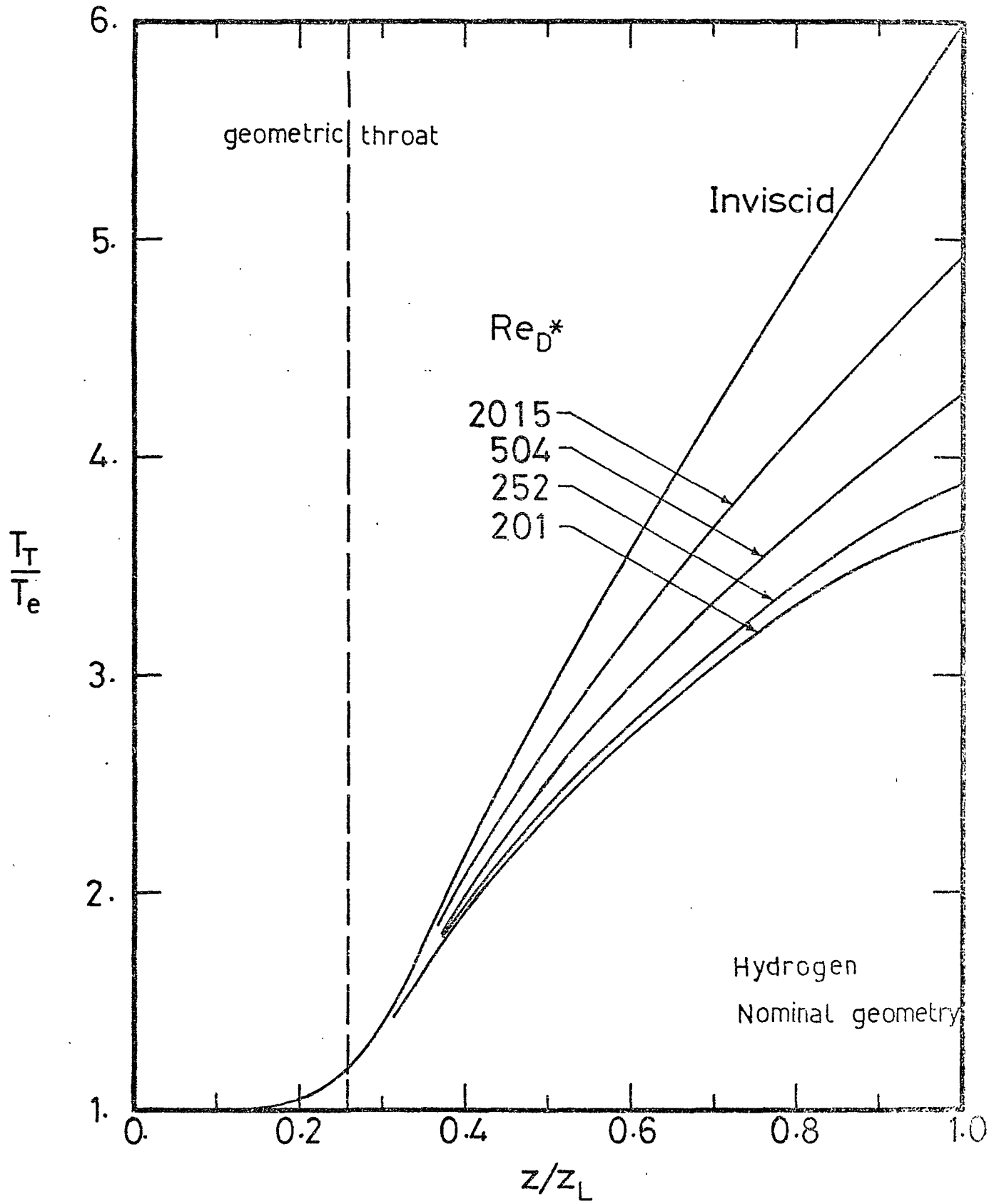

Fig.30 Axial Temperature Profiles (Model One)

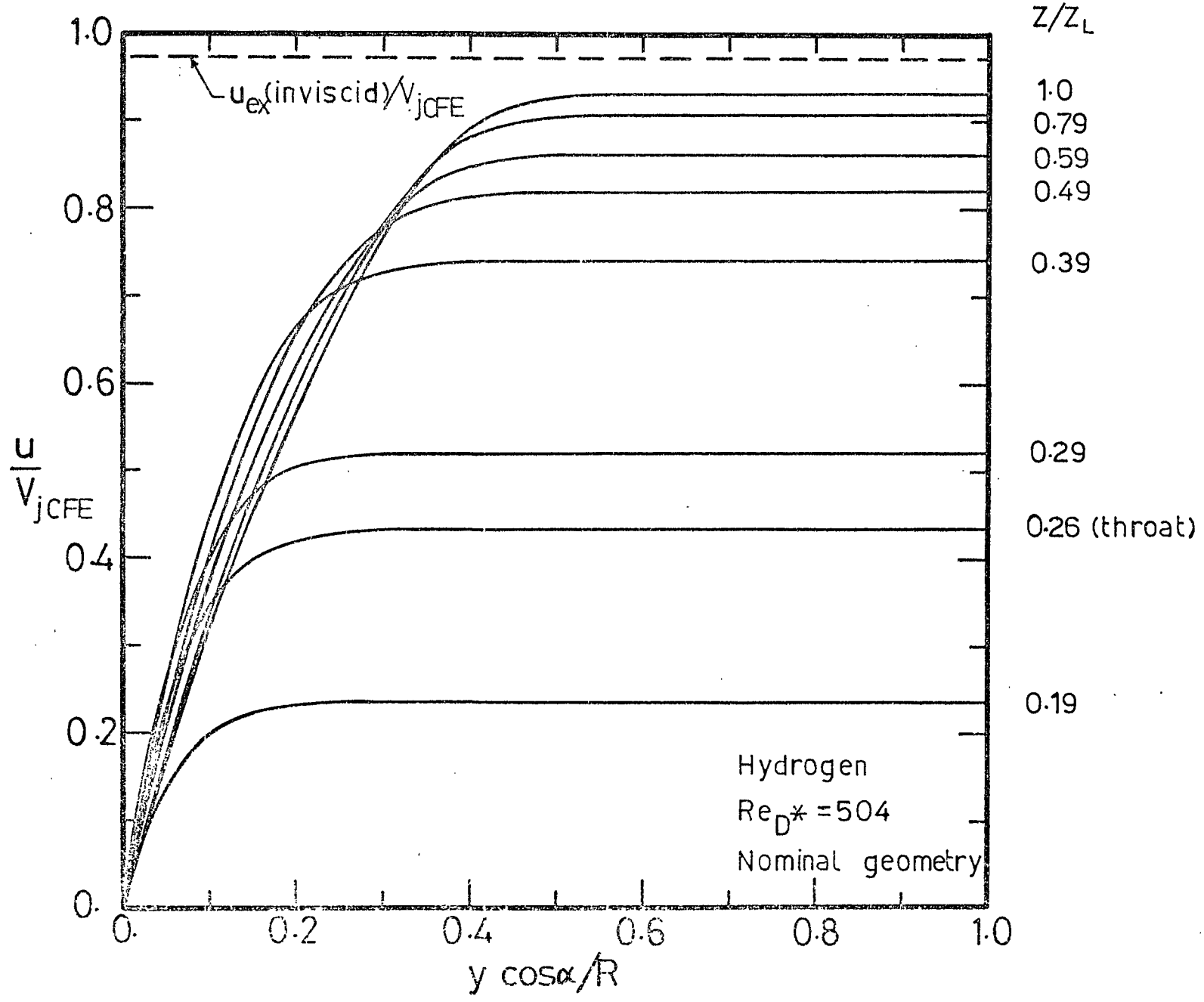

Fig.31 Radial Profiles of Axial Velocity

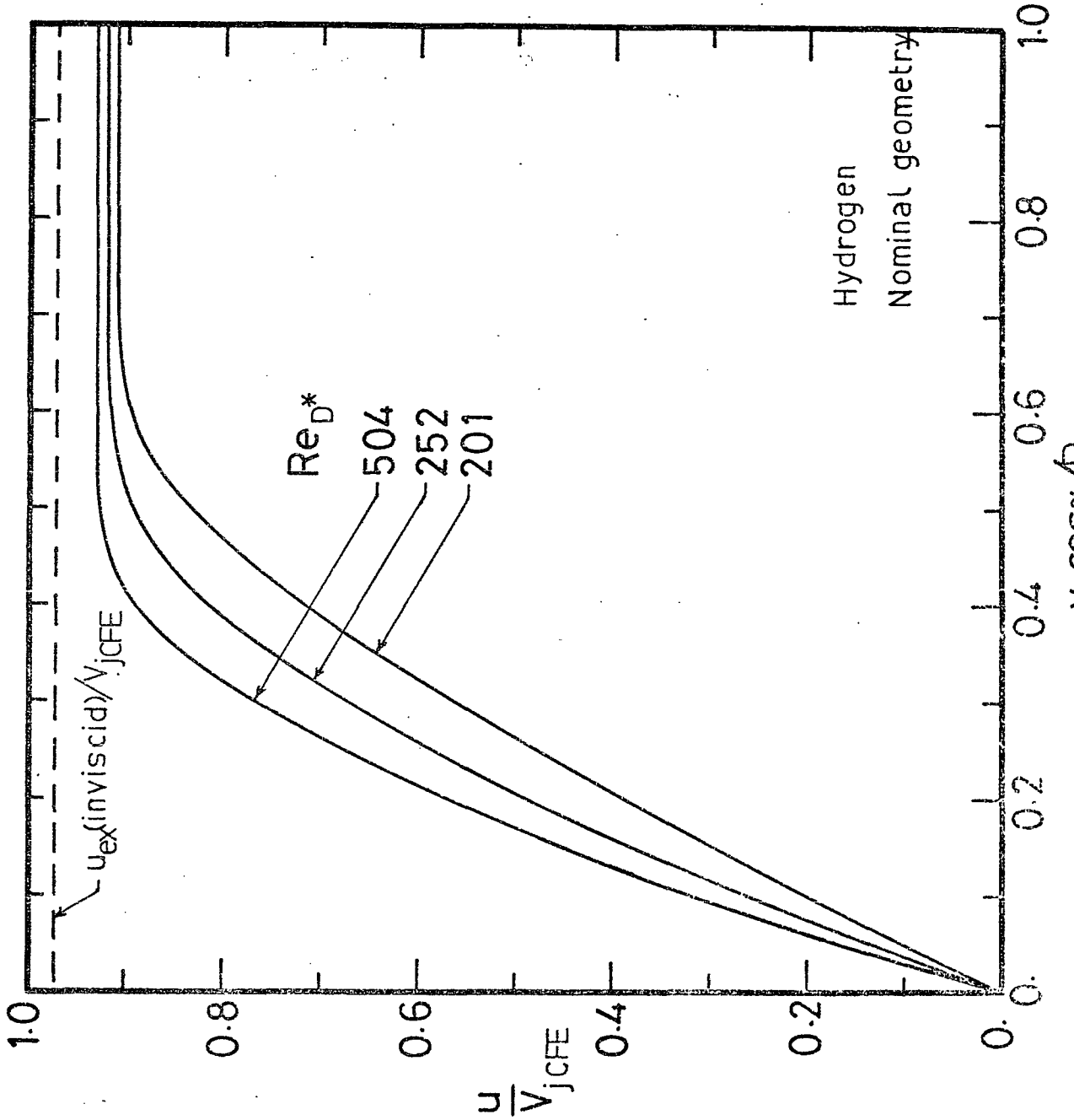

Fig.32 Velocity Profile at Nozzle Exit (Model One)

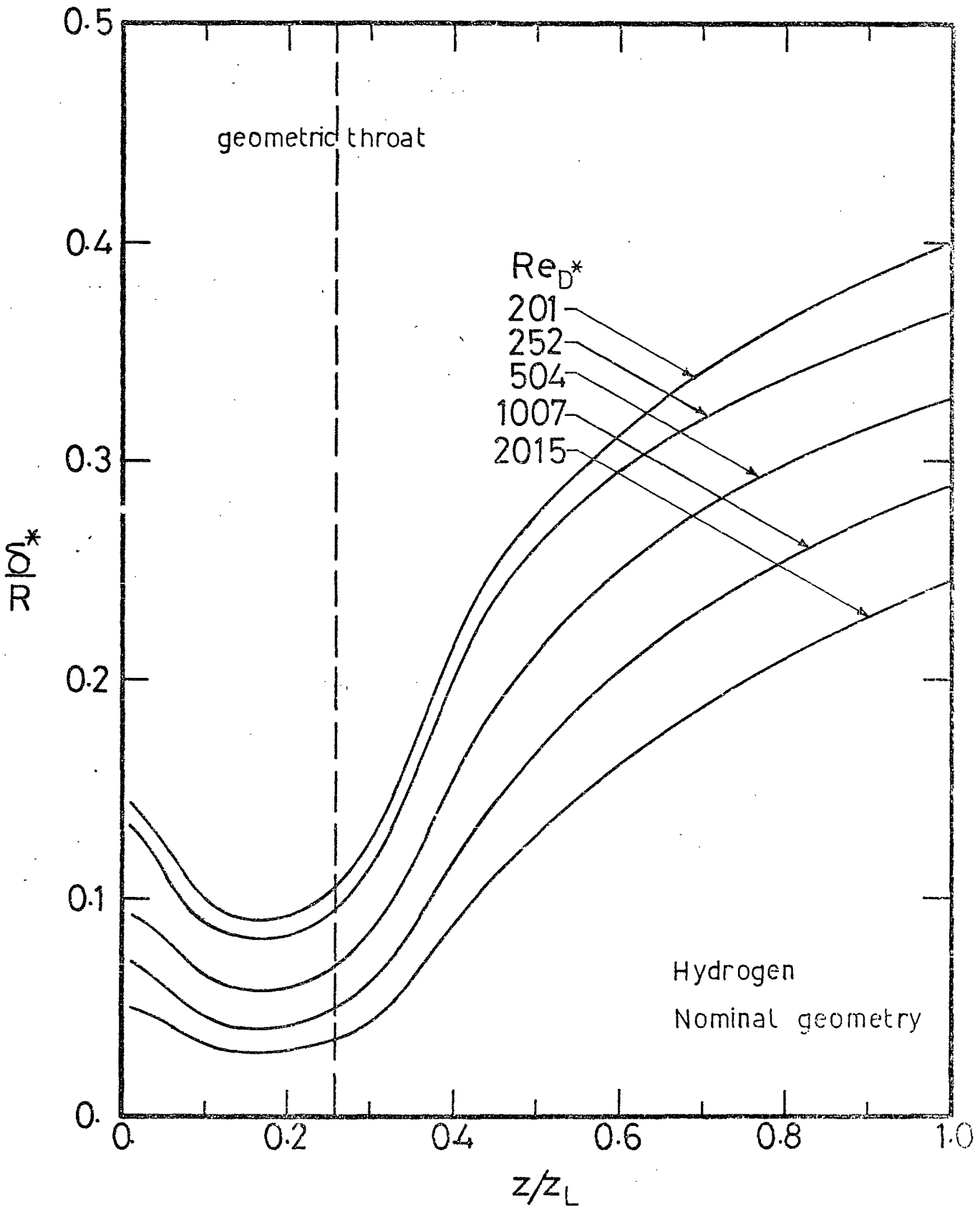

Fig.33 Development of Displacement Thickness (Model One)

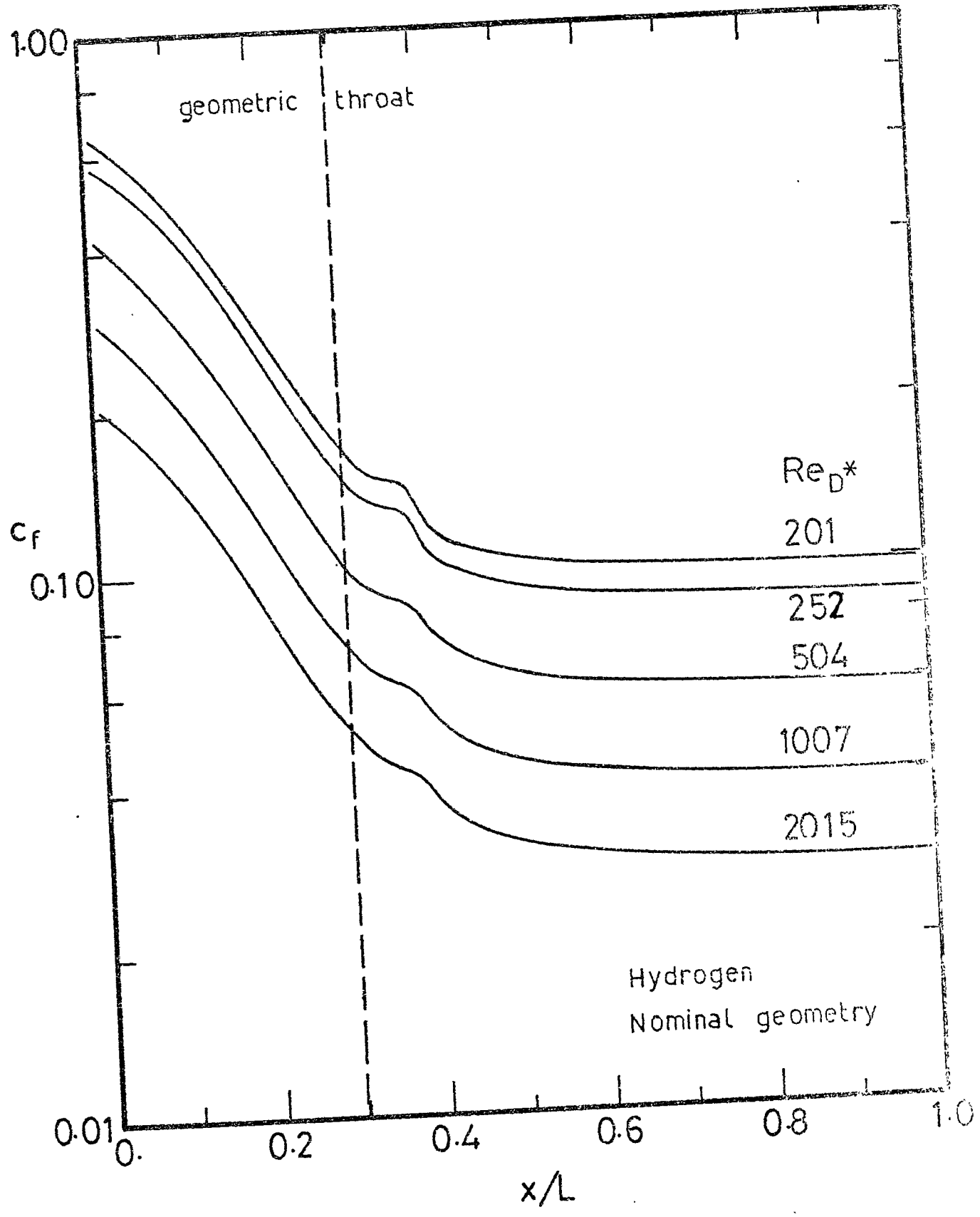

Fig.34 Skin Friction Coefficient (Model One)

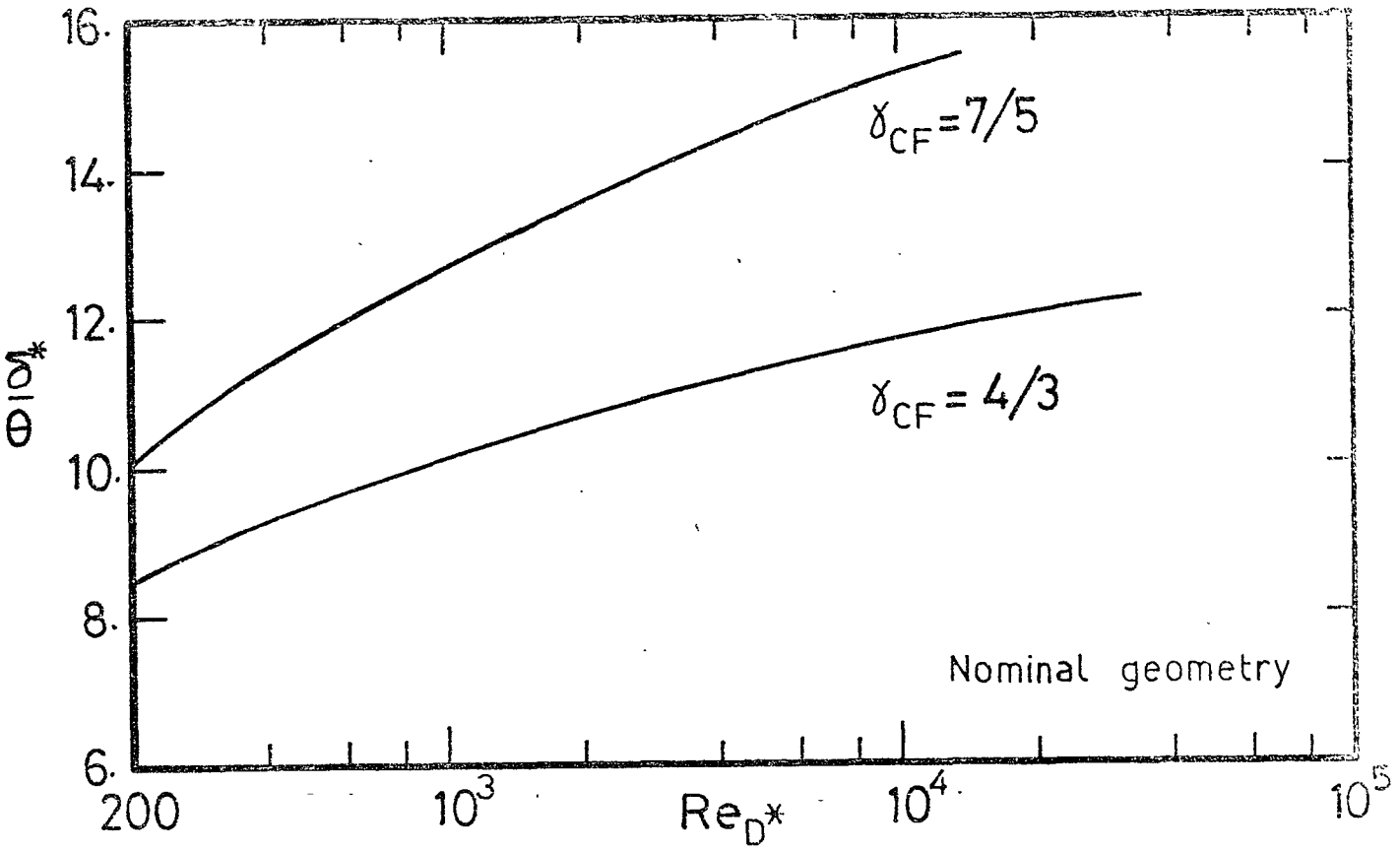

Fig·35a Variation of Form Factor at Nozzle Exit

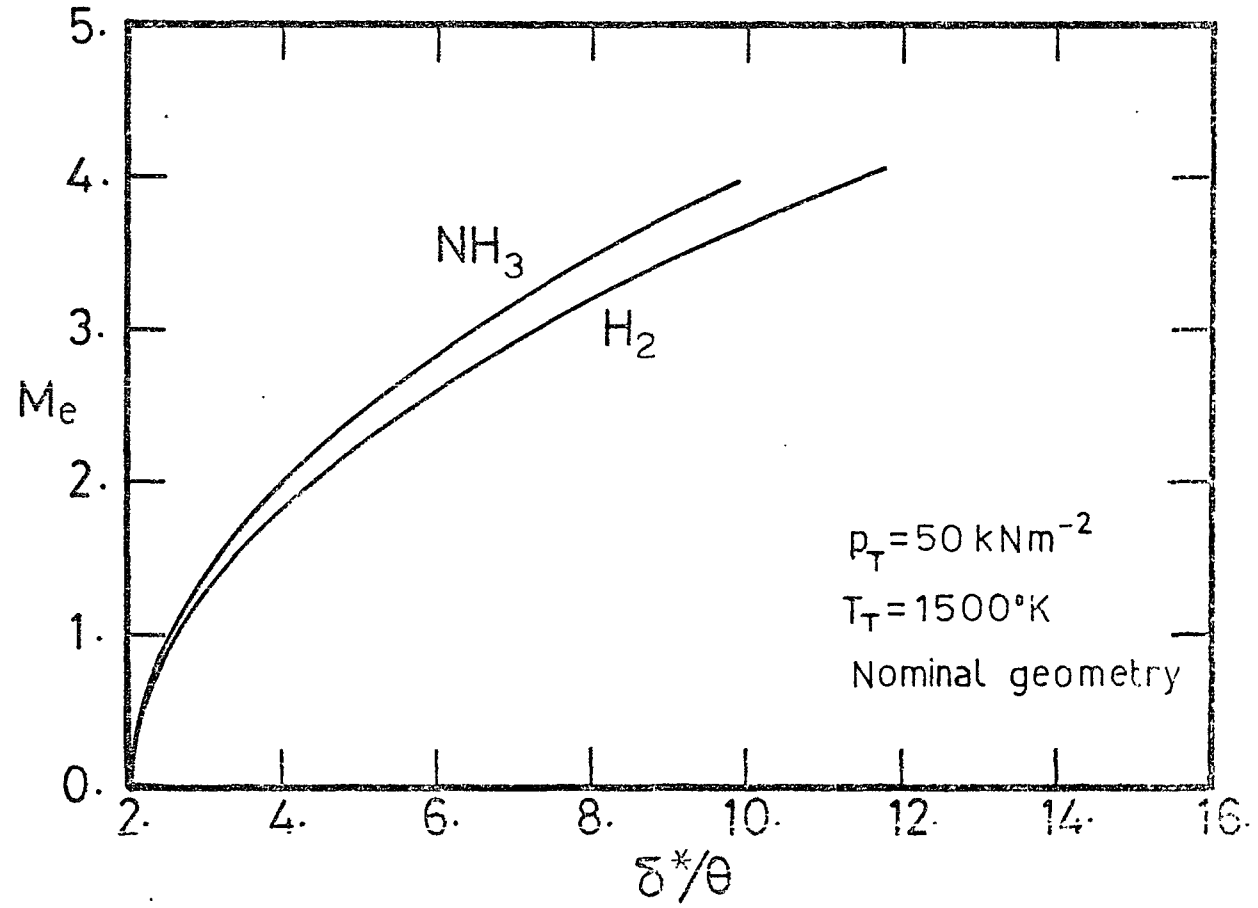

Fig·35b Variation of Form Factor with Mach Number

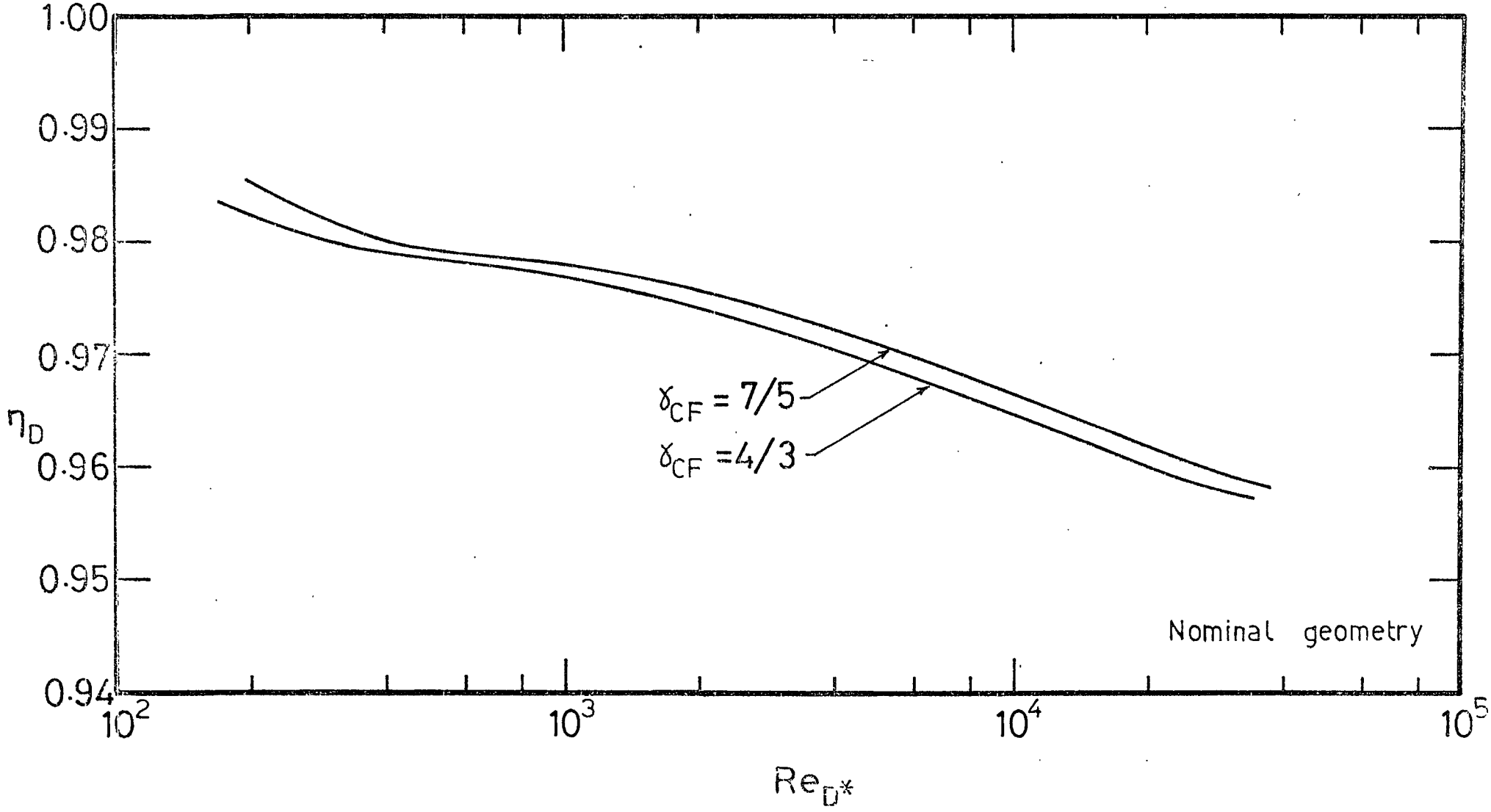

Fig·36 Radial Flow Loss (Model One)

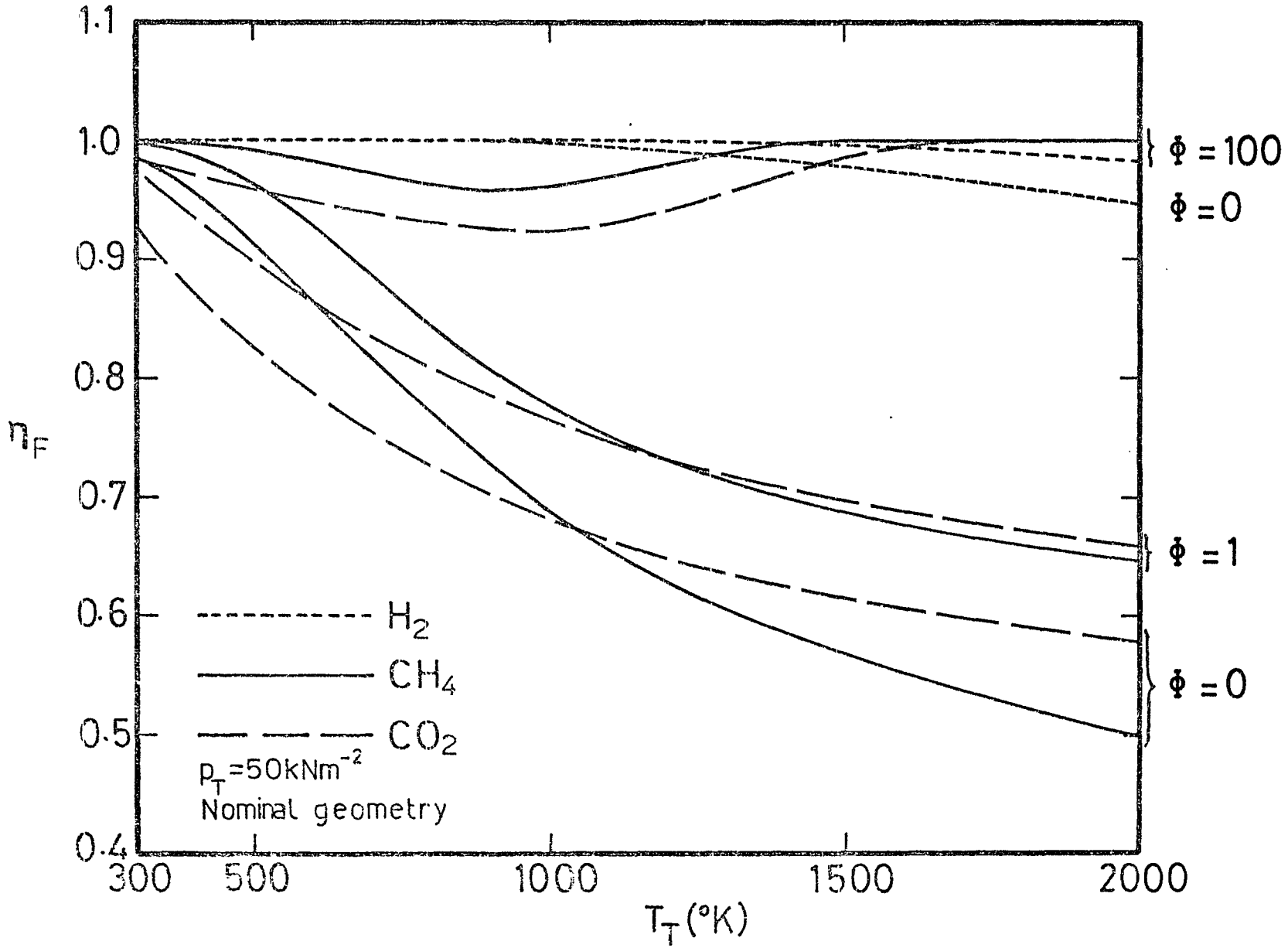

Fig·37 Vibrational Energy Losses of H_2, CO_2 and CH_4 (Model Two)

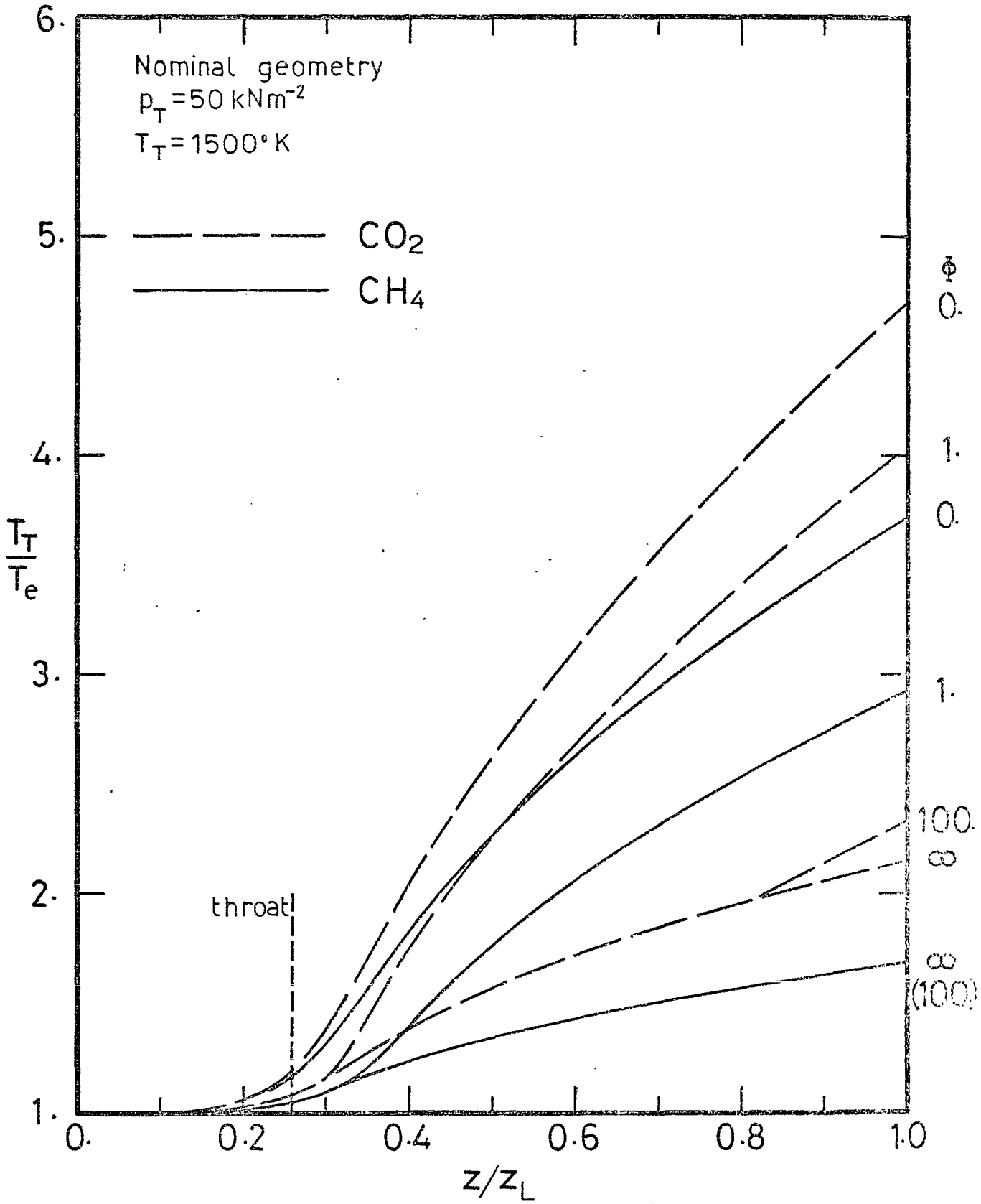

Fig.38 Axial Temperature Profiles for CH_4 & CO_2 (Model Two)

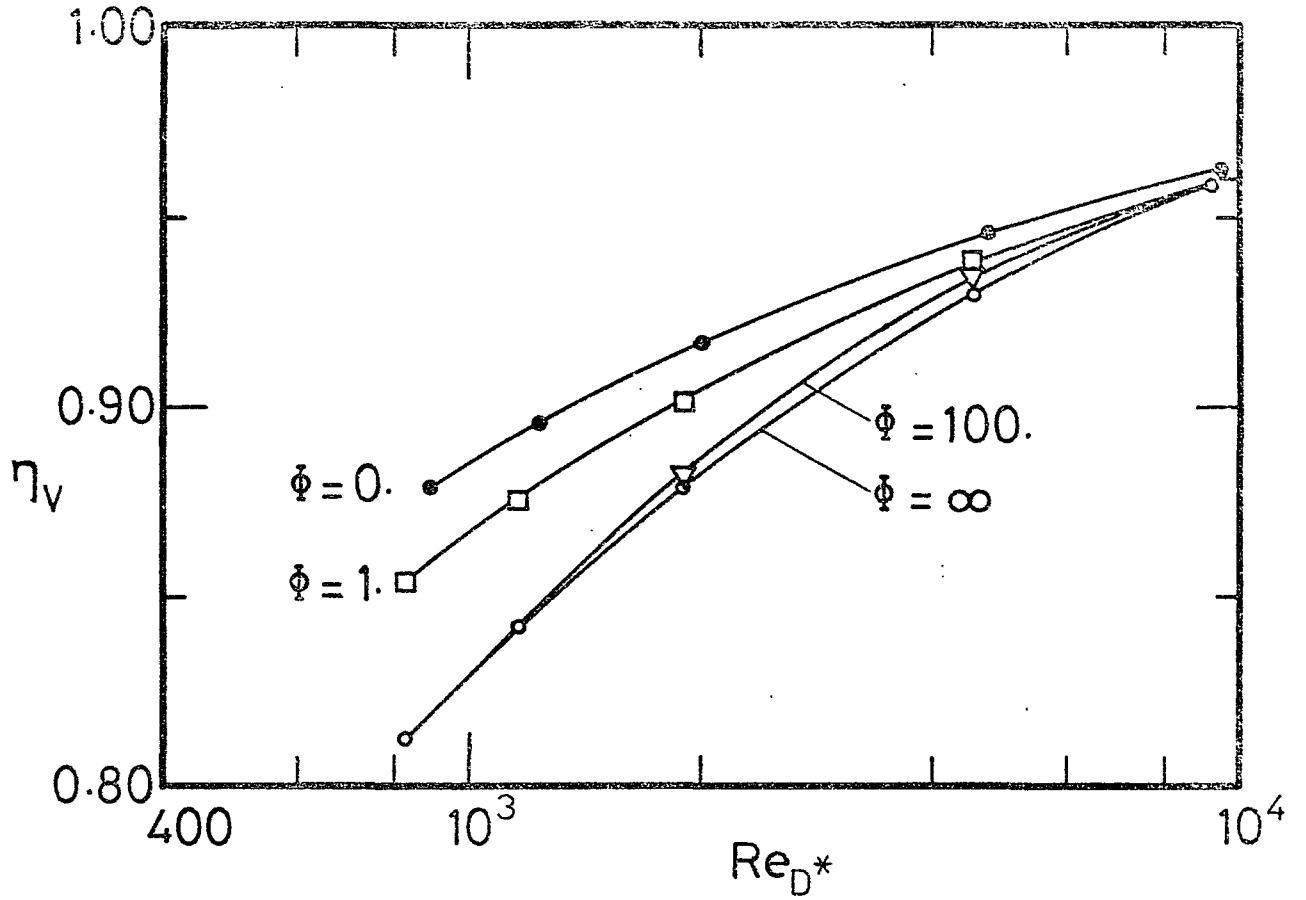

(a) Carbon dioxide

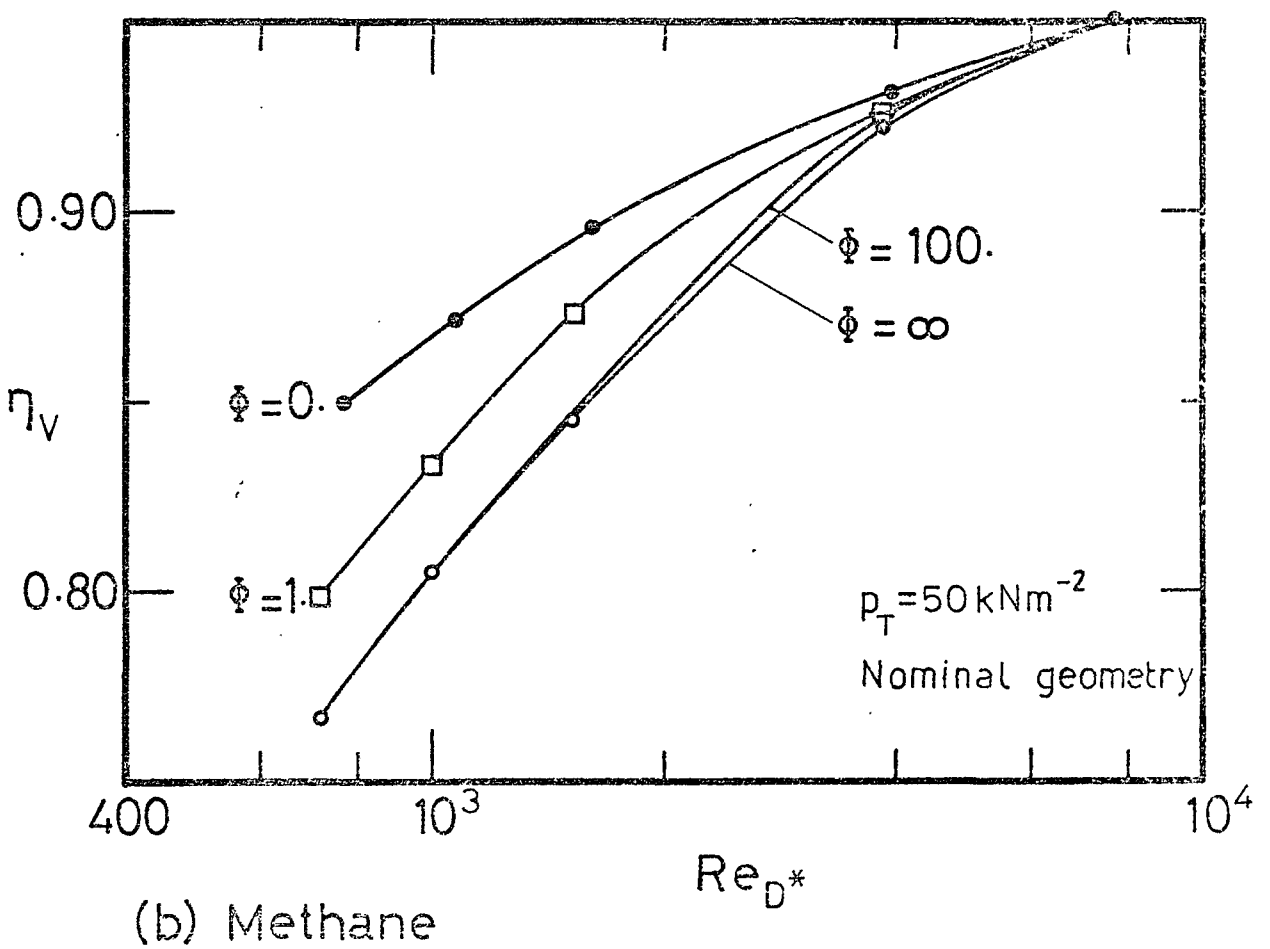

(b) Methane

Fig.39 Effect of Vibrational Rate Parameter, Φ, on η_V

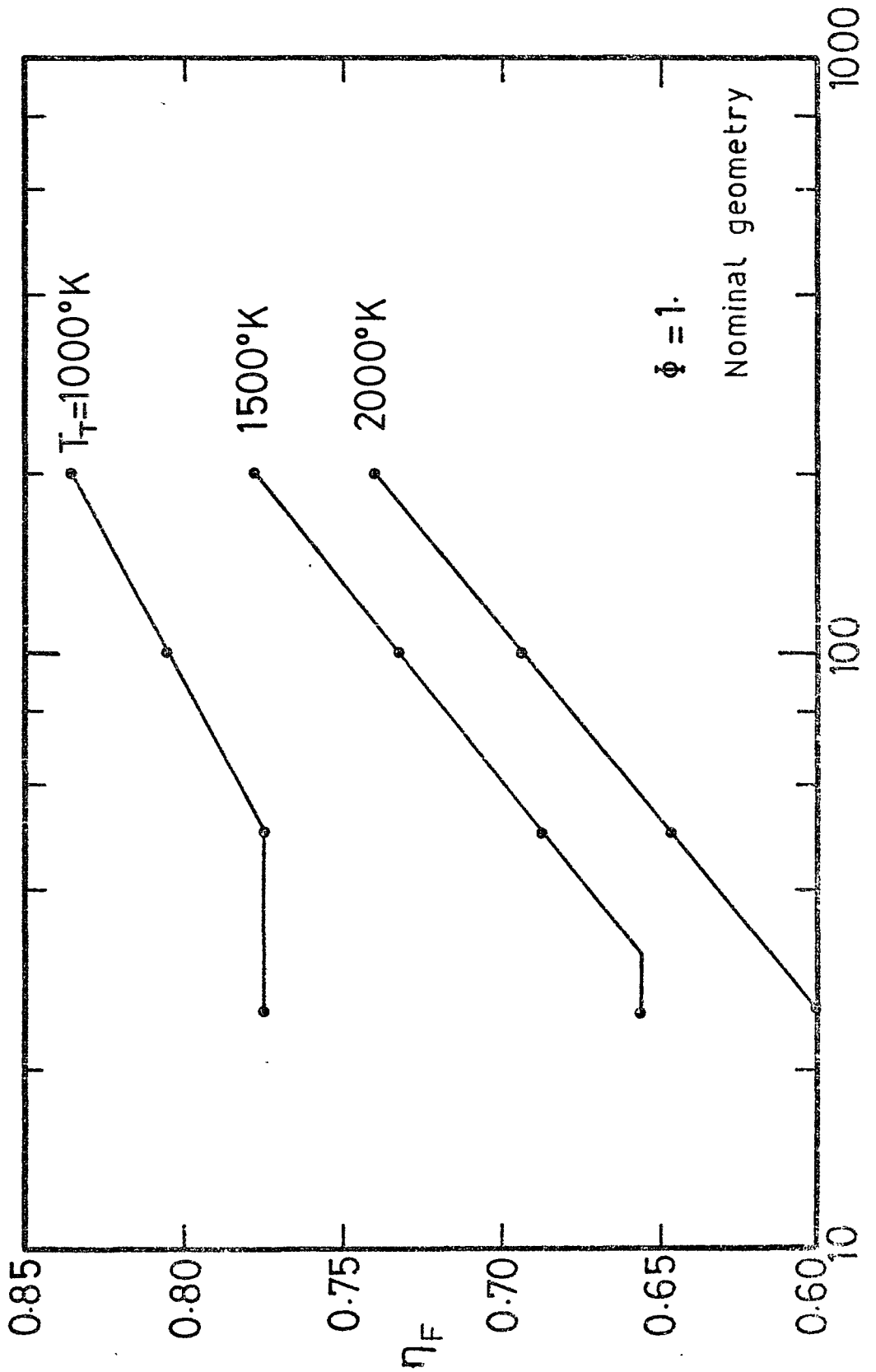

Fig·40 Effect of Plenum Pressure on Vibrational Energy Loss of CH_4

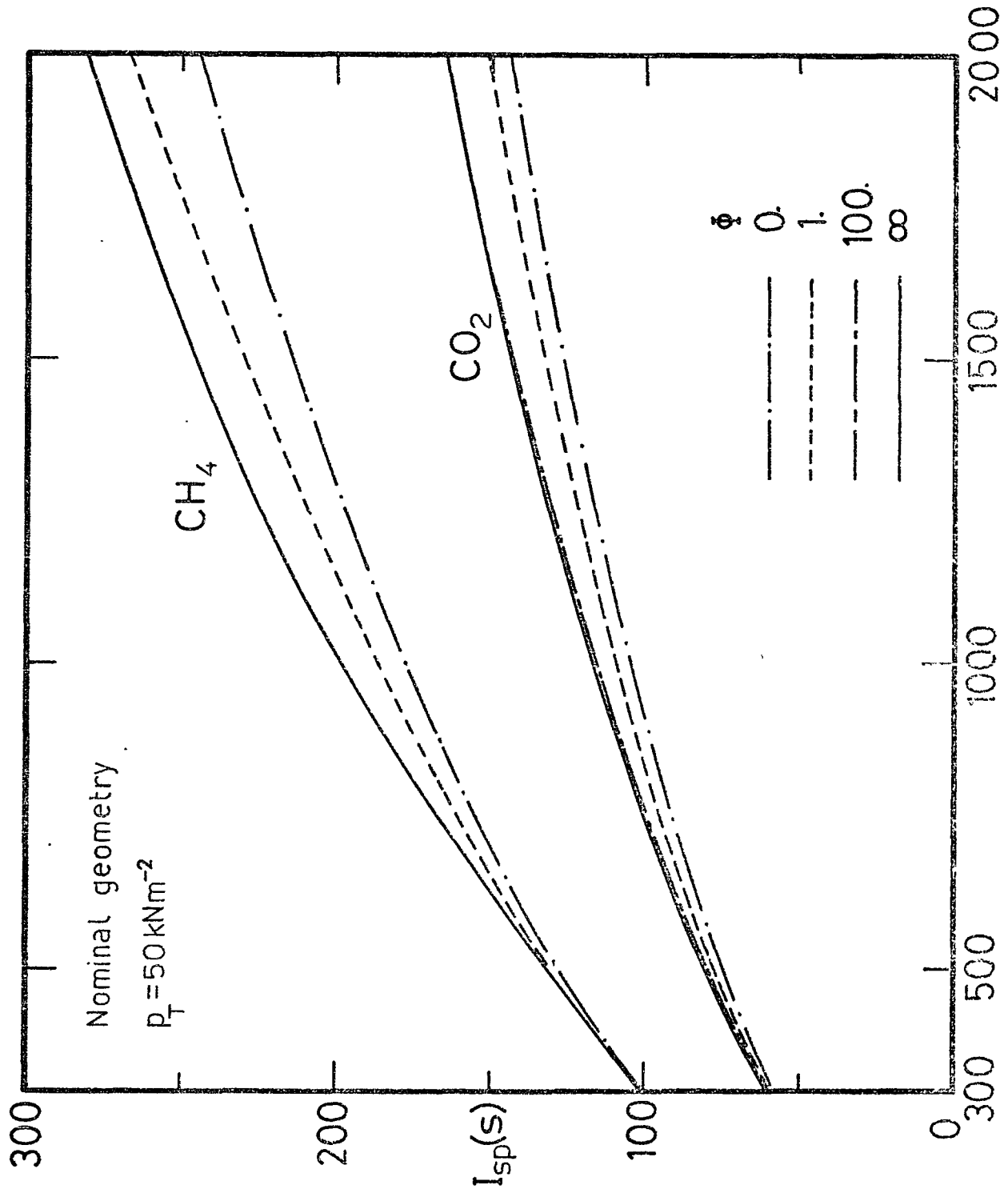

Fig·41 Effect of Vibrational Relaxation on Performance of CH_4 & CO_2

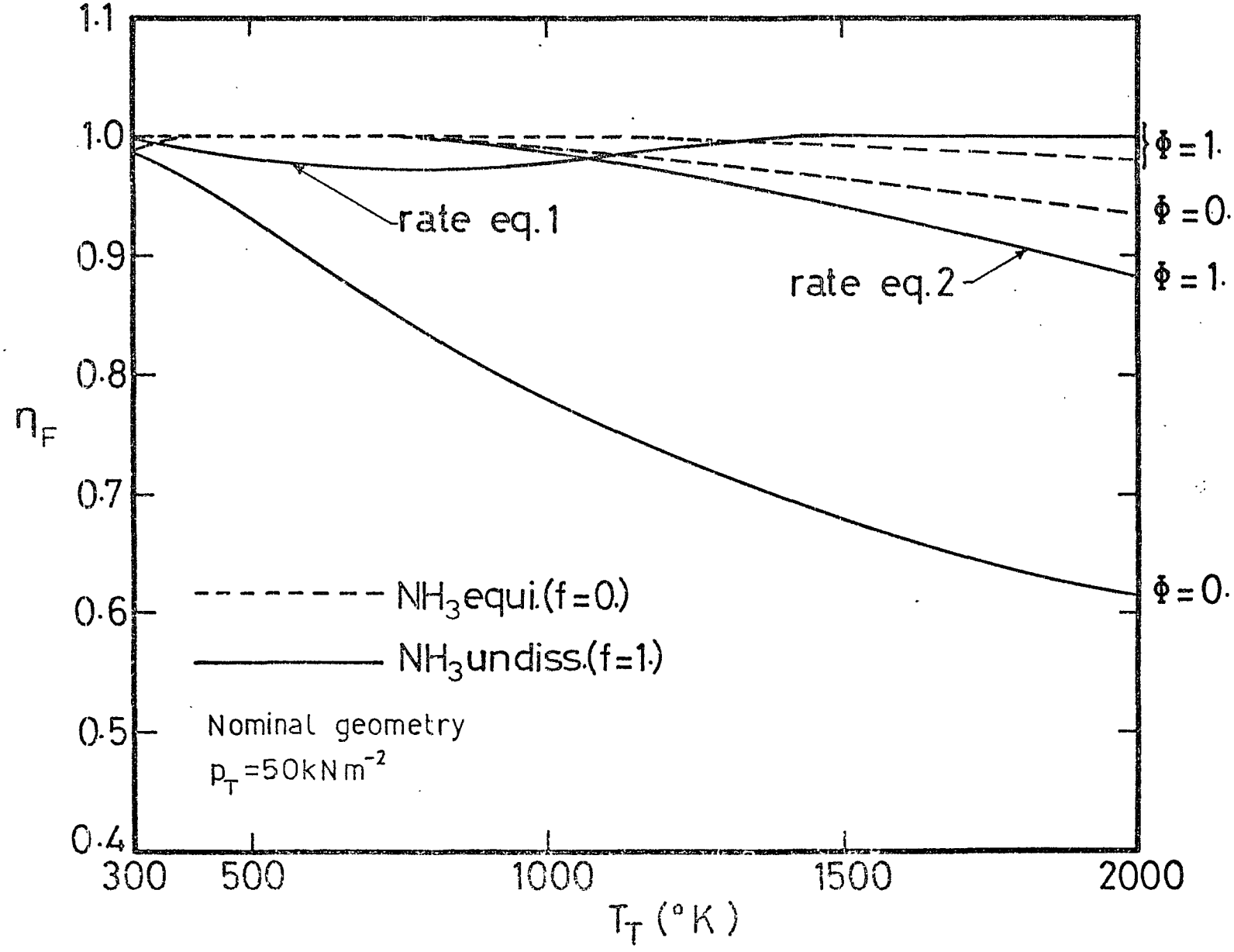

Fig·42 Vibrational Energy Loss of NH_3

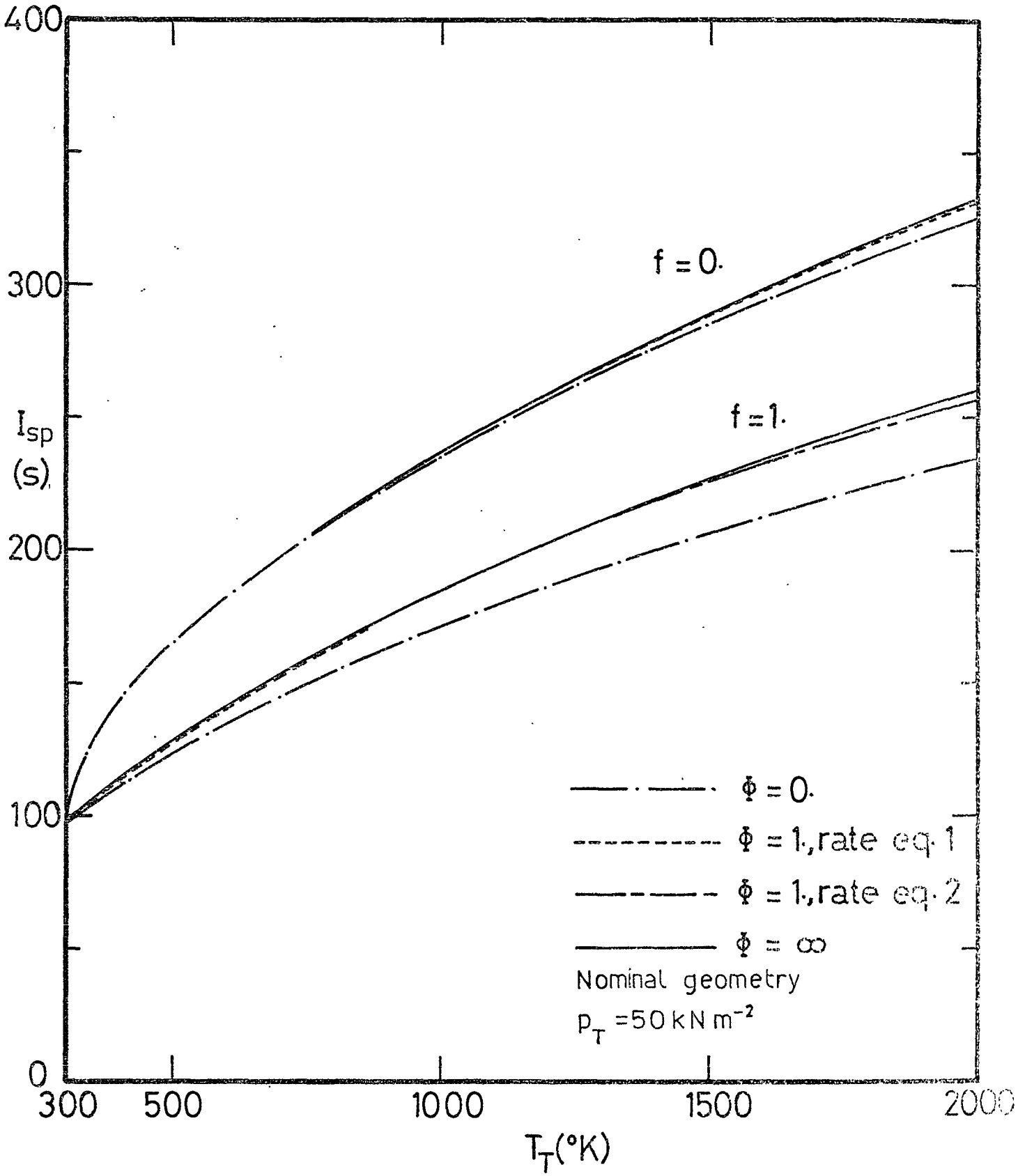

Fig. 43 Effect of Vibrational Relaxation on Performance of NH_3

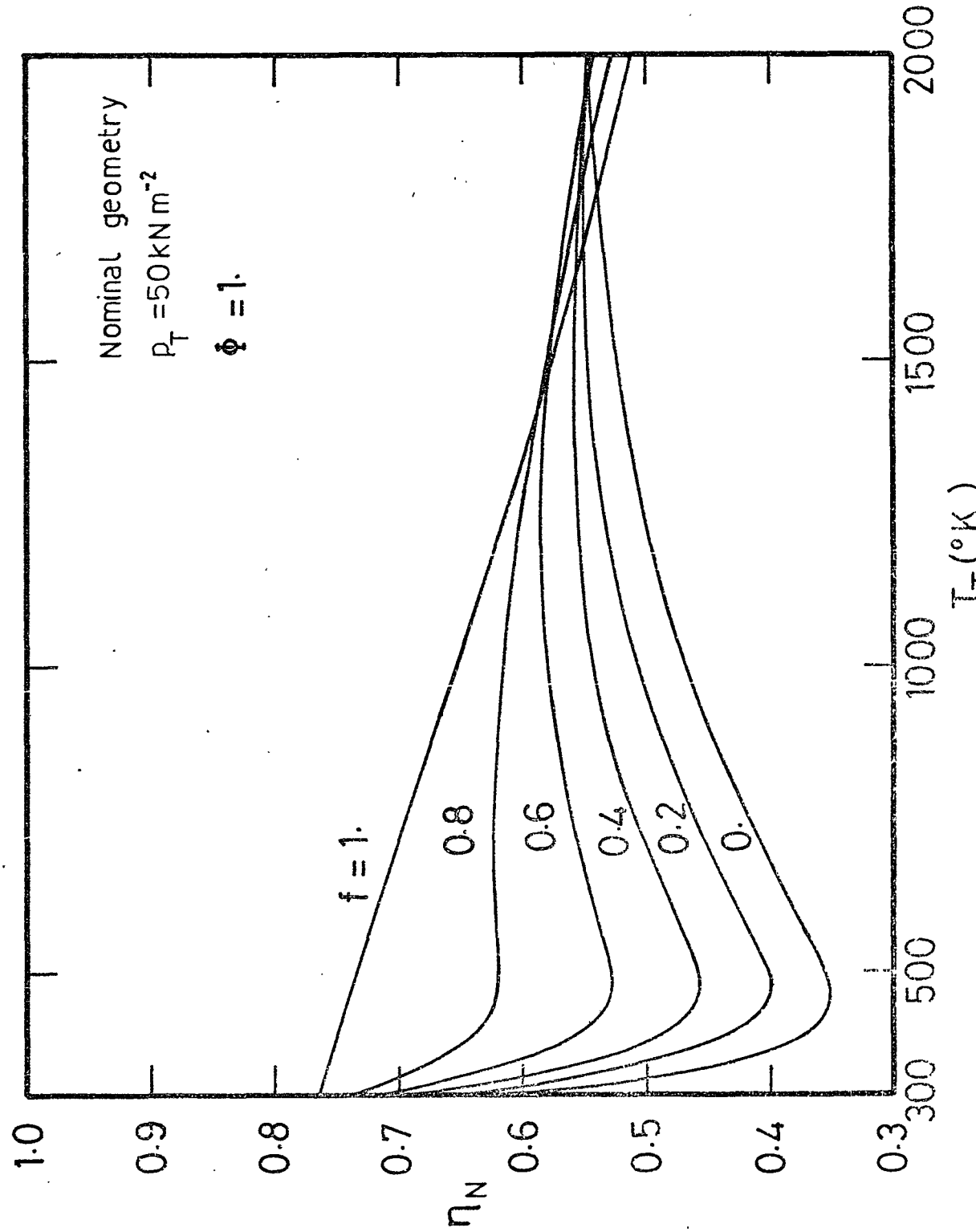

Fig.44 Variation in Nozzle Efficiency with NH_3 Dissociation

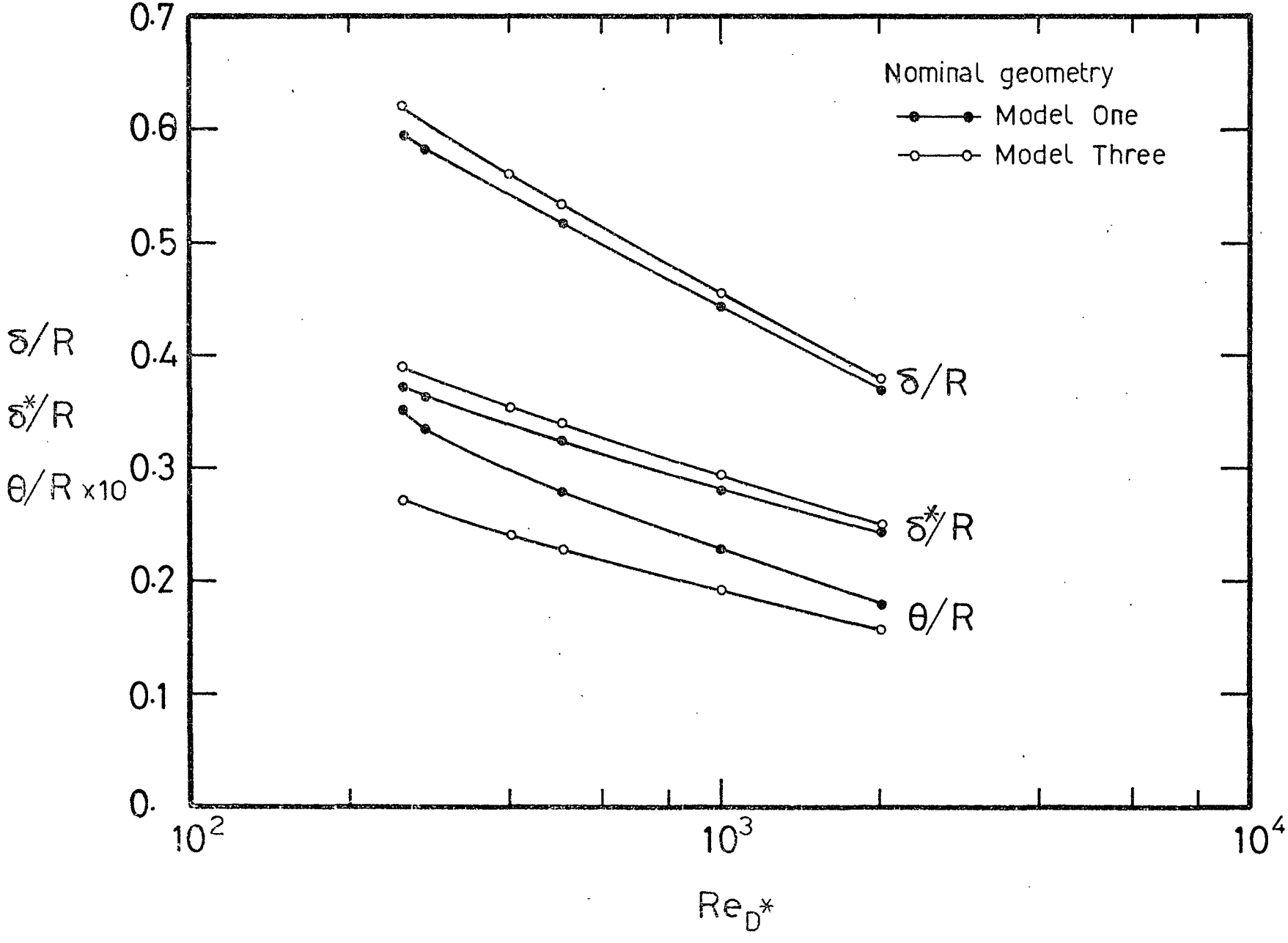

Fig.45 Boundary Layer Thicknesses at Nozzle Exit (Models One & Three)

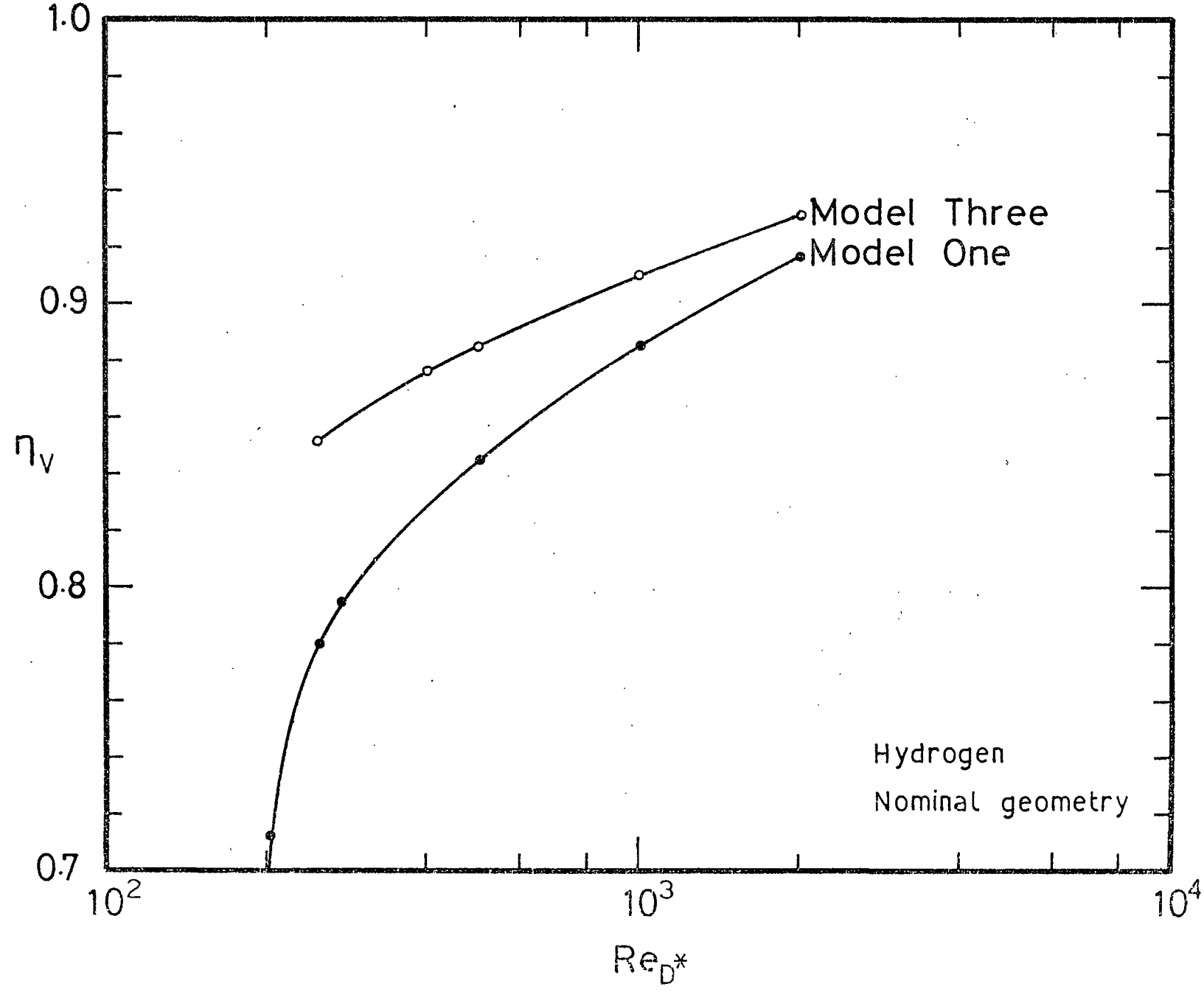

Fig.46 Viscous Flow Velocity Defect — Comparison of Models One & Three

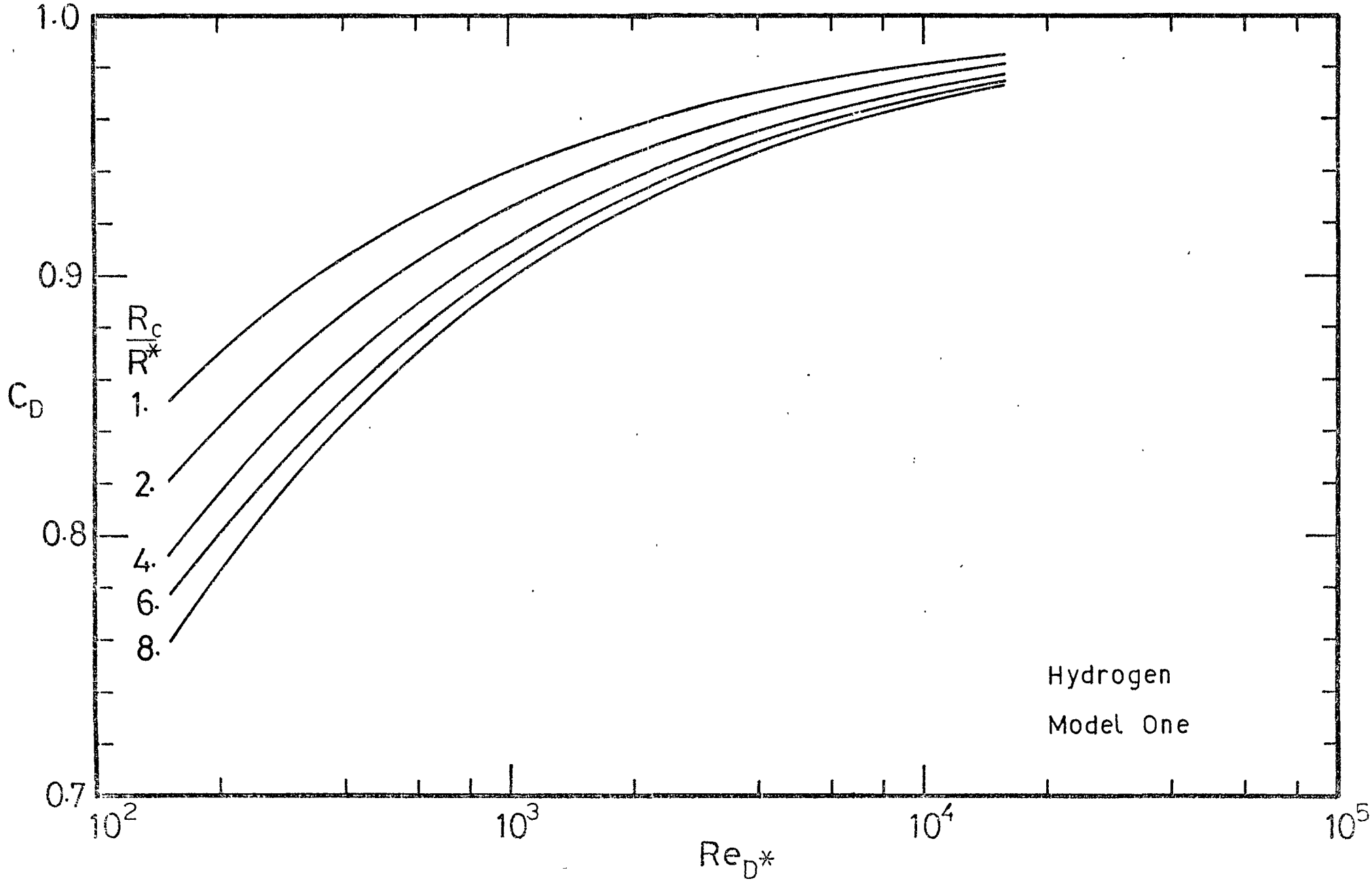

Fig.47 Variation of Discharge Coefficient with Throat Geometry

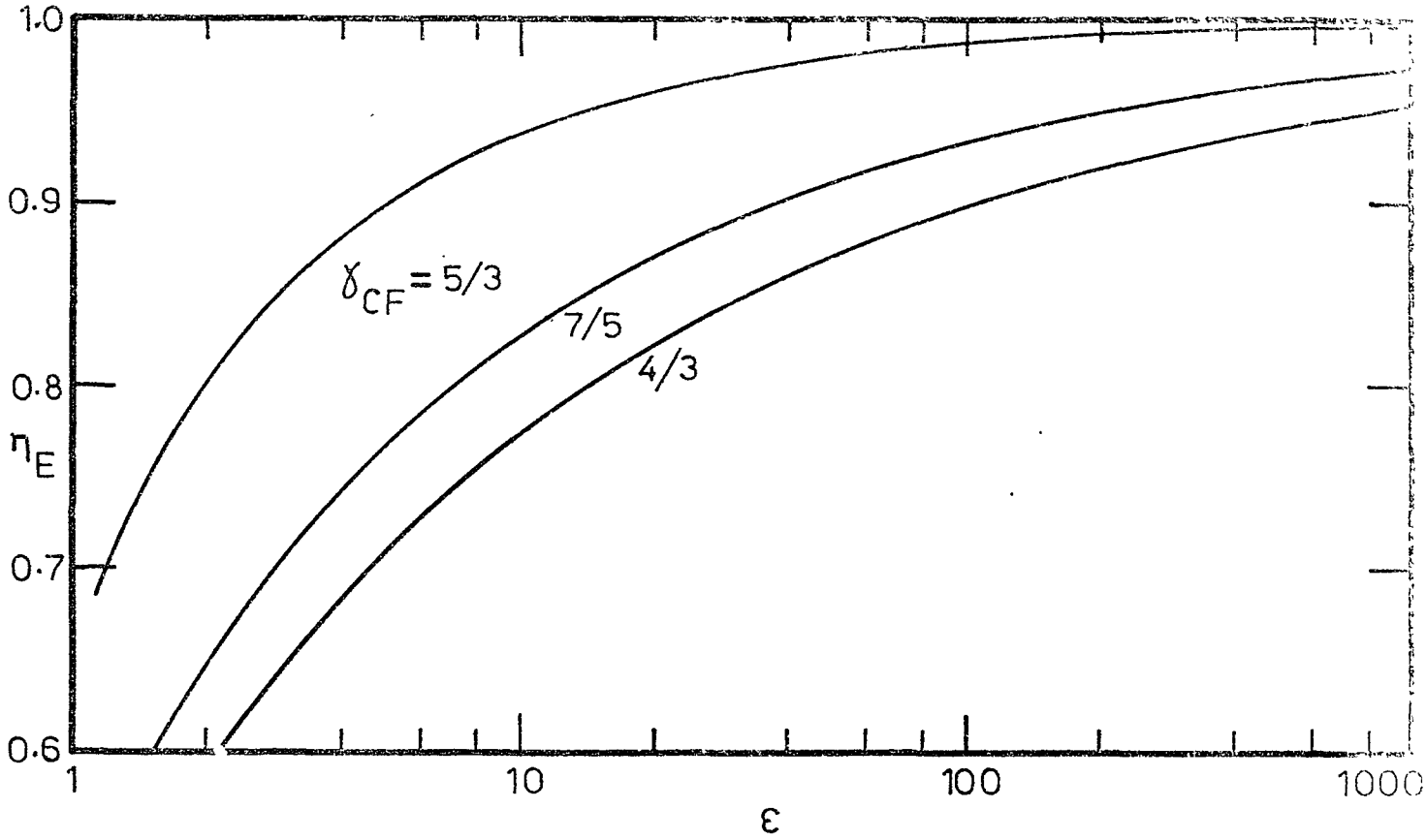

(a) Vibrational Energy Frozen

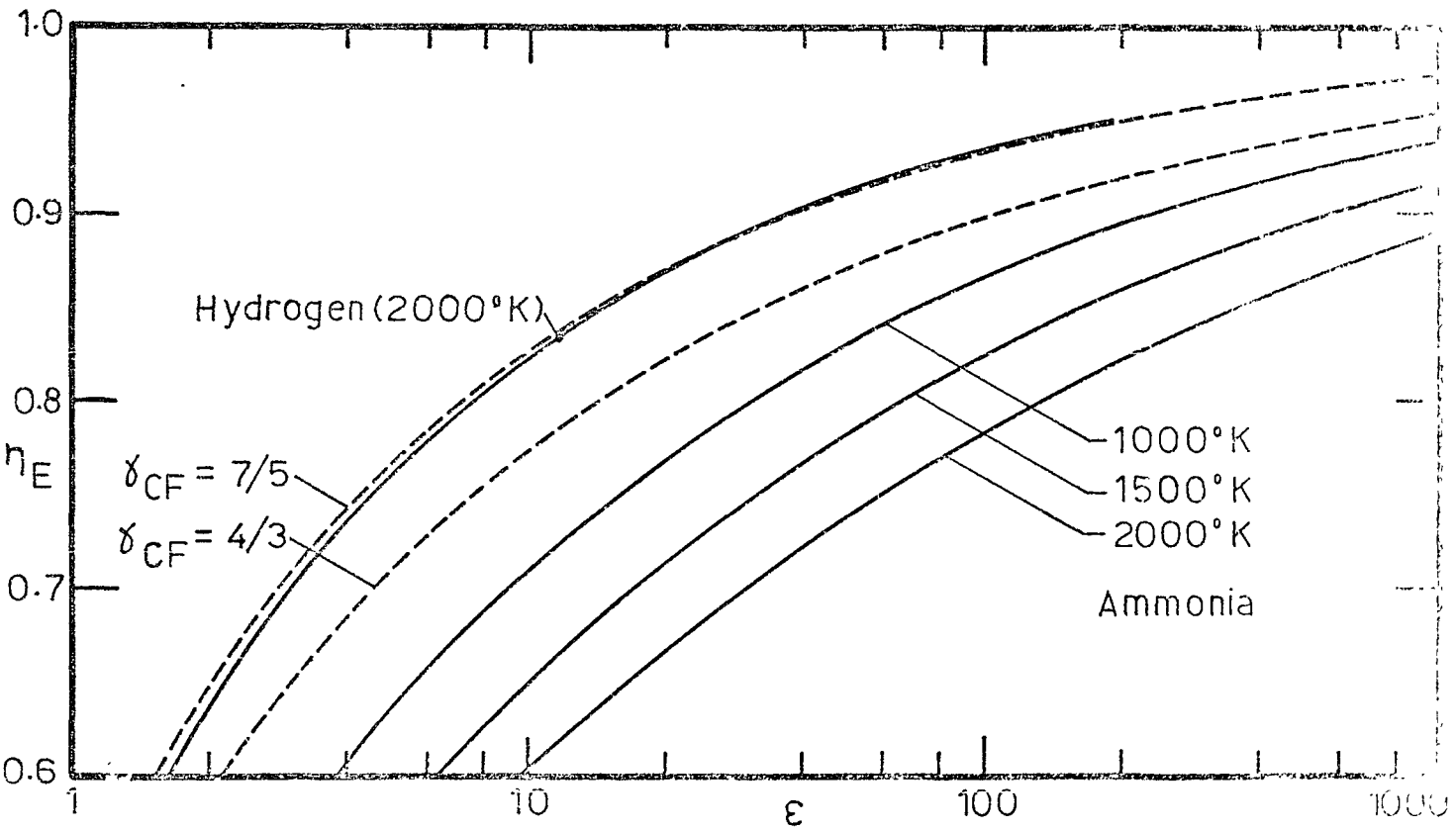

(b) Vibrational Energy in Equilibrium H_2 & NH_3

Fig.48 Incomplete Expansion Loss

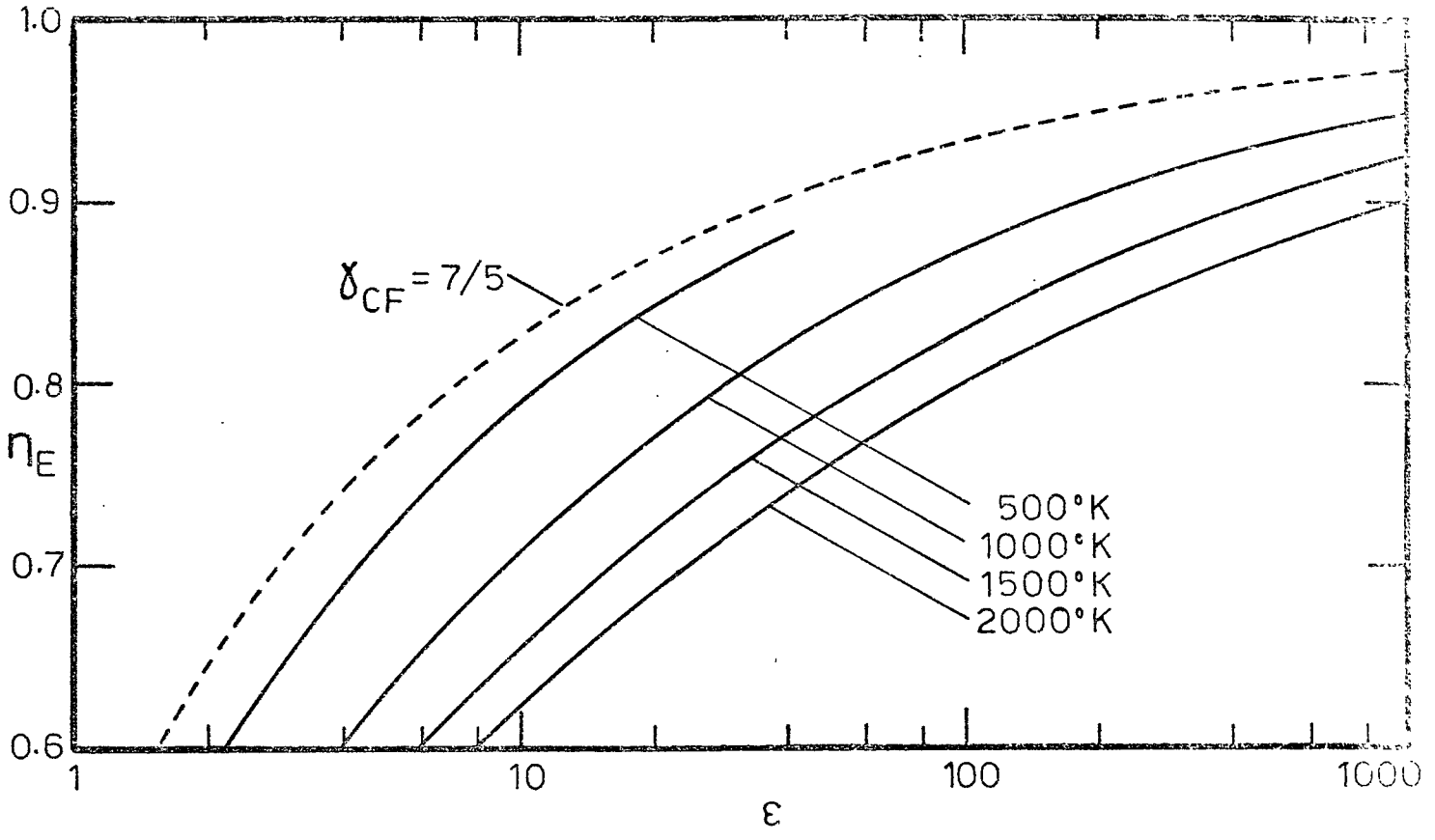

(c) Carbon Dioxide

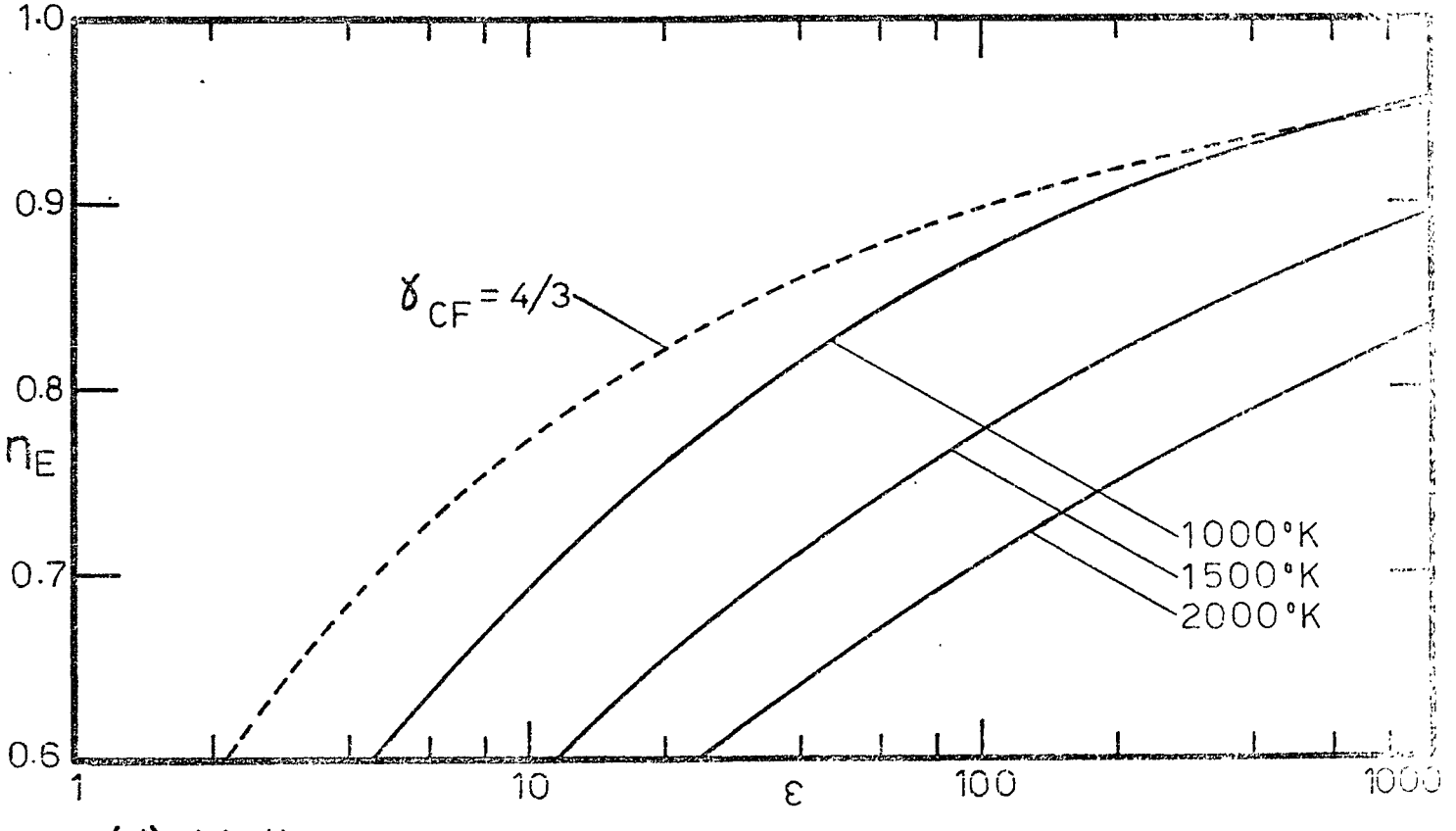

(d) Methane

Fig.48cont. Equilibrium Vibrational Energy

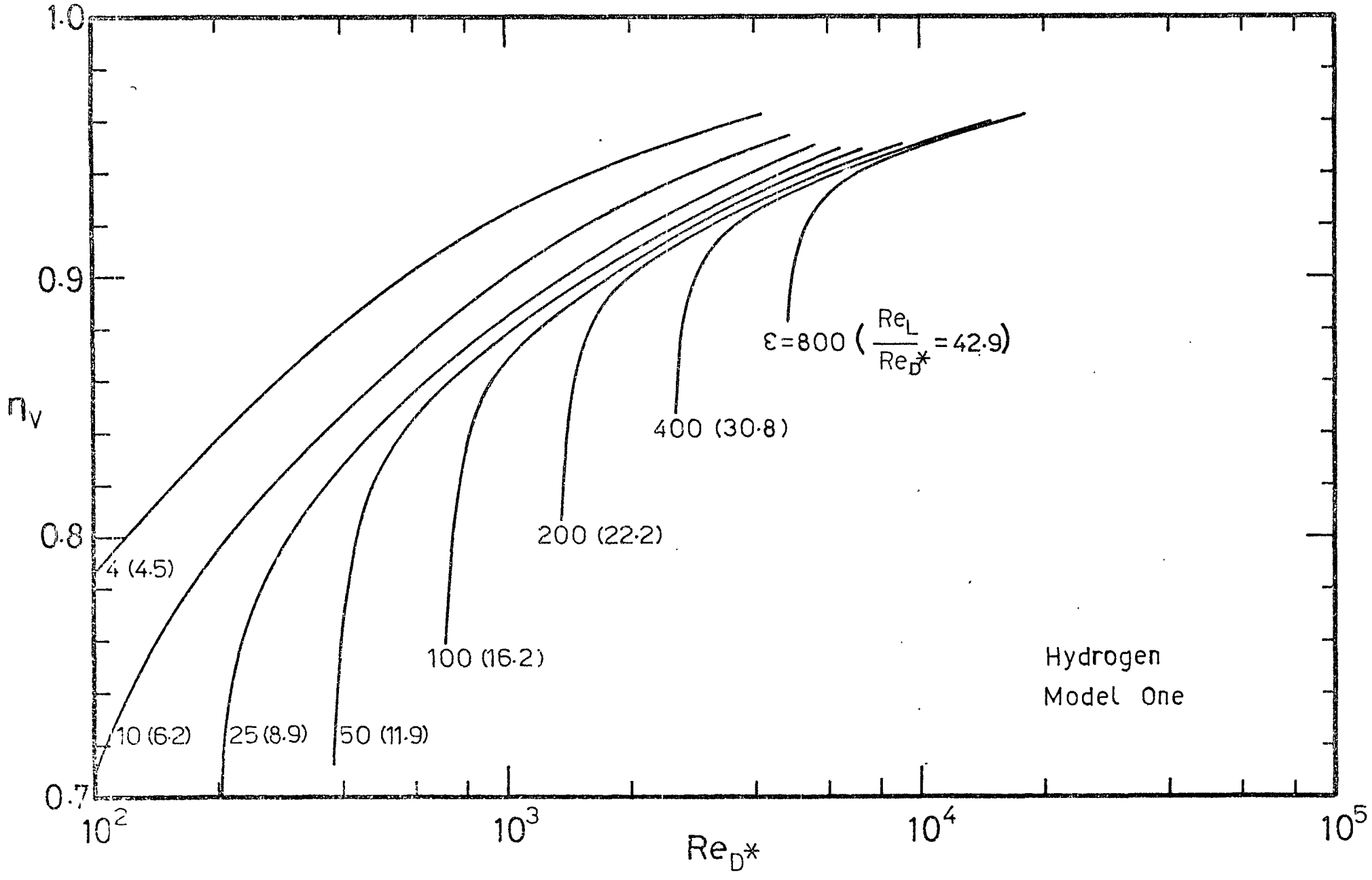

Fig·49 Dependence of Viscous Flow Loss on Nozzle Area Ratio

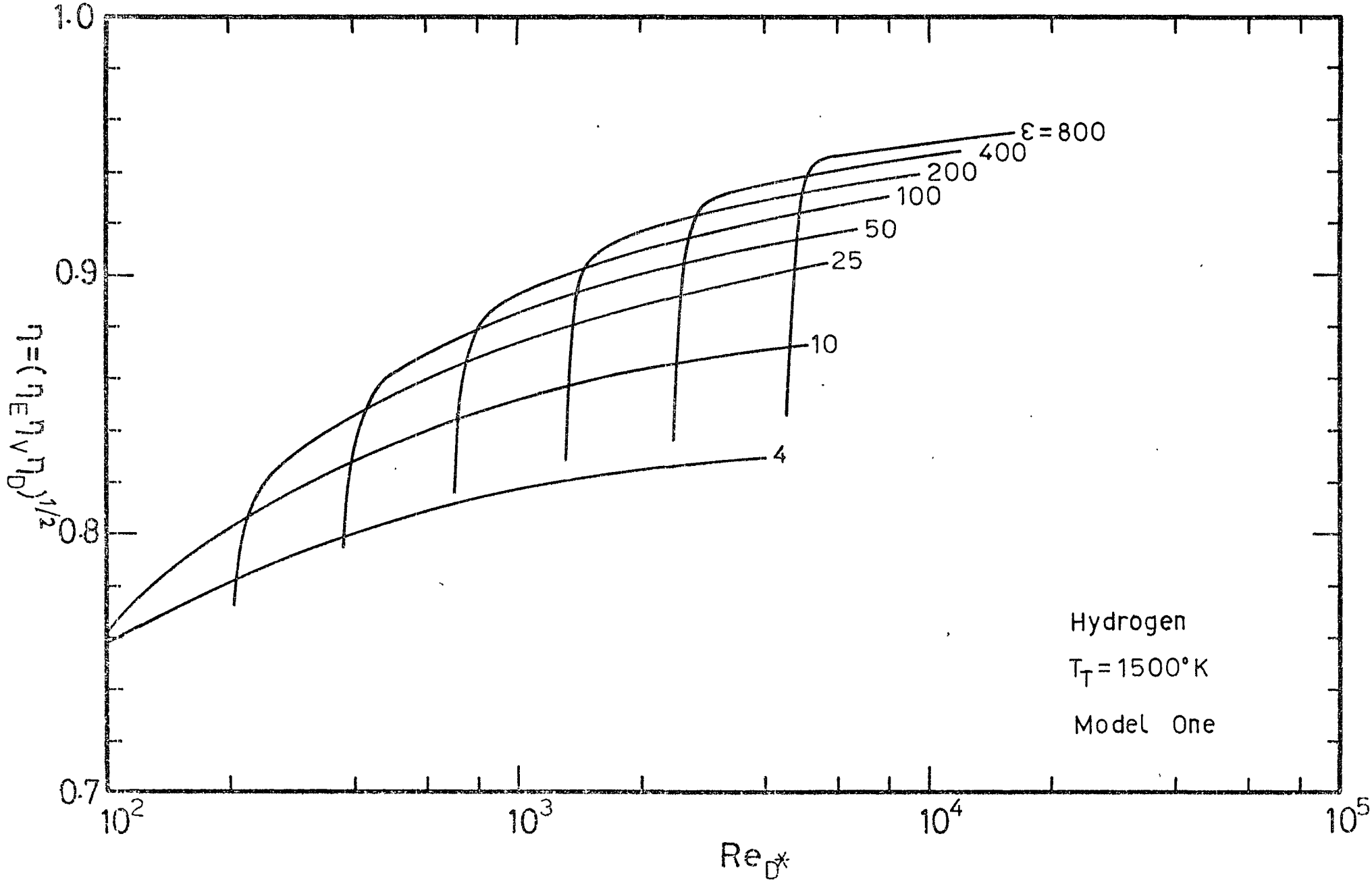

Fig.50 Variation of Nozzle Efficiency with Area Ratio

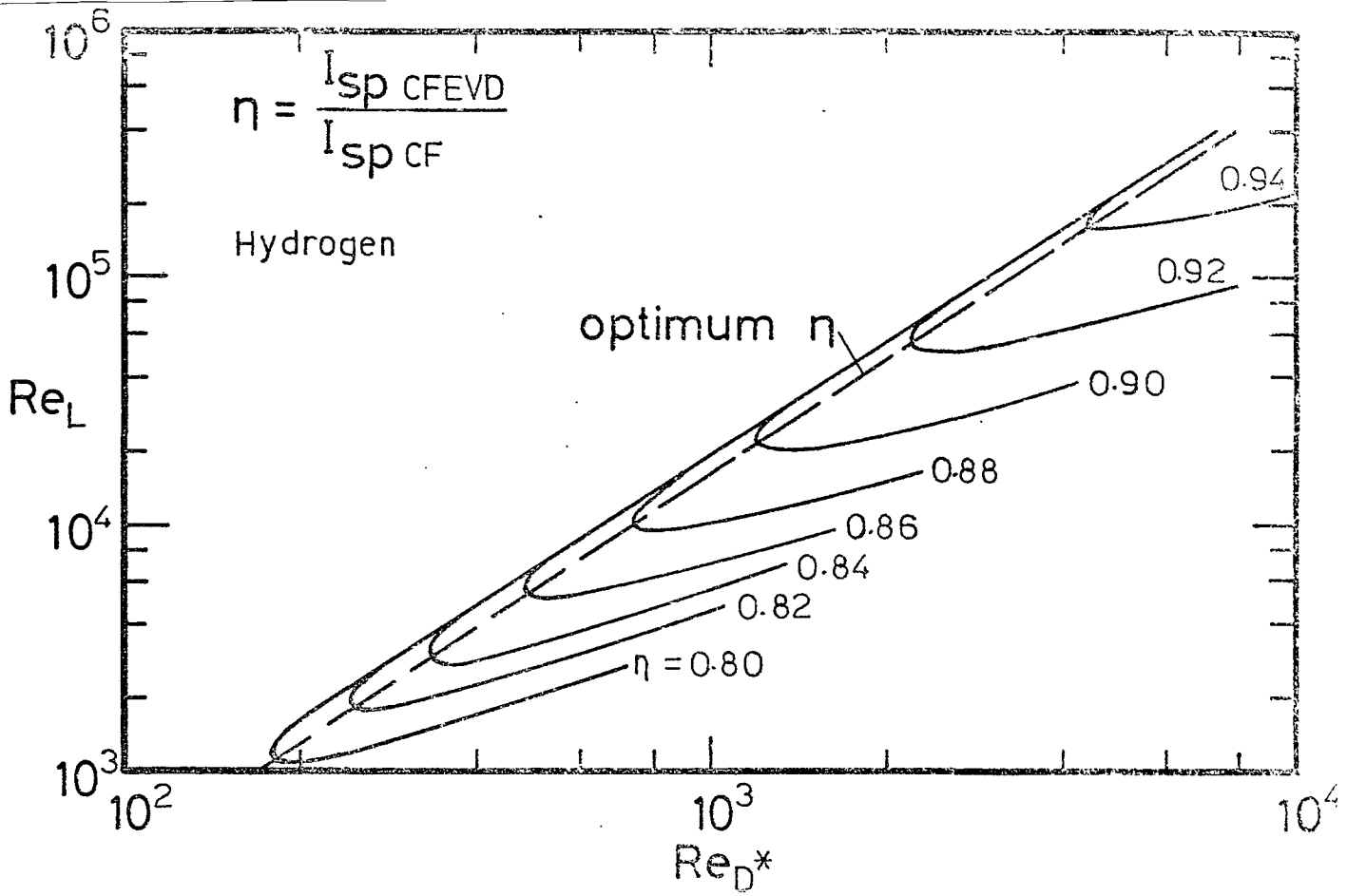

(a) Variation in Efficiency with Re_L and Re_{D^*}

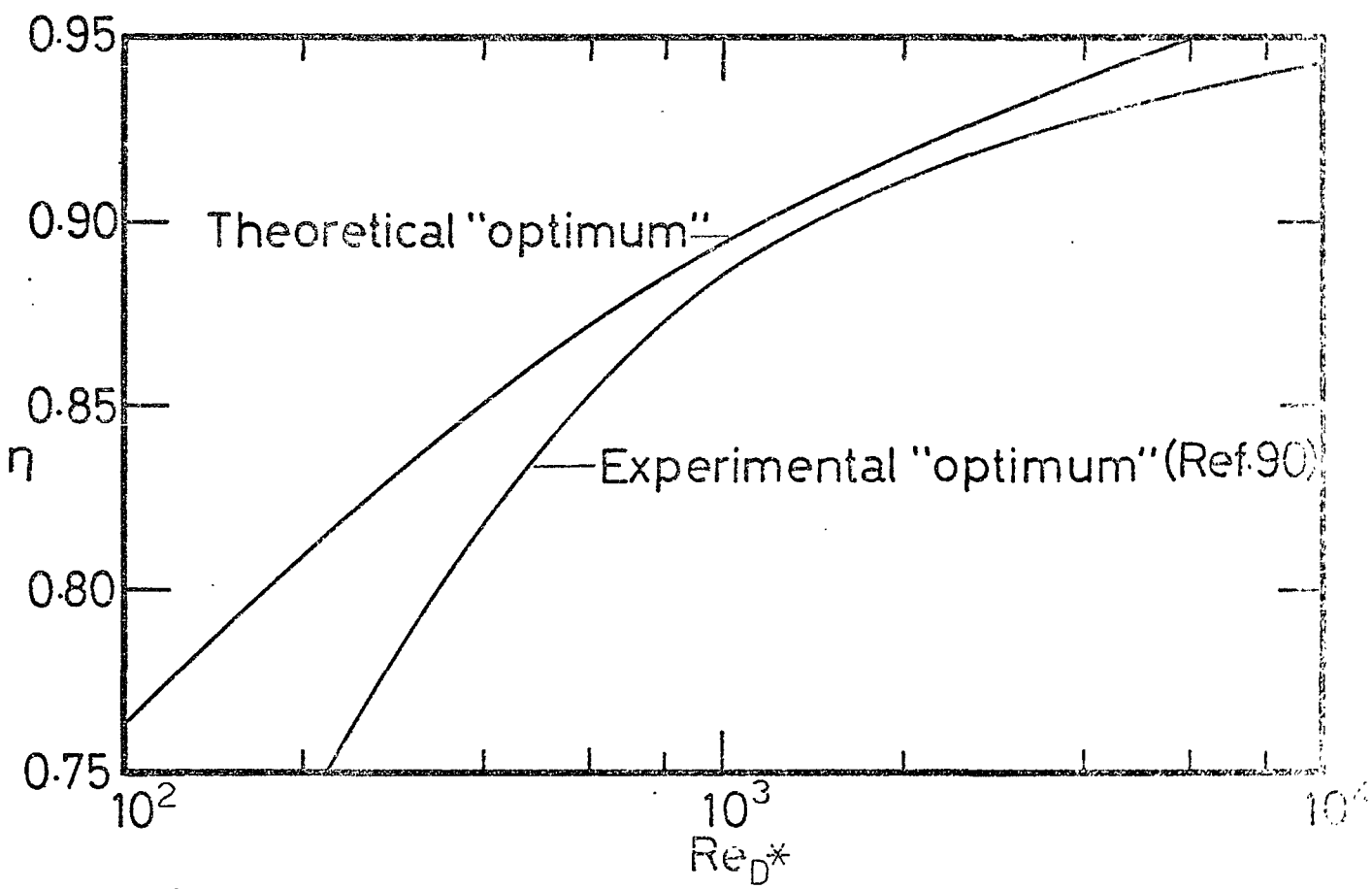

(b) An "Optimum" Efficiency - Re_{D^*} Correlation

Fig.51 Optimisation of Nozzle Area Ratio

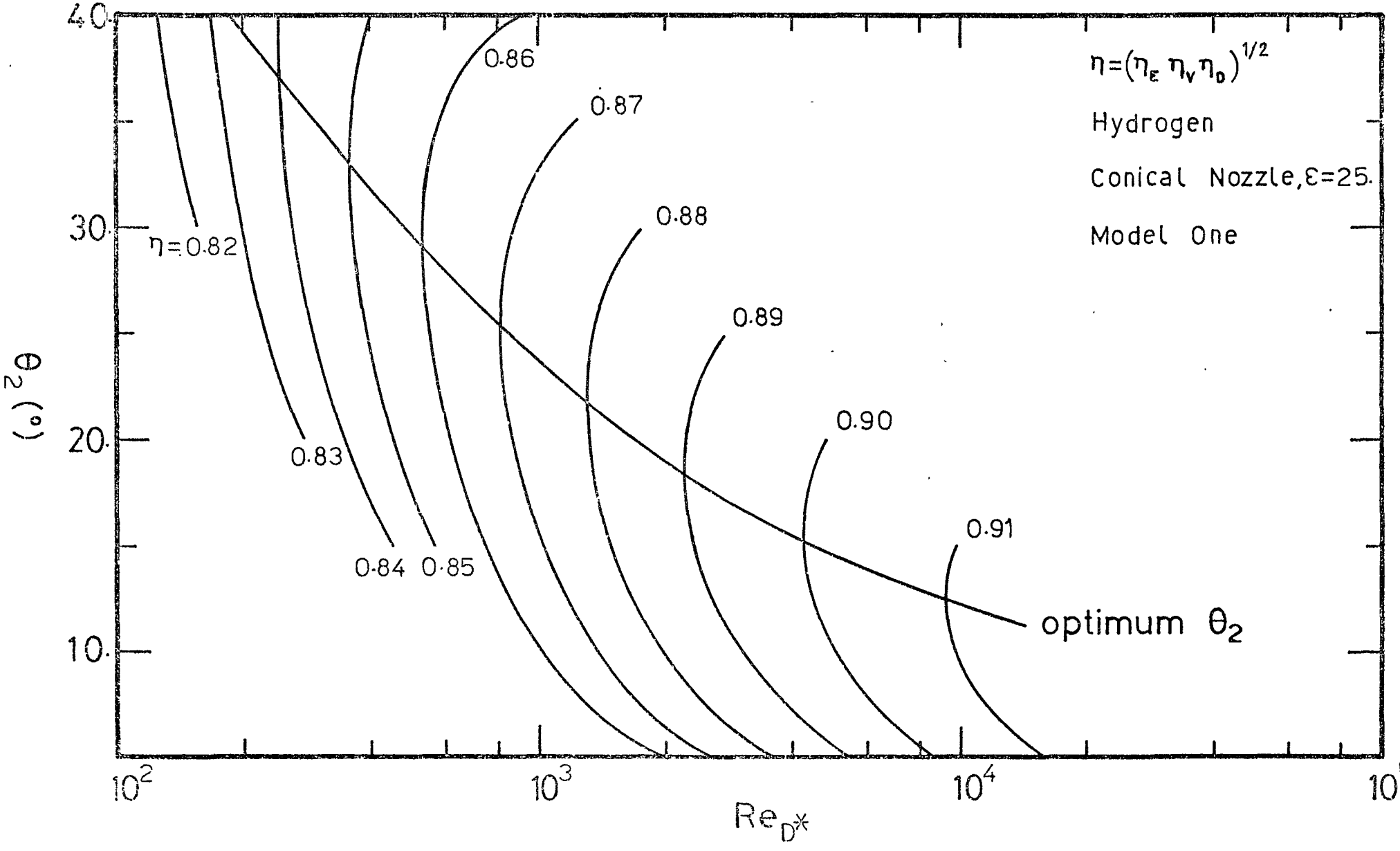

Fig·52 Variation of Nozzle Efficiency with Divergent Half Angle

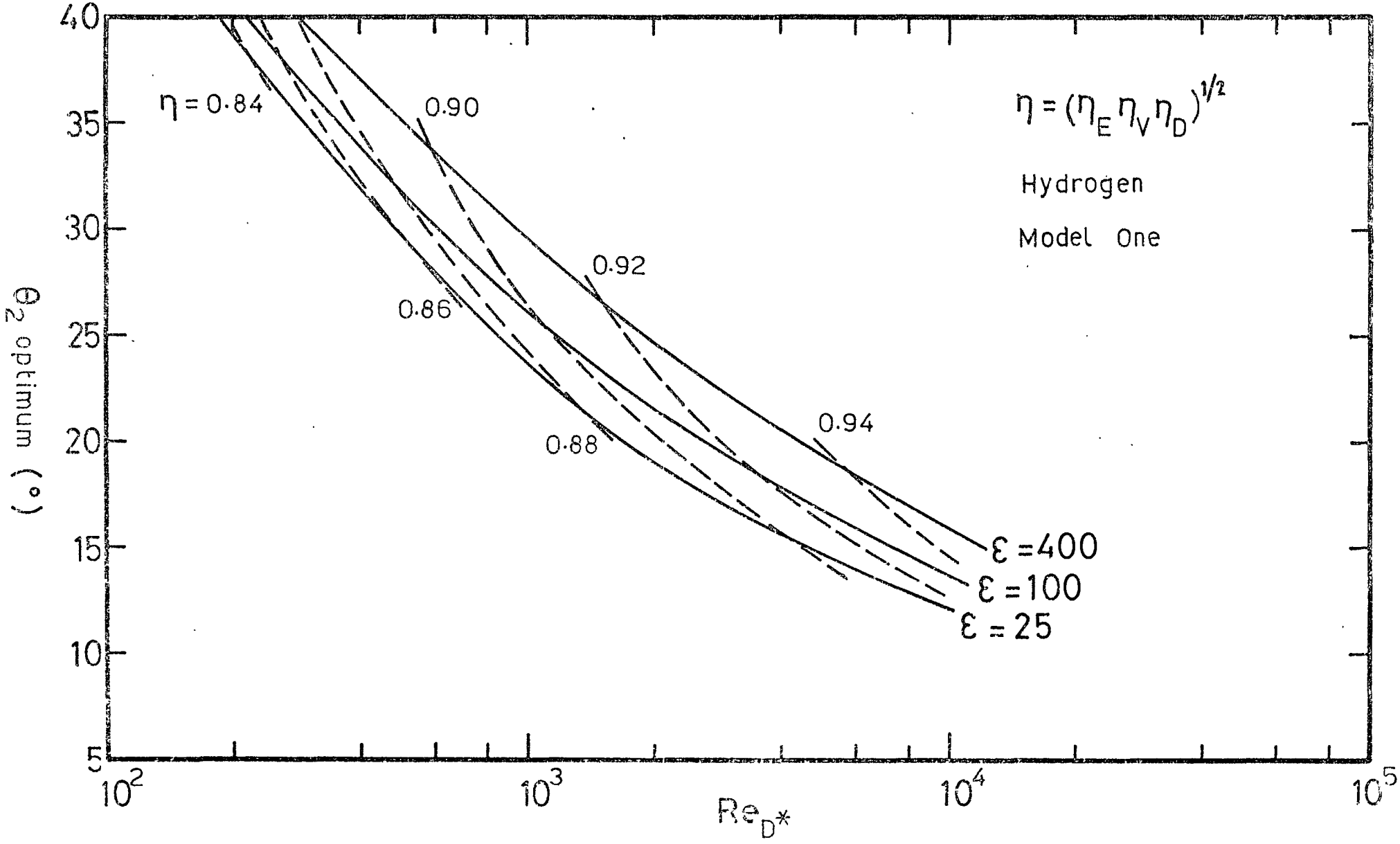

Fig-53 Optimum Divergent Half Angle for Conical Nozzles

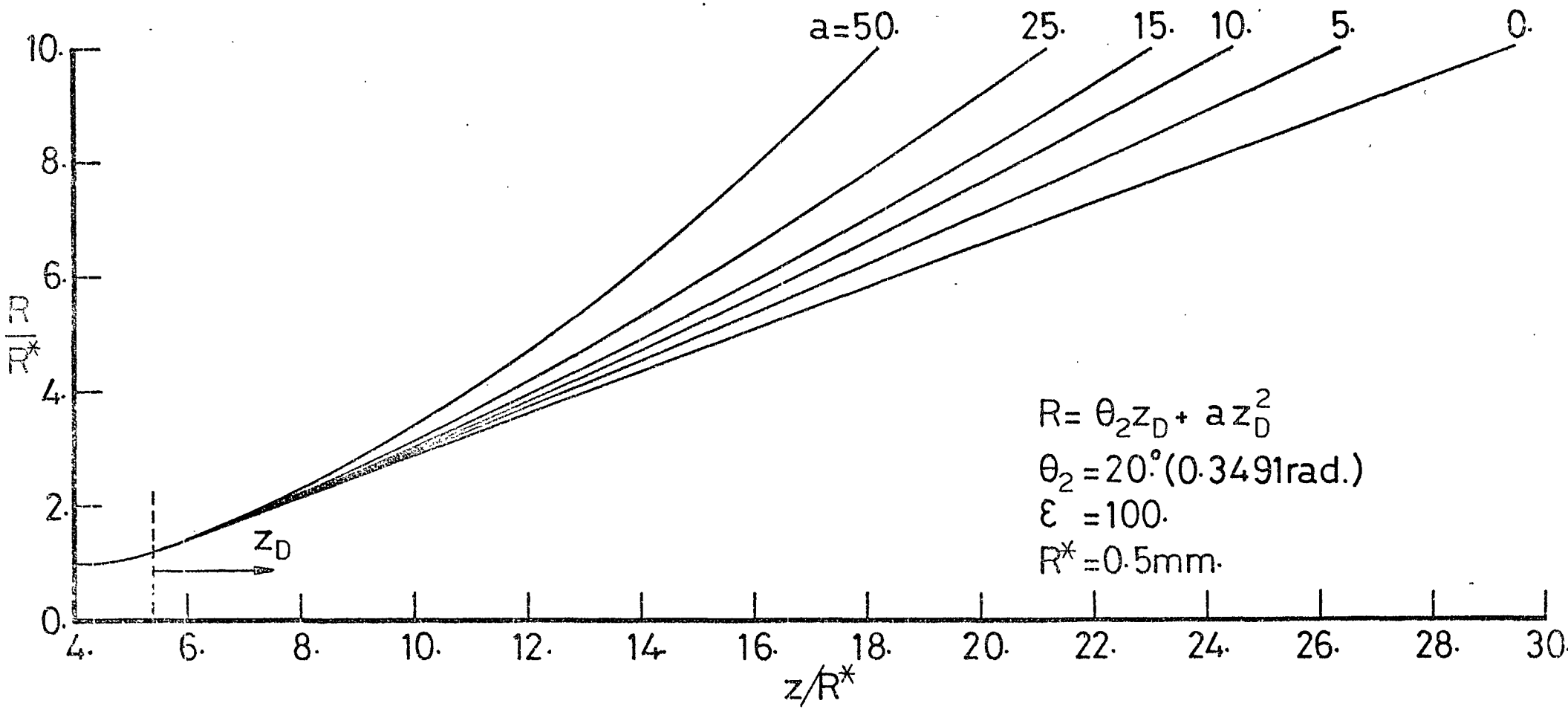

Fig.54 Shape of Nozzle Divergent Section (20xfull size)

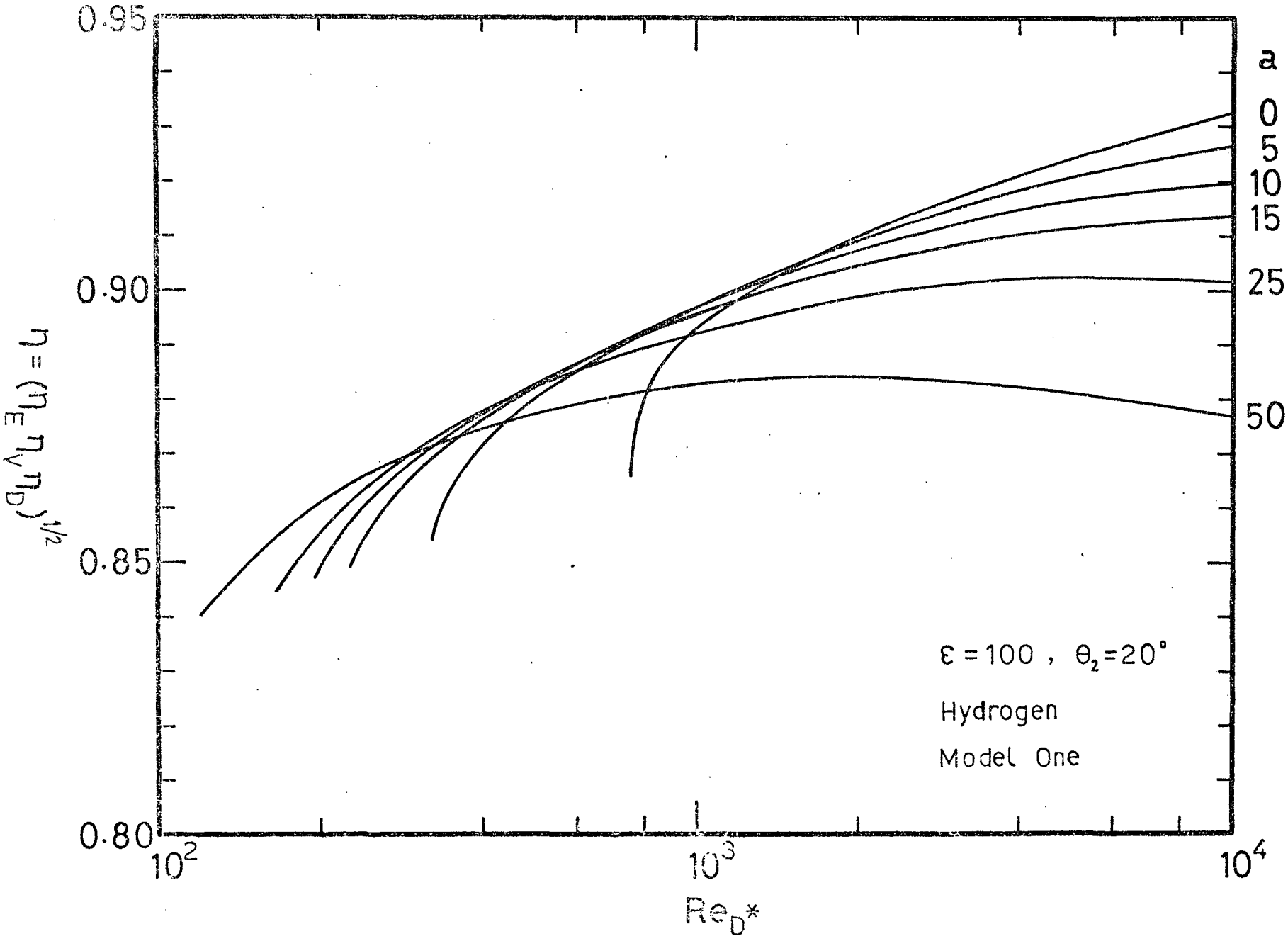

Fig.55 Effect of Shape of Divergent Section on Nozzle Efficiency

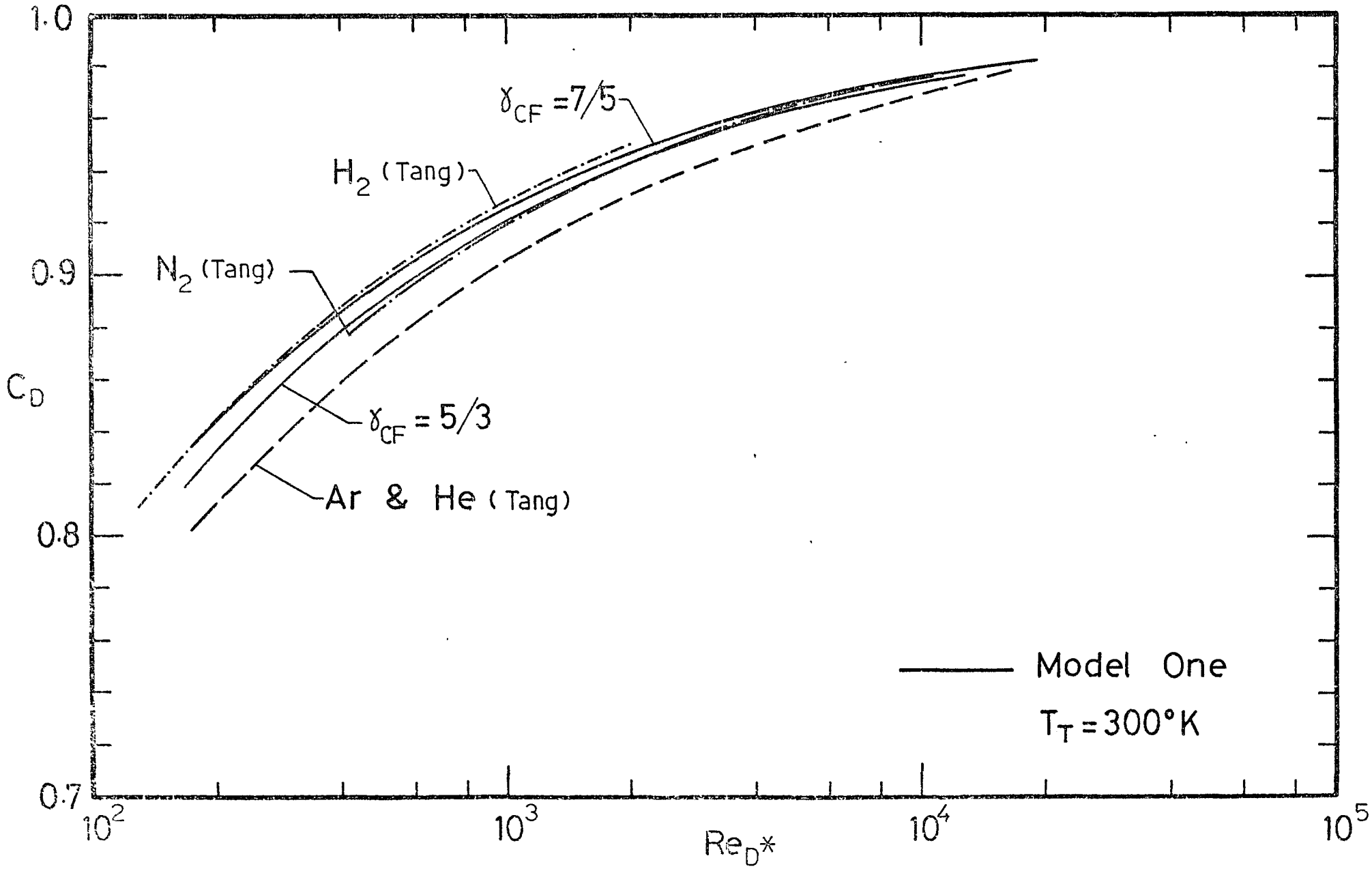

(a) Variation of C_D with propellant

Fig-56 Comparison with C_D Measurements of Tang

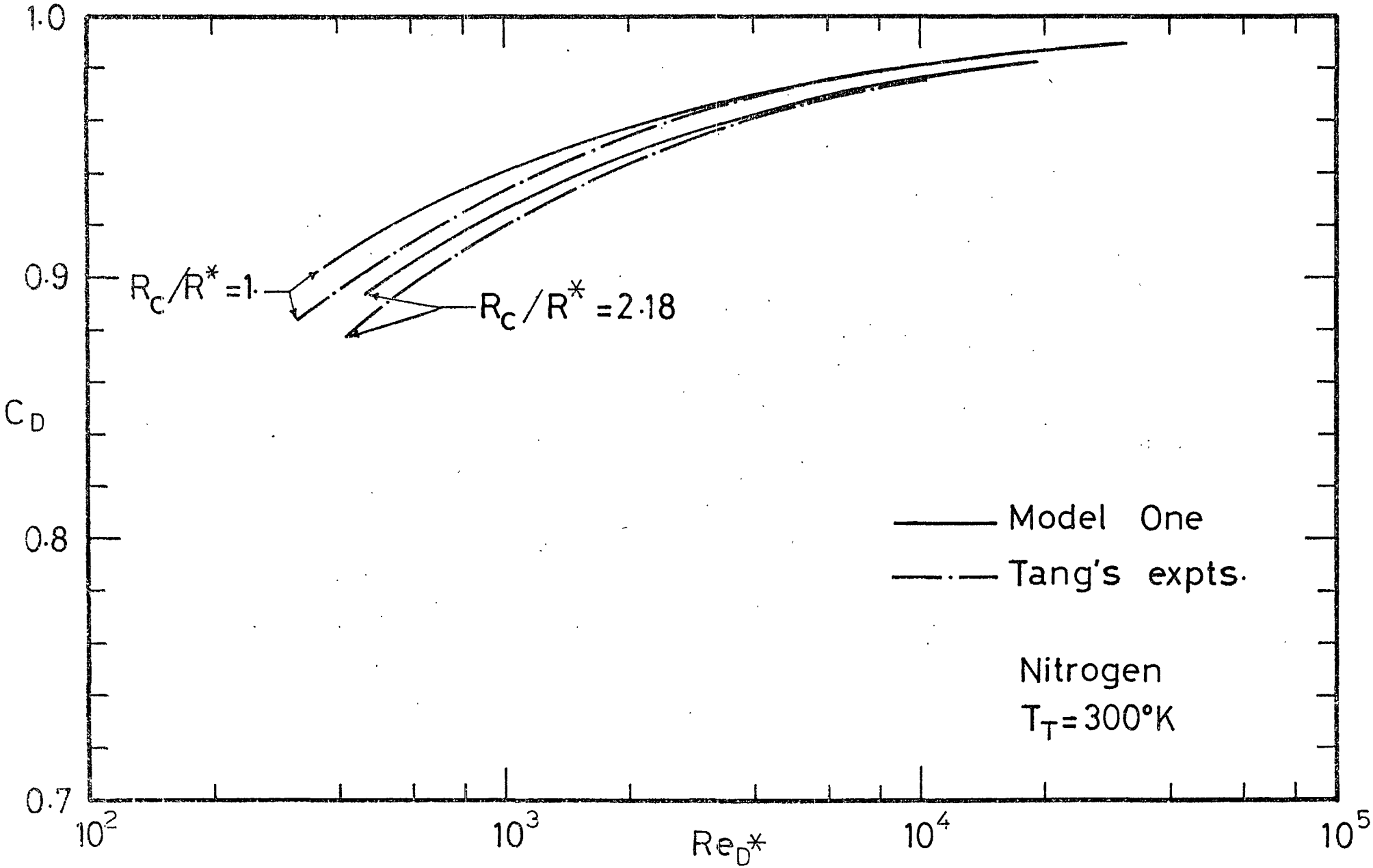

(b) Variation of C_D with throat geometry

Fig·56 continued

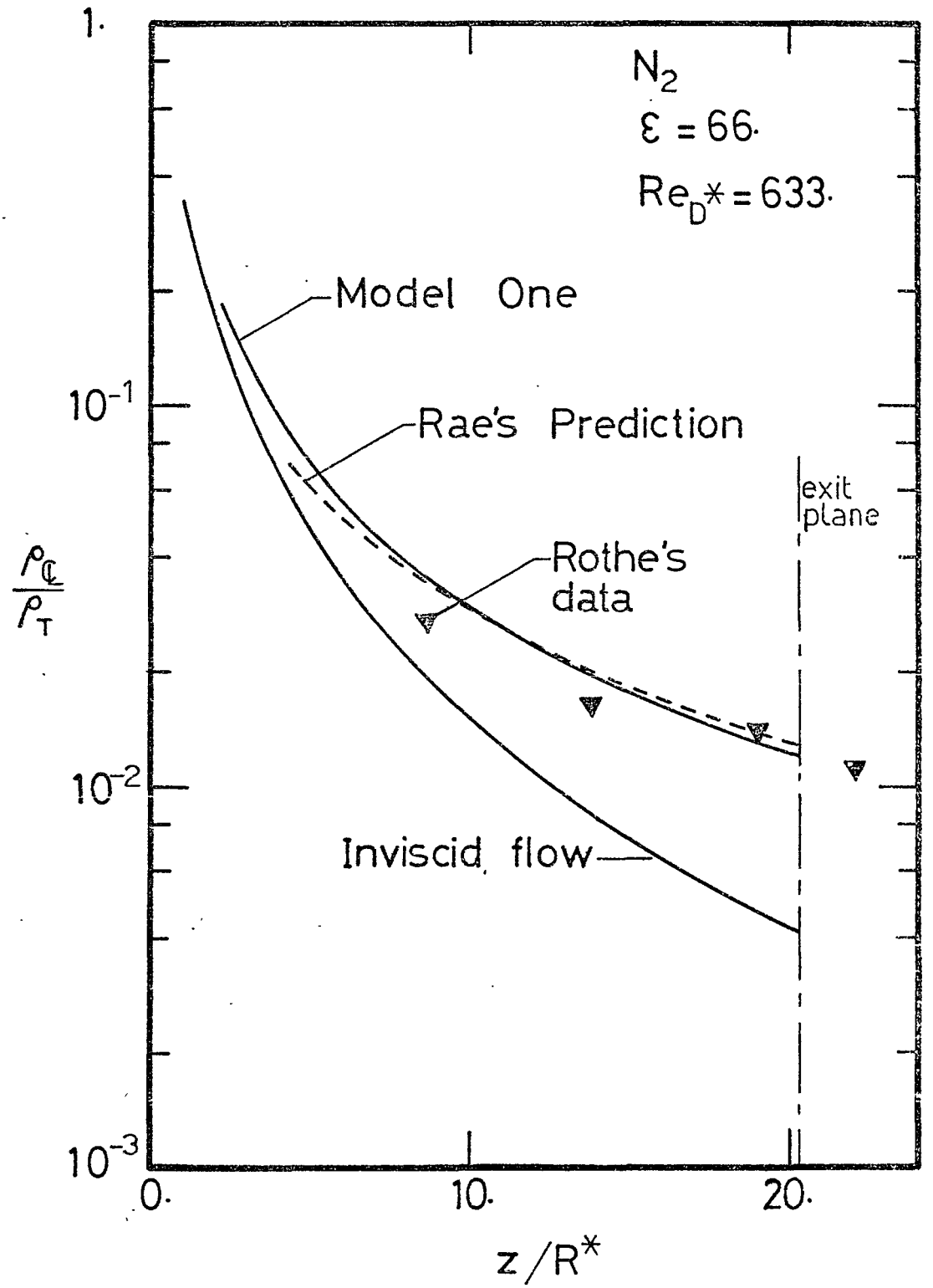

(a) Centreline density distribution

Fig.57 Comparison with the Viscous Nozzle Experiments of Rothe

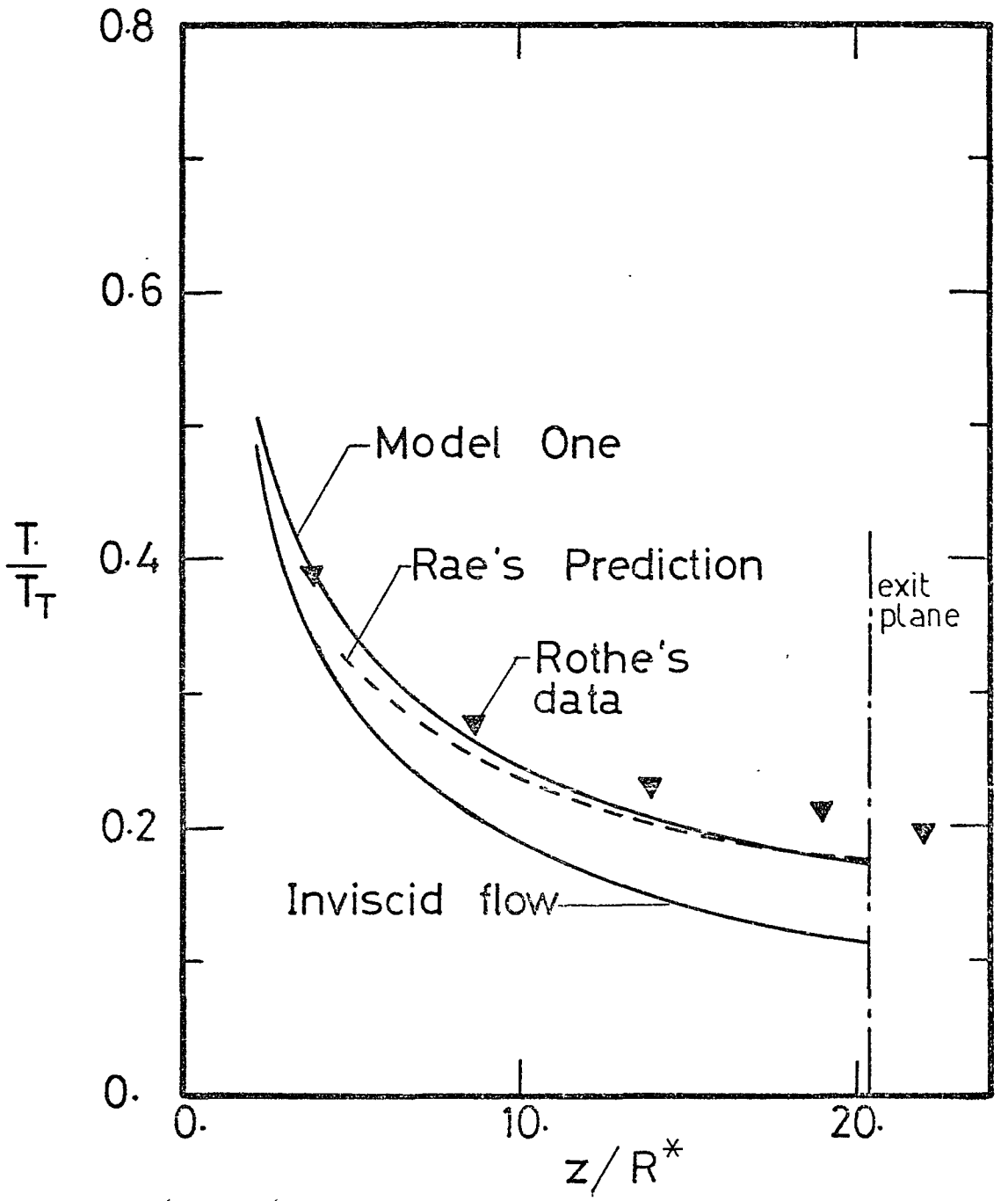

(b) Centreline temperature distribution

Fig·57 continued

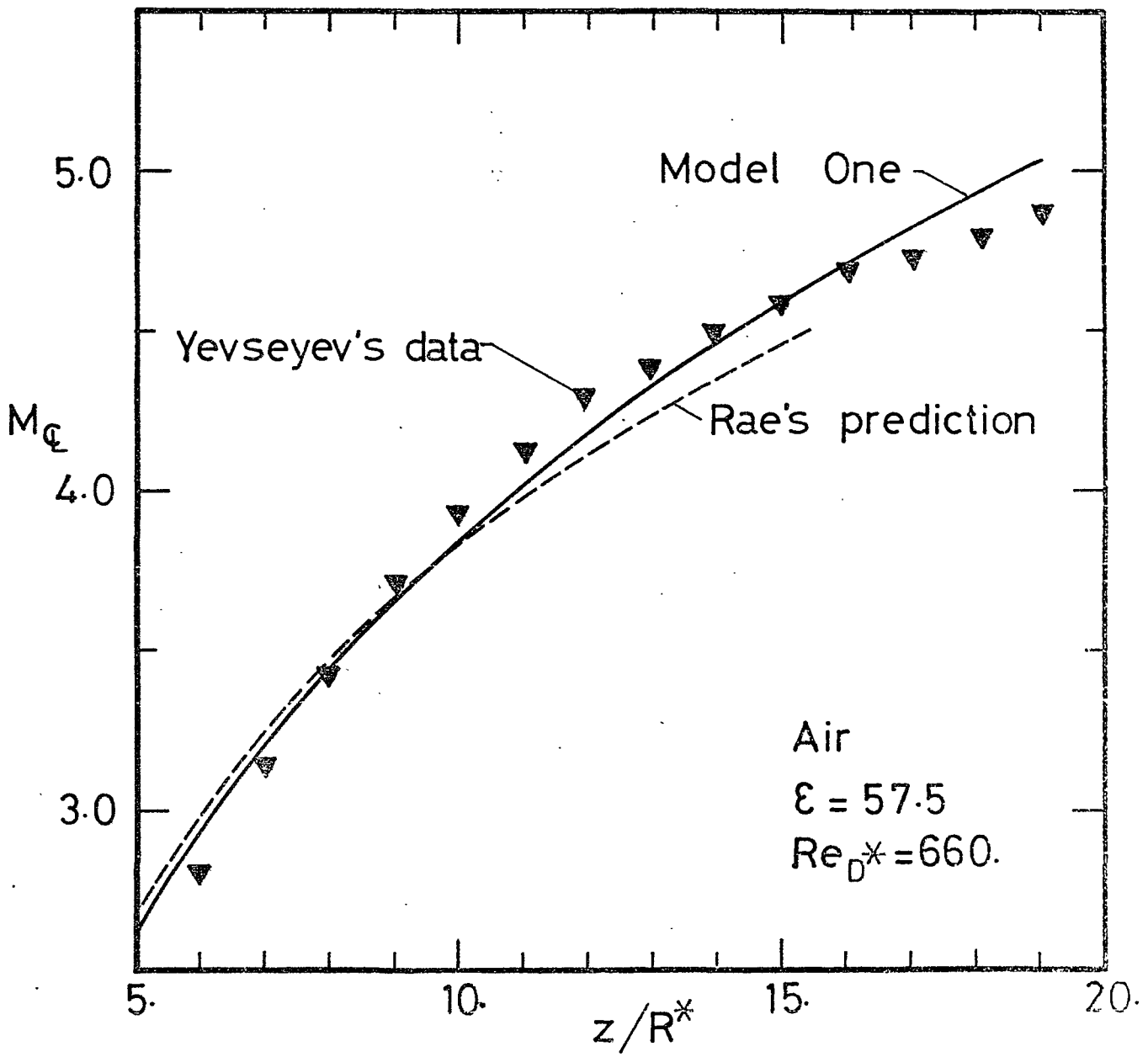

(a) Distribution of centreline Mach Number

Fig.58 Comparison with Experiment of Yevseyev

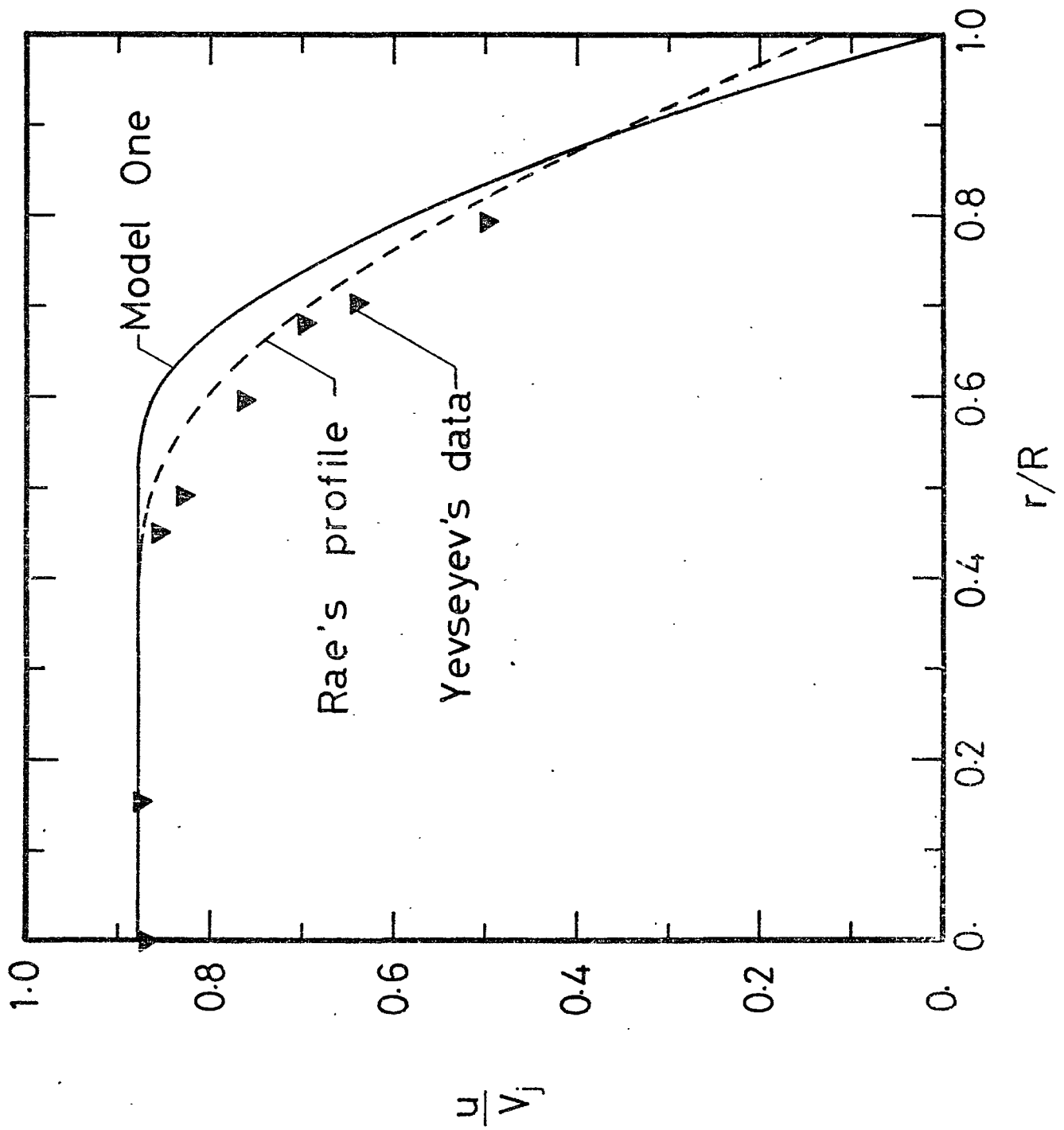

(b) Velocity profile at $z/R^* = 11.1$

Fig.58 continued

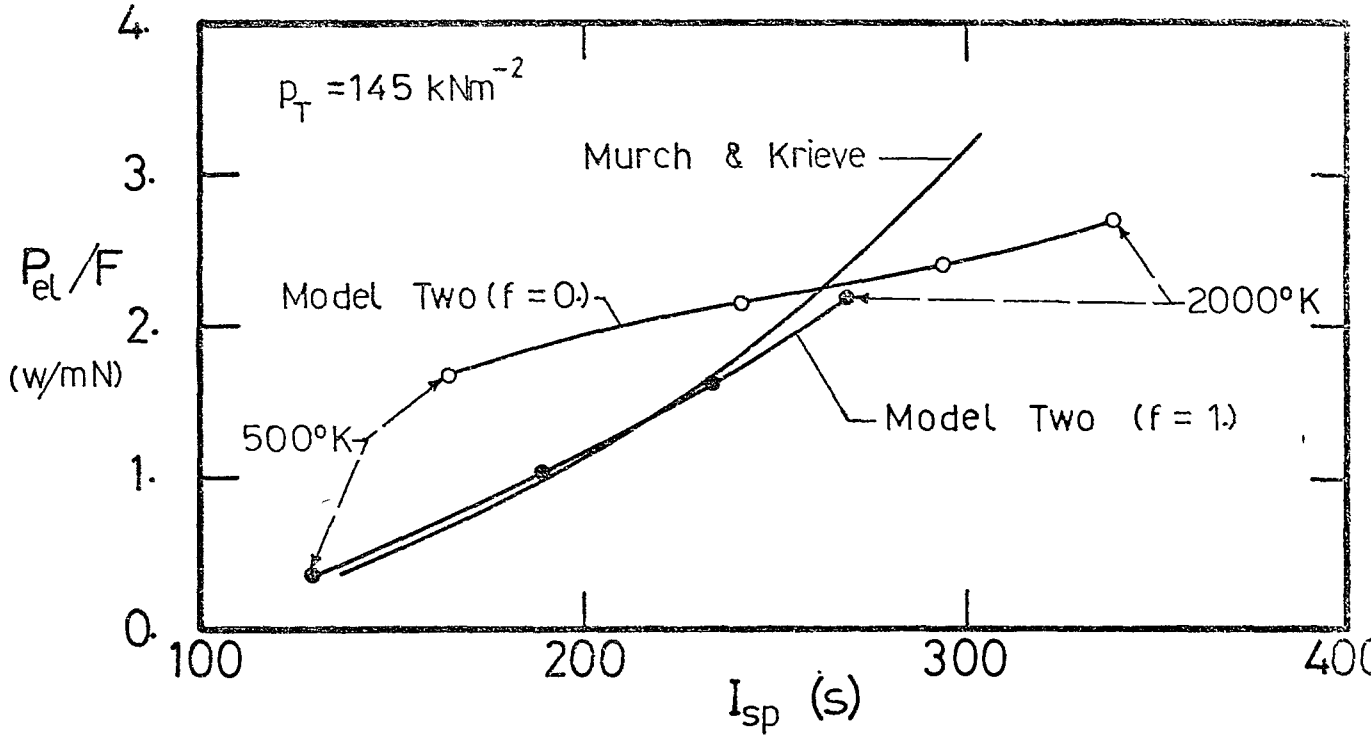

(a) Electric Power/Unit Thrust versus Specific Impulse

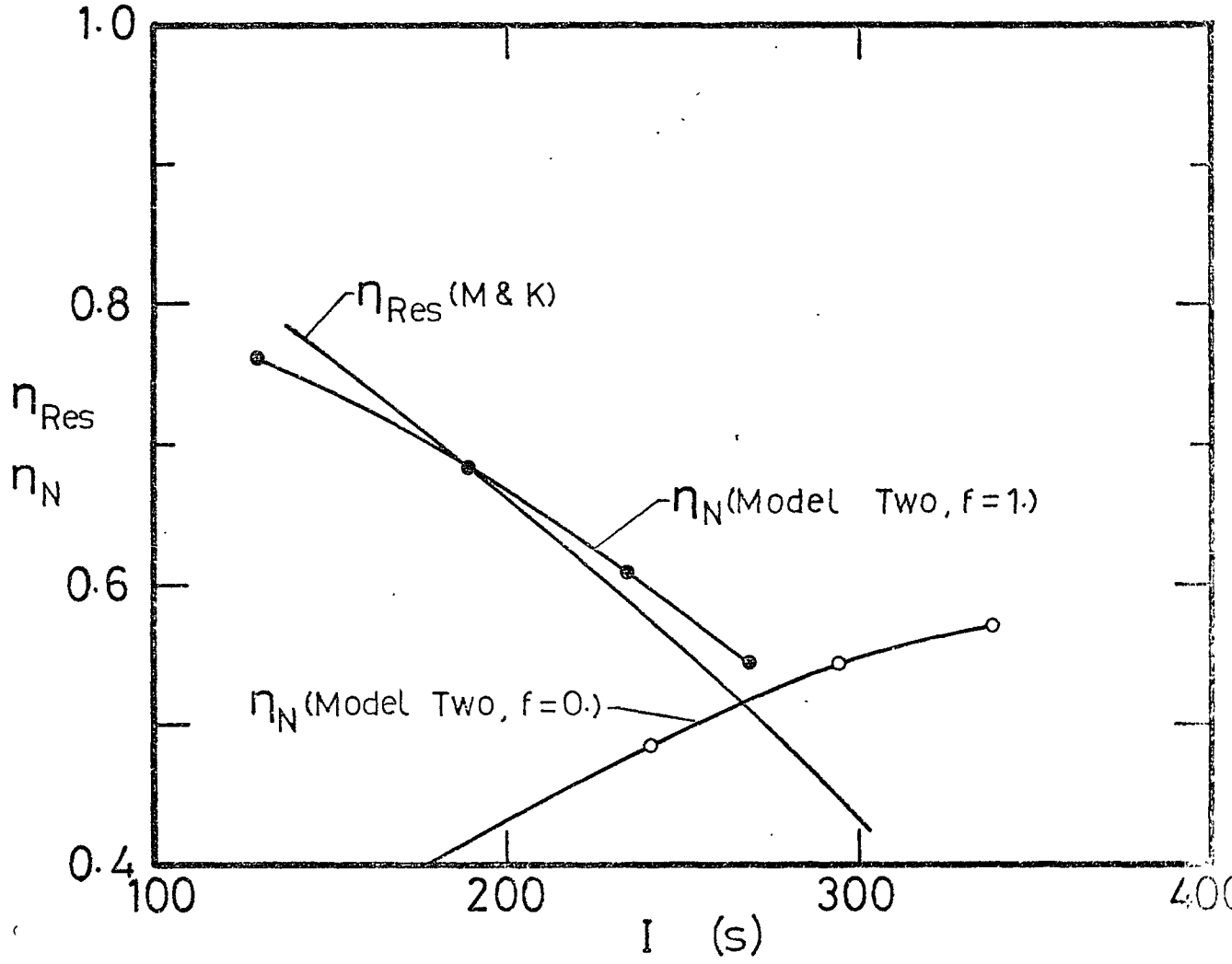

(b) Overall Efficiency

Fig.59 Ammonia Performance--Experimental Comparison

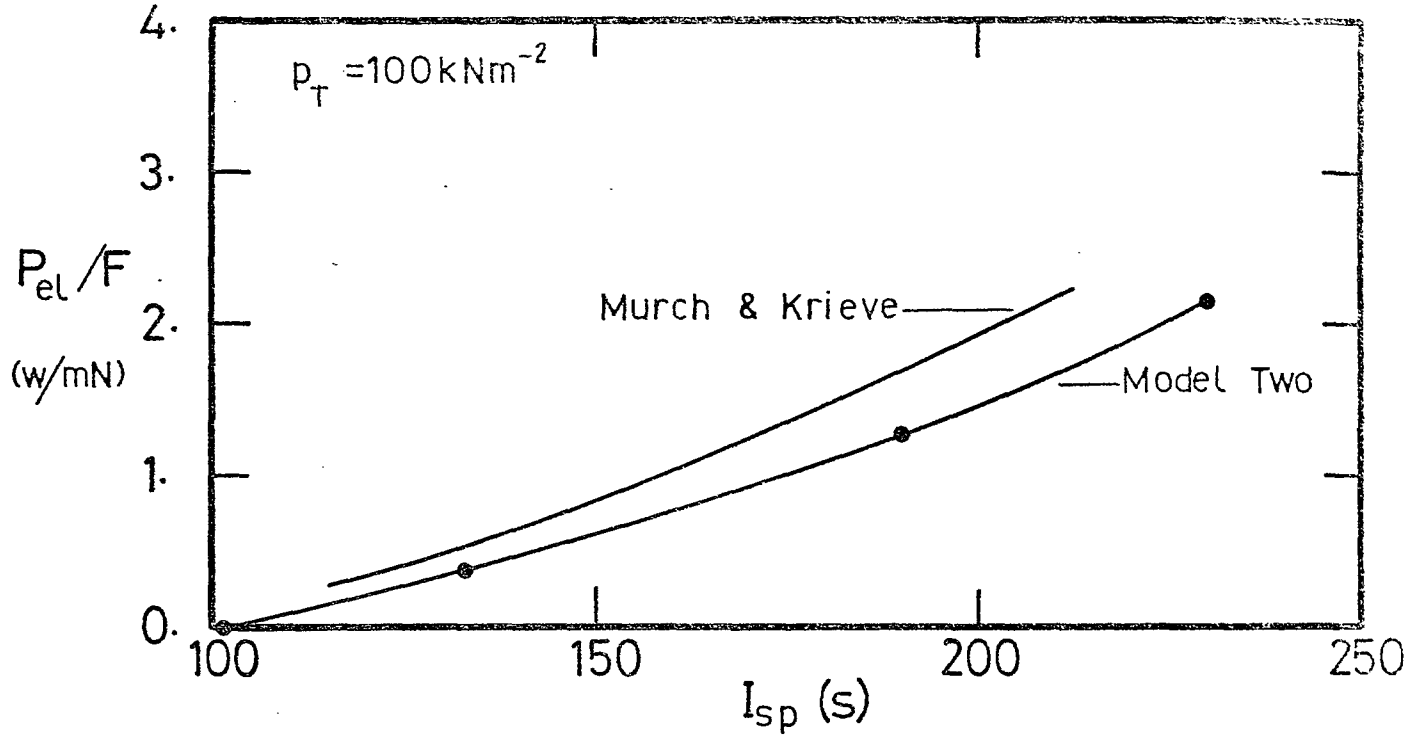

(a) Electric Power/Unit Thrust versus Specific Impulse

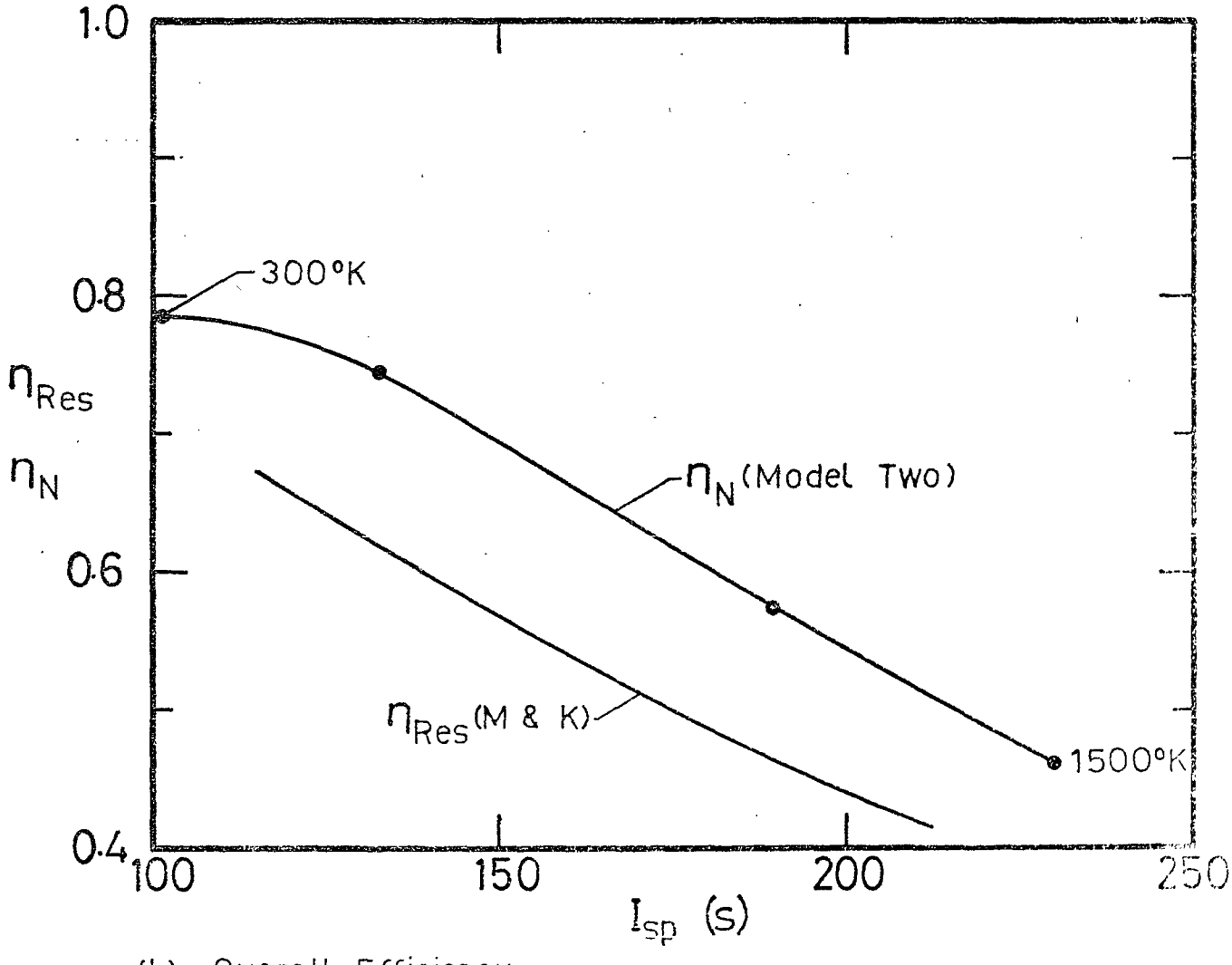

(b) Overall Efficiency

Fig.60 Methane Performance-Experimental Comparison

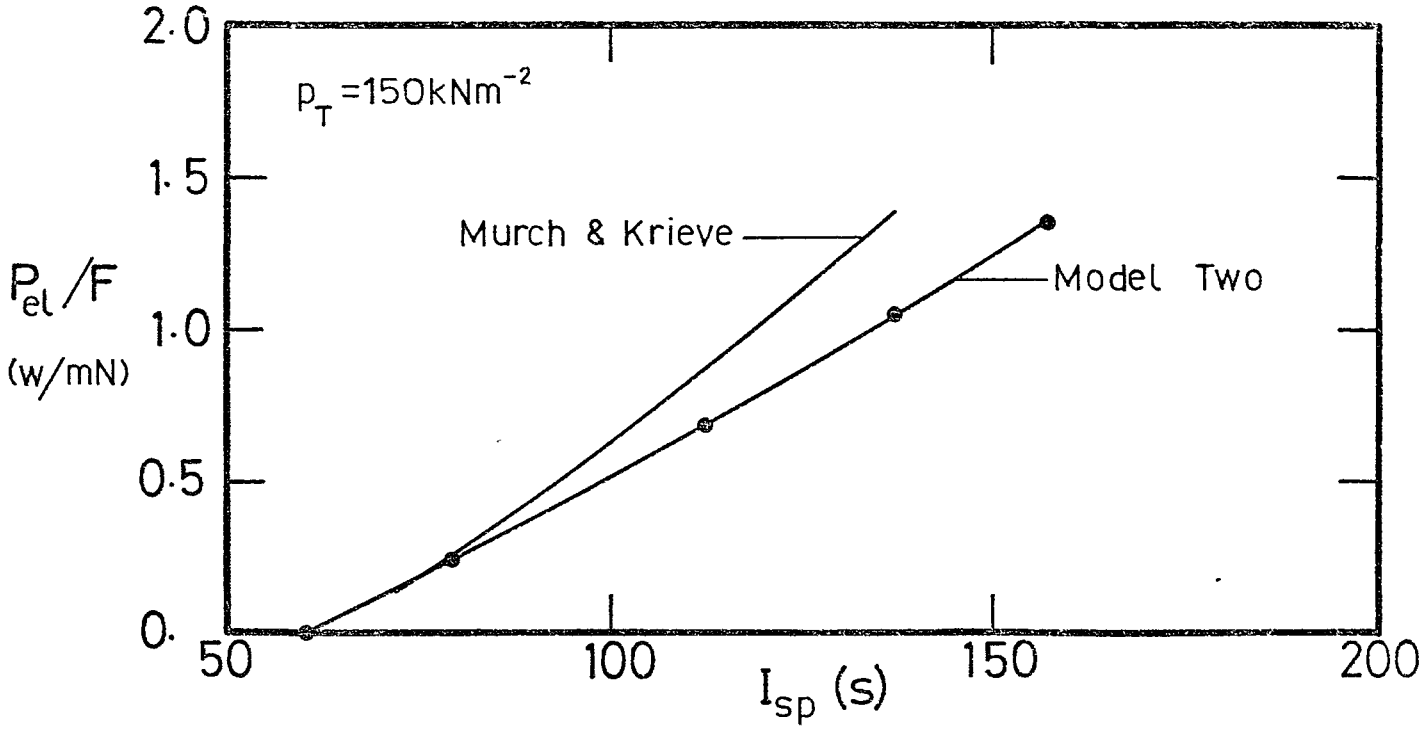

(a) Electric Power/Unit Thrust versus Specific Impulse

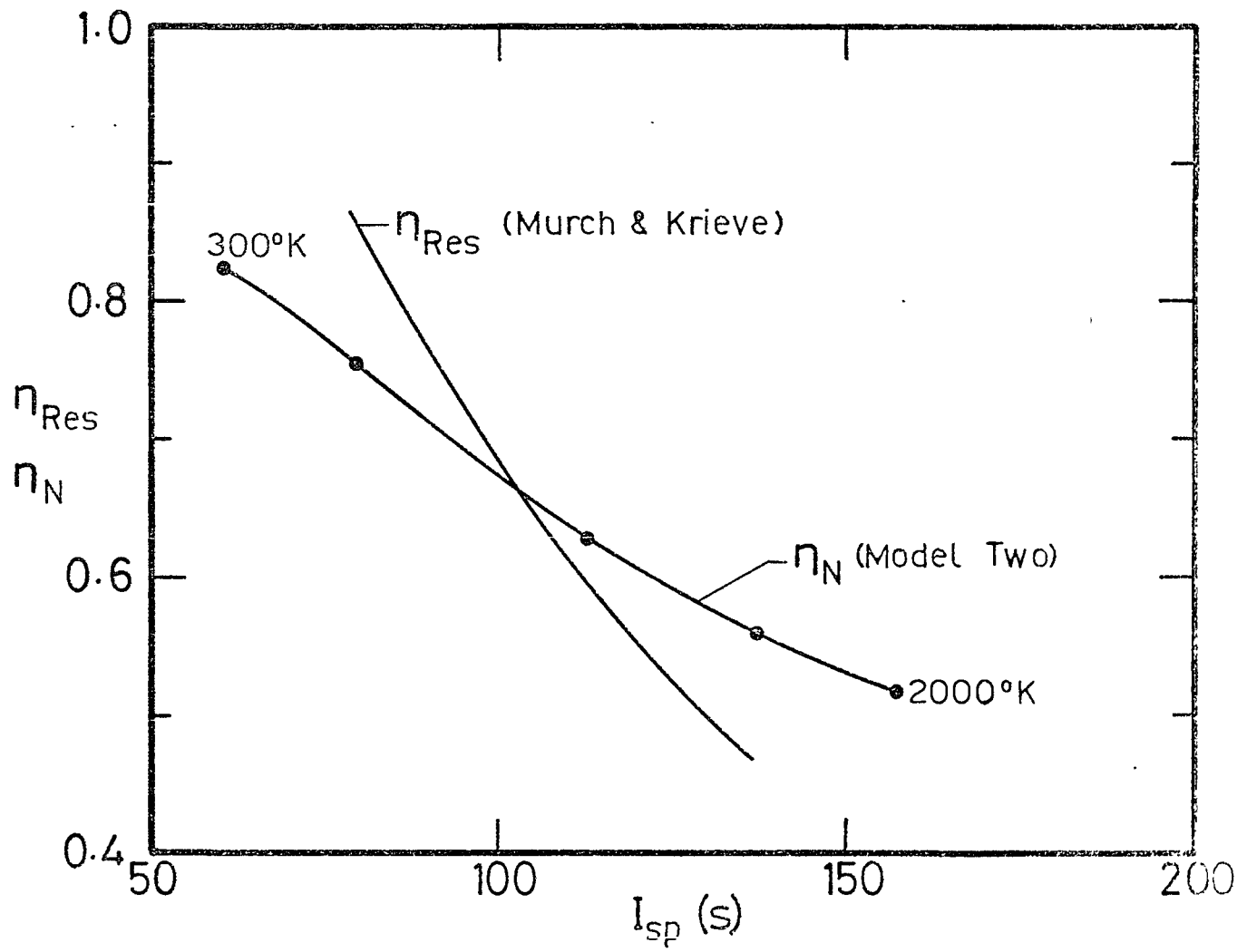

(b) Overall Efficiency

Fig·61 Carbon Dioxide - An Experimental Comparison